Microstructure, Texture and Mechanical Property Evolution during Additive Manufacturing of Ti6Al4V Alloy for Aerospace Applications

A thesis submitted to the University of Manchester for the degree of Doctor of Philosophy in the faculty of Engineering and Physical Sciences

2012

Alphons Anandaraj ANTONYSAMY

School of Materials

CONTENTS

ABSTRACT

Additive Manufacturing (AM) is an innovative manufacturing process which offers near-net shape fabrication of complex components, directly from CAD models, without dies or substantial machining, resulting in a reduction in lead-time, waste, and cost. For example, the buy-to-fly ratio for a titanium component machined from forged billet is typically 10-20:1 compared to 5-7:1 when manufactured by AM. However, the production rates for most AM processes are relatively slow and AM is consequently largely of interest to the aerospace, automotive and biomedical industries. In addition, the solidification conditions in AM with the Ti alloy commonly lead to undesirable coarse columnar primary β grain structures in components. The present research is focused on developing a fundamental understanding of the influence of the processing conditions on microstructure and texture evolution and their resulting effect on the mechanical properties during additive manufacturing with a Ti6Al4V alloy, using three different techniques, namely; 1) Selective laser melting (SLM) process, 2) Electron beam selective melting (EBSM) process and, 3) Wire arc additive manufacturing (WAAM) process.

The most important finding in this work was that all the AM processes produced columnar β-grain structures which grow by epitaxial re-growth up through each melted layer. By thermal modelling using TS4D (Thermal Simulation in 4 Dimensions), it has been shown that the melt pool size increased and the cooling rate decreased from SLM to EBSM and to the WAAM process. The prior β grain size also increased with melt pool size from a finer size in the SLM to a moderate size in EBSM and to huge grains in WAAM that can be seen by eye. However, despite the large difference in power density between the processes, they all had similar G/R (thermal gradient/growth rate) ratios, which were predicted to lie in the columnar growth region in the solidification diagram. The EBSM process showed a pronounced local heterogeneity in the microstructure in local transition areas, when there was a change in geometry; for e.g. change in wall thickness, thin to thick capping section, cross-over's, V-transitions, etc. By reconstruction of the high temperature β microstructure, it has been shown that all the AM platforms showed primary columnar β grains with a $<001>_{\beta}$ || Nz fibre texture with decreased texture strength from the WAAM to the EBSM and SLM processes. Due to a lack of variant selection, the room temperature α-phase showed a weaker transformation α-texture compared to the primary β-texture with decreased texture strength in line with the reduction in β-texture strength.

The large β grains observed in the WAAM process were not significantly affected by changes in the GTAW (Gas Tungsten Arc Welding) process parameters, such as travel speed, peak to base current ratio, pulse frequency, etc. However, an increased wire feed rate significantly improved

the grain size. Another important finding from this work was that by combining deformation and AM the grain size was reduced to a greater extent than could be achieved by varying the arc or, heat source parameters. It has been shown that the large columnar β-grain structure usually seen in the WAAM process, with a size of 20 mm in length and 2 mm in width, was refined down to ~ 150 μm by the application of a modest deformation, between each layer deposited.

The EBSM process showed consistent average static tensile properties in all build directions and met the minimum specification required by ISO 5832-3 (for the wrought and annealed Ti6Al4V). The WAAM samples produced using more effective shielding and the standard pulsed GTAW system also showed average static properties that met the minimum specification required by AMS 4985C for investment casting and hipped Ti6Al4V alloy. Overall, the fatigue life of the samples that were produced by AM was very good and showed a better fatigue performance than the MMPDS design data for castings. However, there was a large scatter in the fatigue life due to the effect of pores.

DECLARATION

No portion of the work referred to in the thesis has been submitted in support of an application for another degree or qualification of this or any other university or other institute of learning.

COPYRIGHT

ACKNOWLEDGEMENTS

I avail this unique opportunity to express my profound sense of gratitude and indebtedness to my supervisor **Prof. Dr. Philip B Prangnell** (Professor of Materials Engineering, School of Materials, The University of Manchester, UK) for his efficacious advice, criticisms and perpetual encouragement throughout the project work, without which it would not have been possible to complete my PhD.

I would like to express my thanks to my Industrial supervisor Jonathan Meyers (Team Leader, AM centre - EADS Innovation works, AIRBUS, UK) and Prof. Dr. Stewart Williams, (Director of Welding Engineering and Laser Processing Centre, Cranfield University, UK), for rendering all kinds of help and technical discussion necessary throughout my project work.

I am indebted to the full financial support provided by **EPSRC IDS Scheme, EP/D029201/1** (under the University of Manchester, **LATEST 2** - Light Alloys towards Environmentally Sustainable Transport Portfolio Partnership 2nd Generation) and **EADS Innovation Works, UK** towards my research, bursary and conferences expenditures throughout period of this project in UK.

I do acknowledge the constant support and blessings from my parents. I also thank my younger and elder sister for continuous encouragement and moral support during these years.

I would like to thank few other specific researchers and industrial collaborators who helped me throughout the period of this project, Dr. Fude Wang (Senior Research fellow, at Cranfield University), Bernard Mulvihill (Research and Technology Strategy Engineer, Bombardier Aerospace, Belfast), Chris Turner (Research Engineering, EADS-UK), and Dr. Sozon Tsopanos (Senior Project Leader at TWI-UK).

I thank Dr. Brad Wynne and Dr. Peter Davies from IMMPETUS, University of Sheffield-UK, and Prof Peter Bate and, Dr. D. G. Leo Prakash from MMSC, The University of Manchester-UK for their assistance with β reconstruction, and for assistance with texture simulations, respectively. Thanks are also given to John Gardiner and Almeida Pedro for their continuous technical assistance and, support during the production of the AM samples at AM Centre, Bristol and at Cranfield University, UK. Special thanks are due to Dr. Joe Robson, Lee Campbell, and Christopher Smith regarding the thermal modelling of AM process using TS4D software. I would also like to thank Prof. Ian Todd for the discussion and more understanding of Arcam machine.

Acknowledgement is made to all lab personnel in the Manchester Materials Science centre for their kind cooperation. Special thanks are due to Farid Haddadi, Thomas Hill, Alexandria Pentali,

Ross Nolen, Samuel Thomas Williams, David Strong, David Griffith, David Mackie Lawrence Ko, Rotimi Joseph Oluleke, Liam Dwyer, Dr. Gideon Obasi, Rebecca Sandala, Dr. Christopher Derry, Dr. Ying Chun, Dr. D Tisivulous, Chruli porn, Jesan, Ley, and other rest of LAP group members at Univ. of Manchester for their continuous support. Last but not least, I express my thanks to all my friends especially Lakshmi L. Parimi, Mahesh Kumar M, Sreevathsan R, Preti Adnani, Aleba Alebangeo, Arun J, Arun R, Dilip Samuel, sreedhar, Anil, Ramesh Constantine, Premila Constantine, Arumugam and his family, Nimal and his family for their continuous support and constant encouragement during this period.

Alphons Anandaraj ANTONYSAMY

DEDICATION

To My Parents… ***&***

To the Researchers Working in Additive Manufacturing Technology

PUBLICATIONS AND ORAL PRESENTATIONS FROM THIS WORK

The following were the contributions from the experimental work undertaken during this PhD work project.

Contribution to International Conferences

- Alphons A. Antonysamy, Phil B. Prangnell and Jonathan Meyer, 'Effect of Wall Thickness Transitions on Texture and Grain Structure in Additive Layer Manufacture (ALM) of Ti6Al4V', International conference on Processing & Manufacturing of Advanced Materials – THERMEC'2011, Quebec, Canada.
- Alphons A. Antonysamy, Phil B. Prangnell and Jonathan Meyer, 'Influence Of Build Geometry On Microstructure And Texture Development During Additive Layer Manufacture Of α-β Ti6Al4V Alloy By Electron Beam Selective Melting', 12th International conference – Titanium 2011, Beijing, China.

Journal papers

- A.A Antonysamy, P.B. Prangnell and J. Meyer, 'Effect of Wall Thickness Transitions on Texture and Grain Structure in Additive Layer Manufacture (ALM) of Ti6Al4V', Materials Science Forum, Vols.706-709 (2012), pp. 205-2010.
- Alphons A Antonysamy, Phil B Prangnell and Jonathan Mayer, 'Effect of Build Geometry on Beta Grain Structure and Texture in Additive Layer Manufacture of Ti6Al4V by Electron Beam Selective Melting' (*to be **re-submitted** to Acta Materialia*).
- Alphons A Antonysamy, Phil B Prangnell, Filomeno Martina, Stewart Williams, 'Effect of Rolling Deformation in the Wire Arc Additive Manufacturing of Ti6Al4V alloy' (*ready to be submitted in Materials Science and Engineering A*).
- Fude Wang, Stewart Williams, Paul Colegrove, Alphons Antonysamy, Philip Prangnell, Microstructure and Mechanical Properties of Additive Layer Manufactured Ti6Al4V Alloy (under *review in Metallurgical and Materials Transaction A*).

- Alphons A. Antonysamy, Fude Wang, Stewart Williams, Philip Prangnell, Microstructure and Mechanical Properties of Wire Arc Additive Manufacturing of Ti6Al4V alloy using GTAW process (ready to be submitted).

Posters

- Winner of the best research poster at the 'National Level Conference on Technology Developments in Titanium' event run by TIG and commenced at NAMTEC's Swinden House, Sheffield UK on the 7th April 2011.

In addition, the posters from this research were also presented at Manchester University in the School of Materials 'PG Conference -2010' and in the 'LATEST2 Joining Conference - 2011'.

Oral presentations

- Alphons A Antonysamy, 'Microstructure Control in Additive Layer Manufacturing Ti6Al4V for Aerospace Application', 3st, 4th and 5th, '*EADS-Airbus PhD Seminar on ALM'* (European level), at EADS Innovation Works, Filton, Bristol, UK.

- Alphons A Antonysamy, 'Microstructure Control in Additive Layer Manufacturing Ti6Al4V using Arc Welding Deposition technique for Aerospace Application', 2nd, 3rd, 4th, 5th, 6th and 7th '*RUAM-National Level Industry Day'* (Ready to Use Additive Manufacturing 2009-11) at University of Cranfield, UK.

In addition, number of oral presentations was presented from this research at Manchester University during PG conferences held in 2009 - 2012 and, during Review of the LATEST (Light Alloys for Environmentally Sustainable Transport) EPRSC-Portfolio Partnership for LATEST 2 funding in 2009.

LIST OF ABBREVIATIONS

AM-Additive manufacture

ALM - Additive layer manufacture

UTS- Ultimate tensile strength

YS - Yield strength

WAAM - Wire arc additive manufacture

SLM- selective laser melting

EBSM - Electron beam selective melting

SEBM – Selective electron beam melting

LC-Laser cladding

GTAW - Gas tungsten arc welding

GMAW - Gas metal arc welding

TIG - Tungsten inert gas

MIG - Metal inert gas

CMT - Cold metal transfer

HF - High frequency

T.S – Travel speed

WFS- Wire feed speed

EBSD –Electron backscattered diffraction

TS4D –Thermal simulation in 4 dimensions

EADS-European aerospace and defence security

RUAM – Ready to use additive manufacture

HCF-High cycle fatigue

IPF – inverse pole figure

SMD - Shaped metal deposition

DLF - Direct laser fabrication

LIST OF FIGURES

LIST OF TABLES

1 INTRODUCTION

The advisory Council for Aeronautics Research in Europe (ACARE) in the 'Flight Path 2050' report have suggested targets for reductions in CO_2 emissions, NO_x emissions, and perceived Noise, based on 2000 levels, by 75%, 90%, and 65% respectively by 2050 [1]. These objectives are to be achieved despite a planned increase in traffic to around 25 million flights per year in Europe, more than double the current level [1, 2]. Therefore, the search for more fuel efficiency air craft and alternative new eco-friendly greener and leaner manufacturing processes has gained momentum.

The innovative process, near-net-shape Additive Manufacturing (AM), has gained considerable attention in the aerospace industry due to its many potential benefits, such as, more geometric freedom, shortened design to product time, reduction in process steps, component mass reduction and material flexibility. AM can reduce the weight of components as well as CO_2 foot print, compared to traditional manufacturing processes, and is therefore greener while saving aircraft manufacturers and airlines time and money. A rule of thumb in the airline business is that every kilogram that can be shaved off the mass of an airframe saves at least $3500 in fuel costs over the aircraft's life span, not to mention concomitant reductions in emissions of carbon dioxide[1, 2]. AM has potential to define the manufacturing landscape of tomorrow and hence, it's important to develop a better scientific understanding of the process to underpin the industrial development of the technology.

1.1 WHAT IS ADDITIVE MANUFACTURING (AM)

AM is a novel near-net-shape fabrication technique used to produce solid components by consolidating layers of powder, or wires or ribbons, by partial or full melting. The materials to be deposited are melted by a focussed heat source, provided by an electron beam (e-beam), laser beam, or plasma or electric welding arc. Each layer is a 2D section from a final 3D CAD component model: i.e., the 3D geometry of a component is formed by building-up a stack of 2-D profiles, layer-by-layer, by local melting [3].

The powder bed AM method is expensive but allows dimensionally more precise components to be produced. Laser beam powder bed AM is used for small parts with high precision, whereas the electron beam-powder bed AM is used for bigger and parts with rougher surface. However, Arc plus wire AM is an alternative cheaper technique that gives higher deposition rates. This technique is restricted to wider wall thicknesses and is more suitable for larger scale products

which can be built out of chamber [4-6]. The benefits and disadvantages of these processes will be discussed in more detail in the forthcoming AM chapter (1.2 and 1.6).

1.2 ADVANTAGES OF AM

AM is a manufacturing process which offers near-net shape fabrication of complex components without dies or substantial machining, resulting in a reduction in lead-time, waste, and cost. A major advantage of the technology lies in the ability to produce complex geometries which allows the manufacture of novel, light-weight structures from a low density alloy [4, 5]. The production of such highly complex titanium components is of great interest for automotive and aerospace applications.

In the last few years, interest in AM has been increased due to the ability of the process to produce rapid prototypes, and near net shape components. The following main factors outline the potential benefits for AM in the aerospace manufacturing industry,

a) AM is a near net shape fabrication technique which transforms a powder, or wire, directly into the final solid component, with minimal finishing operations.

b) Complex shapes can be manufactured with shorter lead times and for less cost due to the absence of the requirement of tools, like forging dies which require several months or years to design and produce.

c) The geometric design flexibility of the process allows the production of more complex geometries that can be currently fabricated by other methods by control of the direction of deposition, spot size, and feed rate of powder and movement of the heat source. This step change in design flexibility of the process alone can result in major weight reductions, by better optimising the geometry of components.

d) AM is commercially highly preferable for sectors like aviation that involve low volume manufacturing, because of the reduced costs in producing bespoke parts

e) The buy-to-fly ratio of components produced via AM is roughly 1.5-5:1 (with less materials being wasted through machining), when compared to 10-20:1 for the normal ingot cast-roll-forging and machining route [6, 7]. This gives major advantages in terms of cost, especially when dealing with expensive reactive materials such as Ti, Co, Ni, and Cr based alloys.

f) Once a part is complete, any powder left over from the powder bed can be removed and re-used. This means AM uses 90% less raw materials than traditional methods [8]. For

example in some instances producing a machined component can mean material waste of up to 95% [7, 9].

g) Vacuum processes like Electron beam selective melting also provide very good protection from oxygen for reactive and expensive high temperature metals.

h) It is possible to produce internal honeycomb, or lattice, structures with controlled morphology and complete pore interconnectivity using AM [10].

i) AM can be used to produce a functionally graded structural components [11, 12].

j) AM allows the chance to more rapidly explore the feasibility of using new materials for same crucial applications [7].

k) AM can be used to manufacture tooling and high integrity repair of sophisticated structures in the aerospace industry.

l) There are low labour and tooling costs involved [13].

1.3 GENERAL LIMITATIONS OF AM

The following main factors outline the limitations of AM in the aerospace manufacturing industry,

a) Relatively low deposition rate and low build volume in the powder bed AM.
b) Though wire deposition provides higher deposition rate, the complex design parts can not be produced.
c) EBSM process needs high vacuum and high initial investment.
d) Control over the presence of defects such as pores, lack of fusion, etc.
e) Repeatability and reproducibility of the part quality.
f) There are no reliable test standards.

1.4 Ti ALLOYS IN AEROSPACE

A high strength combined with a low density (about 4.5 g/cm^3), good creep resistance up to about 550 °C, bio-compatibility, low modulus (high flexibility) and excellent corrosion resistance are the most interesting properties of Titanium alloys [4, 5]. These combined properties makes Titanium alloys an excellent choice for structural parts in the aircraft industry for air frames, aero-engines, bio-medical devices, and components for chemical processing Industries[4, 14]. Titanium alloys are used as an important lightweight material in modern aerospace structures, which need high structural efficiency, with high performance at moderate operating temperatures, as well as good fatigue and creep strength. Aluminium alloys are electrochemically incompatible with carbon fibre polymer composites, forming a galvanic couple when placed in direct contact. This reason,

coupled with the superior mechanical properties of titanium alloys, has lead to their increased usage in advanced commercial aircraft designs, with the Boeing 787 aircraft containing about 20% by weight of titanium alloy [4, 5]. The major concern in the use of Titanium alloys in other fields (such as automobile and chemicals industries) comes from the high production costs and the care required to obtain acceptable levels of quality [4]. Since the conventional production methods of Ti alloys (via casting-rolling-forging) are expensive because Ti is difficult to form and machine, it is therefore, highly desirable to be able to produce low volume complex components through the AM route.

1.5 APPLICATIONS OF AM

Industries requiring small production runs of the complex components in expensive materials such as aerospace, defence, spacecraft, automobile and the biomedical industries are the main areas, where AM is expected to offer the greatest benefits.

(1) Potential aerospace applications:

Currently, the major aerospace manufacturers and related research bodies, such as Rolls-Royce, EADS-AIRBUS, Bombardier, Boeing, GE, Air Force Research Lab-US, Aerosud, GKN Aerospace, etc are very keen to industrialise AM in civil and military aircraft and space vehicles applications. In the aerospace industry AM has four major applications; namely (i) the manufacture of components, (ii) repair, (iii) the manufacturing of the tooling and, (iv) repair of the tooling. The following examples illustrate advantages of the AM process to fabricate complex components for aerospace. Figure 1.1 shows example of components produced via AM for aerospace applications.

(a) Structural components: The majority of aircraft sub-structure consists of rib-web components, such as bulkheads, spars, ribs, and longerons made of either aluminium or titanium based alloys. The main features of these components are mainly planar web structures reinforced with, essentially perpendicular ribs. Such parts are traditionally machined out of die forgings, hand forgings, or plate stock, resulting in typical buy-to-fly ratios of 10-20:1 or higher [4]. For these types of components, large scale near net shape AM provides several potential benefits, including reduced raw material use, and reduced machining operations with a consequential reduced cost and lead time.

Recently, Matthew Tomlin and Jonathan Myer [15] from EADS Innovations works have presented a study on the benefits of the AM using Arcam electron beam selective melting (EBSM) process for an Airbus A320 nacelle hinge bracket component, incorporating the

topology optimisation method for the design optimisation. This exercise was conducted to evaluate the technical and commercial advantages of producing optimised AM parts for aerospace. The original nacelle bracket is made of HC 101 steel and is produced through near-net-shape sand casting and then machined to tolerance. The design is very simple, but the part is quite bulky. The density of the original steel was 7.7 g/cm^3, whereas the suggested new material Ti6Al4V is 4.42 g/cm^3, so there is a weight saving to be expected through the change in density of the material alone [15]. The materials optimised component (as shown in Figure *1.2*) weighed only 326g compared to 920 g for the original component, giving a 64% reduction in weight. The change in material accounts for roughly half of this reduction in mass, however the ability to produce an optimised design geometry alone leads to a considerable amount of reduction in weight [4, 15].

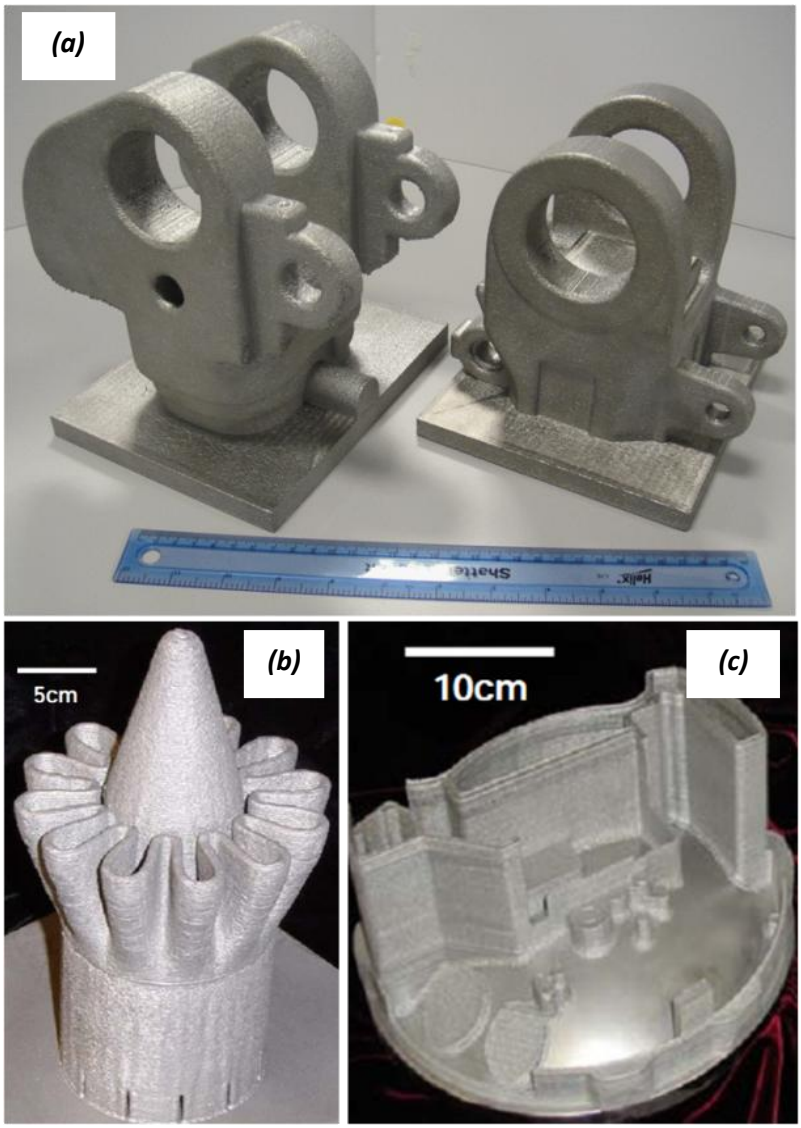

Figure 1.1: *Examples of components produced via AM for aerospace application, (a) end fittings (Courtesy of EADS), (b) gas thrusters in Ti 6-4 (Courtesy of Bell Helicopter Inc.), and (c) a housing (Courtesy of Sandia National Laboratory) for defence applications [2, 7].*

(b) Turbine engine cases: Turbine engine cases are major structural components which form the outer surface of jet turbine engines and generally are made of titanium or nickel based alloys. These cases are typically comprised of thick, cylindrical sections with a small number of low-volume, asymmetric protuberances. The height of these protuberances during forging determines the buy-to fly ratios for engine cases. This can be even higher than those for rib-web components. Thus, similar advantages are expected for AM of these components [13].

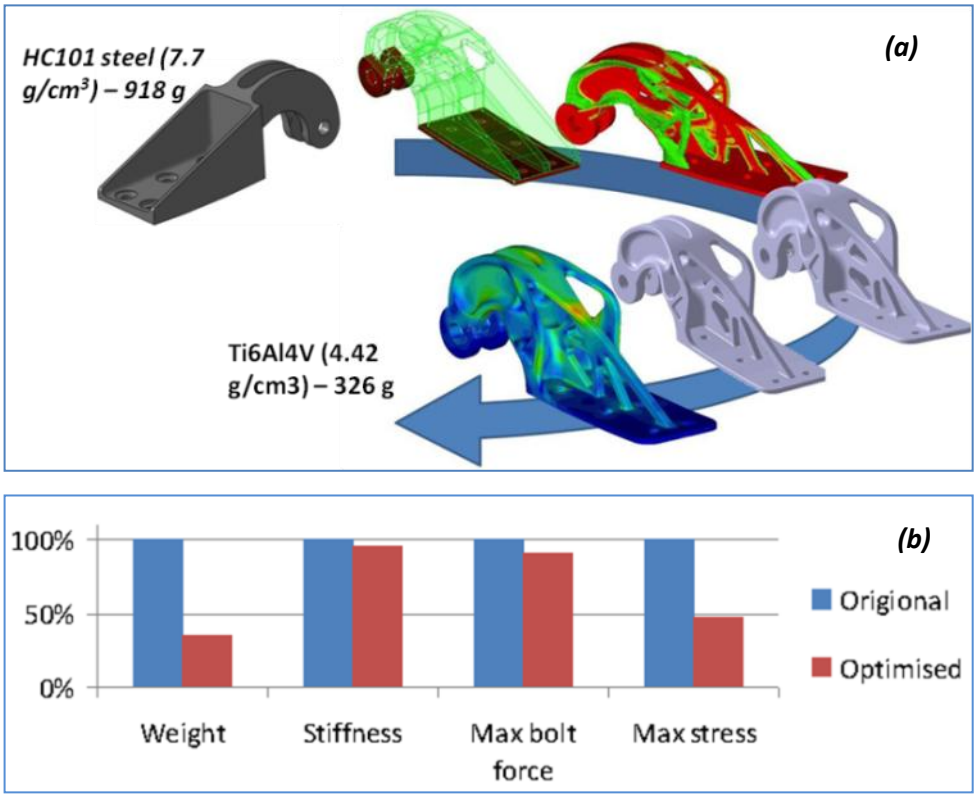

Figure 1.2: *Figure (a) shows the design optimisation loop used with CATIA v5, FEAM, to produce a new Airbus A320 nacelle hinge bracket design for manufacture by AM in Ti6Al4V; (b) shows performance comparison of the original sand cast machined HC 101 steel to the new designed Ti6Al4V with AM processes [15].*

(c) Engine blades and vanes: Engine blades and vanes consist of complex airfoil-shaped geometries with internal passages for cooling systems. These components are made of titanium- or nickel-based alloys and are currently manufactured by very expensive process with low a buy-to-fly ratio, like precision die forging or investment casting. Therefore, by changing to the AM process, it is possible to achieve only a small reduction in buy-to-fly ratio. However, AM still offers significant advantages, as these components are often repaired, or refurbished, as part of a typical engine overhaul. AM has the potential to compete with existing repair methods and to enable previously impossible repairs in certain circumstances. In this case, the cost and restoration of mechanical performance are the key factors. Blown

powder AM has been used to repair advanced turbine engine compressor or Blisk airfoils in addition to the manufacture of the components [7, 13]. Figure ***1.3*** show an example of repairs carried out using AM for Inconel 718 Blisk airfoil components [7, 13].

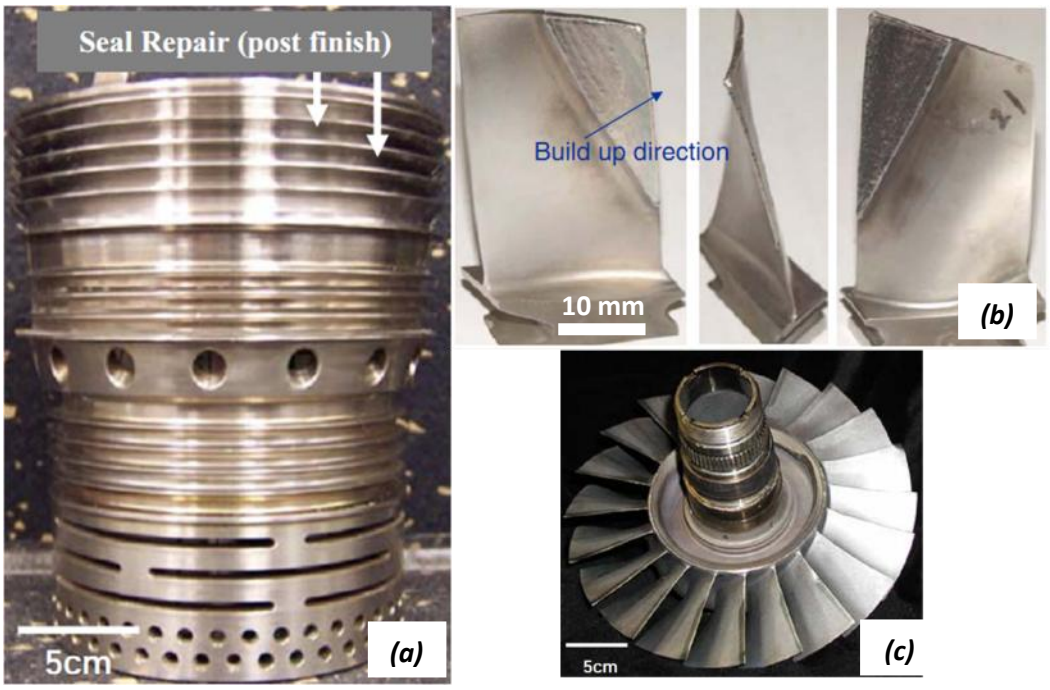

Figure 1.3*: Examples of repairs made by AM on: (a) an Inconel 718 Compressor Seal repaired, Courtesy of RPM & Associates, (b) an Inconel 718 Blisk airfoil repaired by laser powder deposition with the adaptive tool path method, and (c) repair, post finishing for T700 Engine [13].*

(d) Hyper joints: In addition to the above mentioned applications, another interesting use of AM is in hyper joints, which is the concept of combining mechanical and adhesive joining, leading to enhanced properties of the joint due to the synergetic load bearing interaction under service conditions. The goal of hyper-joints is the formation of integral joints between composite materials and a metal component to form a composite structure having excellent load bearing capacity.

The latest generations of jetliner, such as the Boeing 787 and Airbus A350, contain more than 50% by weight composite materials. Hyper joints are a novel way of joining composites to metal parts, which avoids the use of bolted joints in aircrafts structures. With AM, it is possible to grow an array of small arrowhead shaped pins onto the surface of a metal part. These are then embedded into an uncured composite panel, without breaking any of the carbon fibers, and the cured assembly results in an extremely tough metal to composite hybrid joint, where the pins act as anchors, transferring load between the metal and composite, as shown in Figure *1.4* [2].

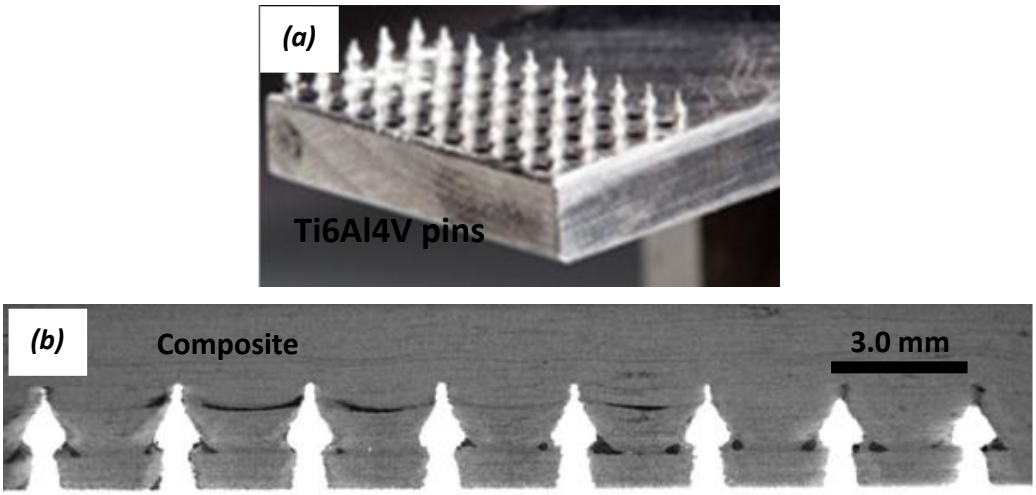

Figure 1.4: *A array of arrowhead pins (a) produced by AM for metal to composite hyper joints (b) [2].*

(2) Applications in the biomedical industry:

Currently, components produced by AM have been extensively adopted in the biomedical industry. Standard and customised implants, such as dental crowns, cranial implants and those for Orthopaedics surgery such as knee, hip replacement, have been manufactured by AM in titanium, stainless steel and Co-Cr alloy as shown in Figure ***1.5***. Since AM allows a freedom to tailor the amount of porosity, pore geometry, relative density and surface roughness, AM can be used to produce Trabecular Structures i.e., engineered porous materials [2, 16-21].

(3) Automobile and sports industries:

AM is also recently being used in the automotive industry (both polymer and metallic). BMW Rapid Technologies Centre- Germany has produced prototype parts, such as various engine parts, rear motor cycle wheels, headlight casings, engine covers, drive train kinematics, shock-connectors, cup holders, covers for centre consoles, etc though AM [22]. Formula one (F1) race teams also widely use AM to produce engine plus exhaust components (Figure ***1.6***)

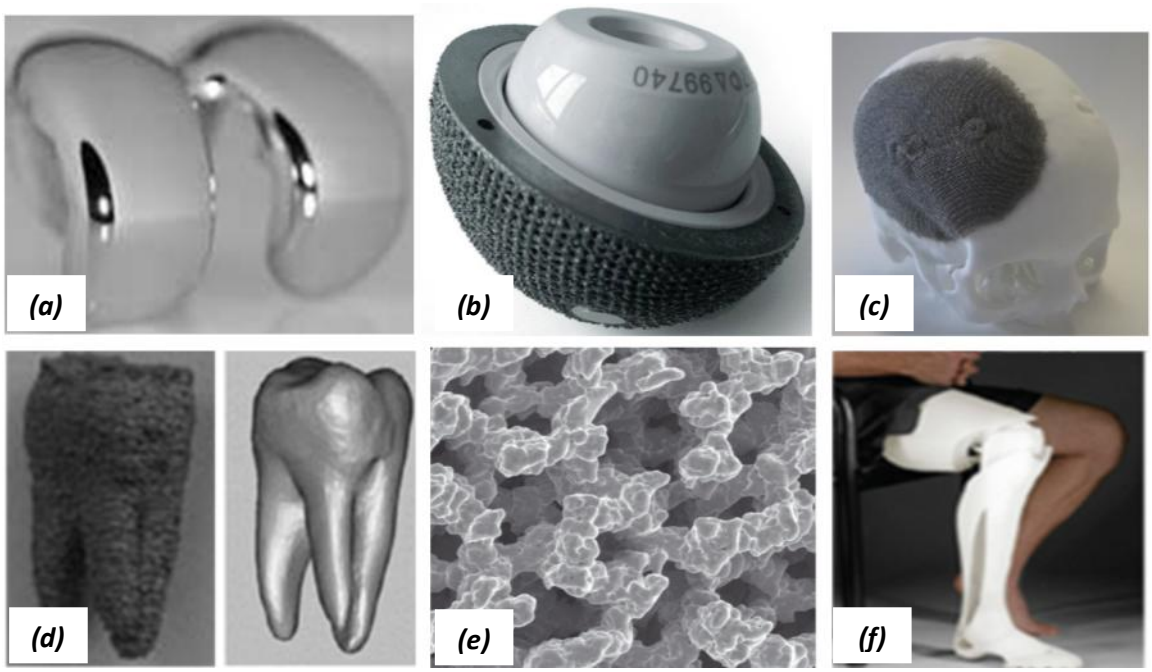

Figure 1.5: *Examples of components produced for bio-medical applications using e-beam additive manufacturing; (a) a femoral knee component (ASTM F75 CoCr alloy), (b) a Fixa Ti-Por, acetabular cup with a continuous, engineered trabecular structure for improved osseointegration, (c) a Human skull plate (Ti6Al4V), (d) customized dental implants of Ti6Al4V ELI Grad, (e) Trabecular structures (Ti6Al4V) and, (f) a bone implant [16, 19, 21, 23] .*

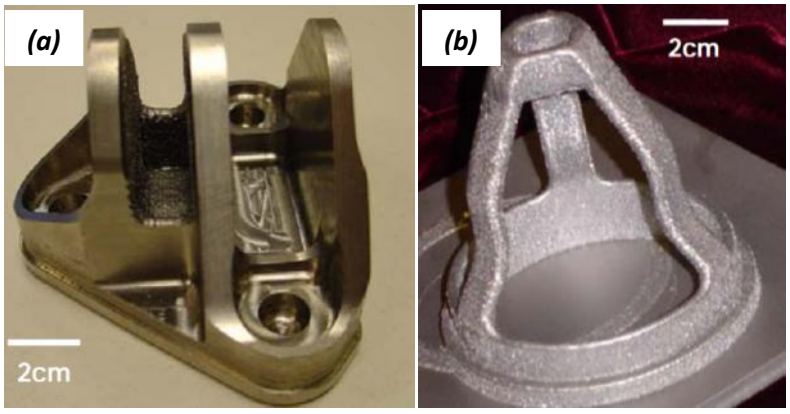

Figure 1.6: *Examples of components produced for the F1 race industry; (a) Ti6Al4V suspension mounting (Courtesy Red Bull), and (b) Ti 6-4 Gearbox Spider (Courtesy Red Bull) [7].*

In addition to the above mentioned three major areas of interest, AM has also been extensively used to produce foot wear by the companies like Nike, and Reebok. Nike has got its own research lab and manufactures footwear with polymer materials from Nike's Advanced Materials Research Centre using AM techniques [24]. AM offers the following major advantages to the footwear industry; 1) the ability to produce complex geometries, 2) the ability to quickly turn around new

products, 3) the ability to personalize products and, 4) Multi-material construction for better performance, without the use of adhesives and solvents.

1.6 WHAT ISSUES ARE THERE WITH METALLIC AM?

Conventional manufacturing techniques, used to produce metallic engineering components, are reasonably understood, both in terms of process control and material performance. The components produced by AM are new and quite different from those produced using conventional manufacturing methods. For example, components produced using thermo-mechanical processes like rolling, the mechanical properties are characterised based on the rolling process parameters (such as rolling temperature, percentage of reduction, etc), and the resulting anisotropic properties of the final component are represented in terms of rolling direction (RD), transverse direction (TD) and normal direction (ND). In comparison components produced by AM are affected by (1) process parameters like energy input, spot diameter, etc, (2) the deposition direction (Z or N_z), the rastering direction parallel to direction of energy source translation (X or R_x); (3) the transition zone between the substrate and the deposit also has its own characteristics. Furthermore, AM is essentially a solidification process whereas rolling + forging are deformation processes, which results in different microstructures. In addition to this the number of possible variations in raw materials, deposition systems and part specific geometric variables complicates the developments of process-property relationships and appropriate process control procedures. This can also result in a lack of microstructural homogeneity within the single part, which leads to difficulties in characterising and predicting structural performance and in designing parts for aircraft assemblies using the AM method [25-27].

The mechanical properties of metallic components are largely influenced by characteristics such as the composition of the alloy, scale of the microstructure and its morphology, crystallographic texture; the size, morphology, and distribution of discontinuities; residual stress; and spatial gradients in these characteristics. Hence, the relationships between process variables and such characteristics must also govern process-property relationships in AM [28, 29]. In AM, the majority of these characteristics are directly related to transport phenomena, such as fluid flow, heat transfer, and diffusion and to metallurgical phenomena, such as melting, solidification, solid-state phase transformations, and solid-state deformation. Because AM involves a number of complex interacting physical phenomena, and the local conditions will be different for every part-specific manufacturing procedure, a prior understanding of the critical parameters required for obtaining the desired microstructure and mechanical properties, and maintaining process control, is important to develop this technique further [27, 30].

1.7 AIMS OF THE PROJECT

The overall objective of this project was to expand the current limited knowledge of the process and component geometry variables that affect the microstructure and its homogeneity, in AM with a Ti6Al4V alloy. Although AM with processes like laser additive manufacturing is now reasonably well established, it has not been optimised in terms of controlling the microstructure of the deposited material for specific applications. It has already been published in the literature that the production of components by AM commonly leads to the formation of undesirable course prior β grains structures in titanium [29], which can have a detrimental effect on mechanical properties. The α+β titanium alloy, Ti6Al4V, is widely used in aerospace applications for engine and airframe components and lends itself to the AM route, because it is a difficult material to process and machine. Much research has been conducted on manufacturing with this material, using a range of AM techniques (e.g. [29-36]), but the amount of detailed information on the microstructural development and texture is quite limited. One general area of concern is that coarse β-grain structures are nearly always observed in AM of Ti6Al4V components [27, 29, 37]. This microstructure is less desirable, in terms of mechanical performance, since it can potentially result in aligned α-plates within the β-matrix and texture macro zones which are known to be detrimental to fatigue life [5, 38].

In the current project, 3 AM processes were studied in parallel; (1) an Electron Beam **-** preheated powder bed system (Arcam A2 Machine) and, (2) a Laser **-** cold bed powder deposition (EOSINT M270 machine) facility, and; (3) a Wire arc - AM technique using tungsten and metal inert gas arc melting (GTAW or GMAW) of these processes the powder bed systems were based at the EADS Innovation works, AM Centre in Filton, and the Arc deposition process was developed at the Welding Engineering Research Centre (RUAM Technology group Project) at the University of Cranfield. The project had the following key objectives,

(i) To produce a simple thermal model to assist in understanding the solidification conditions.

(ii) To understand and address the development of the strong texture and large (mm scale) columnar β grain structures that develop during solidification in AM with a Ti6Al4V alloy.

(iii) To characterise the growth of the coarse prior-β grain structures reported in AM and their effect on the texture of the transformed α structure, in terms of the relationship to the processing conditions and generic geometric build features.

(iv) To characterise how the microstructure reacts to local geometric changes, such as section thickness, web crossovers, wall inclination angles, etc., with the potential for a significant impact on critical areas where stress concentrations will occur.

(v) To investigate the effect of change in process parameters on microstructure in the WAAM process.

(vi) To investigate the benefits of the novel approaches to modify the coarse columnar β-grain structure seen in Arc deposited large-scale AM

(vii) To characterise the fatigue and fracture behaviour of the AM test pieces produced using EBSM and WAAM build platforms.

1.8 THESIS OUTLINE

The thesis has been divided into a literature review, an experimental section and, the results and discussion chapters. The literature review discusses the general metallurgy of titanium, and its alloys, the field of AM and the solidification and phase transformation theory relevant to the AM process. The history of production of metallic components by AM is also discussed alongside the relevant and recent literature available on the e-beam, laser beam and electric arc beam AM processes. The following chapter on experimental and characterization techniques describes the experimental procedures used to carry out all of the investigations in this work and, the methods of metallographic preparation and analysis used to characterise the Ti6Al4V samples. The results and discussion chapter initially describes the solidification condition with simple thermal model. The microstructure evolution of the β-grain structure, influence of build geometry on primary β-grain structure, β-texture and the transformed α-texture are then discussed for all the build platforms, as well as the effect of process and part geometry variables and other novel modifications to the processes. Finally the fracture and fatigue behaviour of AM test pieces are compared for the different production methods. The key conclusions and suggestions for further study as a result of this present investigation are presented at the end of the thesis.

2 LITERATURE REVIEW

The review in this chapter focuses on the published literature that discusses the general metallurgy of titanium, its alloys, general solidification theory, and the field of AM. The production of Ti6Al4V components using different AM processes is also discussed alongside the more limited relevant and recent literature available.

2.1 METALLURGY OF TITANIUM AND ITS ALLOYS

Of the light alloys, titanium and its alloys are of great importance due to the combination of excellent properties (such as high fatigue strength with good creep and corrosion resistance) and high service performance they provide in the aerospace, bio-medical and chemical industries.

2.1.1 History of Ti

Titanium is the fourth most abundant structural metal, comprising about 0.6% in the earth's crust, next to aluminium, iron and magnesium. It is naturally available in the form of ilmenite (FeTiO3) and Rutile (TiO2), since Ti has a high affinity towards oxygen. Gregor (UK) was the first person to identifying this element as an unknown species present in dark magnetic ironsand (ilmenite) in 1791. In late 1795, Klaproth [5], a German chemist was the first person to analyse rutile and identify it as an oxide of an unknown element, which he named as titanium after the Titans, 'the powerful sons of the earth' from the Greek mythology. Many attempts were subsequently made to isolate the metal from oxygen and nitrogen, but the production of ductile, high purity titanium proved to be difficult. During 1937-1940, the first commercial process was successfully developed by Krolls in Luxembourg [5]. This involved the reduction of titanium tetrachloride with magnesium in an inert gas atmosphere. The resulting titanium produced by the Krolls process is called "titanium sponge", due to its porous and spongy appearance. Interest in use of Ti alloys began commercially after the Second World War in the late 1940's and 1950's, and there has been high demand since in the aerospace and defence industries in need of titanium for airframe and engine applications [5, 39].

2.1.2 Ti crystal structure and nature of anisotropy

Pure Titanium is an allotropic element, which adopts more than one crystal structure with change in temperature. At room temperature pure Ti transforms to an hcp form, known as α-phase (with lattice parameters a=0.295 nm and c=.468 nm), whereas at high temperatures when it is heated above 882 ^{o}C, Ti exists in a bcc form, known as β-phase (with lattice parameter a = 0.332 nm), until reaching the melting temperature of about 1670^{o}C [39]. Figure ***2.1***(a) shows the three most

densely packed lattice planes at room temperature for the hcp phase, the (0002) plane, also called the basal plane, one of the three $\{10\bar{1}0\}$ planes, called prismatic planes, and one of the six $\{10\bar{1}1\}$ planes, or pyramidal planes. The three a_1, a_2, and a_3 axes are the close-packed directions, with indices $< 11\bar{2}0 >$. Figure ***2.1***(b) shows the unit cell of the BCC β phase with one variant of the six most densely packed planes $\{110\}$ and the four closed-packed directions of <111> [5, 39].

The elastic properties of Ti alloys are strongly dependent on the loading or deformation directions, due to the room temperature anisotropic nature of the hexagonal structure. Figure *2.2* shows the change in the value of Young's modulus, E, of pure α Ti single crystals at room temperature, as a function of γ, the angle between the c-axis and the stress axis. It can be seen that the modulus of elasticity E varies between 145 GPa (stress axis parallel to the c-axis) and 100 GPa (stress axis perpendicular to the c-axis). Similar strong variations are also observed for the shear modulus G. For example, in single crystals the shear modulus varies between 46 GPa and 34 GPa for shear stresses applied in the $< 11\bar{2}0 >$ direction in the (0002) or $\{10\bar{1}1\}$ planes, respectively. Less pronounced variations in elastic properties are observed in polycrystalline α-titanium with a weak crystallographic texture, and the actual anisotropy in modulus depends on the nature and intensity of the texture observed in the material [5].

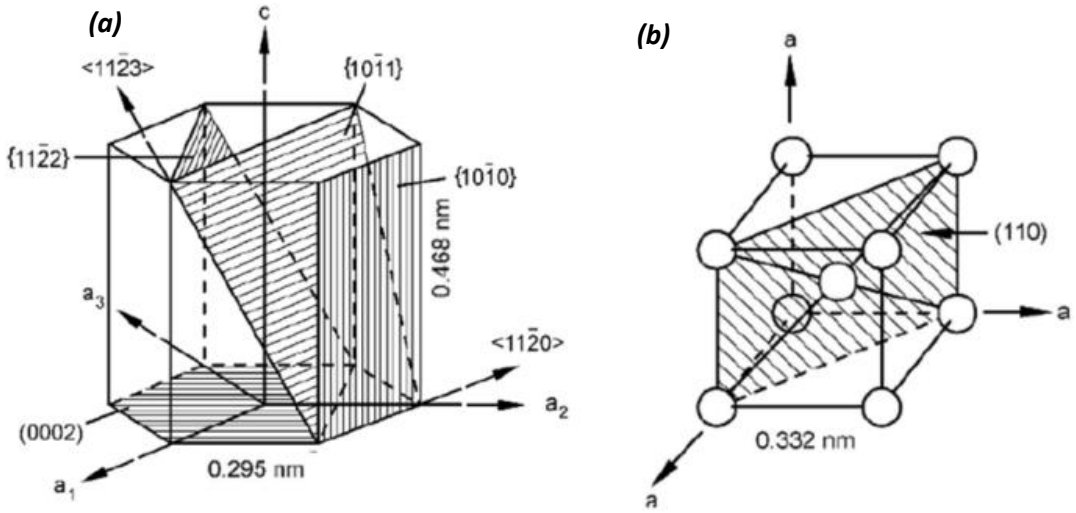

Figure 2.1: *The unit cells for the (a) α and (b)* β *phases in titanium [5].*

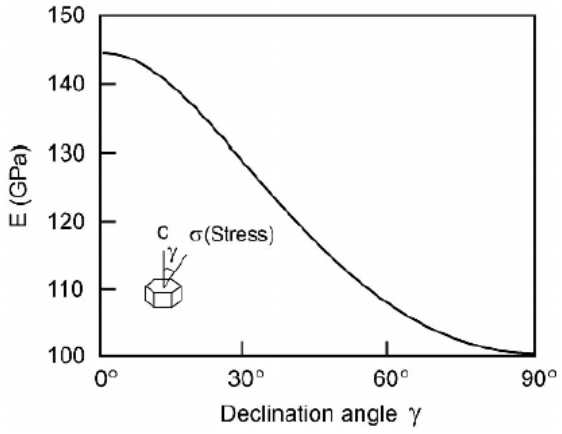

***Figure 2.2** : Young's modulus E of a single titanium crystal as a function of loading direction [5].*

2.1.3 Effect of alloying elements on phase transformation

Alloying elements with Ti can be classified into α stabilisers, or β stabilisers, based on whether the addition of alloying element raises, or decreases, the α → β transition temperature from 882^{o}C [4, 5, 39]. Important α-stabilising elements are Al (substitutional), O, N, and C (interstitial elements) and, their influence on the α-β transformation temperature is shown in Figure *2.3*(a). Al is a widely used as an α stabilising element, since it has a large solubility in the α phase. Other α stabilizers includes Sn, Zr, B, Ga, Ge, and the rare earth elements, but generally they are not added, due to their limited solubility. Oxygen is a strong interstitial α stabilising element, which must be accurately controlled in Ti alloys and is used in CP Titanium to obtain the desired strength level.

The β stabilising elements are divided into two groups, based on their influence on the resulting binary phase diagram, as β-isomorphous and β-eutectoid forming elements. β-isomorphous elements are V, Mo, and Nb. These elements, in sufficient concentration, can even stabilise the β phase to room temperature (Figure *2.3*(b)). Yt and Re are alternative elements used to obtain a β-isomorphous phase diagram, but they are not used in practice due to their higher density. Common β eutectoid forming (Figure *2.3*(c)) elements are Cr, Fe, and Si, whereas Ni, Cu, Mn, and W, are not greatly used except in specialised alloys. Other β eutectoid forming elements, such as Co, Ag, Au, Pt, Be, Pb, and U, are not generally used. Hydrogen also belongs to these β eutectoid forming elements, but it leads to hydrogen embrittlement. A low eutectoid temperature of 300 °C, in combination with the high diffusivity of hydrogen, can however lead to a special process of microstructure refinement, by hydrogenation and dehydrogenation (HDH) [39]. Generally, the maximum hydrogen content in CP titanium and titanium alloys is strictly limited to about 125-150 ppm [5].

The other class of elements, like Zr, Hf and Sn, behave more-or-less neutrally, as shown in Figure *2.3*(d), because at lower concentrations they lower the α/β transformation temperature slightly and then again increases the transformation temperature with higher concentrations. Zr and Hf are isomorphous with titanium and, hence, they exhibit the same β to α allotropic phase transformation. These elements have complete solubilities in α and β phases [5].

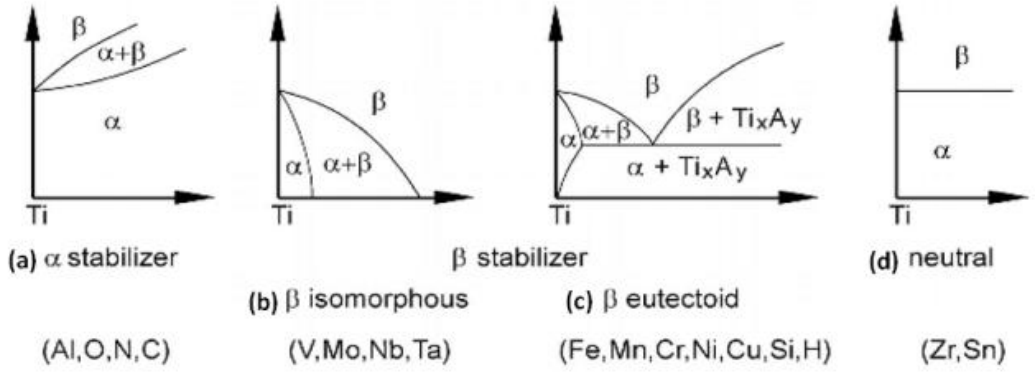

Figure 2.3: *Effect of alloying elements on the α ↔ β phase transformation [5]*

2.1.4 Classification of Ti alloys

Titanium alloys are classified into five major categories based on the chemical composition and microstructure at room temperature, namely *(i)* α alloys, *(ii)* near-α alloys, *(iii)* α+β alloys, *(iv)* metastable β alloys and *(v)* β alloys [5, 14, 39]. The effect of α and β stabilizing elements in multicomponent alloys can be expressed as an Al and Mo equivalent by the following equation,

$$[Al]_{equiv.} = [Al] + 0.17\,[Zr] + 0.33\,[Sn] + 10\,[O]$$

$$[Mo]_{equiv.} = [Mo] + 0.67\,[V] + 2.9\,[Fe] + 1.6\,[Cr] - [Al]$$

Nitrogen and Oxygen are potential α-stabilizers and can be expressed as,

$$[O]_{equiv.} = 2\,[N] + 0.67\,[C] + 10\,[O]$$

A schematic binary phase diagram showing the effect of both α and β stabilising elements is shown in Figure *2.4*. The upper part of the diagram shows the range of each group of the alloys. The martensitic start and finish (M_s/M_f) transformation behaviours are shown in the figure as dashed lines. Only of α + β alloys will be discussed here, with more emphasis on Ti6Al4V, since this is the alloy used in this current study.

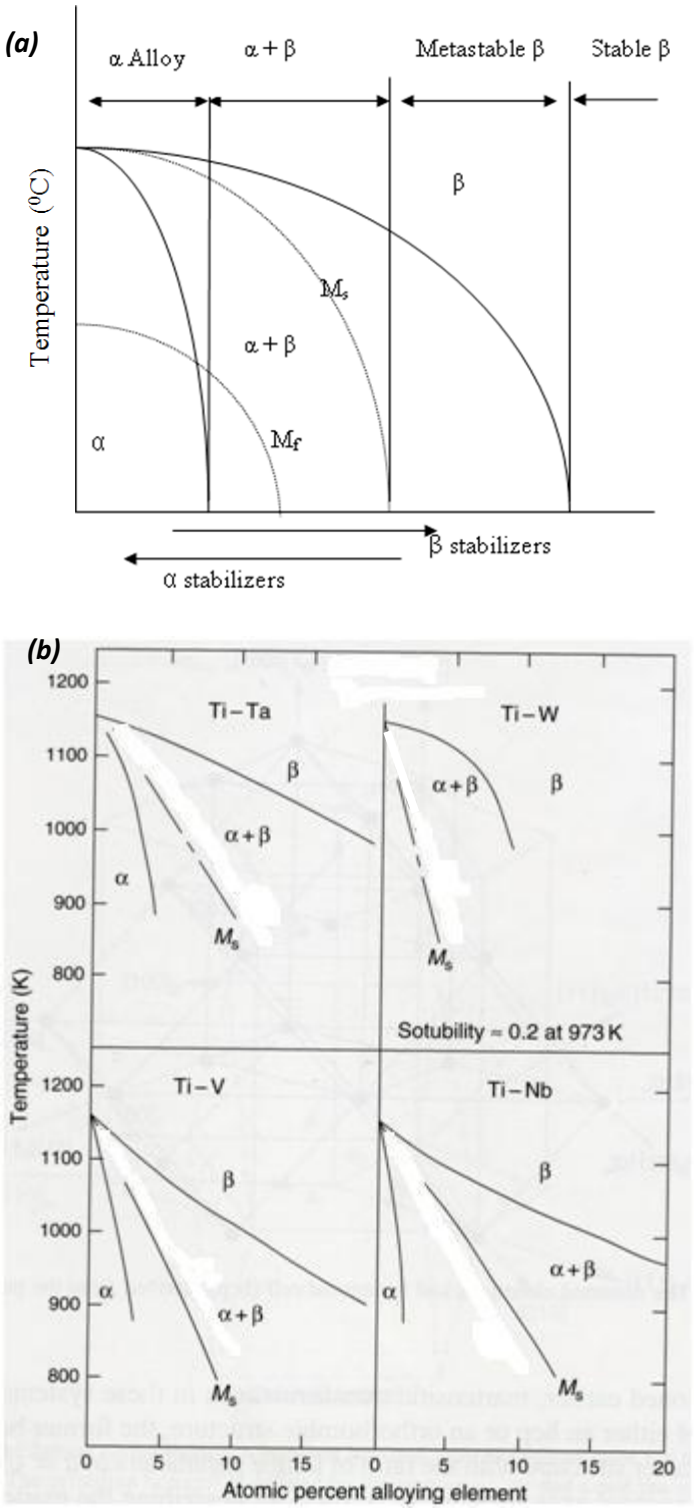

Figure 2.4: *Schematic representation showing the classification of titanium alloys (a) and the effect of alloying elements on the M_s temperature (b) [5, 40].*

2.1.5 The α+β alloys

α+β alloys (Figure *2.4*) typically contain 4-6 wt% of β stabilizers, which improves strength and formability. When cooling from the β phase field, α+β alloys will intersect the M_s and M_f, thus

α+β alloys transform martensitically upon quenching from the high temperature β phase field to room temperature, with a small amount of retained β phase in equilibrium (less than about 10 vol%).

Of the α + β alloys, Ti6Al4V is the most widely used. The Ti6Al4V alloy has an exceptionally good balance of strength, ductility, fatigue, and fracture properties. But, this alloy can only be used up to temperatures of about 300 °C due to low creep performance [5]. The microstructure of this alloy can easily be modified by the use of appropriate heat treatments. Ti6Al4V contains a volume fraction of approximately 15 % β phase at an equilibrium temperature of about 800 °C [5]. At room temperature the α-phase dominates, but when it is heated to above the β transus, at about 995 ˚C it exists as a single β phase [41]. As was mentioned earlier, aluminium is added to increase the strength of the alloy by solid solution hardening and α-phase stabilization. The vanadium addition stabilizes β which significantly improves the room temperature ductility, by obtaining balanced mechanical properties from both α and β phases. The addition of β stabilizers can retard the formation of α phase and promote the β phase to transform as martensite, or remain as retained β phase. The extra low interstitials (ELI) version of this popular Ti6Al4V alloy can yield especially high fracture toughness values, with excellent damage tolerant properties [5]. The heat treatment and microstructure development of α+β Ti alloys will be discussed further in sections 1.1

2.2 SOLIDIFICATION THEORY

In general, solidification behaviour controls the size and shape of grains in cast microstructures, the extent of segregation, the distribution of inclusions, the extent of defects such as porosity and hot cracks, and ultimately the properties of a solidified weld metal. It also controls the primary microstructure formed in translated melt pool processes like welding and in AM. Thus, it is important to understand the development of solidification microstructure by considering nucleation theory as well as the solid phase growth behaviour under solidification conditions. The influence of various parameters such as temperature gradient, growth rate, and undercooling will also be reviewed [42, 43]. As AM involves solidification within a moving meltpool it has many similarities to welding. Hence, the solidification behaviour will be reviewed here in this context. A key reference in this regard is the excellent review by David and Vitek [44]

2.2.1 Nucleation theory

If a liquid is cooled below its equilibrium melting temperature (T_m), there is a driving force for solidification (G^L - G^S) and it might be expected that the liquid phase would spontaneously solidify.

However, theoretically large undercooling of the order of 250 K required for homogeneous nucleus to form. Generally, such large undercoolings are not observed practically, since the walls of the liquid container and solid impurity particles in the liquid catalyse the nucleation of solid at undercoolings of approximately 1 K. This is known as '*Heterogeneous nucleation'*. The large undercoolings, mentioned above, are only obtained when there is no such a heterogeneous nucleation sites available; i.e., when solid nuclei form homogeneously from the liquid, and hence called '*Homogeneous nucleation'.* Practically, homogeneous nucleation does not occur under melt pool conditions [43, 44].

Homogenous nucleation: Homogeneous nucleation is defined as nucleation without the aid of a foreign body such as impurities, inclusions, mould walls or substrates. However, homogenous nucleation provides a referencing point from which the actual nucleation behaviour can be discussed.

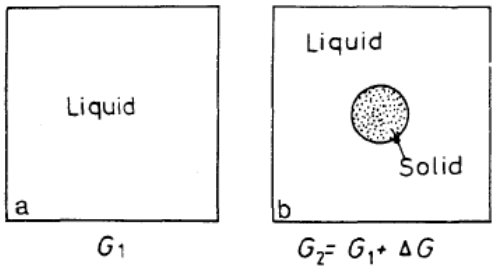

Figure 2.5: *Homogeneous nucleation [43]*

Consider a given volume of liquid at a temperature ΔT below T_m with a free energy G_1 (Figure *2.5*a). The formation of a solid nucleus within a liquid melt is controlled by the change in total free energy, which is sum of both the volume free energy change associated with the liquid-to-solid transformation and, the additional surface energy required to form the nucleus. If some of the atoms of the liquid cluster together to form a small sphere of solid (Figure *2.5*b), the free energy of the system will change to G_2, given by:

$$\boldsymbol{G_2 = V_S G_v^S + V_L G_v^L + A_{SL}\gamma_{SL}} \quad \text{..... Equation 1}$$

Where, V_S is the volume of the solid sphere, V_L is the volume of liquid, G_v^S and G_v^L are the free energies per unit volume of solid and liquid respectively. A_{SL} is the solid/liquid interfacial area and, γ_{SL} the solid/liquid interfacial free energy. The free energy on forming the nucleus is therefore given by:

$$\boldsymbol{\Delta G = V \Delta G_v + A_{SL}\gamma_{SL}} \quad \text{..... Equation 2}$$

Where, ΔG_v is the change in free energy per unit volume in forming the solid (a negative quantity) and, ΔG_v is directly related to undercooling ΔT, which is the driving force for the solidification. ΔG_v**,** can be calculated, as follows, from the difference in the free energy between actual liquid temperature (T) and solid close to melting point (T_m), as shown in the Figure *2.6*.

If a liquid metal is undercooled by ΔT below T_m before it solidifies, solidification will be accompanied by a decrease in free energy ΔG_v (J/mol), as shown in Figure *2.6*. This free energy decrease provides the driving force for solidification. The magnitude of this change in free energy can be obtained as follows,

$$\Delta G_v = \Delta H_v - T\Delta S_v \quad \text{..... Equation 3}$$

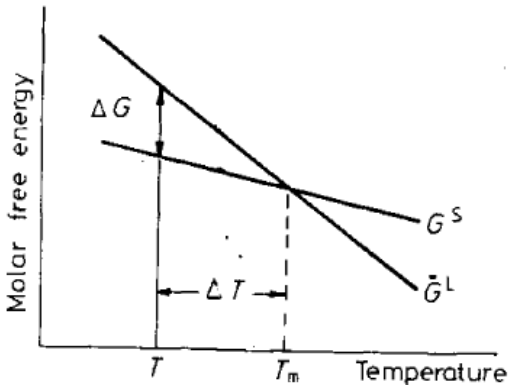

Figure 2.6: *Difference in free energy between the liquid and solid phases close to the melting point. The curvature of the G^L and G^S lines has been ignored [43].*

At the equilibrium melting temperature, T_m, the free energies of the solid and liquid are equal, i.e. $\Delta G = 0$, consequently:

$$\Delta Sv = \frac{\Delta H}{T_m} = \frac{L}{T_m} \quad \text{..... Equation 4}$$

Where ΔS, is the entropy of fusion, and L is the latent heat of fusion per unit volume. It is observed experimentally that at the melting point, the entropy of fusion is a constant R (8.3 J mol^{-1} K^{-1}) for most metals (Richard's rule). ΔH and ΔS are therefore approximately independent of temperature.

Thus, $\Delta Gv \approx L - T\frac{L}{T_m}$ i.e. for small ΔT,

$$\Delta G_v \approx \frac{L\,\Delta T}{T_m} \quad \text{..... Equation 5}$$

The total free energy of formation ΔG of a spherical solid particle of radius r (with no change in the composition) is thus given by:

$$\Delta G = \frac{4}{3}\pi r^3 \Delta G_v + 4\pi r^2 \gamma_{SL} \quad \text{..... Equation 6}$$

Below T_m, ΔG_v is negative so that the free energy change associated with the formation of a small volume of solid has a negative contribution due to the lower free energy of a bulk solid, but there is also a positive contribution due to the creation of a solid/liquid interface. It can be seen from Figure *2.7* that for a given undercooling there is a certain radius, r*, which is associated with a maximum excess free energy. If r < r* the system can lower its free energy by dissolution of the solid, whereas when r > r* the free energy of the system decreases if the solid grows. Unstable solid particles with r < r* are known as clusters or embryos, whereas stable particles with r > r* are referred to as nuclei and, r* is known as the critical nucleus size.

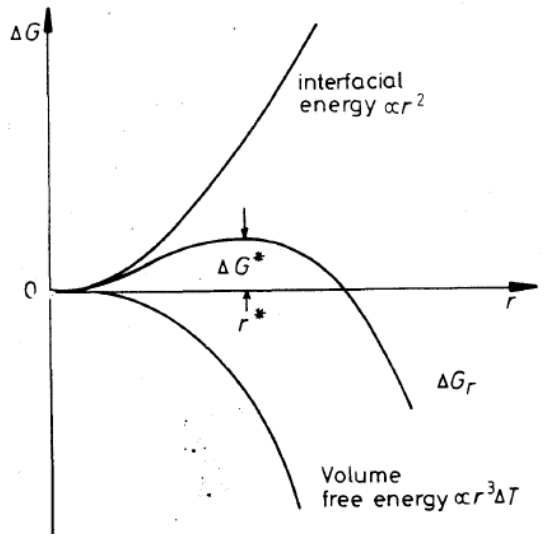

Figure 2.7: *The free energy change associated with homogeneous nucleation of a sphere of radius, r [43].*

Since ΔG = *0,* when r = r* the critical nucleus is effectively in (unstable) equilibrium with the surrounding liquid. By differentiation of (Equation 6), it is possible to obtain the critical nucleus size, r^*, and using the critical nucleus size the critical energy barrier for the nucleation ΔG^*_{hom} can be obtained,

$$r^* = \frac{2\gamma_{SL}}{\Delta G_v} = \left(\frac{2\gamma_{SL} T_m}{L_v}\right)\frac{1}{\Delta T} \quad \text{..... Equation 7}$$

$$\Delta G^*_{hom} = \frac{16\pi\gamma^3_{SL}}{3(\Delta G_v)^2} = \left(\frac{16\pi\gamma^3_{SL} T^2_m}{3L^2_v}\right)\frac{1}{(\Delta T)^2} \quad \text{..... Equation 8}$$

Therefore, it can be seen that the thermodynamic barrier to homogeneous nucleation (r* and ΔG^*) decreases rapidly with increasing undercooling (ΔT) .

Heterogeneous nucleation: Although large thermal undercoolings have been obtained under homogeneous nucleation conditions during solidification, generally undercoolings of more than a few degrees kelvin are rare [42-44]. This is because homogeneous nucleation conditions are extremely difficult to achieve. Instead, heterogeneous nucleation is far more common, in which nucleation takes place on preferred sites, such as inclusions or substrates. During such heterogeneous nucleation the barrier to nucleus formation is significantly reduced by decreasing the magnitude of the surface energy term.

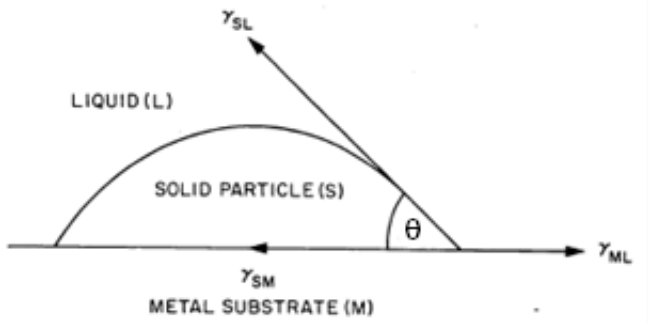

Figure 2.8: *Surface forces present during heterogeneous nucleation of particle on solid substrate [45].*

In heterogeneous nucleation the critical free energy of formation (ΔG^*_{het}) is less than the corresponding free energy for the homogeneous nucleation (ΔG^*_{hom}) by a factor S(θ):

$$\Delta \boldsymbol{G^*_{het}} = \Delta \boldsymbol{G^*_{hom}}\, \boldsymbol{S(\theta)} \quad \text{..... Equation 9}$$

For a hemispherical cap model, the geometric factor s(θ) is given by,

$$\boldsymbol{S(\theta)} = \frac{(2+\cos\theta)}{4}\,(1-\cos\theta)^2 \quad \text{..... Equation 10}$$

The shape factor S(θ) has a numerical value ≤1 dependent only the wetting angle θ. Therefore, the activation energy barrier against heterogeneous nucleation is smaller than homogeneous, and depends on the degree of wetting between the substrate and nucleus. In practice this is governed by the interfacial energy between the substrate and solid nucleus. i.e. a high degree of coherency and lattice matching will result in good wettability and a low energy barrier to nucleation.

The rate of nucleation is an important parameter which defines how fast the solid nuclei will appear in the liquid at a given undercooling. If the liquid contains C_0 atoms per unit volume, the number of clusters that have reached the critical size (C*) can be obtained given by:

$$C^* = C_0 \, exp\left(\frac{-\Delta G^*_{hom}}{kT}\right) \; clusters/m^3$$

The addition of one more atom to each of these clusters will convert them into stable nuclei and, if this event happens with a frequency of f_0, the homogeneous nucleation rate is given by:

$$N_{hom} = f_0 C_0 \, exp\left(\frac{-\Delta G^*_{hom}}{kT}\right) \quad nuclei \; /m^3/s^{-1}$$

Where, f_0 is a function that depends on the vibration frequency of the atoms, the activation energy for diffusion in the liquid and, the surface area of the critical nuclei. The homogeneous nucleation rate is given by:

$$\boldsymbol{N_{hhom} = f exp\left(\frac{-Q}{K.T}\right) C_0 \, exp\left(\frac{-\Delta G^*_{hom}}{kT}\right) \, nuclei \; /m^3/s^{-1}} \quad \text{..... Equation 11}$$

From (Equation 8), ΔG^* is related to $1/(\Delta T)^2$ therefore, as a result of the ΔT^2 term, inside the exponential, N_{hom} changes by orders of magnitude from essentially zero to very high values over a very narrow temperature range. Heterogeneous nucleation can be defined in the same way, based on number of (n_1) atoms in contact with the substrate and the concentration of critical nuclei is given by:

$$\boldsymbol{n^* = n_1 \, exp\left(\frac{-\Delta G^*_{het}}{KT}\right)} \quad \text{..... Equation 12}$$

The volume rate of heterogeneous nucleation can then be expressed as,

$$\boldsymbol{N_{het} = f_1 C_1 \, exp\left(\frac{-\Delta G^*_{het}}{kT}\right)} \quad \text{..... Equation 13}$$

Where, (f_1) is a frequency factor similar to (f_o) in the homogeneous nucleation rate calculation, and C_1 is the number of atoms in contact with heterogeneous nucleation sites per unit volume of liquid. ΔG^*_{het} is less than ΔG^*_{hom} by $S(\theta)$**.** This has a massive influence on the nucleation rate and allows nucleation to be possible at low undercoolings with efficient nucleants. Nucleation in welding melt pools is typically observed to take place with an undercooling of 1-2 K compared to ≥ 200 K for homogeneous nucleation.

2.2.2 Growth behaviour

After nucleation, growth of the solid occurs by the addition of atoms (diffusion) from the liquid to the solid at the pre-existing solid/liquid (S/L) interface. There are two main different types of S/L interface namely; (1) atomically rough interfaces associated with metals and (2) atomically flat, or sharply defined interfaces associated with non-metals [43, 44]. Rough interfaces migrate by a continuous growth process. Whereas, flat interfaces migrate by a lateral growth process involving ledges, i.e. either though a (1) steps created by a surface nucleated disc shaped ledge, (2) or at the solid where a dislocation intersects the S/L interface or, (3) at re-entrant twin boundaries.

A key important factor which determines the nature of S/L interface is heat flow and the associated thermal gradients in the melt pool. Mass flows associated with compositional gradients are also crucial in establishing the shape of the stable solidification front. The interaction of thermal gradients with the growth rate and other solidification conditions determines the final microstructure of the primary phase during solidification. The interface stability is critical since this will strongly influence the morphology, distribution of grains, and compositional variations in the final microstructure. Based on the steady state microscopic shape of the S/L interface at the growth front, solidification occurs by means of planar, cellular, or a dendritic manner [43, 44].

Planar morphology: a planar S/L interface that advances into the liquid is characterised by the lack of development of a substructure as, shown in Figure *2.9* and Figure *2.10*. The planar type of growth is controlled by the heat flow conditions and the direction of growth is perpendicular to the solidification front, i.e. against the maximum thermal gradient. The role of a phases crystallography is limited to the selection of optimally orientated grains only.

Cellular morphology: Break down of the planar front to form cells, where the directions of growth of cells are controlled by the heat flow conditions. Growth crystallography influences the grain selection process, but doesn't play a significant role in determining the orientation of the cells. The S/L growth front is made up of many uniformly spaced cells growing parallel to one another generating a directional substructure (Figure *2.9* and Figure *2.10*).

Dendritic growth morphology: Dendritic growth occurs by growth along specific crystal directions, known as easy growth directions, along which the growth rate and atom attachment kinetics are fastest. The growth of the S/L front is controlled significantly by crystallographic considerations. Therefore, dendritic growth is anti-parallel to the heat flow direction, but is not necessarily parallel to the easy growth directions. Heat flow determines which one of several

equivalent crystallographic directions is selected, based on the principle of optimum alignment between the maximum thermal gradient and the growth direction.

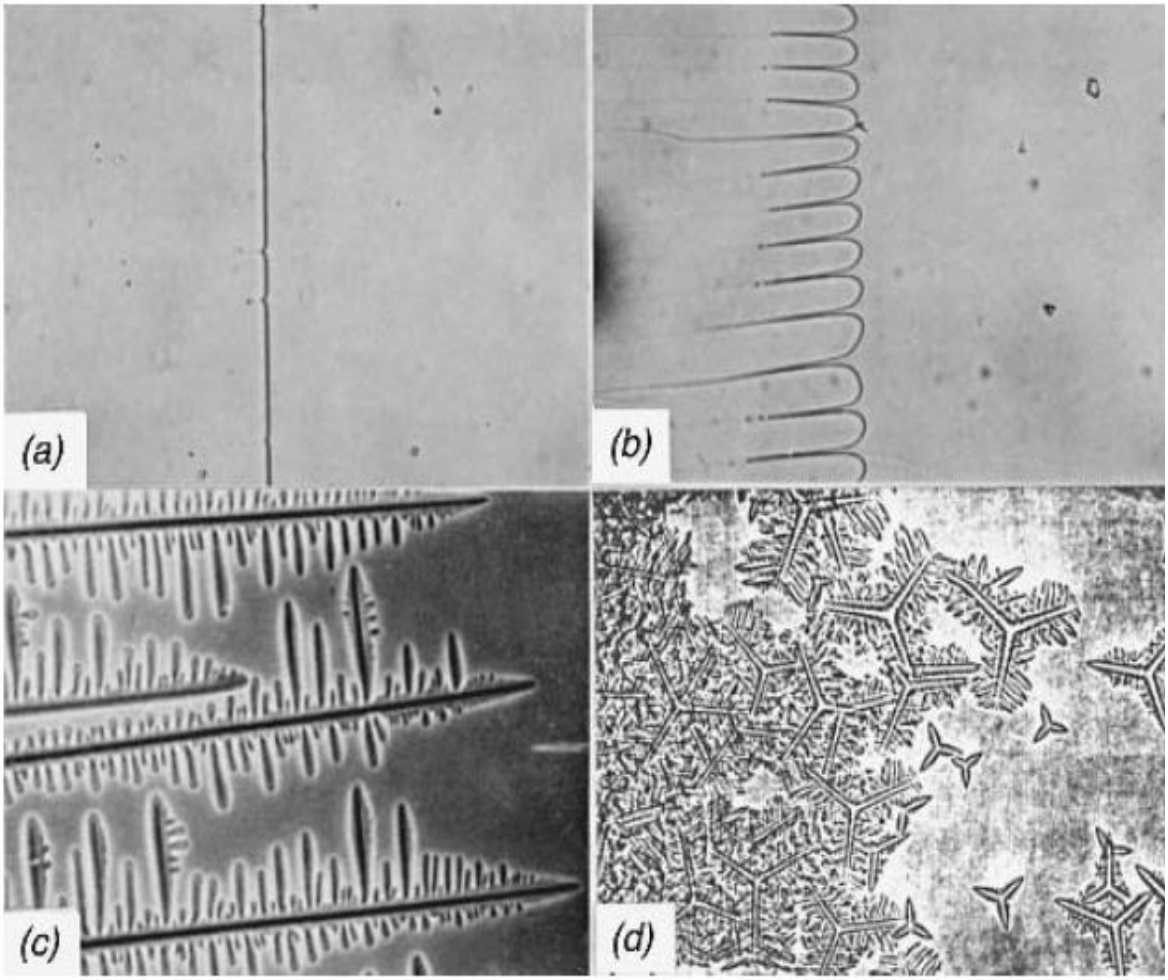

Figure 2.9: *Basic solidification modes; (a) planar solidification of carbon tetrabromide; (b) cellular solidification of carbon tetrabromide with a small amount of impurity present; (c) columnar dendritic solidification of carbon tetrabromide with several percent impurity; (d) equiaxed dendritic solidification of cyclohexanol with impurity [46].*

Dendritic growth can be divided into two major types: ***Columnar dendritic growth and Equiaxed dendritic growth*** *[44]*. The *Columnar dendritic growth* is characterised by the constrained growth of a packet of dendrites along the same general direction. These essentially parallel dendrites grow in the main direction of heat flow (i.e. inwards from a mould wall), and combine to form one grain with a well developed substructure (see Figure *2.9* and Figure *2.10*). Branching of these dendrites may, or may not, be present. With no branching, the columnar dendritic structure is very similar to the cellular solidification structure and may be referred to as a *cellular dendritic structure*. The difference between cellular and cellular dendritic structures is determined by the

orientation of the substructure with respect to the heat flow direction and the crystallographic orientations. *Equiaxed dendritic growth* is shown in Figure *2.9* and Figure *2.10.* This morphology is characterised by the growth of dendrites of different orientations in a liquid cooled sufficiently below its liquidus temperature so that spontaneous nucleation is possible. Neighbouring dendrites are not necessarily parallel to each other and hence, each dendrite becomes a separate grain in the final solidified structure.

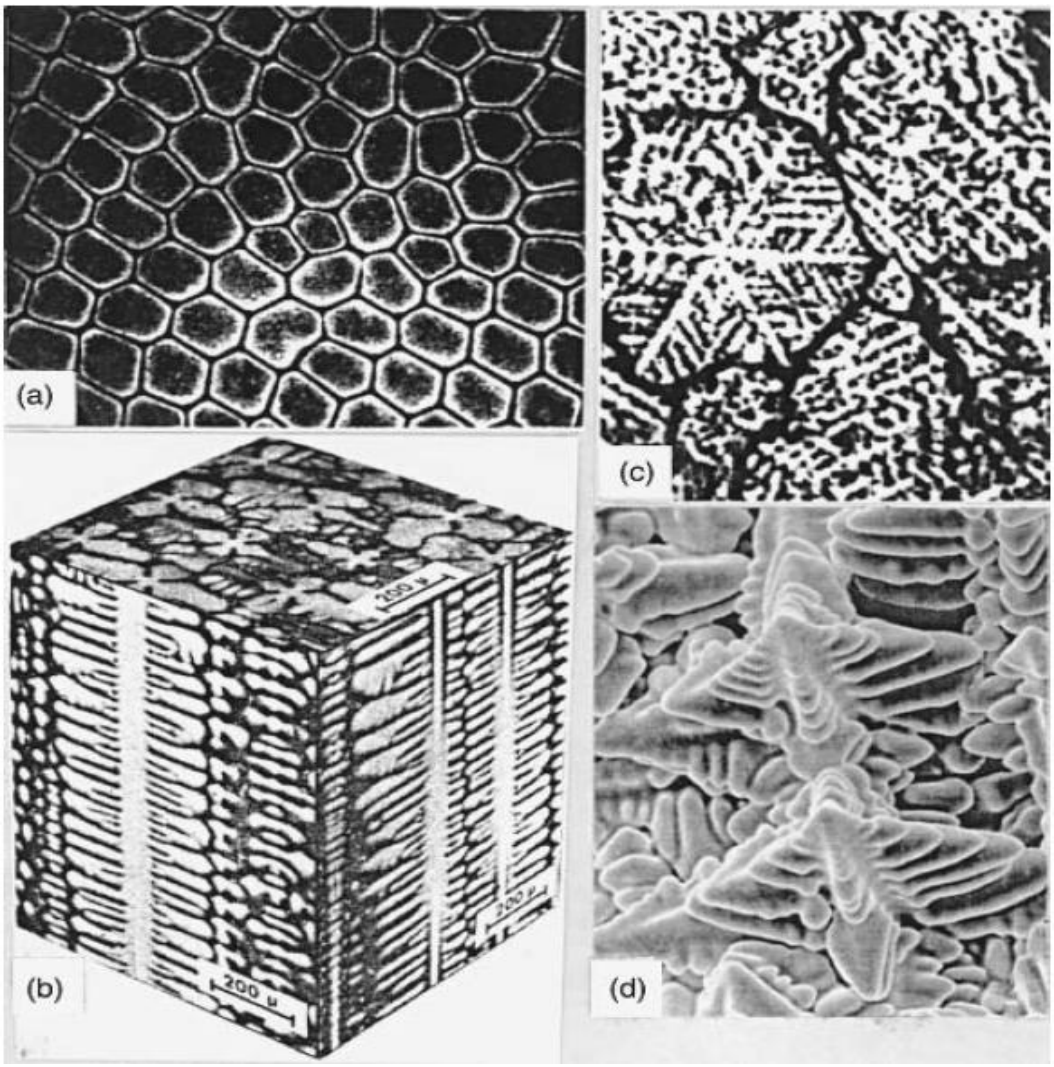

Figure 2.10: *Nonplanar solidification structures in alloys; (a) transverse section of a cellularly solidified Pb–Sn alloy; (b) columnar dendrites in a Ni alloy; (c) equiaxed dendrites of a Mg–Zn alloy ; (d) three-dimensional view of dendrites in a Ni-base superalloy [44, 46].*

Constitutional supercooling (alloys)

Solidification of an alloy is commonly subdivided into three cases according to the solidification conditions: Case I-corresponds to equilibrium solidification in which complete diffusion takes place in the solid and liquid. The final solid is uniform in composition with the nominal alloy

composition. This case is not applicable to welding conditions and is not considered further. Case II-assumes little, or no, diffusion takes place in the solid, while complete mixing in the liquid occurs as a result of convection and diffusion. This case applies mainly to micro segregation in weld microstructures, and will not be discussed here. Case III - assumes no diffusion in the solid and only limited diffusion in the liquid, with no convection and it is the most appropriate condition to describe morphological stability and microstructural development in welds, and due to the similar solidification conditions [43, 44], also in AM.

The solidification morphology of alloys is controlled by the diffusion of solute into the liquid (similar to the removal of latent heat in pure metals) and the temperature gradient in the solidifying liquid. A variation in solute content of the liquid exists ahead of the solidification front (Figure *2.11*(a)) and as such, the equilibrium solidification temperature (T_e) also varies with distance from solidification front (Figure *2.11*(b)) based on the alloy partition co-efficient, $k=C_S/C_L$, where C_S and C_L are the equilibrium compositions of the co-existing solid and liquid, respectively, at a given temperature. The temperature of the liquid (T_L) varies with distance and a temperature gradient exists in the liquid near the S/L interface. The solidification behaviour is determined by comparison of T_L with T_e. If T_L is less than T_e, the liquid temperature lies below the equilibrium temperature and the liquid is supercooled. This phenomenon is a result of compositional (or constitutional) effects and is known as constitutional supercooling; stable protuberance, (i.e. non-planar growth) can only exist under these conditions. The tip of any protuberance that forms will be at a higher temperature than the planar front. However, as long as the temperature of the tip is less than T_e, solidification can occur and the tip may grow in a cellular/dendritic manner.

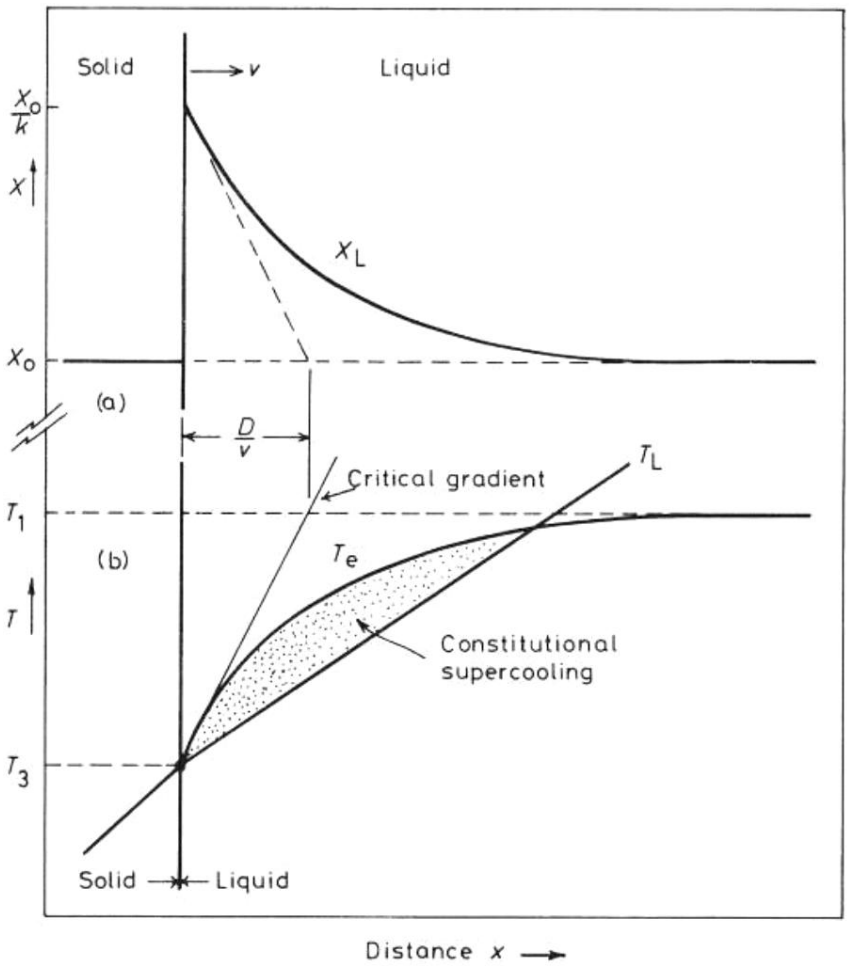

Figure 2.11: *Constitutional supercooling ahead of a planar S/L front showing (a) composition, and (b) temperature profile. T_e and T_L = the equilibrium and liquid temperature during solidification [43]*

If T_L is greater than T_e, any protuberances formed are at a higher temperature than the planar front and are also above the equilibrium solidification temperature. In this case, the temperature of the tip is raised above the liquidus temperature and melts back thus, planar growth is stable. By comparing the actual thermal gradient in the liquid G_L with the gradient in the liquidus, due to the compositional gradient G_C, the following criterion for constitutional supercooling can be derived:

$$\boldsymbol{G_L = m_L G_C} \quad \text{..... (Equation 14)}$$

Where, m_L is the slope of the equilibrium liquidus line. The compositional gradient for steady state plane front growth can be determined by considering a solute mass balance at the planar interface. The compositional gradient (G_C) can be expressed as:

$$\boldsymbol{G_C = -\frac{RC_0(1-k)}{k} D_L} \quad \text{..... Equation 15}$$

where, R is the growth rate and D_L is the solute diffusion coefficient in the liquid. This can be expressed as:

$$\frac{G_L}{R} < -\frac{m_L C_0(1-k)}{kD_L} \quad \text{(or)} \quad \frac{G_L}{R} < \Delta T_0/D_L \quad \text{..... Equation 16}$$

where , ΔT_0 is the temperature interval between liquidus and solidus at composition C_0. The ratio of thermal gradient to growth rate (G_L/R) is thus an important quantity which dictates the level of constitutional supercooling. Constitutional supercooling and the associated instability of a planar front that results in formation of a cellular or dendritic structure, is based on the condition that the gradient in liquidus temperature adjacent to the interface (corresponding to the compositional gradient) is greater than the actual thermal gradient. The influence of the degree of constitutional supercooling on the final microstructural morphology can be readily seen as shown in the Figure *2.12* for decreasing (G_L/R) ratios [46].

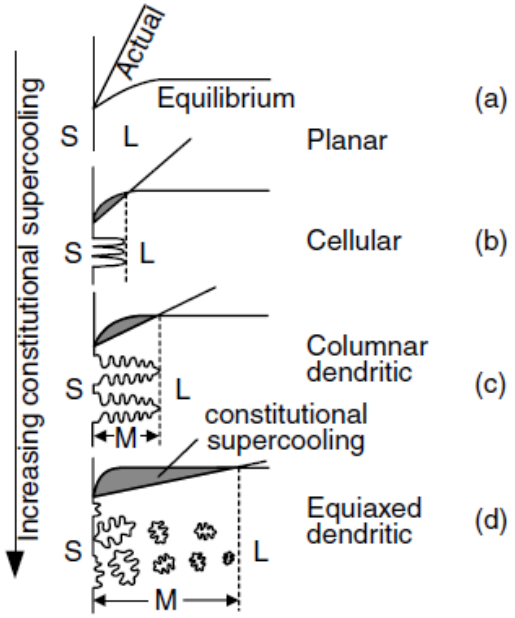

Figure 2.12: *Effect of constitutional supercooling on solidification mode: (a) planar; (b) cellular; (c) columnar dendritic; and (d) equiaxed dendritic morphology (S, L, and M denotes solid, liquid and mushy zone respectively) [46].*

2.2.3 Important variables that controls melt-pool solidification behaviour

The growth rate, temperature gradient, melt pool shape, travel speed, undercooling, and alloy constitution will all control the final microstructure of a solidifying melt pool in welding and AM [26, 29, 43, 44, 47, 48].

Growth rate: The solidification rate, or growth rate (R), is the rate at which the solid/liquid interface in the melt pool advances. R is directly related to the travel speed of the heat source (v). The rate at which the solidification front moves has a significant effect on the scale of

solidification substructure, the growth undercooling, and the solute redistribution during solidification [43, 44]. In a steady state condition, in welding or AM where the heat source is moving at a constant-speed (v), solidification growth must occur in such a way that it is able to keep pace with the heat source travel speed, and this is illustrated in Fig. 4.51. It is seen that for R, to keep pace with the welding speed (v) the condition must be met that [43, 44]:

$$\boldsymbol{R = v\ \cos\theta} \quad \text{..... (Equation 17)}$$

Where, θ – is the angle between the surface normal *n* and the heat source travel direction. Thus, at the top surface, assuming that the solidification front is normal to the surface, the growth rate would vary from R= 0, when θ= 90° along the fusion line to a maximum of R = V (travelling speed of heat source) when θ= 0° along the centreline of the melt track.

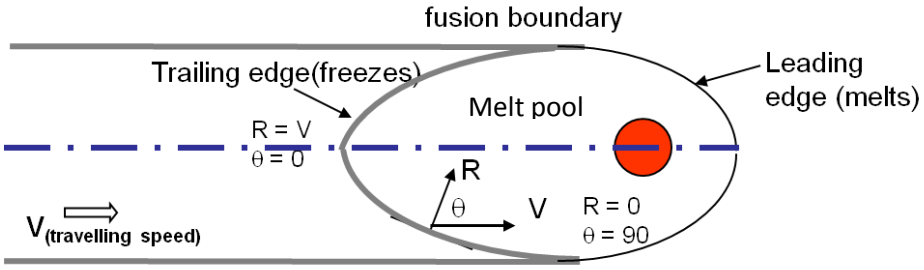

Figure 2.13: *Schematic diagram showing relationship between heat source rate or travelling speed and, solidification front growth rate [44, 45].*

The local average growth direction during solidification of melt pool is approximately perpendicular to the S/L interface and parallel to the maximum thermal gradient against the heat flux. However, the growth rates are also influenced by the crystallography through specific preferred growth directions, known as 'easy growth directions'. For cubic metals, the easy growth directions are the $< 100 >$ directions, whereas in hexagonal close packed systems they are the close packed $< 11\bar{2}0 >$ directions since these directions can grow much faster than other directions kinetically during solidification of liquid metals [42-44]. During welding of a polycrystalline material, a wide range of grain orientations are present. A grain selection process will thus take place in which grains whose easy growth directions are optimally aligned with the solidification front normal will selectively outgrow less optimally aligned grains. This selection process occurs for planar, cellular, and dendritic growth [43, 44].

Influence of travel speed: By Increasing the heat source travel speed, the shape of the melt pool changes from an elliptical shape to a narrower, pear shape as shown in Figure *2.14*. Since growth at the S/L interface will try to follow the steepest temperature gradient, the effect of changing the welding speed is to alter the solidification behaviour as illustrated in Figure *2.14*. In the elliptically

shaped melt pool (low and moderate speed), the maximum heat input and the peak temperatures occur along the centreline. The higher temperatures in the solid immediately behind the melt pool, along the centreline, cause less rapid heat loss and result in a minimum thermal gradient along this direction (Figure *2.14a).* Meanwhile, the rate of liberation of latent heat is also a maximum at the centreline since it is directly proportional to the growth rate. Consequently, a critical growth rate exists for an elliptical melt pool beyond which the minimal thermal gradient present at the centreline cannot dissipate the generated heat of fusion sufficiently quickly. For growth rates above this critical value, the melt pool shape changes and, becomes more elongated and tear drop shaped, as shown in Figure *2.15*b. With this melt pool shape, the maximum growth rate is always less than the travel speed, since θ never equals 0 at the centre line. The tear-shaped melt pool (Figure *2.14*b) maintains a fairly constant thermal gradient up to the centre-line, corresponding to the more angular geometry of the melt pool in this case. Furthermore, the growing crystals are not required to change their growth direction as occurs with slower speeds (Figure *2.14*a).

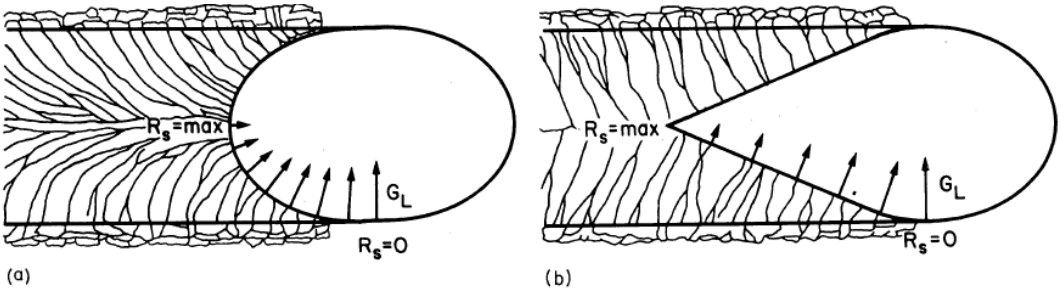

Figure 2.14: *Diagram showing variation of thermal gradient G_L and growth rate R_S along solidification front for different travelling speed; (a) elliptical shape (low and moderate speed); (b) tear drop shaped (high speed) [44].*

David and Vitek [44] have reported the effect of weld pool shape on growth rate with respect to two different speeds of 1.7 mm/s and 16.7 mm/s, in electron beam welding of niobium (Figure *2.15*). At, 1.7 mm/s, the growth rate along the weld centreline equalled that of the welding speed. However, the growth rate was observed to be 5·4 mm/s, when the welding speed was 16·7 mm/s (Figure *2.15*). The weld pool shape was also found to be elliptical for lower welding speed of 1·7 mm/s and, became an elongated tear drop shape for a higher welding speed of 16.7 mm/s [44].

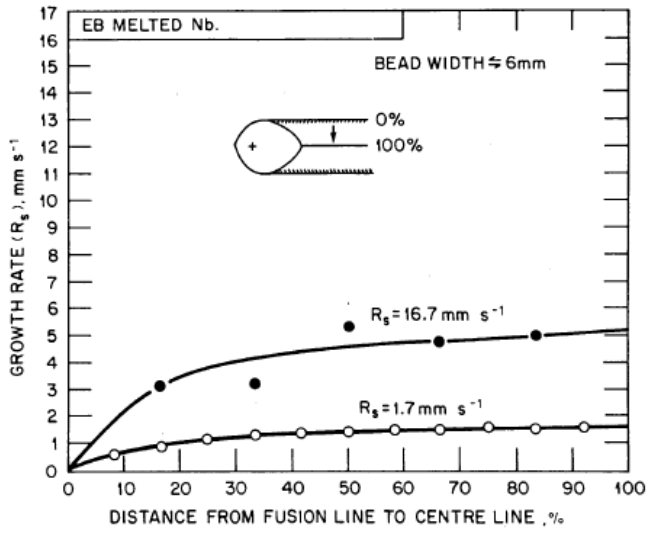

Figure 2.15: *Growth rate as a function of location for electron beam welded pure niobium sheet for two different welding speed 1.7 mm/s and 16.7 mm/s, respectively [44].*

Thermal gradient: The thermal gradients in the solid G_S and in the liquid G_L at the solid/liquid interface play a significant role in determining the solidification substructure in the melt pool. Of the two gradients, G_L is more critical in determining the morphology and is directly proportional to the heat flux in the liquid at the solid/liquid interface. The thermal gradient G_L can also be strongly affected by convection. The sign of G_L is also very significant. Under normal melt pool solidification conditions $G_L > 0$ and it is impossible to obtain thermally undercooled melts, $G_L < 0$ [44]. The exact measurement of the gradients in the weld is very difficult. The thermal gradient increases as the thermal conductivity of the material decreases. For high energy density processes, using electron beams or lasers, the thermal gradient is larger than in low energy density processes such as arc welding. For low energy density processes, increasing the heat input increases the size of the weld pool and lowers the thermal gradient. The thermal gradient also varies considerably with location in the melt pool. As noted above, along the melt track centreline the gradient is at a minimum [43, 44].

Cooling rates: An important variable in determining the melt pool microstructural characteristics is the cooling rate ($\dot{T}$) which is the product of the temperature gradient (G) and the growth rate (R), *(GR* = ($\dot{T}$)*)* and primarily affects the scale of the microstructure. In comparison the ratio *(G/R)* controls the microstructural morphology. In solidification processes, castings, with cooling rates ranging from, 10^{-2} to 10^{2} K/s lie on one end and, rapid solidification involving range of cooling rates 10^{4} to 10^{7} K/s in the other end of the spectrum. Melt pool solidification with intense travelling heat sources lies between these two extremes. Cooling rates in welding and AM may vary from 10 to 10^{3} K/s for processes, such as shielded metal arc, and gas tungsten arc welding (GTAW). For processes using electron beams and lasers, cooling rates may vary from 10^{3} to 10^{6}

K/s, depending on the parameters [44]. Furthermore, the local solidification conditions and cooling rates vary significantly within the melt pool. Solidification maps show the variation of microstructure as a function of G and R and the effect of these two variables as shown in Figure *2.16* [44].

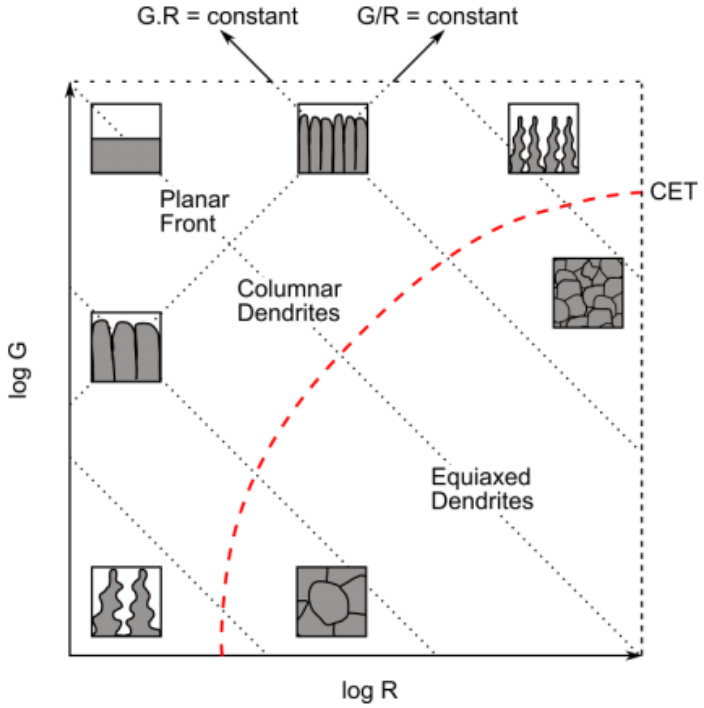

Figure 2.16: *Solidification map showing the variation of melt pool microstructures as a function of the temperature gradient (G), growth rate (R), and combinations of these two variables as GR (cooling rate), and G/R (constitutional supercooling) [42, 44].*

2.3 SOLID STATE PHASE TRANSFORMATIONS IN TITANIUM (β → α)

The transformation from β → α phase is very important in α- β Ti alloys, as it greatly influences the final microstructure. Depending on the alloy composition and cooling rate, the transformation in titanium alloys from the bcc β → hcp α phase can occur martensitically, or by a diffusion controlled nucleation and growth process. The crystallographic orientation relationship between α(hcp) and β(bcc) was first been studied by Burgers in zirconium and later was confirmed for titanium, and is therefore named the Burgers orientation relationship (BOR)- as shown in Figure *2.17* [49].

$$\{110\}\beta_{bcc} \,||\, \{0002\}\alpha_{hcp} \;\&\; <111>\beta_{bcc} \,||\, <11\bar{2}\,0>\alpha_{hcp}$$

It has been shown that for an *hcp-bcc* two phase mixture, the Burgers OR provides an interface with lowest total energy since the crystal lattice d spacing misfit is minimum when the close packed planes and directions are aligned as $(0002)_\alpha || (011)_\beta$ and $[11\bar{2}0]_\alpha || [111]_\beta$ [49].

According to this relationship, a bcc crystal can transform to 12 hexagonal variants, having different orientations with regard to the parent β crystal. Vice versa, there are six β orientations that can transform from a single α crystal. Theoretically, there are in total seventy two possible Burgers orientation relationships during an α → β → α phase transformation [50], but practically this is not often seen, because of variant selection . However, only 57 variants are only possible due to orientation overlapping based on crystal symmetry . Variant [51]selection has been reported both in martenstic and diffusional phase transformations in Ti6Al4V [49, 52-55].

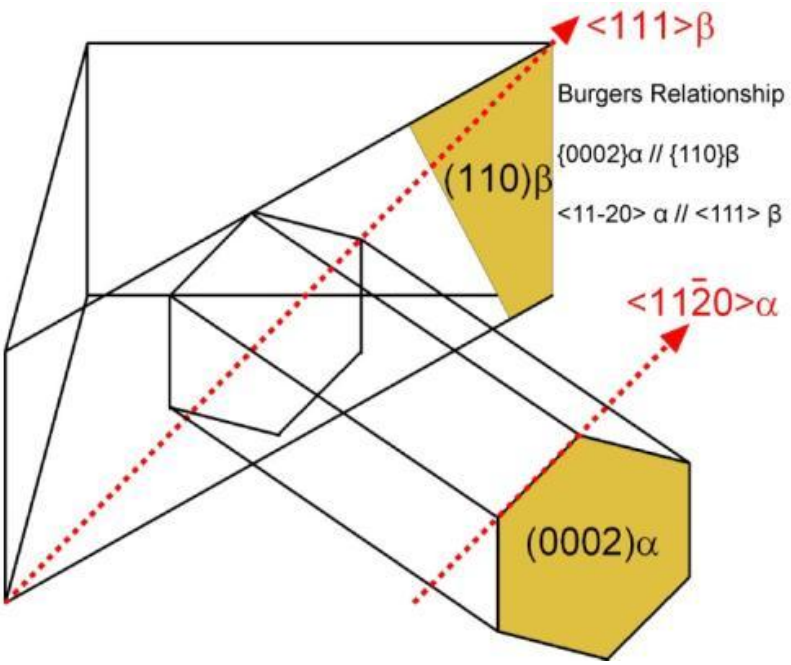

Figure 2.17: *The Burgers relationship in Titanium alloys [51].*

Specific Morphologies of the Room Temperature α-phase: The high temperature β phase can transform to several different types of α-morphologies when it cools down to room temperature depending upon the cooling rate [39],

Diffusionless transformation:

I. Martensitic α phase (e.g. α' or α'') with pocket or acicular morphology,

Competitive diffusionless and diffusional transformation:

II. Massive α morphology(α_m) and α',

Diffusion controlled transformation:

III. Grain boundary allotriomorphic α,
IV. Colony α and,
V. Widmanstäten α morphology.

2.3.1 Diffusionless transformation:

2.3.1.1 Martensitic transformation (β→α')

The martensitic transformation is a diffusionless, or displacive, transformation which can be achieved by high cooling rates (water or oil quenching), whereas a diffusional transformation is realized at slower cooling rates, such as from furnace cooling or air cooling. Upon high cooling rates from the β phase field, the transformation of titanium and its alloys from the β (bcc) to α (hcp) occurs by a displacive transformation to form a martensitic structure designated as α' (shown in Figure *2.18*). Depending on the alloy content, the morphology of α' can be classified into two microstructures, namely massive (packet) or acicular martensite [5]. Massive packet martensitic microstructures are comprised of large irregular regions without any features observed by optical microscopy. However, these regions consist of packets of small parallel α' plates belonging to the same α'variants. In contrast, acicular martensite consists of mixtures of individual α' plates each belonging to different Burger orientations [56]. In addition, as the β stabilizing solute increases the α' loses its hexagonal structure to a orthorhombic structure designated as α'' [5, 39, 41]. The values given in literature for the required cooling rate and Ms-temperature for martensitic microstructure vary widely as shown in Table *2.1*.

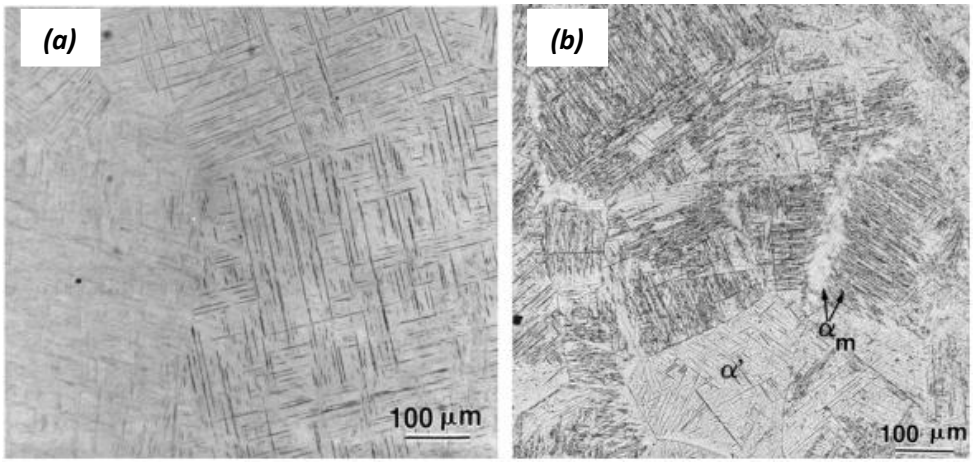

Figure 2.18 : *Illustration of (a) α' at a cooling rate of more than 525 ˚C/s; and (b) massive α_m at a cooling rate of 20 to 410 ˚C/s seen in Ti6Al4V alloy [41].*

Table 2.1: *Literature on the M_S temperature, cooling rate and composition of Ti alloys.*

Cooling Rate (K/s)	**Start Temperature** (M_S in ˚C)	**Composition**	**Reference**
-	~750	Ti-4.25V	[57]
-	625	Ti6Al4V	[58]
-	800	Ti6Al4V	[59]
-	800	Ti6Al4V	[60]
>410	575	Ti-6.04Al-4.03V-0.12Fe-0.09O-0.03C-0.009N-23 ppm of H	[41]
-	775	Ti6Al4V	[61]

2.3.2 Competitive diffusionless and diffusional transformations:

2.3.2.1 Massive transformation (β→α_m)

It has been reported by Ahmed and Rack [41] that the massive transformation (β→α_m) is possible in Ti6Al4V at moderate cooling rates. Massive transformation, α_m, can form in competition with lamellar and martensitic transformations at low and high cooling rates within the overall cooling rate region. During a massive transformation the composition of α_m remains the same as that of parent β phase, but the crystal structure changes from bcc to hcp. This transformation generally occurs at a sufficiently low temperature due to the restricted diffusional growth of α phase [62, 63]. The growth mechanism of a massive transformation requires thermally activated migration of individual atoms over small distances across an incoherent interface, i.e. it is not martensite. It has been shown that massive α preferentially nucleates at β grain boundaries at the highest cooling rates, and is followed by martensitic plates forming adjacent to the prior β grain boundary, and finally individual martensitic plates within the prior β grains [41]. α_m appears as an irregular shaped grain boundary precipitate, as shown in Figure *2.19*. TEM studies indicate that α_m has a blocky morphology with a heavy dislocated substructure [41].

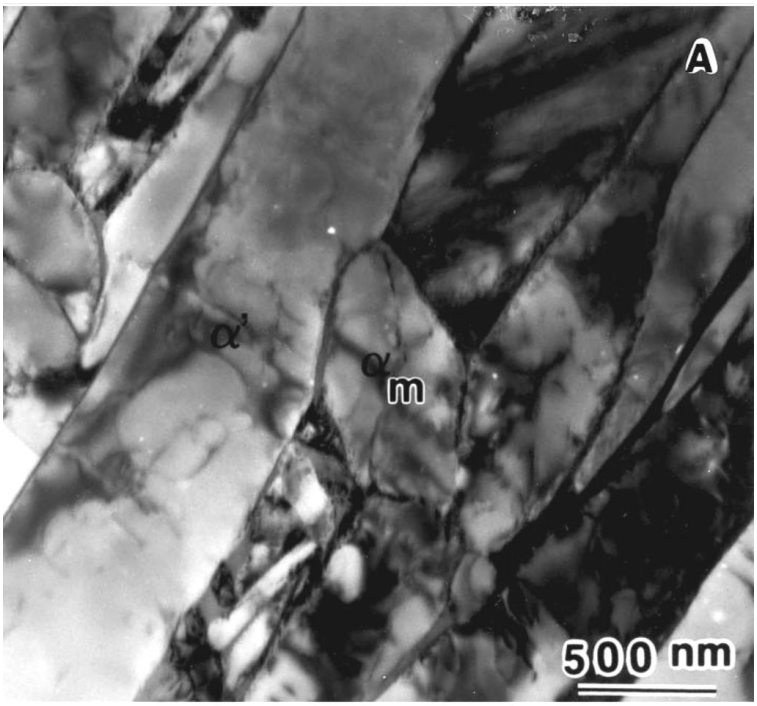

Figure 2.19: *TEM Image of massive α with heavy dislocated substructure in Ti6Al4V alloy [41].*

2.3.3 Diffusion controlled lamellar α microstructures:

The Allotriomorphic grain boundary α ($\alpha_{g.b}$), colony primary α (α_p) and the Widmanstätten α within the prior β grains are all diffusion controlled transformation products involving solute partitioning.

Allotriomorphic grain boundary α ($\beta \rightarrow \alpha_{g.b}$): When Ti alloys are cooled at relatively slow cooling rates from above the β transus temperature, the α phase nucleates preferentially at the prior β grain boundaries, forming a continuous, or discontinuous layer, of grain boundary α, as shown in the continuous cooling transformation (CCT) diagram in Figure ***2.20***(b-c). It has been reported that discontinuous grain boundary α forms under faster cooling rates and is associated with higher amounts of β stabilisers [52].

Upon cooling from the β-phase field, the first α to forms as allotriomorphs at the prior β-grain boundaries, since the presence of the grain boundaries always acts as an effective nucleation site. The orientation relationship of the grain boundary α to the β parent phase has been reported by Bhattacharyya et al., Stanford and Bate, etc [49, 53]. They found that in most cases the grain boundary α exhibited a Burgers orientation relation with one of the prior β grains.

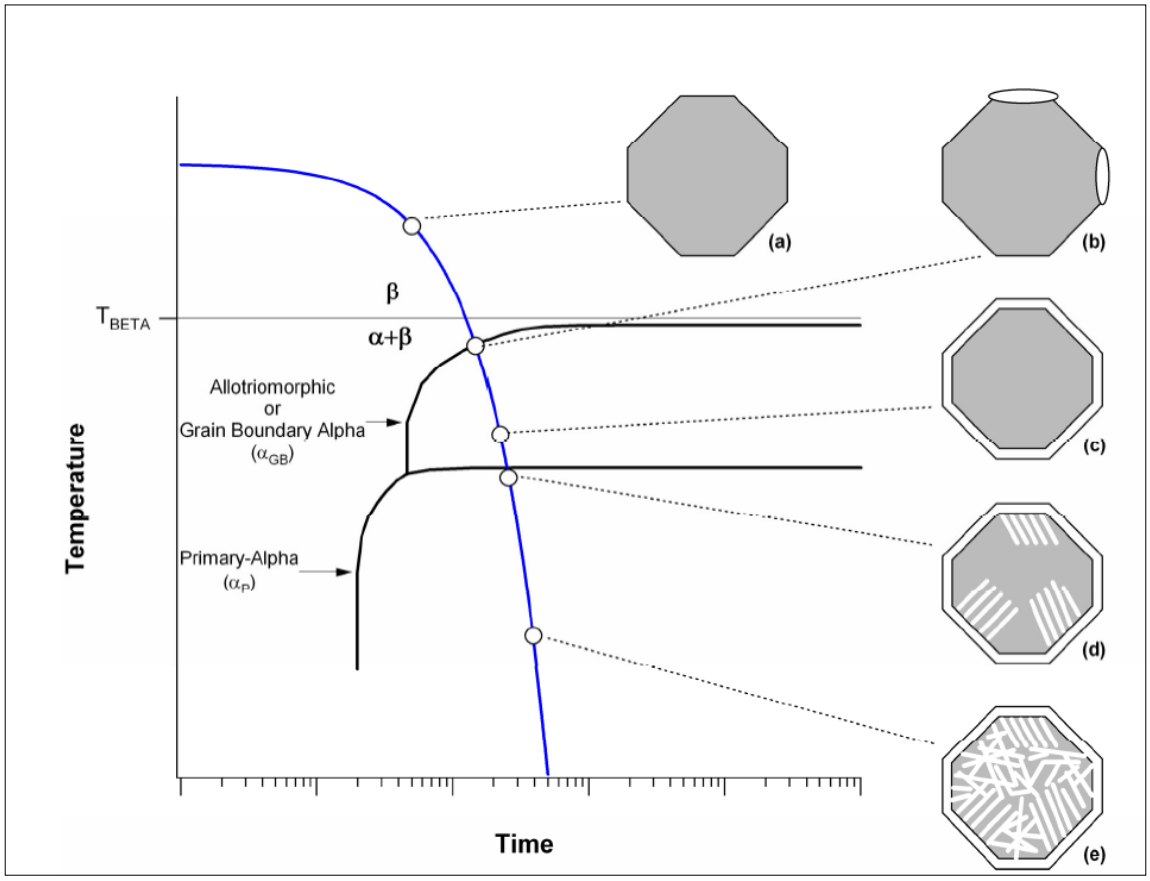

Figure 2.20: *Schematic illustration of the sequence of diffusion controlled phase transformation events, occurring during continuous cooling of Ti6Al4V through the* β *transus; (a) a single* β *grain is shown in gray; (b) the first* α *phase to form is allotriomorphic* α *at the* β *grain boundaries, (c)* α *continues to grow along the* β *grain boundaries, (d)* α *plates begin to nucleate and grow first at the grain boundary* α *as colonies of primary* α *side plates and finally with increased undercooling, (e)* α *nucleates within the remaining* β *in a basketweave morphology [39, 64].*

Colony primary α morphology (β→ colony α_p): Upon further undercooling, Widmanstätten α, with a number of side plates, begins to grow and form a colony from the grain boundary α into the prior β-grain, with which a Burgers orientation is maintained. This primary-α colony consists of high aspect ratio plates of α. Individual α-plates are arranged parallel to one another to maintain a favourable orientation with the corresponding β parent grain. The primary α- plate colonies nucleate and grow into the β grains until they are met by other α plates that nucleated from the other side of the grain, which may belong to different variants of the Burgers relation. The α-plates exhibit a low angle grain boundary when they nucleate from the grain boundary α interface and satisfy the Burgers orientation relationship with the prior β phase. This microstructure, resulting from a diffusional transformation, consists of parallel plates of α separated by the retained β matrix between them, and is termed a *'lamellar microstructure'* [5,

39]. An example of GB α ($\alpha_{g.b}$), and primary colony α (α_p) morphologies are shown in the BSE micrograph in Figure *2.21*. With increasing cooling rates, the width of individual α plates becomes thinner and the colony size reduces with the number of α plates within a colony becoming fewer [39, 41].

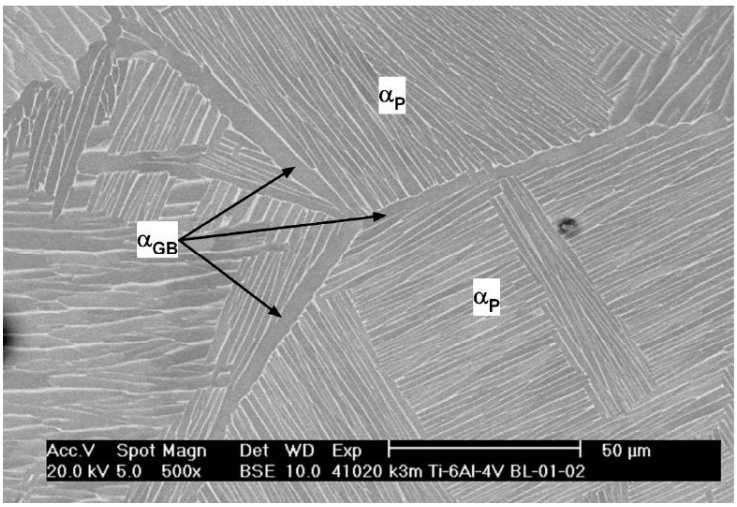

Figure 2.21*: SEM Image showing grain boundary α and primary lamellar α colonies in Ti6Al4V alloy [64].*

Basketweave Widmanstäten α morphology (β → Widmanstäten α): At higher cooling rates, because the driving force is increased, the nucleation of α not only occurs on grain boundaries, but also from existing α plates in the grain interior. As a result, within the remaining β basketweave Widmanstätten α (shown in Figure ***2.20***(e)) forms in a pseudo-random fashion (1 of 12 crystallographic variants). This microstructural morphology, consisting of thinner α plates within the colonies, is designated as a "basket weave" Widmanstäten structure [5]. Figure *2.22* shows examples of SEM micrographs of these different morphologies, including grain boundary α, colony α, and the basketweave α microstructures in Ti alloys. The sequence of diffusional transformation is illustrated in Figure *2.23*.

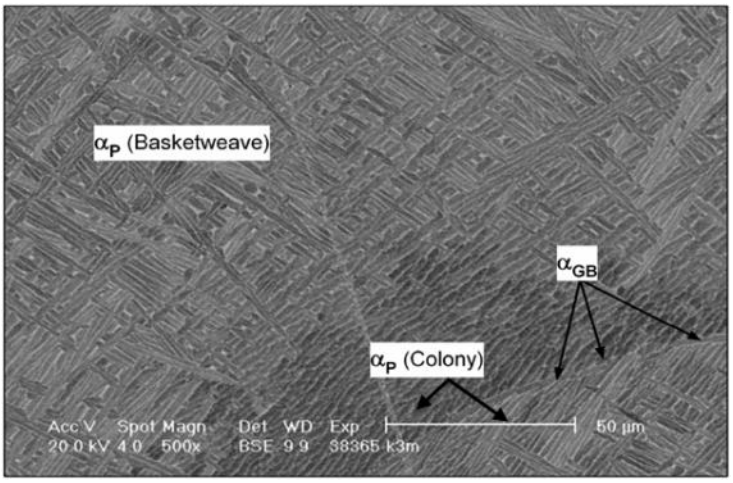

Figure 2.22: *SEM BSE image showing the presence of Widmanstätten α, with grain boundary and colony α-morphologies in a Ti6Al4V alloy [39, 64].*

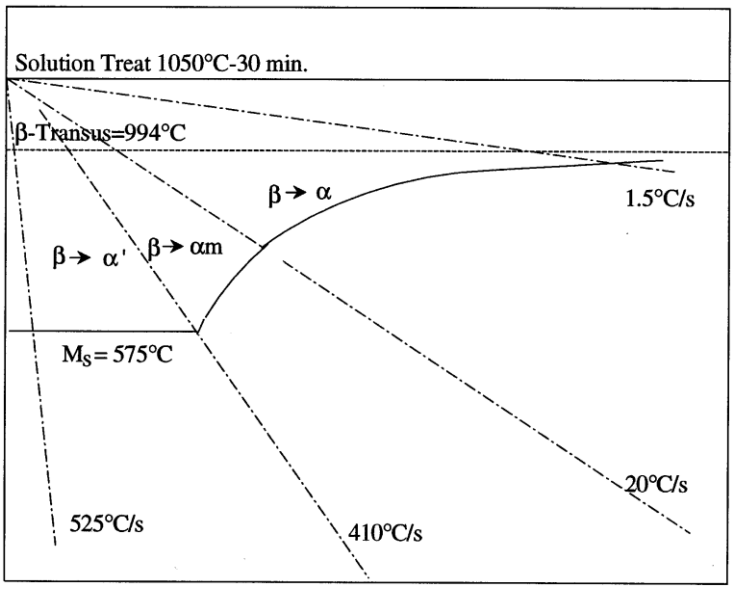

Figure 2.23*: Schematic representation of cooling curves in a Ti6Al4V alloy [41].*

Investigations have been carried out to understand the influence of rapid cooling on the microstructure of the Ti6Al4V alloy by Ahmed and Rack, using a modified Jominy end quench test method from the β-phase [41]. The resultant morphologies with different cooling rates are shown in Figure *2.23*, and the corresponding values are tabulated in Table *2.2*. Formation of a fully martensitic microstructure has been observed at cooling rates above 400 °C/s, a massive transformation was observed between 410 and 20°C/s and, this transformation is slowly replaced by diffusion controlled Widmanstätten α phase at lower cooling rates.

Table 2.2: *The approximate cooling rates required to achieve different morphologies in a Ti6Al4V alloy during heat treatment [41].*

Cooling Rate (K/s)	**Start Temperature**	**Transformation**	Remarks
CR >410	M_S = 848K	Martensitic (α') Pocket like or acicular morphology	Diffusionless process (β→α')
20< CR <410	1243-1273K	Massive (α_m)	Competitive Diffusionless and diffusion controlled process (β→α_m)
CR < 20	~1173K & ~ 1223K (Ref.[29-30])	Widmanstäten (α)	Diffusion controlled process (β → α with Widmanstäten morphology or at grain boundary)
CR < 20	1243-1273K	Allotriomorphic (grain boundary α)	

2.4 HEAT TREATING Ti ALLOYS

Titanium and its alloys are heat treated for a different reasons, to reduce residual stresses (stress relieving heat treatment), to obtain a optimum combinations of ductility, machinability, and dimensional stability (annealing), to increase strength (solution treatment and aging) and, to optimize specific properties, such as fracture toughness, fatigue strength, and high temperature creep resistance. Recovery, Recrystallisation and Grain Growth is an important phenomenon usually happens during thermo-mechanical processing of metals.

Recovery, Recrystallisation and Grain Growth processes refer to the microstructural changes that take place on heating cold worked or deformed metals with no change in the chemical composition and crystal structure. On cold working, the density of point defects and dislocation increases. These crystal defects have strain energy associated with them. Upon heating or annealing, metal tends to lose the excess energy obtained during cold working and goes back to the original state. This loss of excess strain energy provides driving force for the recovery, recrystallisation and grain growth. On heating recovery, recrystallisation and grain growth occur in that order at successively higher temperature [43, 65].

2.4.1 Recovery

Recovery is the annihilation and rearrangement of point imperfections and dislocations without the migration of high angle grain boundaries. As the annealing temperature is increased, the excess point imperfections anneal out in different ways, i.e. a pair of a vacancy and an interstitialcy can mutually annihilate each other. The point imperfections also find a sink at high angle grain boundaries and at edge dislocations. Excess dislocation can disappear at edge dislocation making them to climb up. On further increase of the annealing temperature, the recovery processes start. A positive and a negative edge (or screw) dislocation on the same slip plane can mutually annihilate each other. Excess dislocations of the same sign leftover after this, lower their energy by arranging themselves in low angle boundaries and this process is known as *'Polyganisation'* [43, 65].

2.4.2 Recrystallisation

Recrystallisation is the nucleation and growth of new, strain free crystals from the cold worked metal. The driving force for the recrystallisation is the stored energy in the cold worked or deformed metal. The nucleation may not occur in the usual sense during recrystallisation. An existing grain boundary with local differences in dislocation density on either side may simply migrate into the region of higher dislocation density. If recrystallisation occurs during deformation, then it is called as *'dynamic recrystallisation'* and if recrystallisation happens after deformation, it is called as *'static recrystallisation'*. The recrystallisation temperature can be defined as that temperature at which 50% of the metal recrystallises in 1 hr. The following are the well known laws of recrystallisation [43, 65],

(i) The higher is the amount; the lower is the recrystallisation temperature.

(ii) The finer is the initial grain size; the lower is the recrystallisation temperature. Because, the prior grain boundaries act as sites from where the recrystallized grains start to grow.

(iii) Increasing amount of cold working and decreasing initial grain size produce finer recrystallized grains.

(iv) The higher is the temperature of cold working, the less is the strain energy stored in the metal. The recrystallisation temperature is correspondingly higher.

(v) The recrystallisation rate increases exponentially with temperature.

2.4.3 Grain growth

Grain growth is the increase in average grain size following recrystallisation. The grain size distribution does not change during normal grain growth. During, abnormal grain growth called secondary recrystallisation, the grain size distribution may radically change, i.e., some very large

grains may be present along with fine grains. When the average grain size increases, the grain boundary area per unit volume of the metal decreases with a corresponding decrease in grain boundary energy per unit volume. This provides the driving force for grain growth, which is about an order of magnitude smaller than that for recrystallisation[43, 65].

It has been reported that the β phase undergo a more deformation at lower rolling reductions than the α phase in the two phase α+β Ti6Al4V alloy at room temperature, since β phase is softer than the α phase [66]. Upon reheating the deformed Ti6Al4V just above β transus, the deformed room temperature β phase act as an potential nucleation site and grow by consuming the deformed α phase. Table *2.3* shows the heat treatment cycle for different heat treatments, and the resulting final microstructure [67-69].

Table 2.3: *Heat treating of α-β Ti alloys [67].*

Heat treatment designation	*Heat treatment cycle*	*Microstructure*
Duplex anneal	Solution treat at 50–75°C below $T(\beta)$, air cool and age for 2–8 h at 540–675°C	Primary α, plus Widmanstätten α–β regions
Solution treat and age	Solution treat at ~40°C below $T(\beta)$, water quench(a) and age for 2–8 h at 535–675°C	Primary α, plus tempered α' or a β–α mixture
Beta anneal	Solution treat at ~15°C above $T(\beta)$, air cool and stabilize at 650–760°C	Widmanstätten α–β colony microstructure
Beta quench	Solution treat at ~15°C above $T(\beta)$, water quench and temper at 650–760°C for 2 h	Tempered α'
Recrystallization anneal	925°C for 4 h, cool at 50°C h^{-1} to 760°C, air cool	Equiaxed α with β at grain-boundary triple points
Mill anneal	α–β Hot work plus anneal at 705°C for 30 min to several hours and air cool	Incompletely recrystallized α with a small volume fraction of small β particles

In more heavily β-stabilized alloys such as Ti–6Al–2Sn–4Zr–6Mo or Ti–6Al–6V–2Sn, solution treatment is followed by air cooling. Subsequent aging causes precipitation of α-phase to form an α–β mixture.

2.5 TEXTURE REPRESENTATION

Crystallographic textures are very important in terms of the mechanical and physical behaviour of materials, since the preferred orientation of grains is a very common phenomenon in many crystalline materials during processing. Deformation, welding, casting and heat treatment, can all lead to directionality in properties. Overall, if all possible orientations of crystallites occur with equal frequencies (i.e. in a random texture) then the orientation dependence will disappear on average and thus the materials will behave isotropically. Here, the Electron Back-Scattered diffraction (EBSD) technique, associated with the Scanning Electron Microscopy (SEM) has been used to analyse the microtexture or orientation distribution of the grains formed in the AM deposits [70-73]. Rolling texture in materials are commonly expressed in terms of <*u v t w*>, which

means the {*h k i l*} planes of grains that lie parallel to the sheet plane, and the <*u v t w*> directions parallel to the rolling direction [54]. In solidification fibre textures are more common [39, 65].

Fibre textures have a uniaxial (fibre) symmetry that can result from processes such as the drawing of wire, or in extrusion bars [74]. The drawing process causes individual crystals to align in certain crystallographic directions parallel to the wire axis and is also observed in artificial and natural fibres.

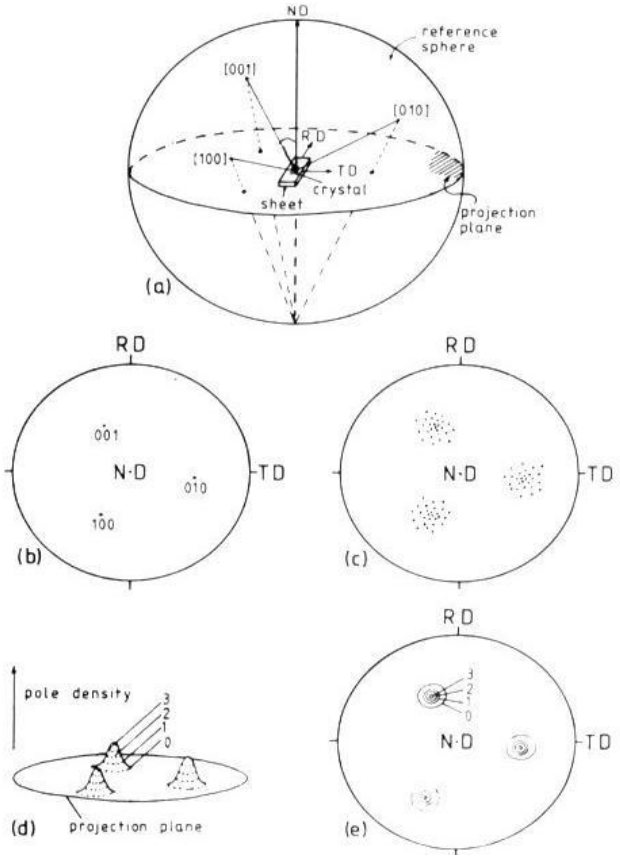

Figure 2.24: *Schematic diagram of a pole figure; (a) projection of (100) poles onto a reference sphere and then onto a projection plane, (b) projected poles of a single grain, (c) projected poles of textured grains,(d) pole density distribution and (e) a contour map of the pole density [75].*

The crystallographic texture of materials is usually represented by (i) Pole Figure (PF), (ii) Inverse Pole Figure (IPF), and (iii) Orientation Distribution Function (ODF).

(i) *Pole figure* is commonly used to show rolling textures, by variation of the pole density with pole orientation, for a particular set of different planes in a two dimensional stereographic projection, relative to the specimen reference frame as shown in Figure ***2.24*** [73].

(ii) *Inverse Pole Figure* represents the intensity of orientation with respect to a single axis; can also be used to depict other types of texture symmetry. For example, the above mentioned uniaxial fibre textures can be described by inverse pole figures.

(iii) *Orientation Distribution Function* is the representation of texture, based on the three Euler angles of rotation required to co-orientate a unit cell with a reference coordinate system.

2.6 MICROSTRUCTURAL EFFECT ON THE MECHANICAL PROPERTIES OF Ti6Al4V

The mechanical properties of interest in this section are yield and tensile strength, fatigue strength, ductility and hardness. The presence of the α+β phases in Ti6Al4V allows the properties of the alloy to be modified by the heat treatment, which controls the formation of different microstructural features, including the size of the prior β-grains and the precipitation of the α-phase components. As a result, a more balanced and wide range of mechanical properties can be achieved, such as good strength at room temperature and for short periods of time at the elevated temperatures [5]**.** The microstructural factors which affect the mechanical properties of the Ti6Al4V alloy are the β-grain size, α-colony size, thickness of grain boundary α and lamellar α, the size and shape of the primary α-grains, the volume fraction of α and β, and tempered martensite. According to Lütjering [38] the most important factor that determines the mechanical properties of lamellar α+β alloys is the α-colony size (as shown in Figure *2.25*a). With decreasing α-colony size (decreasing slip length), the yield strength, the ductility, and crack propagation resistance together with crack nucleation resistance (which determines the LCF strength) are improved. In contrast, the macro-crack propagation resistance and fracture toughness are improved by a large α-colony size due to increased crack roughness and crack closure phenomena [38]. The α-colony size depends on the cooling rate from the β-phase field and the prior β-grain size, which limits the maximum α-colony size. In high cycle fatigue, resistance to crack nucleation is the major limiting microstructural factor. On the other hand, the resistance to propagation of small surface cracks (micro cracks) is crucial. It has also been reported by the same author that the colony boundaries and martensitic plates are strong barriers to the crack propagation. Alloying elements such as oxygen can decrease ductility, through age hardening, by promoting the formation of coherent Ti_3Al particles.

In addition to this, it has been reported that the texture of the α-phase can also affect the mechanical properties of the Ti6Al4V. Gey et al. [76] showed that, in hot rolled Ti6Al4V products, the degree of deformation at high temperature in the β phase field significantly affects the inherited selection of resulting α-texture. It has been reported by Lütjering [38] and M.R. Bache and W.J. Evans [77] that the orientation of the basal plane, with respect to the loading direction is

important. Loading in the transverse orientation, perpendicular to the basal planes preferentially lying co-incident, promotes relatively high yield strength and UTS (as shown in Figure *2.25*b).

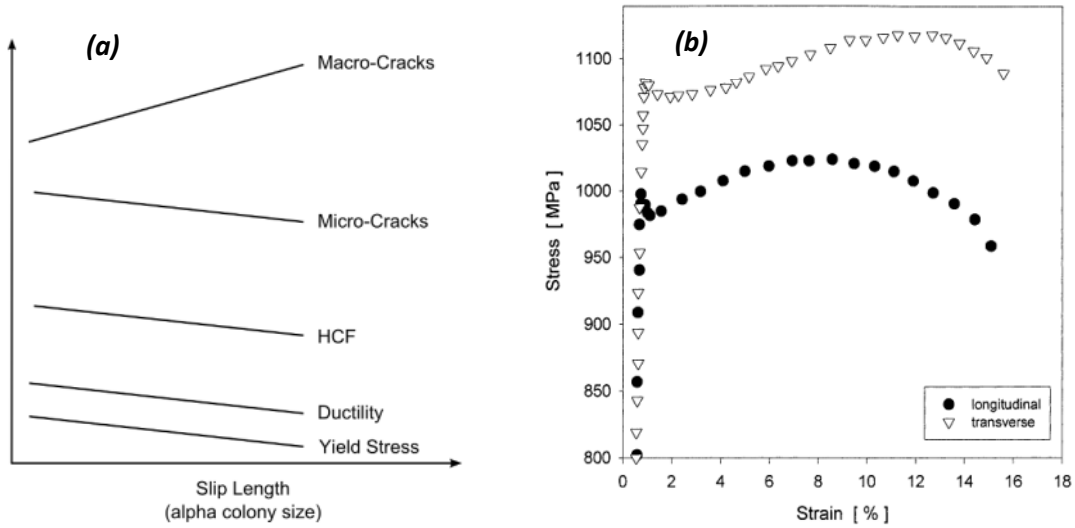

Figure 2.25: *(a) The influence of slip length (α-colony size) on the mechanical properties [38] and, (b) monotonic stress-strain curves for specimens oriented parallel to the longitudinal and transverse plate directions [77].*

2.7 DEFORMATION MECHANISMS

When a material is subjected to static or dynamic stress at room, or elevated temperatures, deformation occurs elastically or plastically depending upon the magnitude of the stress level. In polycrystalline metals plastic deformation results from the motion, or slip, of large numbers of dislocations by the mechanism of sliding or translation, of an array of crystal planes along the most favourably oriented crystallographic planes. Slip typically involves movement of dislocations in the close-packed crystallographic direction in a plane having the highest atomic density. The combination of slip plane and slip direction is termed as 'the slip system'[5, 78]. In the α+β titanium alloys, the slip occurs both in α and β phases according to Burgers Orientation Relationship (BOR) ie., $(0002)_\alpha$ || $(110)_\beta$ and $< 11\bar{2}\,0 >_\alpha$ || $<111>_\beta$ as shown in Figure *2.17*. When the load is applied, the dislocation moving on the (0002) plane of the α phase (in $< 11\bar{2}\,0 >$ direction) can easily transfer into the (110) plane of the β phase in <111> direction. The easy transfer across the α/β interface is mainly due to the lowest total interface energy, since the crystal lattice (d) space misfit is minimum in the closed packed planes and directions of α and β are aligned as per Burgers orientation relationship [53, 79].

Titanium has an axial c/a ratio of 1.587, which is slightly squashed when compared to the ideal hcp crystal structure which has a c/a ratio of 1.63 [5]. As a result of low symmetry, the number of active slip systems is restricted at room temperature. Because of this, additional deformation modes of twinning can be activated, particularly in low temperature during deformation. The crystallographic orientation relationship and limited number of easy slip systems during deformation or recrystallisation leads to the formation of a strong texture. The texture is always reflected in the anisotropy of any material and, in particular, in terms of the mechanical properties [38, 54, 65, 67, 74].

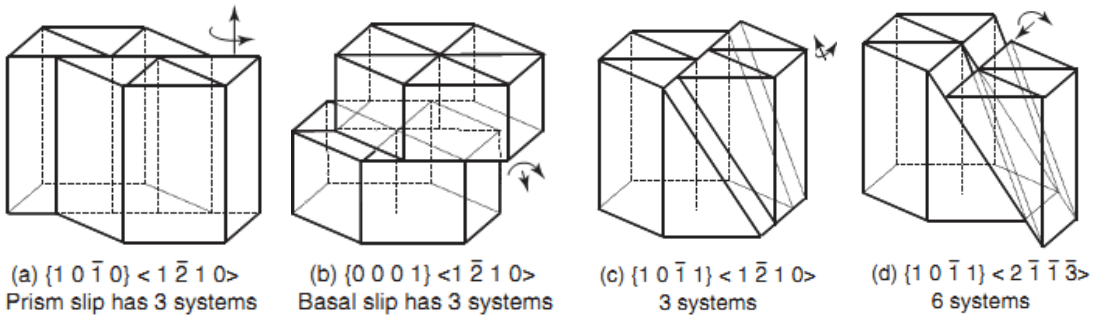

Figure 2.26: *(a) Prism slip* $\vec{a}$*, (b) Basal slip* $\vec{a}$*, (c) Pyramidal slip* $\vec{a}$*, and (d) combination of* $\vec{c} + \vec{a}$*. Arrows represent the axis of crystal rotation due to slip; only prismatic slip does not change the orientation of the c-axis [78].*

There are three main slip directions in HCP Ti namely the closed packed $< 11\bar{2}0 >$ directions a_1, a_2, a_3 [5, 39, 44]. The slip planes containing this $\vec{a}$ type of Burgers Vector are the three (0002) plane, the three $\{10\bar{1}0\}$ planes, and the six $\{10\bar{1}1\}$ planes. From these three different types of slip planes, together with the possible slip directions there are a total of 12 slip systems (Table *2.4*). These can be reduced to 8 normally independent slip systems. Slip on the pyramidal slip plane does not contribute to the number of independent slip systems, since the combined effect of the prism and basal slip component gives pyramidal glide and, as such, cannot be considered as an independent slip system. However, this number is further reduced to only 4 independent slip systems because the shape changes that are produced by the combined action of slip system types 1 and 2 (Table *2.4*) are exactly the same as those of slip system type 3. The three glide planes with the slip vector in the basal plane constitute a total of four independent slip systems, as shown in the Figure *2.26* [5, 78]. According to the Von Misses criterion, 5 independent slip systems are required for homogeneous plastic deformation of a polycrystals. However, only 4 independent slip systems are available for hcp metals. Thus, for the Von Misses criterion to be valid one additional slip system, either $\vec{c}$ type with a [0001] slip direction, or the $\vec{c}$ + $\vec{a}$ type with a $< 11\bar{2}0 >$slip direction needs, to be activated.

Table 2.4: *Types of slip systems active in titanium alloys [5].*

ca	Burgers Vector type	Slip direction	Slip plane	No. of slip systems	
				Total	Independent
1 (Basal)	$\vec{a}$	<11$\bar{2}$0>	(0002)	3	2
2 (Prismatic)	$\vec{a}$	<11$\bar{2}$0>	{10$\bar{1}$0}	3	2
3 (Pyramidal)	$\vec{a}$	<11$\bar{2}$0>	{10$\bar{1}$1}	6	4
4	$\vec{c}+\vec{a}$	<11$\bar{2}$3>	{10 $\bar{2}$ 2}	6	5

Twinning modes are especially important for plastic deformation and ductility at low temperatures, if the stress axis is parallel to c-axis and the dislocations with basal Burgers vector can not move. Twinning leads to either extension or compression along the c-axis, depending on the c/a ratio. In the case of titanium, the $\{10\bar{1}2\}$ and $\{11\bar{2}1\}$ twins are activated during deformation in *tension*, leading to an extension along the c-axis. The most frequently observed twins are of the $\{10\bar{1}2\}$ type, could also display the smallest twinning shear of 0.167 (Table ***2.5***). The shape change associated with a $\{11\bar{2}1\}$ twin has a much larger magnitude of twinning shear (as shown in Figure *2.27*a). Under *compression*, loading parallel to the c-axis $\{11\bar{2}2\}$ twins are activated allowing a contraction along the c-axis (see Figure *2.27*b). It was also reported by Lütjering [5], that increasing concentrations of solute atoms in α-titanium, such as oxygen or aluminium, suppress the occurrence of twinning. Therefore, twinning as a deformation mode, to allow shape changes parallel to the c-axis, plays a major role in pure titanium or in CP titanium with low oxygen concentrations. Most of the studies in Ti6Al4V alloy shows that the twinning modes are completely suppressed by the high solute content [5, 69, 80]. However, recent studies by Leo Prakash et al. and F Coche et al. have confirmed the presence of twins during the deformation of Ti6Al4V [81, 82].

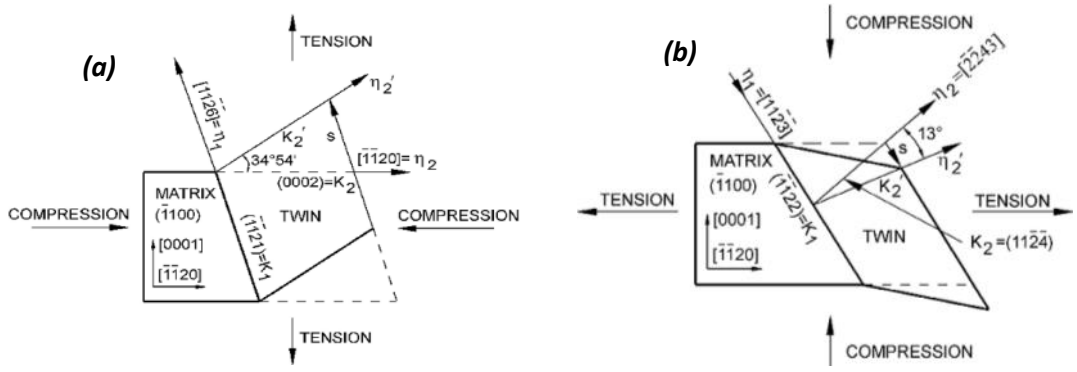

Figure 2.27: *Shape change by (a)* $\{\mathbf{11\bar{2}1}\}$ *and (b)* $\{\mathbf{11\bar{2}\bar{2}}\}$ *twinning [5].*

Table 2.5: *Twinning elements in α-titanium alloys [5]*

Twinning plane (1st un-deformed plane) (K_1)	Twinning shear direction (η_1)	Second undeformed plane (K_2)	Direction of intersection of plane of shear with K_2 (η_2)	Plane of shear perpendicular to K_1 and K_2	Magnitude of twinning shear
$\{10\bar{1}2\}$	$<10\bar{1}\bar{1}>$	$\{\bar{1}012\}$	$<10\bar{1}1>$	$\{1\bar{2}10\}$	0.167
$\{11\bar{2}1\}$	$<11\bar{2}\bar{6}>$	(0002)	$<11\bar{2}0>$	$\{\bar{1}100\}$	0.638
$\{11\bar{2}2\}$	$<11\bar{2}\bar{3}>$	$\{11\bar{2}\bar{4}\}$	$<22\bar{4}3>$	$\{\bar{1}100\}$	0.225

2.8 ADDITIVE MANUFACTURING

2.8.1 Introduction

Additive Manufacturing (AM) is a novel near-net-shape fabrication technique used to produce solid components by consolidating partial, or fully melted, layers of powder, or wires, or ribbons. The materials to be deposited are melted by a focussed heat source, such as an electron beam (e-beam), or laser, or plasma in arc welding [8, 26, 33, 83-85]. Each layer is a section of a final 3D CAD final component model: i.e., the 3D geometry of the final component is formed by building-up a stack of 2-D profiles layer-by-layer by local melting. This process has been given many different names; and in the field has been referred to as: rapid prototyping (RP), rapid tooling (RT), rapid manufacturing (RM), freeform fabrication (FFF), solid freeform fabrication (SFF), additive manufacture (AM), amongst others. Unless otherwise appropriate, AM will be used for the remainder of this work to describe the aforementioned processes. Figure *2.28* shows a schematic representation of the AM technique [23].

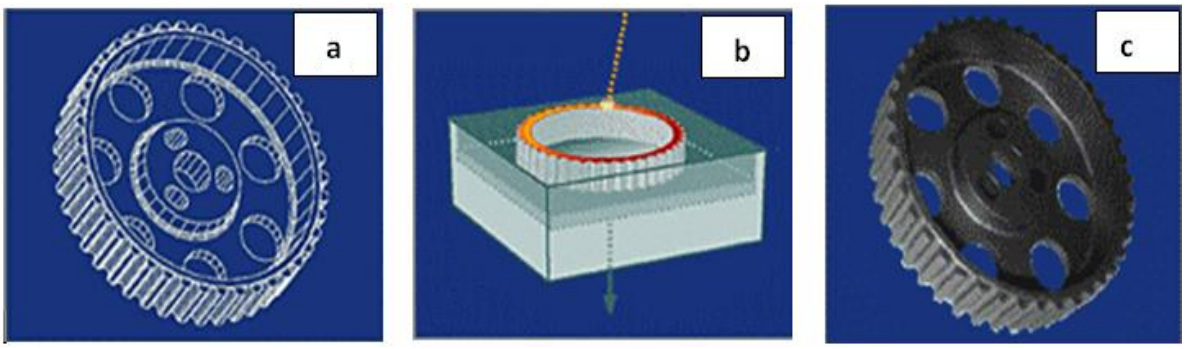

Figure 2.28: *(a) The 3D CAD model of a component to be produced by AM; (b) the actual component being built-up through the powder bed method of deposition, using electron beam local melting, and (c) the final component produced by the AM technique [23].*

In powder bed deposition, the spot size of the beam depends on the heat source and is typically in the range of 50 µm to 1 mm [8, 30]. Building is usually carried out under vacuum (e-beam) or in an inert gas (laser beam) environment to avoid contamination [8]. Wire or ribbons are used as feedstock to produce larger sized components, with gas arc welding or high power electron or laser beams for the heat source. The AM technique is not a new process and is essentially a rapid proto-type technique that has been used for many years to produce 3D parts in the field of polymeric materials processing. However, in the past few years a considerable amount of attention has been given to the direct deposition of metallic materials, especially in sectors like aerospace, defence, automobile and medical industries [9, 10, 27, 86-90].

2.8.2 Classification of AM processes

Overall, rapid or near-net-shape manufacturing can be classified as shown in Figure ***2.29*** [91]. Metal additive layer manufacturing can also be classified based on the heat source and, the materials feedstock [33, 84, 92-95], as shown in

Table ***2.6***. The electron and laser beam, powder bed method and, arc plus wire additive layer manufacturing processes will be discussed later in more detail (in the experimental chapter), as they are the build platforms used in this project.

Table 2.6: *Classification of additive manufacturing processes.*

Heating source	Fusion						Solid state	
	High energy beam				Electric Arc (TIG or MIG Arc)		Ultrasonic	Cold consolidation
Method of layering	Electron beam		Laser Beam					
	Method	Manufacture	Method	Manufacture				
Powder-bed	EBSM	Arcam	DMLS keltools SLM SLS	EOS 3D Systems MTT group 3D Systems	-		-	Solid phase laser sinter ing (by Phenix systems)
Powder-blown	-		LENS LAM DMD DMP	Optomec Aeromet POM group ProMetal RCT	-		-	Laser consolidation (by Accufusion)
Wire	EBF^3	Sciaky	SMD DLF	Rolls-Royce Trumpf	SMD WAALM	Rolls-Royce WERC, Cranfield University-UK	UC (by solidica)	-

*EBSM-Electron Beam Selective Melting, EBF^3-Electron Beam Free Form Fabrication, DMLS- Direct Metal Laser Sintering, SLM-Selective Laser melting, SLS- Selective Laser Sintering, LENS-Laser Engineered net shaping, LAM – Laser Additive Manufacturing, DMD – Direct Metal Deposition,

DMP- Direct Metal ProMetal, SMD- Shaped Metal Disposition, DLF- Direct Laser Fabrication, WAAM – Wire Arc Additive Layer Manufacturing, UC- Ultrasonic Consolidation .

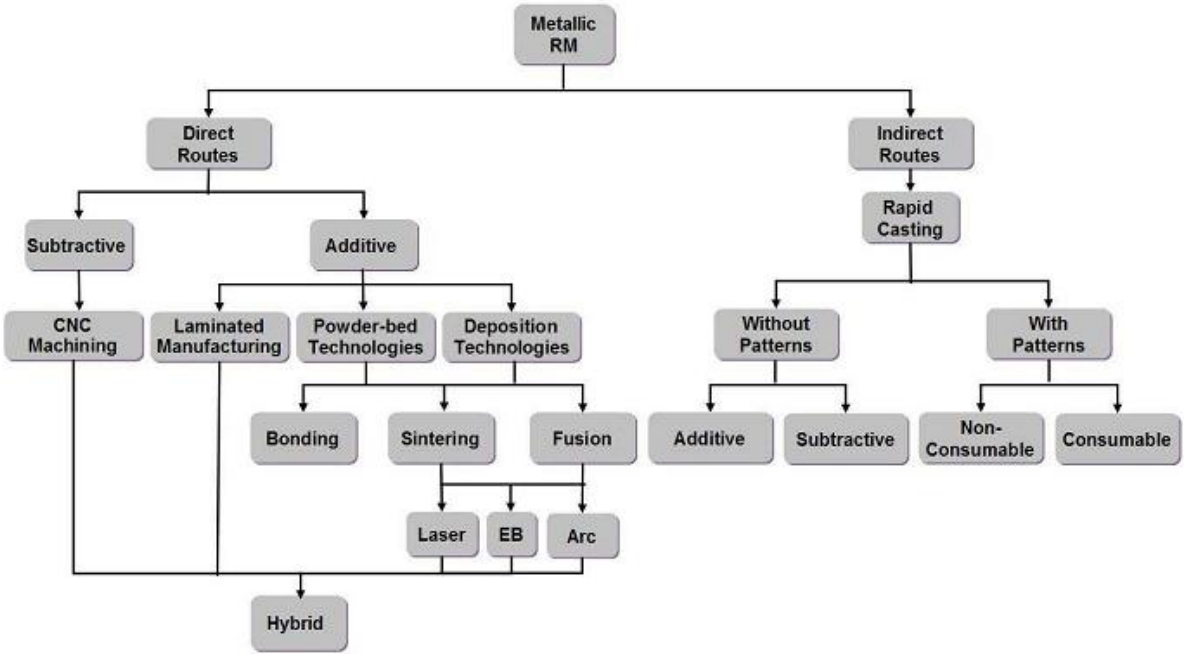

Figure 2.29: *Classification of metallic rapid Manufacturing processes [91].*

2.8.3 AM using an electron beam heat source

AM with an electron beam heat source can be divided into two types based on the method of material feeding; namely (a) powder bed deposition and, (b) wire deposition techniques.

(a) Electron beam selective melting (EBSM) - Powder bed deposition technique: In EBSM, the CAD volume model is sliced into layers of equal thickness. The EBSM machine writes each layer onto a powder bed, where powder layers of equal thickness are spread by a powder handling system. The electron beam gun melts specific areas that are equal to the cross section of the components in each section slice. Figure *2.28* shows the working principles of the standard electron beam melting machine. EBSM works within a vacuum environment. A two stage process is necessary to avoid charging of the powder particles during coupling with the electron beam. In a first phase, the powder particles in the area to be melted are more gently preheated to sinter them together, in the second stage, the power density is increased and rapid melting occurs. Control of the rapidly moving electron beam over these 'two heating stages' allows quasi-simultaneous heating and melting of the powder materials [90]. For titanium the temperature of the material already fused is generally maintained in the temperature range of 560 to 740 ˚C during processing [8, 83, 84]. The prime advantages of using EBSM process over laser processing are,

(i) the e-beam can be focused more precisely than an electromagnetic wave of light,
(ii) the efficiency in e-beam generation is high,
(iii) the efficiency of e-beam coupling into the work piece or powder materials is high,
(iv) the power and focus location of the e-beam can be controlled without inertia (no moving mechanism),
(v) the vacuum environment necessary for the use of an electron beam ensures that the process is clean and an inert gas atmosphere is not required,
(vi) The initial investment in the electron beam system is higher than laser-based systems because of the vacuum system. However, replacement filaments for electron beam systems are relatively cheap. Whereas, the replacement lasers can be very expensive.

The *Advantages of Powder bed deposition* are: (I) very good precision of deposition, (II) good surface finish, (III) automatic operation, (IV) better at overhung surfaces, (V) good utilisation of powders, (VI) can make shapes which were previously impossible, (VII) small parts only. Whereas, the *Limitations of powder bed deposition* are, (I) relatively low build rates, (II) the need to build on a flat base and, (III) the relatively low build volume [30, 84].

(b) Electron beam free form fabrication (EBF^3) - Wire feedstock deposition technique: The EBF^3 process was developed by NASA Langley research centre with a company called Sciaky Inc. Compared to the EBSM technology, the EBF^3 process uses a wire feedstock that is introduced in a melt pool generated by the electron beam in a vacuum environment of about 1 $x10^{-4}$ torr or lower. The process is similar to a traditional welding approach, but allows the manufacturer of free standing structures. The products produced from this process must be finish-machined, but it is capable of producing larger structures [6, 32, 91, 96].

Figure *2.30* shows the EBF^3 machine setup, and the shapes of the components produced at NASA Langley. The EBF^3 process is nearly 100% efficient in feedstock consumption and approaches 95% efficiency in power usage [6]. The e-beam couples effectively with any electrically conductive material, including highly reflective alloys, such as Al and Cu. The machine is also capable of bulk metal deposition at deposition rates in excess of 2500 cm^3/hr (150 in^3/hr) [6]. The diameter of the wire feedstock and e-beam, determines the smallest details attainable using this process. Fine diameter wires may be used for adding finer details, and larger diameter wires can be used to increase deposition rate for bulk deposition.

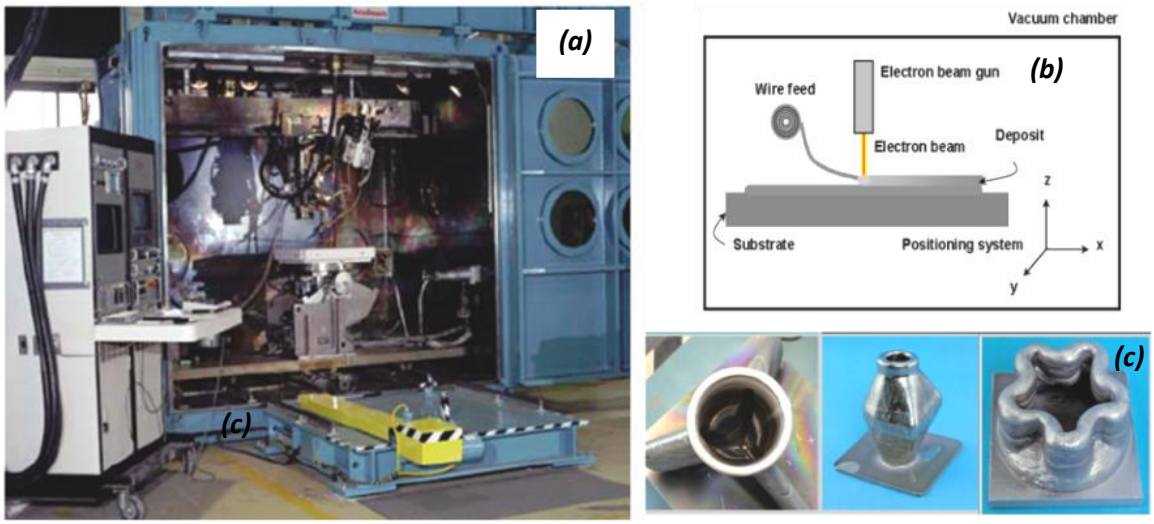

Figure 2.30: *The EBF^3 system at NASA Langley Research Centre (a); Schematic of EBF^3 system components (b) and, (c) some typical components produced via EBF^3 [6, 9, 32].*

2.8.4 AM using a laser beam heat source

Laser AM can be divided into three types based on the method of material feeding; namely (a) powder bed deposition, (b) powder blown deposition and, (c) wire deposition techniques.

(a) Selective laser beam melting (SLBM or SLM) - Powder bed deposition technique: The SLM technology works in the same principle as that of EBSM powder bed deposition except the heat source is a laser beam. Figure ***2.31*** shows a schematic representation of key components of the selective laser melting (SLM), or direct metal laser sintering (DMSL), process. As shown in Figure ***2.31***, the machine comprises a process chamber, an optical system with a ytterbium fiber laser (operating at 1060 - 1100 nm), and a process computer. The powder is spread on the retractable platform and then levelled using a powder wiper system. The optical system creates and positions the laser beam guided by an expanded fibre laser, scanner mirrors, and a focusing objective to fuse the metal powder by melting it locally. In such highly complex geometries can be created directly from 3D CAD data, fully automatically [30, 33, 97, 98].

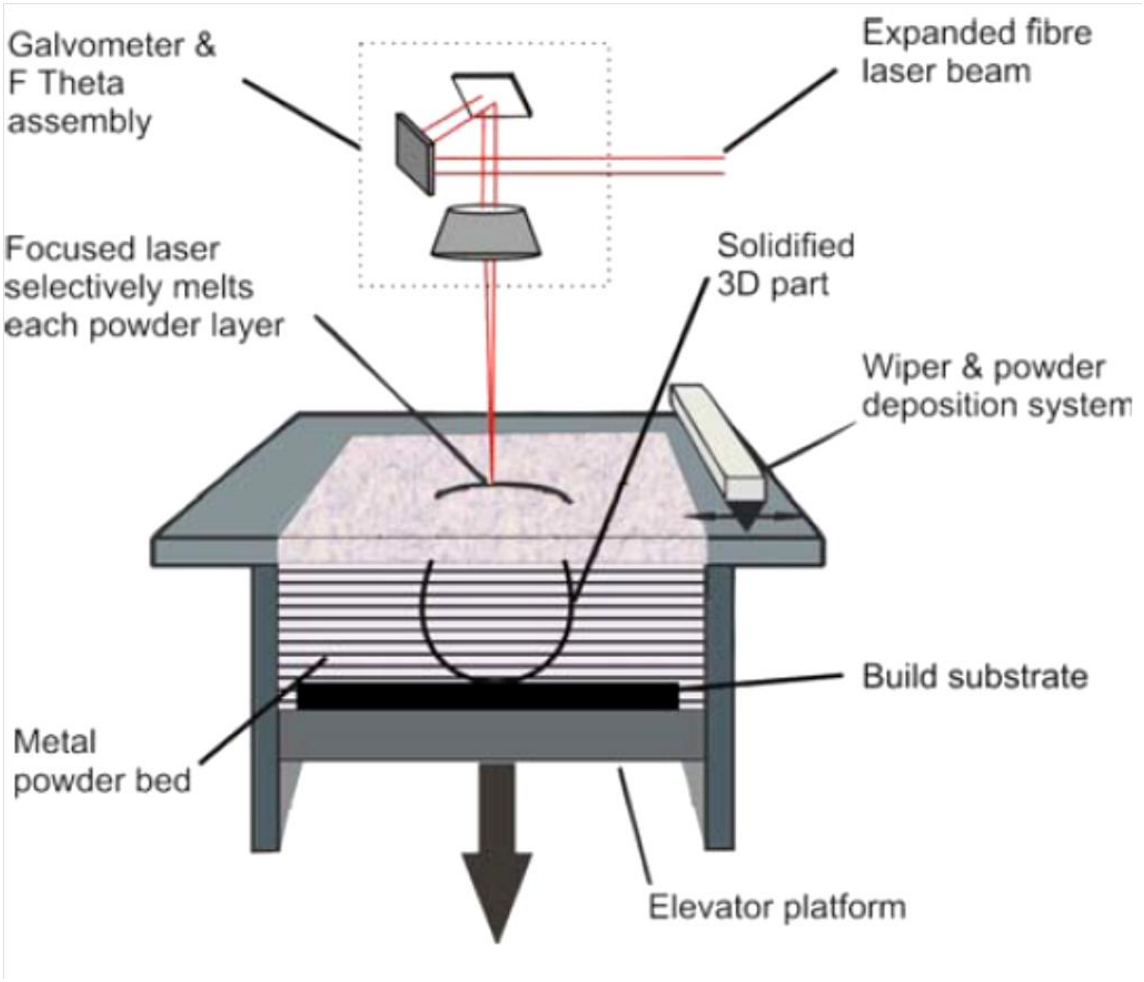

Figure 2.31: *Schematic diagram of typical powder bed SLM system [30, 97, 99]*

If the sufficient power is applied, the powder melts and forms a liquid melt pool, which solidifies to room temperature rapidly and forms the final densified product. After the cross-section of each layer is fused by scanning, the build platform is lowered by an amount equal to the layer thickness of about 20 to 30 µm, and a new layer of powder is spread across the cross-section. This process is repeated until the final shape of the product is completed. The build chamber is evacuated and then filled with inert gases, such as argon, so that an atmosphere with low oxygen content can be maintained during the components building. This technique can produce parts with high accuracy with better resolution, and surface quality than the Arcam electron beam machine. More details of the working principle of the SLM machine can be found in references [8, 20, 30, 33, 98, 99].

(b) Direct laser fabrication (DLF) - Blown powder technique: This technique also uses a laser beam as the source of heating. However, the powder is introduced to the melt pool through nozzles surrounding the laser head as shown in the Figure *2.32*. The entire setup is placed within an argon atmosphere. In the blown powder method, argon also acts as a powder

carrying gas [11, 34]. The laser powder blown technique can deposit material at a rate of about 0.9 to 4.5 Kg/h [25].

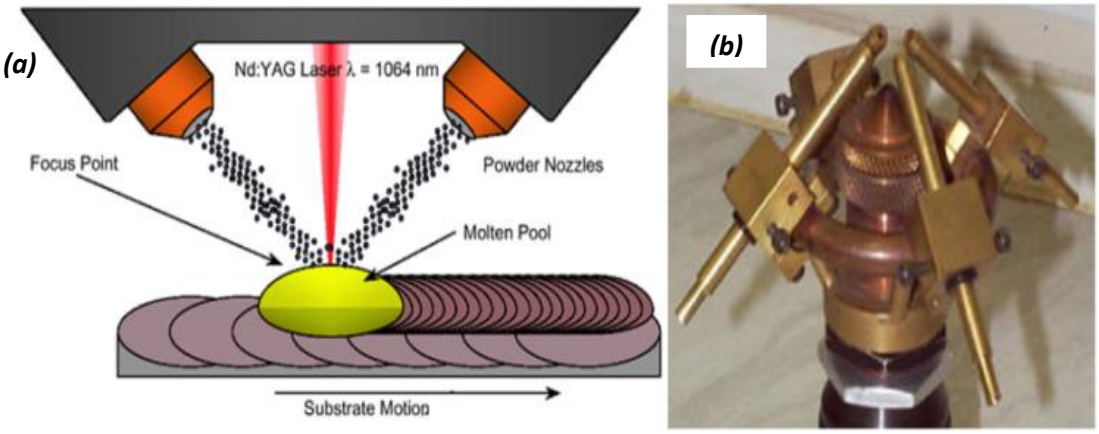

Figure 2.32: *(a) Schematic of a direct laser fabrication - blown powder system and, (b) a four port nozzle used for powder injection [11].*

The advantages of the powder blown method over powder bed methods are, (I) a high deposition rate capability, (II) this usable for repair, (III) a relatively wide process window, (IV) a low heat input to the substrate, (V) easy inert atmosphere operation, and (VI) greater ease of manufacturing functionally graded structures. Whereas, *the limitations* are (I) low powder usage efficiency, (II) it is poor for overhung surfaces, (III) it tends to leave a rough surface finish, and (IV) the need for complex manipulation systems for 3D parts.

(c) Direct metal deposition (DMD) - Laser and wire feedstock: This technique uses a laser beam as the heat source, but wire is introduced in to the melt pool, as shown in Figure *2.33*. The entire chamber also works under an argon inert gas atmosphere. The main advantage of a laser-wire combination is to have a higher deposition rate to build larger components [11, 37, 100, 101]

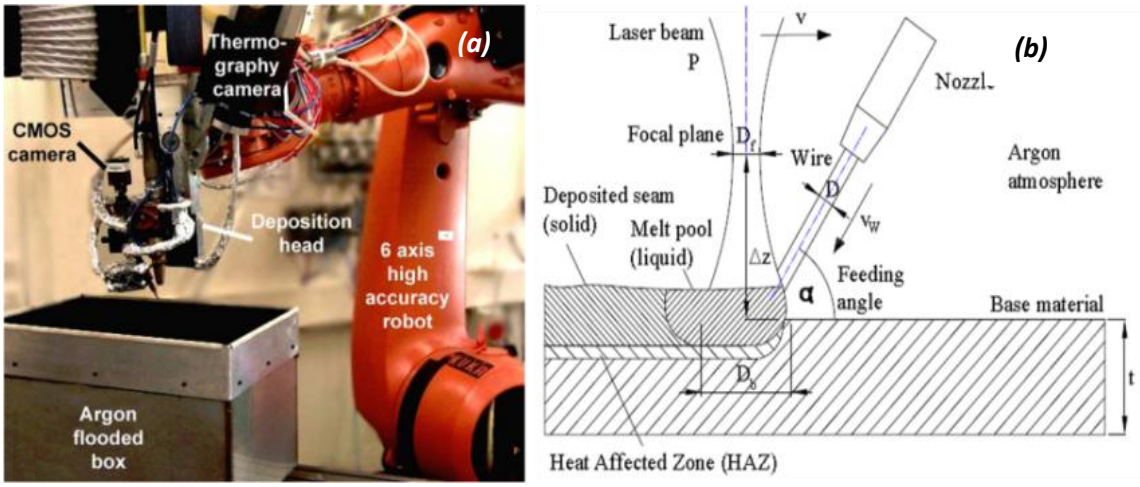

Figure 2.33: *(a) Experimental setup of a direct metal deposition technique, and (b) diagram of direct metal deposition using laser and wire [37, 100].*

2.8.5 Wire plus arc AM (WAAM)

Wire + Arc Additive Manufacture (WAAM) technique can be classified further into two major processes, based on the type of electric arc torch used to melt and fuse the wires; (1) tungsten inert gas arc welding (GTAW or TIG welding) + wire deposition , and (2) metal inert gas arc welding (GMAW or MIG welding) + wire deposition.

The wire is fed into the melt pool produced by the electric arc source, similar to in the EBF[3] process. Recently, wire instead of powder has been exploited in the AM processes, in order to increase deposition rates, to overcome contamination problems and the high prices of high quality powders. WAAM has gained the considerable interest in the recent years due to its high deposition rate and 100% efficiency [102-104]. This process is also called as Shaped Metal Deposition (SMD) technique. The process uses an argon flooded hood with a 6 axis robot, wire feeding system and the electric arc torch as shown in Figure ***2.34***, deposition can also be performed in an argon floated chamber. The approximate cost of parts produced via WAAM (with MIG - CMT) can be seen from the Figure *2.35* [105]. WAAM deposition rate capabilities can extend to 1 kg/hr for cold wire fed GTAW, while several kilograms per hour can be achieved by utilising a GMAW based system. For example, the GMAW -CMT mode can deposit up to 2.5 kg/hr with the wire diameter of 1.2 mm [106].

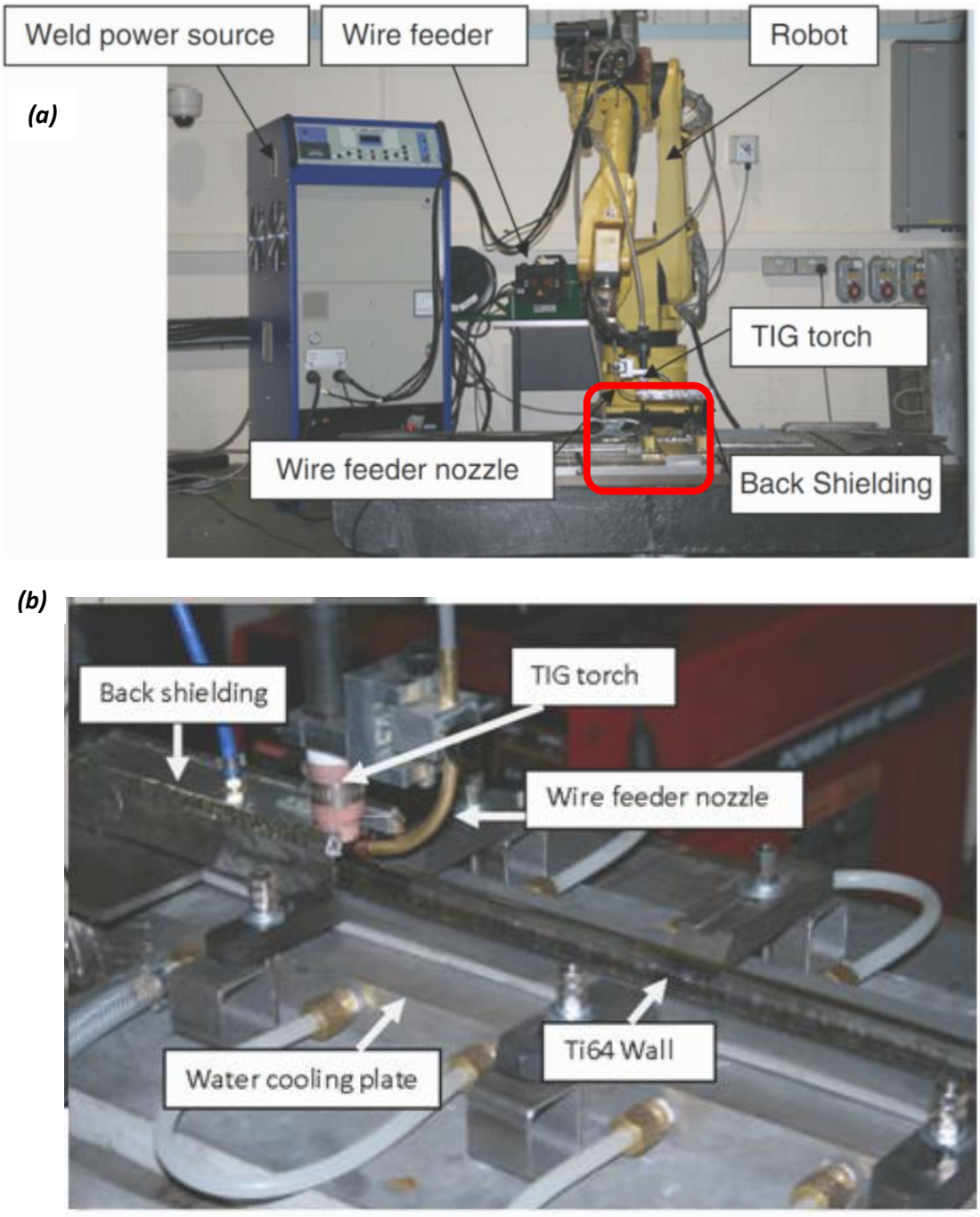

Figure 2.34: *(a) TIG plus wire based additive manufacture experimental setup and (b) a closer view of the TIG torch during the deposition (highlighted as a red box in (a)) (courtesy of Welding Engineering Research Centre, Cranfield University, UK 2009) [105].*

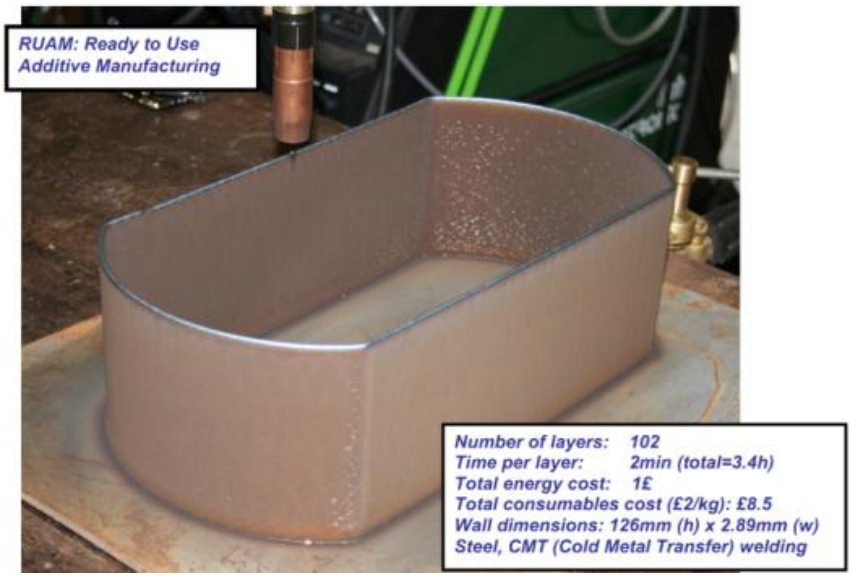

Figure 2.35: *Shows the approximate manufacturing cost of a WAAM deposited sample with a MIG-CMT technique at the Welding Engineering Research Centre, University of Cranfield, UK [105].*

The *advantages of WAAM* are,

(I) It is suitable for large aerospace structural components,

(II) A single machine can repair and re-produce worn metal parts of turbine blades, and large aircraft structures simply from scanned data or 3D CAD model

(III) The continuous wire feed helps very high deposition rates with less time to manufacture,

(IV) Low initial investment compared to other processes,

(V) Low cost of the final component,

(VI) Easy to handle and maintain,

(VII) No need for vacuum like in the case of electron beam deposition,

(VIII) No problems of reflectivity of laser light,

(IX) Allows the use of additional pre-heating or water circulating cooling systems to control the cooling rates and resulting properties,

(X) Easy of welding in all position with the help of automatic 6-axis robot,

(XI) No need of high skilled man power as its traditional manufacturing process.

The ***limitations of the process*** are that it, (I) can not be used to produce small and complex shaped components and, (II) needs final machining for a good finish.

Table *2.7* shows comparison of the capabilities of different AM processes by different heat sources, input materials and methods of deposition.

Table 2.7: *Comparison of advantages of different AM processes [6, 8, 27, 29, 32, 33, 47, 95] .*

Source	**method**	**Resolution**	**Deposition rate**	**Power efficiency**	**Coupling efficiency**	**Cleanliness**	**Cost**	**Surfaces Finish**
Laser	Powder bed	++	-	-	-	0	-	+++
	Powder blown	+	++	-	-	0	0	+
	Wire	0	++	-	-	-	-	0
e-beam	Powder bed	0	+	++	++	++	-	+
	Wire	-	++	++	++	+	+	0
Arc	Wire	-	+++	++	++	-	+++	-

(++) = excellent , (+)=good, (0)=neutral, and (-) negative

2.9 AM BUILD QUALITY AND MICROSTRUCTURE

This section will focus on a review of the literature concerning the microstructure and properties of samples produced by AM with a Ti6Al4V alloy. In particular, the presence of defects, primary grain structure, transformation microstructure, banding, and texture will be considered.

2.9.1 Porosity

The presence of porosity will not be discussed in depth since this project mainly focused on the evolution of primary β-grain structure and its influence on texture and mechanical properties. However, it is important to be aware of the amount of porosity typically seen in AM samples.

In Powder bed AM process such as EBSM and SLM, the powders are consolidated using electron or laser beam to produce the final 3D components, and hence the amount of porosity in the final component can be reduced by maintaining the strict process control over important process parameters, such as different scanning strategies, cleanliness of the powder, power density (to re-melt the last layer without the lack of penetration defects), layer thickness, hatching or overlap. It has been reported by many authors that the EBSM technique can produce the 99.9% dense parts by maintaining optimised process parameters using carefully prepared powders, via gas atomised (G.A) and, plasma rotating electrode processes (PREP) [8, 20, 23, 31, 90, 93, 107]. However, the samples produced via SLM techniques shows a bulk density of 98 to 99 %, which is lower than the EBSM techniques [30, 33, 98, 108]. Entrapped argon gases (more in the case of powder blown laser deposition), opaqueness of laser light to rough surfaces, cleanliness of the used powder, and rapid melting at room temperature tend to micro-porosity associated with the laser powder bed technique, are reported to be the key reasons for the increased amount of porosity in SLM components. The influence of change in scan strategy, hatching pattern, beam travel velocity, layer thickness and energy density have been systematically studied by the Thjis et al. [98] in the SLM techniques. By using different scanning strategies, it is however possible to generate different specimens with artificial porous structures for biomedical implant applications [10, 19, 88]. In contrast, it has been reported that 99.99 % density components can be achieved with the Arc-wire deposition AM technique. The main sources of gas defects in this case are moisture and contamination of the wire materials [106].

2.9.2 Development of microstructure in AM processes

During the AM process the powder, or wire, is fed into a local melt pool, produced by a sharply focused heat source, and the component is produced layer-by-layer through rastering the source of heat. Solidification occurs rapidly in a small localized volume and the resulting microstructures are affected by repetitive thermal cycling. During processing, solidification times are short and steep thermal gradients may exist particularly when an intense laser source is used [26, 48]. The deposited material is also thermally affected by the deposition of subsequent layers, resulting in complex thermal histories. Such thermal histories make the prediction of precise microstructures difficult [34]. This is especially true in alloy systems that under go multiple phase transformations; such as the liquid → solid β (bcc) → solid α (hcp) phase reactions seen in titanium alloys. Many AM process variables can also influence the microstructure formation and its characteristics. For example, in direct laser fabrication the process parameters that affect the microstructure and resulting properties include; the type of laser, laser power, spot size, shape of the beam, laser traverse speed, line spacing, deposit layer thickness, deposition pattern, powder shape and size distribution, powder feed rate, powder velocity, initial substrate temperature, substrate surface finish, substrate thickness, substrate microstructure and its texture, the size and the shape of the deposit [11, 26, 28, 29, 33, 34, 48, 98, 109, 110].

2.9.2.1 Electron beam – AM literature

The available literature on the microstructures produced using electron beam processes by AM is limited. The Ti6Al4V alloy has been the most heavily researched and has been of specific interest in the field of biomedical science [10, 16, 19, 20, 111] for its biocompatibility. Recently, Al-Bermani et al. has published the most comprehensive study to date of the microstructure and texture seen in Ti6Al4V AM test pieces [112]

2.9.2.1.1 Typical macrostructure:

Whether EBSM powder bed, or EBF^3 wire feedstock, systems are used, a significant microstructural morphology identified by many authors [9, 32, 92] is the coarse columnar primary β microstructure. Al-bermani et al. have reported that there are three different transient regions in the EBSM builds as follows;

(iv) an initial chemical transient region,
(v) a region of equiaxed to columnar prior β grains,
(vi) a martensite region in the final layer.

Figure *2.36* shows the typical overall macrostructure of an AM component built in the Ti6Al4V alloy. The transverse section shows the presence of huge columnar prior β-grains, which grow every layer of deposit, approximately in the opposite direction to that of the global heat extraction (i.e., parallel to the direction of the build). Al-bermani et al. have reported that after an initial transient region, a columnar β grain structure develops within the bulk sections that grow epitaxially parallel to the build direction. This has been claimed to occur because there is a steep thermal gradient in the liquid at the growth front and the predominant direction of heat flow is perpendicular to the base plate, along the Z axis [112]. An example of a columnar microstructure seen in EBSM powder bed and, EBF^3 wire deposited Ti6Al4V samples can be seen in Figure *2.36*, in which the z-axis runs from bottom to top of the page. The same large columnar β grains have also observed by other authors with laser and electric arc welding deposition techniques [11, 26, 29, 31, 37, 103, 112]. Upon remelting of previous layers, the columnar parent β-grains grow epitaxially across every layer, due to the similar composition of the liquid and substrate. Because the solidifying material is the same as the substrate, wettability is very efficient and theoretically the wetting angle (θ) will tend to 0˚. This implies no nucleation barrier during solidification and hence epitaxial growth [43, 44].

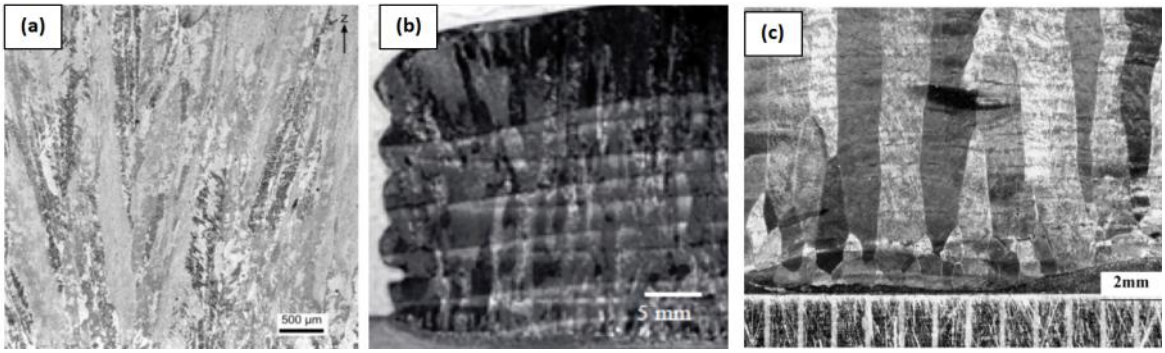

Figure 2.36: *Overall macro-structural views of typical Ti6Al4V parts produced by; (a) the EBSM powder bed method, (b) EBF^3 wire feedstock (z-axis from bottom to top) and Laser powder blown deposited Ti6Al4V (for comparison) under optical microscopy [6, 9, 11, 112]*

EBSD maps by Al-bermani et al. [112], parallel and perpendicular to the z-axis, are shown in Figure *2.37*. Figure *2.37*(a-b) in IPF coloring with respect to the z-axis of the indexed α and β phases, respectively, from a region just above the interface with the SS base plate and upward in the direction of build. In Figure *2.37*a, areas of similar α orientation are visible that are likely to have originated from the same prior β grains. In Figure *2.37*b, the base of the build appears to be 100 % fine β phase with equiaxed grain morphology, due to comelting and alloying with the austenitic stainless steel base plate with the initial Ti6Al4V layers [112]. Al-bermani has also

reported that, EDX analysis of this region revealed the presence of Cr, Fe, and Ni, that act to stabilize the β phase. Figure *2.38* shows the bottom of the build in BSE image mode, where clear evidence of atomic contrast along the Z - axis suggests the base of the build differs from the bulk composition in the EBSM components [112]. The benefit of melting onto an SS base plate is easy removal of components, since the interface between the base plate and component becomes brittle and, also thermal mismatch stresses enable cracks within the comelted region, so that parts can be easily removed manually, with no mechanical cutting [44, 112]**.**

Al-bermani et al. have reconstructed the prior β-grain structure from the α-phase orientations through the Burgers relationship, as shown in Figure *2.37*c, and confirmed that the high-temperature β- grain structure is highly columnar with some grains millimeters in length, displaying high aspect ratios. The largest aspect ratio of a completely reconstructed prior β grain was reported to be 11.8. Some reconstructed maps showed an equiaxed to columnar transition directly above the β-stabilized region [112]. This results from powder grains that initially form individual random prior β-grains, before epitaxial growth along preferred directions dominates. In cubic metals the most favourable orientation for growth is normally the preferred <001> direction [42, 44]. The heat flow conditions at the solid/liquid interface thus favour the growth of optimally oriented grains which over-run the other non-optimally oriented grains [44].

2.9.2.1.2 Morphology of the β grains:

Al-bermani et al. have reported that the observed 'Wavy' shape of the β columnar grain boundaries, with a period of ~ 200 µm, was associated with a change in electron beam scanning direction [112]. During hatching (bulk melting), it is build because the direction of e-beam motion is rotated by 90 degree about the z-axis for every new layer [112]. The beam thus hatches alternately along the x and y directions, while building the parts in 100 µm layers. The electron beam hatches along the same axis every 200 µm. This wavy grain boundary appearance has also been reported in laser-deposited Ti6Al4V by Koryn and Semiatin [29].

Figure *2.37*(d-e), show IPF coloring, with respect to the z-axis of the α-phase and reconstructed prior β-phase perpendicular to the z-axis. The Prior β-grains appear equiaxed and, in some locations, rectilinear in section with regions where grains appear to lie in rows and columns in a grid-type arrangement. According to the IPF map in Figure *2.37*e, the majority of the orientations are red in colour, which suggests that the prior β grains grow strongly with an <001> direction, parallel to the build direction [112].

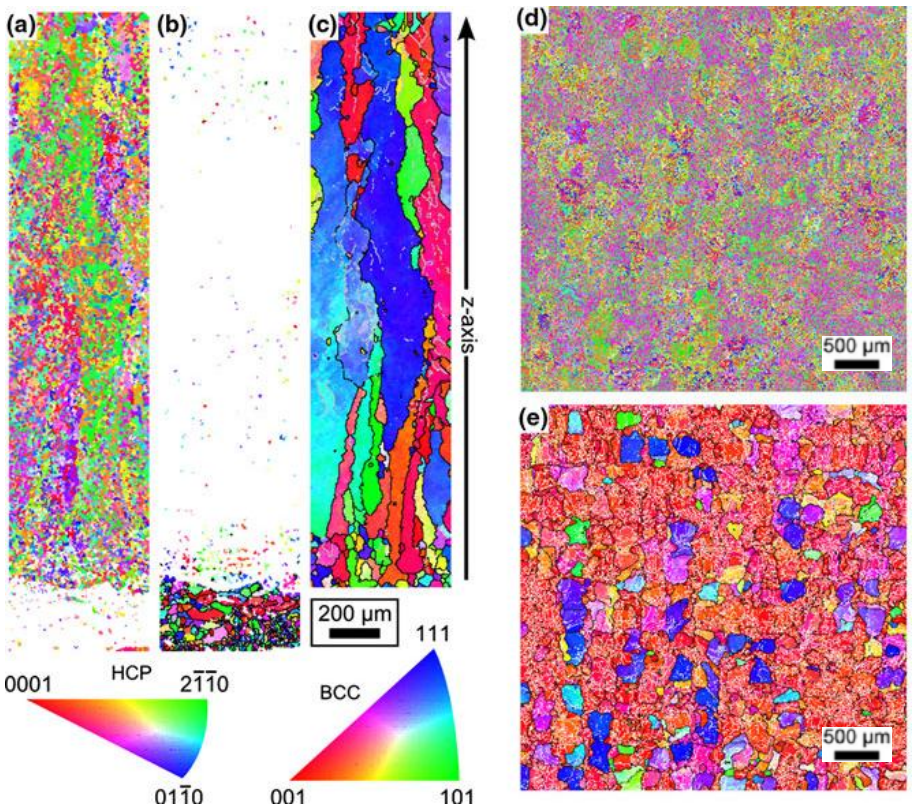

Figure 2.37: *EBSD data for samples sectioned (a-c) parallel and (d-e) perpendicular to the z-axis. (a-d) show the indexed α-phase, (b) shows the indexed β-phase, and (c-e) show the reconstructed prior β-grain grains. Black lines delineate high-angle grain boundaries with >15°misorientation, whereas white lines represent low-angle grain boundaries with > 5° misorientation [112].*

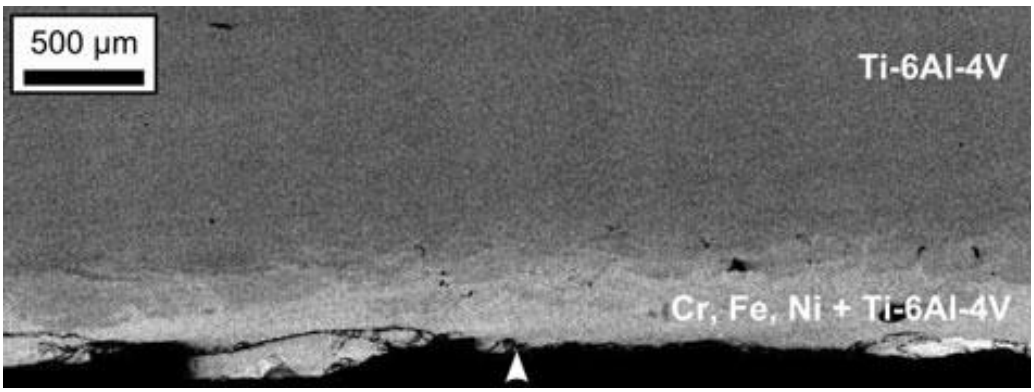

Figure 2.38: *The base of a Ti6Al4V component built by the EBSM process (indicated by arrowhead)-Z axis (from bottom to top) contrast originating results from the initial comelting of Ti6Al4V powder and the SS base plate can be seen. The brittle nature of this region is noticeable by visible cracking [112].*

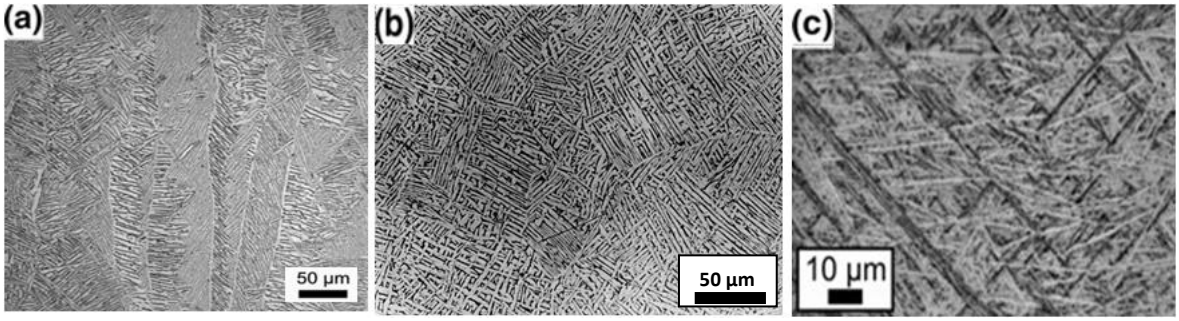

***Figure 2.39** : Typical transformed microstructure in EBSM Ti6Al4V part; (a) columnar prior β-grains with (b) Widmanstätten and colony α-morphology, and (c) Diffusionless α' martensitic region over a distance of ~ 500 observed in the top layer of the build at the top of a 2-mm-tall sample [20, 111, 112].*

2.9.2.1.3 Transformed room temperature bulk microstructure:

In the transformed microstructure (from EBSM), the columnar prior β grains are seen to be delineated by grain boundary α (Figure ***2.39***a). A transformed fine lamellar α+β microstructure with colony α-, basket weave Widmanstätten α-, and a coarse acicular α- (plate like) morphologies is seen within the β grains shown in the Figure ***2.39***(a, b). The same result has also been reported by other authors [10, 20, 88, 111]. Figure ***2.39***c shows the presence of a martensitic region, which extends over a distance of ~500 µm from the top of sample; this is indicative of a high cooling rate imposed during solidification and subsequent cooling in the solid state of the last layer. Literature suggests that a cooling rate of > 410 K/s from above the martensitic start temperature (Ms) may result in the formation of martensitic α' phase in the final layer [112].

2.9.2.2 Laser beam – AM literature

Selective Laser Melting (SLM) emerged as the main additive manufacturing techniques in the late 1980s and 1990s. In an SLM machine, layer by layer power deposition and melting, using a laser, takes place at room temperature over the substrate plate and hence, the SLM process is also referred to as a 'SLM-Cold Powder bed' AM technique [20, 99]. Since SLM involves cold powder bed deposition, this results in rapid solidification and the build-up of thermal stresses, which leads to the presence of non-equilibrium phases such as martensite in Ti6Al4V alloys [20]. The solidification behaviour of the melt pool and, its stability and dimensions will determine the amount of the porosity and the surface roughness, apart from the roughness created by the layer wise building; i.e. the staircase effect [33, 98]. Therefore, a better understanding of the process parameters is necessary to obtain better control over the mechanical properties of final components. The most important parameters are the laser power, the laser spot diameter, the

scanning parameters, such as the scanning velocity, the scanning strategy; and the material properties such as the surface tension, the thermal conductivity, freezing range of the alloy. The chamber environment conditions also play a large role [20, 30, 98, 99, 108].

2.9.2.2.1 Macrostructure of Ti6Al4V parts by SLM:

Recently Thijs et al. [98], have systematically studied the evolution of the SLM microstructures in rectangular samples with a width, length and height of 5 mm, 10 mm and 5 mm, respectively. Upon deposition of every layer, the scheme of applied scanning direction was identical in each layer with the zigzag scanning vectors shown in Figure ***2.40***(d). Table *2.8* shows the process parameter used to build these samples in Ti6Al4V. It has been reported by Thijs et al. that the Ti6Al4V parts produced with SLM process always showed an elongated prior β grain structure (See Figure ***2.40***b and c), which more, or less, grow along the building direction, with lengths of 100 µm to several millimetres, i.e. much longer than the layer thickness [98]. The β-grains in the front view (Figure ***2.40***b) are aligned with the building direction and, have an approximate width of 75 µm, which suggests a one-to-one correlation of the scan tracks and the resulting grain widths [98]. SLM parts, don not show a layer of grain boundary α, between the prior β-grains, since deposition takes place with the substrate at room temperature in the SLM technique. The horizontal bands visible in the side view (Figure ***2.40***c) are located 30 µm apart, which is approximately equal to the layer thickness of the SLM process and therefore, presumably result from the layer-wise building. The change in inclination of the prior β-grains toward the top layer in the side view (Figure ***2.40***c) is caused by imperfect sectioning: i.e., the cross-section is not exactly parallel in the xz-plane, as a result the scanning direction at the top part of micrograph is opposite to the one at the bottom of the part.

Due to the line and layer-wise building, the macrostructure of the sample produced by SLM will differ in the three views as shown in Figure ***2.40***. 'Wavy' β grain boundaries are also observed in SLM due to the change in direction of laser heat source. The macrostructure of the top view (Figure ***2.40***a) reflects clearly the zigzag nature of the scanning strategy shown in Figure ***2.40*** d. The width of the individual tracks is equal to the hatch spacing, i.e. 75 µm. Thus, the different tracks in the top view represent the different scan vectors. The herringbone pattern see in Figure ***2.40***a, was caused by the alternate scanning direction. When the laser beam is raster from left to right, the β-grains are slanted as ///; from right to and left as \\\, since the S/L interface moves normal to the tilted melt pool surface against the maximum thermal gradient. This suggests that the local heat transfer conditions, more specifically the heat conduction direction plays a larger role in exterminating the orientation of the grains, rather than the global direction of heat extraction to the substrate [98].

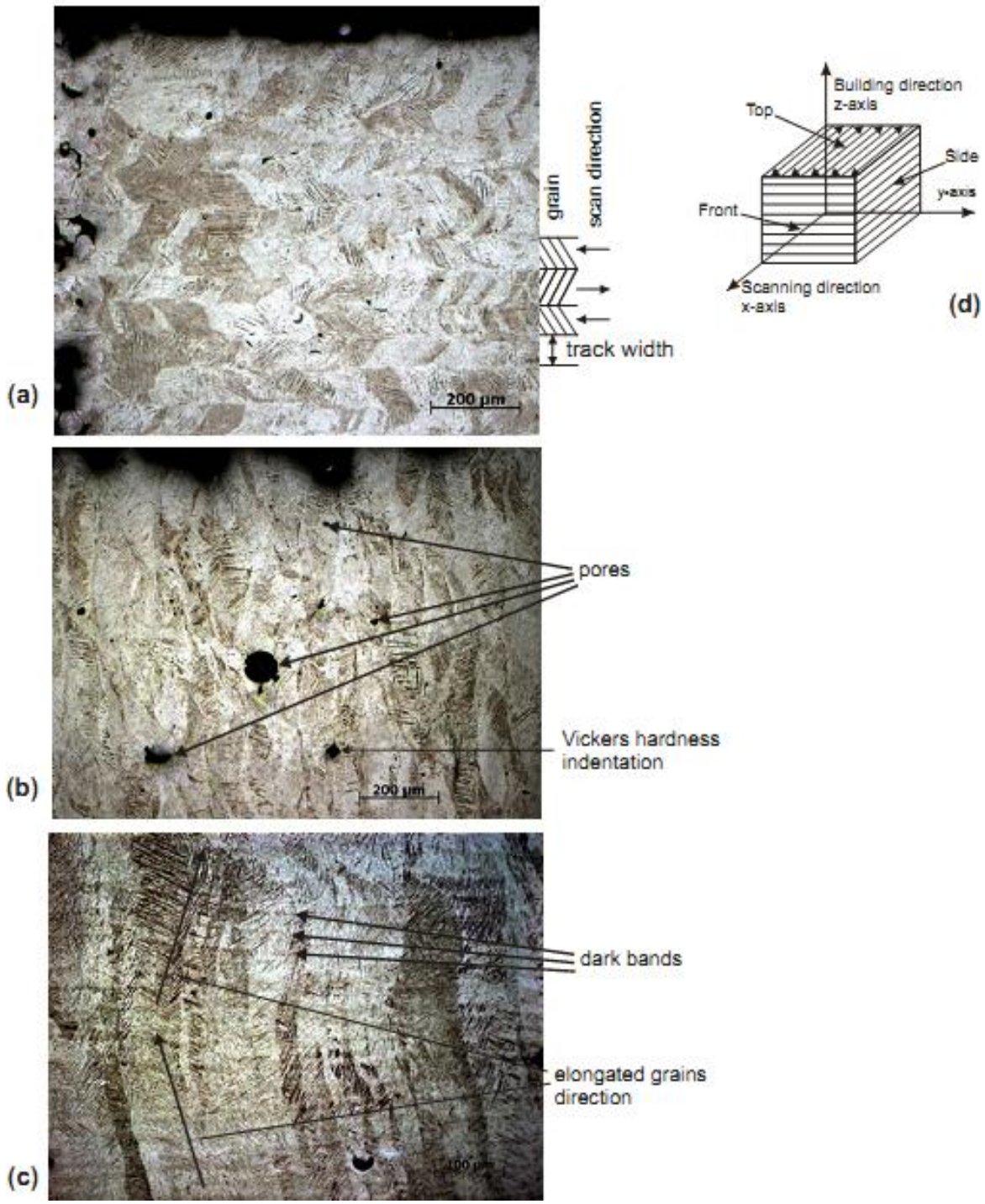

Figure 2.40: *Micrographs from an SLM Ti6Al4V build: (a) top view; (b) front view; (c) side view; and (d) scheme of the applied scanning strategy, which involves the same zigzag rastering direction in each layer* [98].

Table 2.8: *Process parameters used to produce Ti6Al4V samples with SLM technique, by Thijs et al. [98].*

Parameters of the build	**Optimised SLM parameter**
Scan strategy	Identical layers with Zigzag scan vectors
Power, P (W)	42
Velocity, v (mm/s)	200
Hatching spacing, h (μm)	75
Layer thickness, t (μm)	30
Energy density, E (10^{-9} J m^{-3})	93
Relative density (%)	99.6

2.9.2.2.2 Transformed room temperature bulk microstructure using SLM:

Murr et al. have reported that the microstructure of Ti6Al4V samples using SLM is characterized by primarily martensite (α') plates with no apparent layer features [20]. Figure ***2.41*** shows section views corresponding to optical metallographic images for a SLM Ti6Al4V rectangular build from transverse (top) and longitudinal (face) sections.

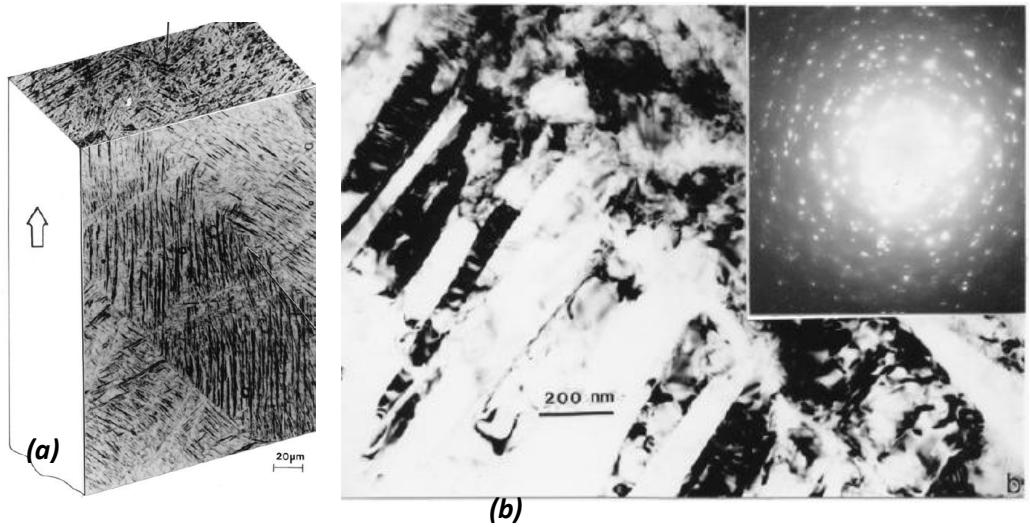

Figure 2.41: *(a) Optical metallographic images for a SLM rectangular build showing transverse (top) and longitudinal (face) sections. The microstructures are characterized by primarily martensite (α') plates, (b) TEM (bright-field) image showing the α' martensite microstructure in the SLM vertical rectangular build. The SAED pattern, indicates with some intermixing of α' and α'' phases [20].*

The microstructures are characterized by primarily martensite (α') plates (the large arrow at the left shows the build direction). Furthermore, Murr et al. went on to confirm the presence of martensite by TEM as shown in Figure ***2.41***b [20, 111]. Thijs et al. also observed that the microstructure of the SLM build was very fine acicular α' martensite (as was reported by Murra et al.) due to the high cooling rates that occur during the SLM process [20, 98, 111].

2.9.2.3 Influence of process parameter on microstructures in SLM

P.A. Kobryn et al. [28, 29], have reported the influence of the process parameters on the formation of the deposited microstructure in AM with a Ti6Al4V alloy. Depending on the type of laser used (degree of power of laser), the morphology and the thickness of the room temperature α varied.

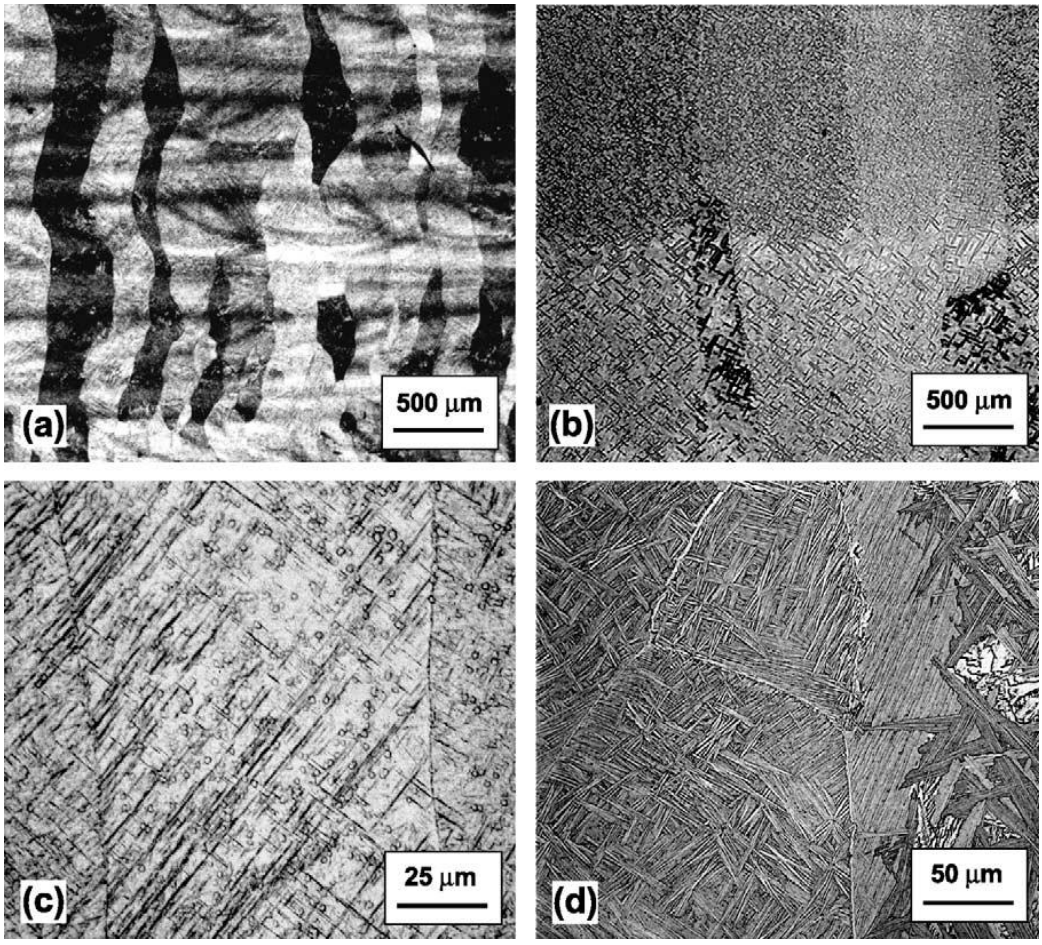

Figure 2.42: *Optical micrographs showing macrostructures (a, b) and microstructures of Nd:YAG (a, c) and CO_2 laser AM deposits (b, d) in the Ti6Al4V alloy [26, 29].*

The microstructures of the deposits from a lower heat input Nd:YAG laser were compared to a CO_2 laser system. The Nd:YAG laser resulted in very fine Widmanstäten α, with very small equiaxed α particles distributed both within the grains and along the grain boundaries (Figure ***2.42***). However, presence of α particle is surprising and has not been reported by any other authors. This could be due to particle from metallographic preparation. The presence of small equiaxed α was considered as evidence that the cooling rate after solidification was very high. The microstructures of the CO_2 deposits were much coarser and the internal grain structure was primarily Widmanstäten in nature, with the occasional small α colonies along grain boundaries. In addition, a layer of grain-boundary α was found along some of the grain boundaries in the CO_2 deposits, indicating a somewhat slower cooling rate than with the Nd: YAG laser system [29].

Influence of scanning strategy: The effect of three types of scanning strategy (Figure ***2.43***) on the prior β grain structure have been investigated by Thijs et al. [98]; namely, unidirectional scan vectors, identical scanned layers using zigzagging, and the cross-hatching scanning with zigzag scanning direction rotating 90˚ every new layer.

To determine the correlation between the grain growth direction and the scanning direction, the other parameters were kept constant. With the unidirectional scan vector the scanning pattern was the same for all layers. As shown in Figure ***2.43***a, in the top view, the herringbone pattern is lost due to the unidirectional scan vectors. Whereas, the zigzag rastering (Figure ***2.43***b) results in a pronounced herringbone pattern due to the reversal of the laser beam, as was explained above. In the side view with unidirectional scanning (Figure ***2.43***a) the elongated grains are parallel to each other, but tilted 19˚ away from the direction of build, since the grains grow perpendicular to the melt pool base, which is consistently tilted due to the unidirectional scanning of laser beam from right to left [30, 98].

It was also reported that once the zigzag rastering direction was rotated by 90˚ from layer to layer, a grid pattern was formed in the top view of the microstructure (Figure ***2.43***c). The grains become more equiaxed with a size of about 74 µm wide, which could be related to the beam path step offset of 75 µm. Thijs et al. have reported that the introduction of cross-hatching led to two different grain orientations in the side and front view; one orientation parallel to the direction of build and the other at 25˚ tilted to the build direction [30]. This type of cross-hatching scanning strategy led to an improved isotropic microstructure and relatively high density of ~ 99.9%. Moreover, the pores that are produced with the cross-hatching scanning strategy were more spheriodized in shape, which is less deleterious to the mechanical properties [30].

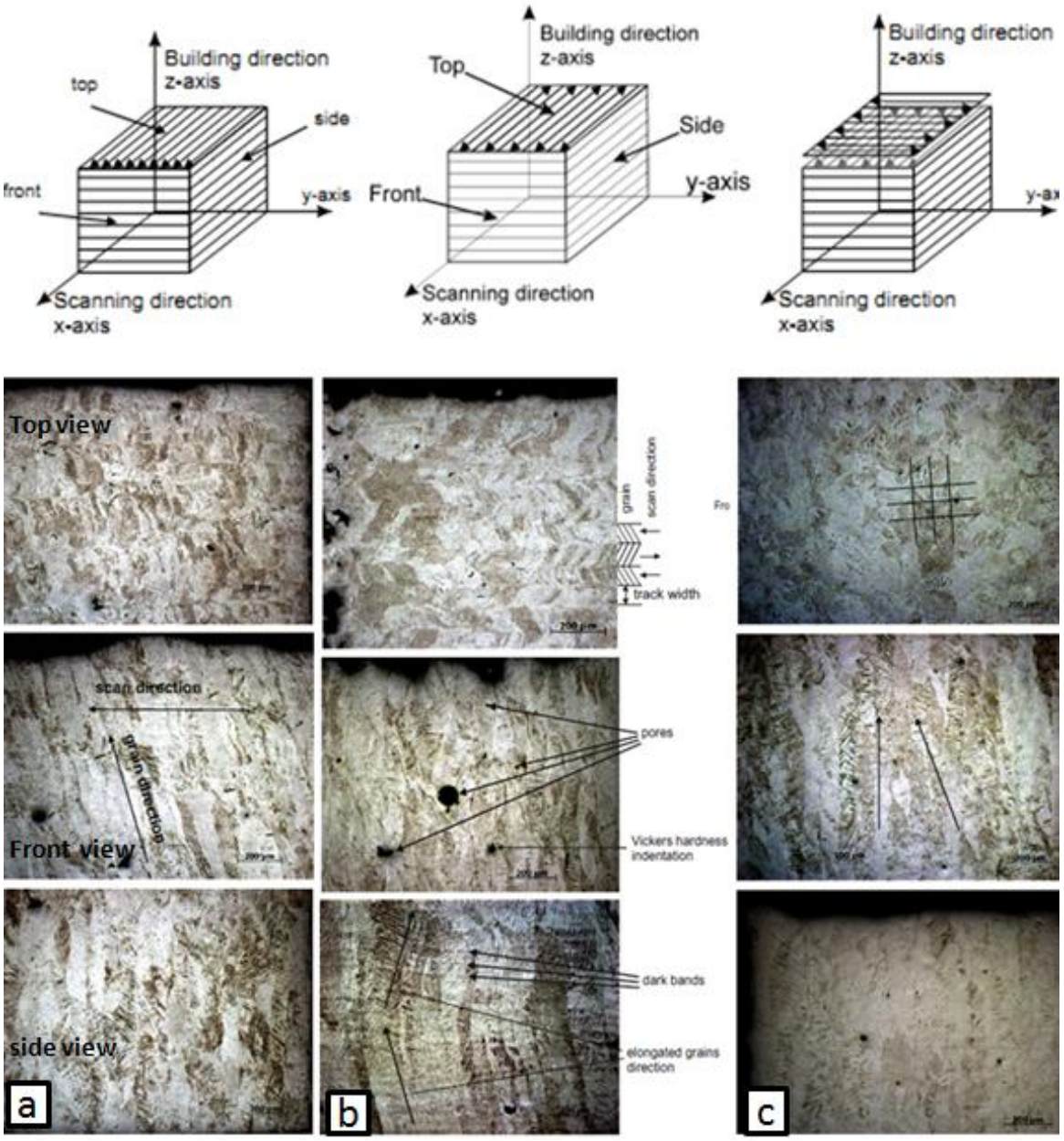

Figure 2.43: *The three different scanning strategies in SLM studied by Thijs et al. (a) unidirectional scan vector, (b) repeated identical zigzag rastering and, (c) cross-hatching with 90˚ rotation each layer. The corresponding optical micrographs are shown from Ti6Al4V samples. The other process parameters for the three builds were the same: v= 200 mm/s, h= 75 µm, P= 42 W and layer thickness t = 30µm [98].*

2.9.2.4 Effect of alloy type:

In order to study the effect of the titanium alloy, two types of feedstock have been fed simultaneously into the laser focal point, a burn resistant (BurTi) alloy Ti–25V–15Cr–2Al–0.2C powder and a Ti–6Al–4V wire by Wu et al. [110]. The local composition of the alloy was changed by altering the ratio of powder to wire by varying the feed rate. With the addition of Bur-Ti, it was

found that the β grain size was much finer than normally seen in laser fabricated Ti6Al4V and became equiaxed, as shown in Figure *2.44*. The reason for the fine equiaxed grain formation was reported to be the high constitutional supercooling during the solidification BurTi alloys when compared to Ti6Al4V which has a narrow freezing range and high partition coefficient ~ 1 [110, 113]. The presence of 0.2 % carbon in the BurTi alloy has increased the freezing range of alloy with less partition co-efficient which responsible for the higher constitutional supercooling [110, 113-115].

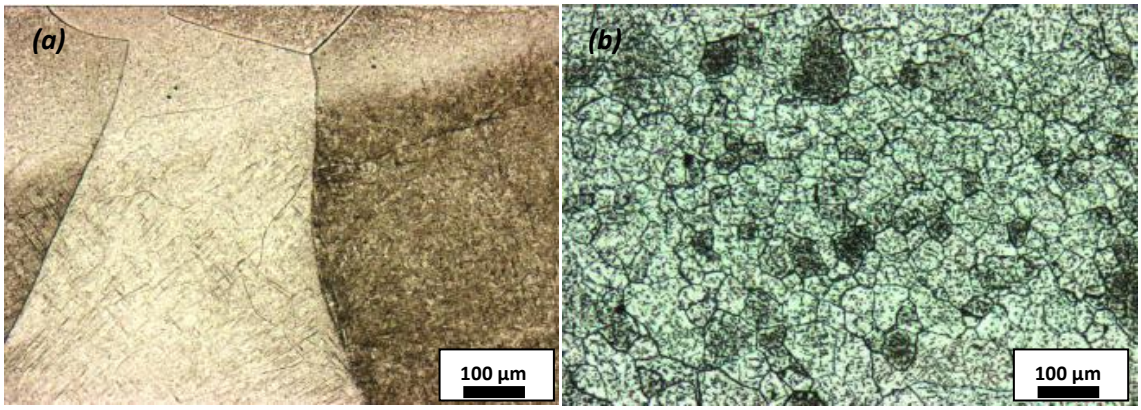

Figure 2.44: *Optical microstructure showing (a) large columnar prior* β*-grains with the Ti6Al4V alloy, and (b) fine equiaxed prior* β *grains with the BurTi alloy [11, 110] produced by SLM*

2.9.2.5 Wire + arc deposition AM literature

Recently, wire instead of powder has been used in AM processes for producing larger components, in order to overcome contamination problems the slow build rate, and the high price of high quality powders. As mentioned previously, wire based AM parts can be produced using various heat sources such as: (1) Nd: YAG or CO_2 Laser beam, (3) Electron beam - EBF3 technique and, (3) using Electric Arc beam (TIG or MIG processes). The current literature review is mainly focussed on Wire + Arc Additive Manufacturing as this method was investigated in this project (WAAM). WAAM is a comparatively cheaper, near-net-shape technique, when compared to the other AM techniques. WAAM has gained considerable interest in the recent years due to its high deposition rate and 100% efficiency [102-104]. The process is capable of building large components; but the geometries that can be achieved are much more limited than with powder bed techniques. Since the process is new, the available literature on the WAAM to process metals by AM is very limited.

2.9.2.5.1 Surface morphology of the build:

The WAAM process typically builds walls one weld track wide. Thus, it has been reported that the WAAM components show periodic bulges that reflect the separate layers of each deposit and the large thermally grooved columnar grains [25, 116]. These prior β-grains which have grown

epitaxially develop up through the weld layers, as shown in Figure *2.45*. Furthermore, by reversing the travel direction of the weld head, the inclination of the coarse columnar β grains can be changed. The same large columnar grains were also observed in laser fabricated AM components [25, 29, 34, 37] and electron beam deposition [6, 32]. It was also reported that a coloured surface was seen are due to the oxide layer formed on the deposit, despite the use of a high purity Argon atmosphere. However, the measured bulk oxygen concentrations of 0.16 wt.% and nitrogen concentrations of 0.0041 wt.%, were similar to the original concentration of the wire. Hence, it was reported that the colorization is just a cosmetic fault that does not degrade the properties [116].

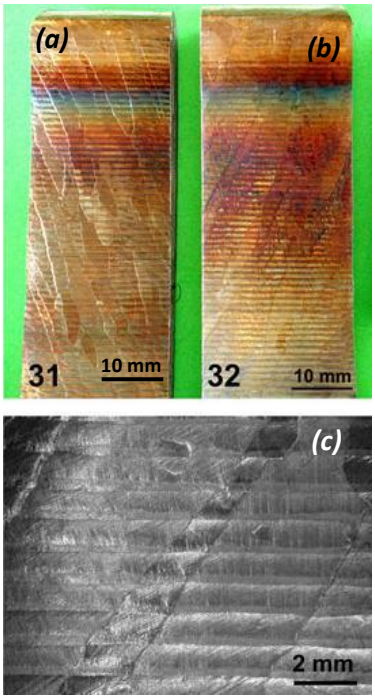

Figure 2.45: *View of the outer surfaces of a WAAM wall with (a) clockwise deposition, and (b) anti-clockwise deposition; (c) the surface shown in more detail, highlighting the layers and the inclined, elongated prior* β*-grains [116].*

2.9.2.5.2 Typical microstructure of the build:

Etched cross sections of the components also revealed slanted prior β-grains and two distinct regions of microstructural banding (Figure *2.46*a-b) namely, a bottom region with parallel bands and, a top region without bands. The microstructural banding will be discussed in more details in 2.9.3. It was also reported that, the microstructure in both regions consisted of Widmanstätten α structures. This structure consists of α-phase lamellae in a β-phase matrix exhibiting a basket weave structure. The top region displays very fine lamellae (Figure *2.46*c), whereas the bottom region consisted of much thicker lamellae (Figure *2.46*d). The fine Widmanstäten structure in the top and a coarse Widmanstäten structure in the bottom region result from the repeated heat

treatment upon deposition of every new layer and will be discussed more details in 2.9.3 section [116].

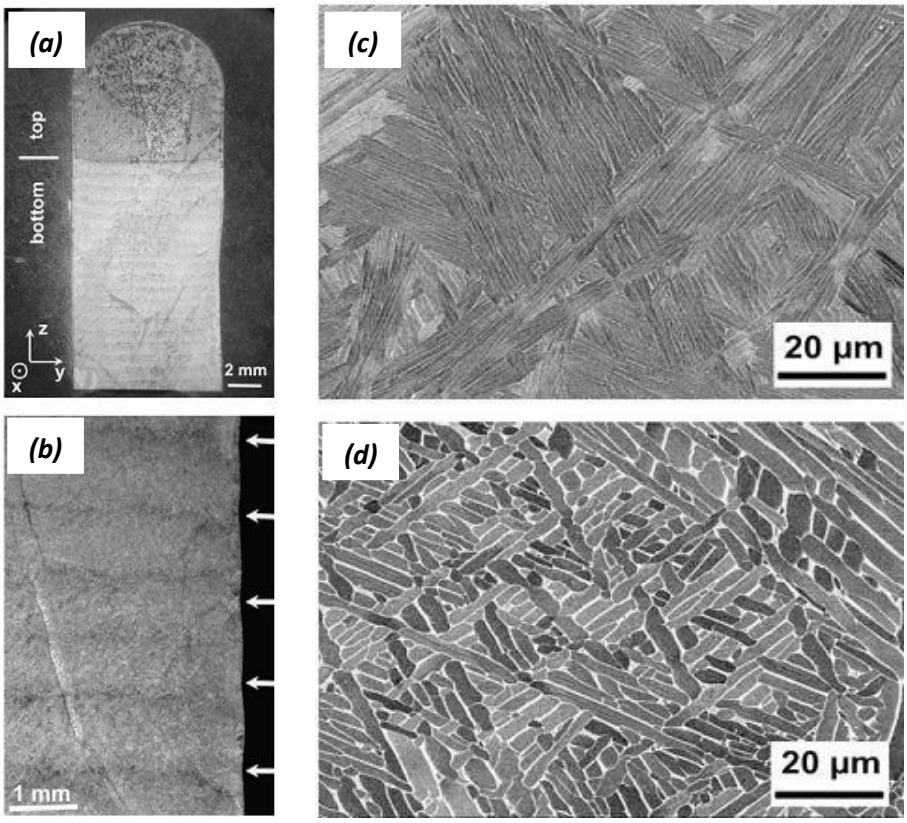

Figure 2.46: *(a) Optical micrographs of etched cross sections of a WAAM component near the top of the build; (b) higher magnification of the parallel bands seen below the last 3 layers; (c) and (d) SEM image in the BSE imaging mode near the top and, bottom region of the build.*

2.9.3 Banding in AM deposits

Banding in AM deposits is a commonly observed phenomenon. It is usually observed in the build direction in macrographs and is caused by a systematic variation in the microstructure in the normal direction due to the repeated thermal field experienced by the material below the deposited layers when it is consolidated by rastering in a 2D plane. The band width thus corresponds to the each deposited layer height.

In laser powder bed AM although the microstructures observed by Kobryn and Semiatin were very fine Widmanstätten α in nature [29], macroscopic "banding" was observed in all of the specimens of the Ti6Al4V components (see Figure ***2.40*** and Figure ***2.42***(a-b)). It was reported that this was caused by differences in the amount of 'equiaxed α particles' within the bands. Very fine equiaxed α particles were seen distributed (Figure ***2.42***(c)) both within the grains and along the grain boundaries. The reason given for this structure given was that the cooling rate after

solidification was very high resulting in a fine structure, which was then annealed by reheating of the previously deposited material with each subsequent deposition pass. In essence, a new heat-affected zone was formed locally in the deposit every time the laser passed thereby resulting in the observed microstructural changes [28, 29]. The presence of 'equiaxed α' particles is surprising and has not been reported by any other authors.

Kelly and Kampe have investigated in more detail the microstructural features of banding in Ti6Al4V, with thermal modelling, in laser deposition [25]. They have shown that the microstructure exhibits large, columnar prior-β grains with a gradient in the individual α-lath thickness between the deposited layers, except for in the last three layers [25]. It was reported that the layer bands consist of a colony α morphology (Figure *2.47*(b)), whereas the microstructure between layer bands exhibits a basket-weave Widmanstätten morphology (Figure *2.47* (a)). They claimed that the layer-bands and gradient in morphologies are due to the complex thermal history experienced by the build and not as a result of segregation of chemical elements or oxygen [25].

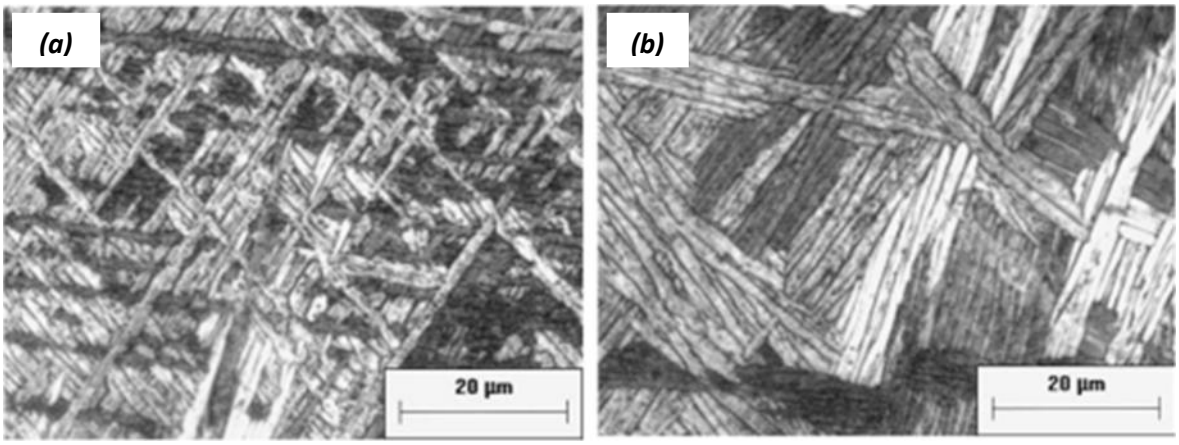

Figure 2.47*: (a) Widmanstätten α basketweave morphology, and (b) a coarse colony Widmanstätten α morphology in the banded layers seen in laser deposition of a Ti6Al4V alloy [25]*

Kelly and Kampe have shown that after establishing a steady state, the gradient α and layer-band morphologies form in layer *n* after the deposition of *n*+ 3 layers with the four most recently deposited layers showing a distinctly different microstructure. Layer banding was identified as n through n+3, as illustrated in Figure ***2.48***. According to Kelly and kempe, when the first layer n is deposited, it cools very quickly from the molten state to form β grains with a fine-colony Widmanstätten α-morphology as seen in layer *n* in the final layer (Figure *2.49*(c)). It was reported that the origins of the fine-colony morphology are unresolved and was speculated that it may be a 'nonequilibrium product' formed during a solid state phase transformation (*e.g*., martensitic or massive α) due to the relatively high cooling rates observed at the top of a newly deposited layer.

Then the next layer, *n* + 1, is deposited on top of *n*, remelting a portion of layer *n* and heating the remaining portion high into the β phase field. This heating is followed by rapid cooling, leading to a fine basket weave α morphology with dispersed fine-colony morphology (Figure *2.49*(b)). Layer *n*+2 is deposited on top of *n* and *n*+1, again causing re-heating of layer *n* into the β-phase field, but for to a lower peak temperature, and period of time above the β transus, and giving a lower cooling rate than previously experienced, resulting in the formation of a basket weave Widmanstätten α morphology. Upon deposition of layer *n* +3, only a narrow region near the top of layer *n* will see an excursion into the β-phase field, followed by a an even slower cooling rate to form the colony morphology, and a layer band is formed. The material below the layer band does not see a thermal cycle that is of sufficient temperature, or time, to produce the colony morphology. Instead the previously existing fine basket weave morphology in layer *n*, caused by the deposition of layer *n+* 2, is transformed into a graded basket weave morphology due to the gradient in peak temperatures and cooling rates experienced. With further layer depositions (*e.g.*, *n*+4), the peak temperatures will not be sufficient to produce significant changes in the microstructure, and the graded basket weave and layer-band morphologies developed during the prior three thermal excursions will be retained [25].

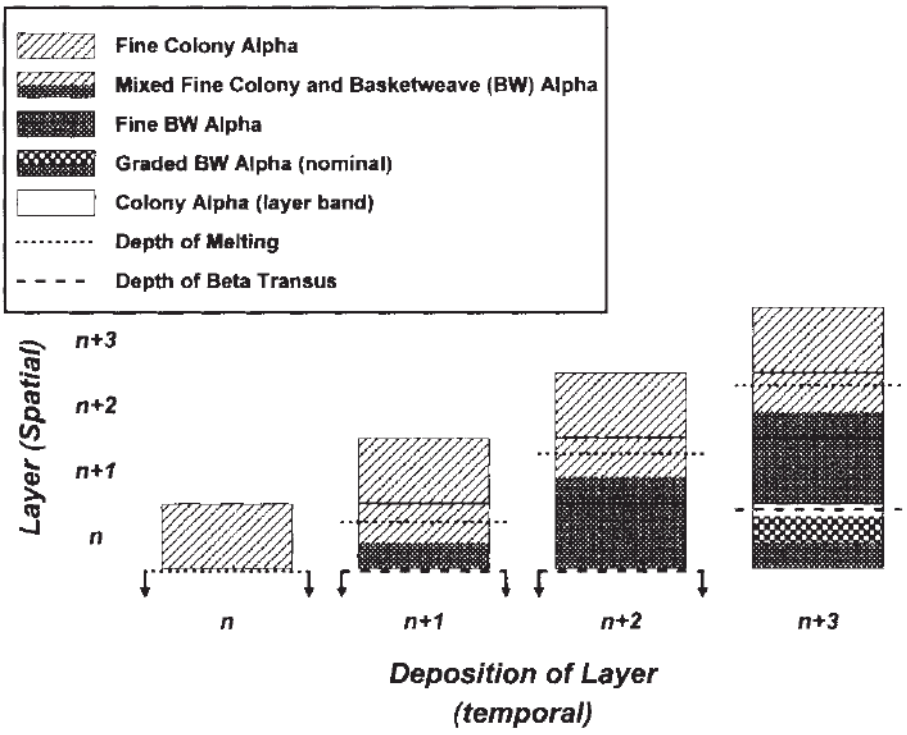

Figure 2.48: *Schematic representation of different microstructures morphologies observed in banded layers in a Ti6Al4V alloy deposited by the laser additive manufacture process [25].*

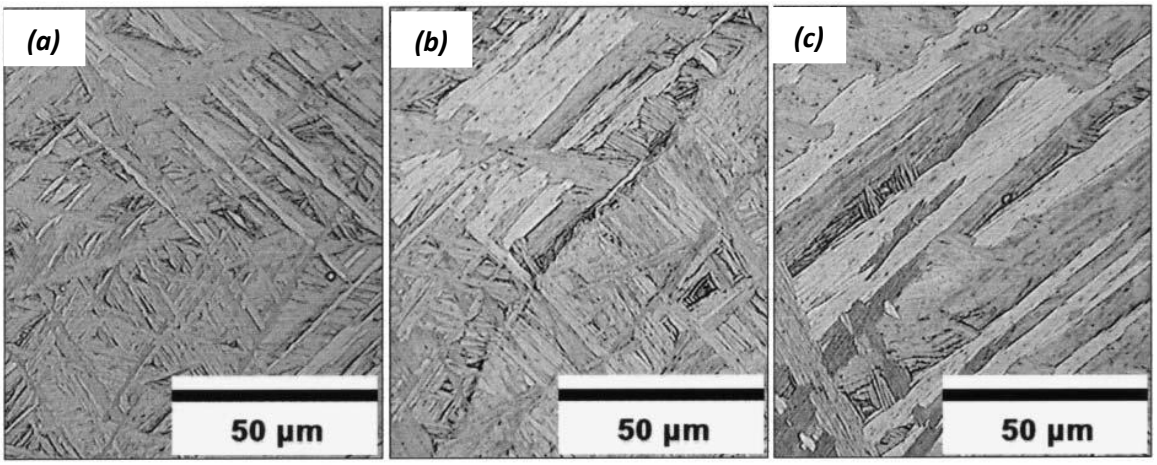

Figure 2.49: *Micrographs from the last 3 layers deposited in a laser deposition AM build from Kelly and Kampe[25]; (a)the last but 2nd deposit, L16 (n+1) showing a fine Basketweave and fine colony Widmanstätten α, (b) the last but 1st deposit, L17(n+2) showing a fine colony α with some areas of fine Basketweave Widmanstätten α, and (c) the final layer, L18 (n+3), exhibiting predominantly fine colonies of α [25].*

2.9.4 Texture evolution in AM

The textures formed in AM deposits have not been widely studied. Generally it is found that the prior β grain grow with an <001> fibre texture parallel to the build direction [29].

In one detailed study of e-beam AM Al-Bermani et al. reported that the <001> pole figure of the prior β-grains show a strong cube texture with an intensity of about 10 times random. It was reported that during the processing of EBSM, the epitaxial columnar prior β-grains start to grow preferentially along $<001>_{\beta}$ [112]. However, The same author have also reported that the growth of the columnar grains is predominantly in the favoured <001> direction [112], resulting in a $<001>_{\beta}$ fibre texture. Al-bermani et al. further noted strong cube and 45° rotated cube components in the orientation maps, which suggests a relationship with the electron beam rastering directions. However, because of the coarse β-grain structure, it was difficult to obtain reliable sampling statistics in this work. The β-grains themselves were further noted to contain substructure which was attributed to relaxation of internal stresses and, or, impingement of imperfectly orientated cell, or dendrite arms, during solidification. Other work by Kobryn and Semiatin has also indirectly demonstrated the presence of a strong $<001>_{\beta}$ fibre texture in the laser AM of titanium [29].

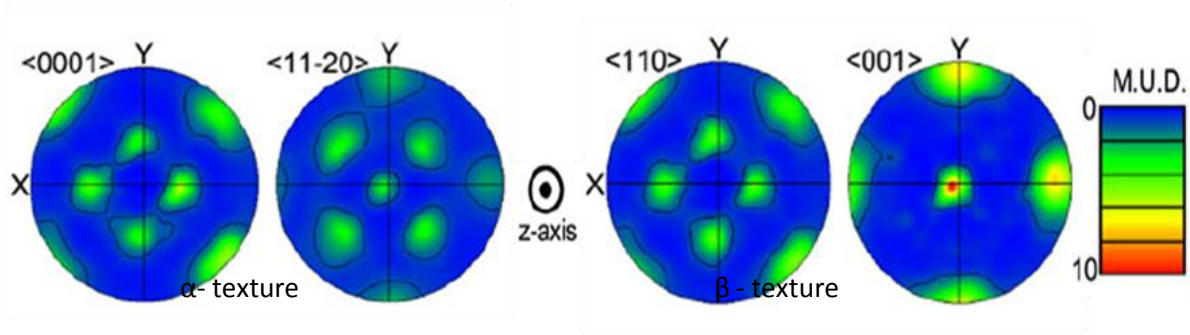

Figure 2.50: *Pole figure of the α-phase and reconstructed prior β phase perpendicular to the z-axis from EBSD maps of Figure* ***2.37****d and Figure* ***2.37****e respectively [112] in EBSM deposited Ti6Al4V.*

The presence of an <001> fibre texture in AM has been previously observed by Moat et al. [117] in their work on laser metal deposition of Waspaloy, where reconstruction of the primary phase was not required. However, in this study the <001> fibre axis was found to be tilted away from N_Z in the direction of beam travel (as shown in Fitgure *2.51*), by an amount that varied with the process conditions. This effect was attributed to the scanning pattern used, that involved a single beam path that always moved in the same direction, and the curvature of the rear of the melt pool which changed with different beam parameters. The intensity distributions of the <0001> and <110> pole figures of the α-phase and post-transformation β phase in Figure *2.50* from the work of Al-Bermani et al. [112] are almost identical and this indicates that variant selection does not occur during transformation.

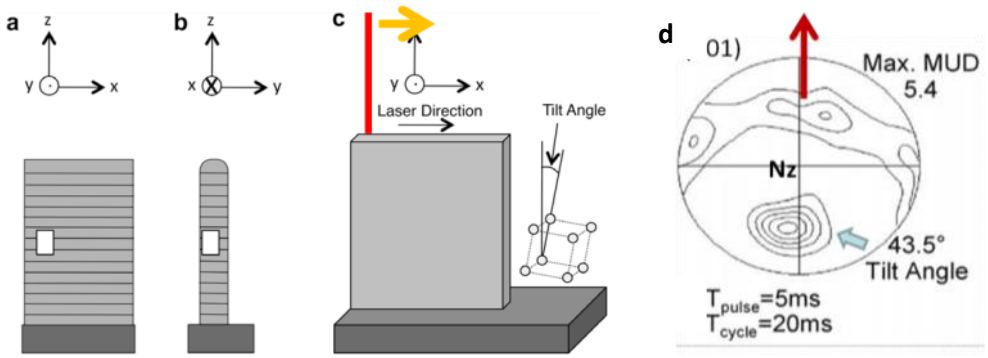

Fitgure 2.51: *Schematic diagram of the sample cross-section geometry and texture measurement location (white rectangle box) for (a) the longitudinal direction, and (b) the transverse direction, (c) the definition of the 001 plane tilt with respect to the geometry and, d) a pole figure showing fibre texture tilted by 43.5˚ from Nz due to the unidirectional movement of the heat source along X: taken from moat el al [117] from the laser deposited waspaloy.*

2.9.5 Thermal modelling

Thermal modelling has been applied to the number of AM processes in order to predict the size of the melt pool and solidification rates and thermal history of the deposited material [29, 48, 112, 118]**.** Since the layer deposition process is associated with rapid cooling of a small volume of metal in a localised region, resulting in a steep thermal gradient at the solidification front in the melt pool, the AM processes is more likely to produce a columnar structure by repeated epitaxial growth upon deposition of further layers.

EBSM technique: Al-bermani et al. have used the Rosenthal point source model [119], to predict temperature field in EBSM, due to a moving heat source under steady state conditions. The Rosenthal point source solution in a thick plate is given by:

$$T - T_0 = \frac{\eta q}{2\pi k R} exp\left(\frac{-v(x+R)}{2\alpha}\right) \quad \text{.....Equation 18}$$

Where, T_0=initial temperature (K), η=fraction of absorbed beam power, q= beam power (W), $R = \sqrt{x^2 + y^2 + z^2}$, K= thermal conductivity (W/m/K), ν = beam travelling velocity (m/s), and α=thermal diffusivity (m^2/s). The authors [112] went on to demonstrate the effect of changing both the beam currents (6 to 12 mA) with beam velocities (between 0.188 and 0.608 m/s) on the temperature field and depth of melt pool. Within the EBSM software a speed function is used so that the current and speed are linked with an increase in current causing an increase in beam speed, to attempt to maintain a constant melt depth regardless of travel speed.

Al-bermani et al. have showed that an efficiency factor of η = 0.6, save good agreement in all cases [112]. In contrast, Bontha et al. used an efficiency value of 0.35 during the laser deposition of Ti6Al4V [48, 118]. However, the electron beam process is known to be more efficient than laser processing, due to the lack of reflectivity issues involved with lasers. White and Bakish [120] also report an efficiency value of 0.55 during the electron beam welding of Ti6Al4V. Figure ***2.52*** shows the predicted melt pool shape by Al-Bermani et al. [112] along the melt track centre lines for different beam currents. 6 mA, 8 mA, 10 mA, and 12 mA currents produce melt tracks of almost the same depth with an increase in length caused, by the increase in speed that compensates for the increasing power through the speed function in the EBSM software. However, at a current of 6 mA, both experiment and prediction showed that speed compensation was not large enough.

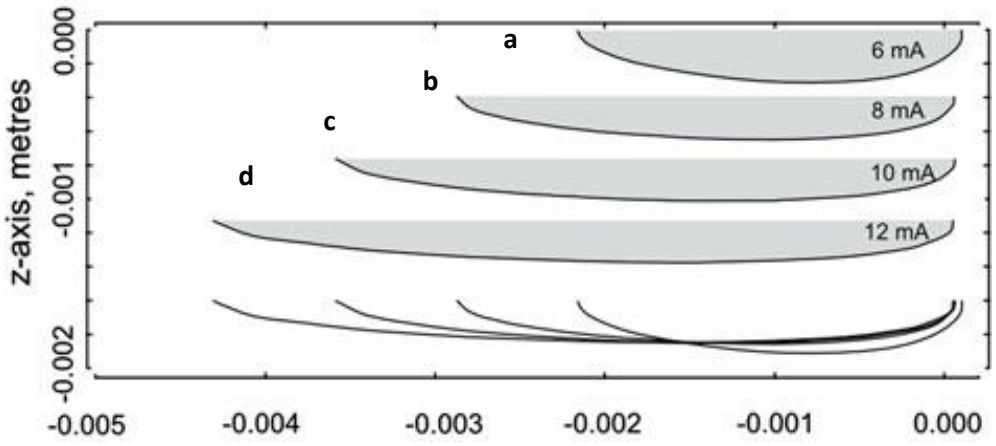

Figure 2.52: *The predicted melt pool shapes along y = 0 parallel to beam motion for beam currents of (a) 6 mA, (b) 8 mA, (c) 10 mA, (d) 12 mA by the Rosenthal analytical point source solution. Efficiency of heat input = 60% and T_0 = 923 K(650 ˚C) [112].*

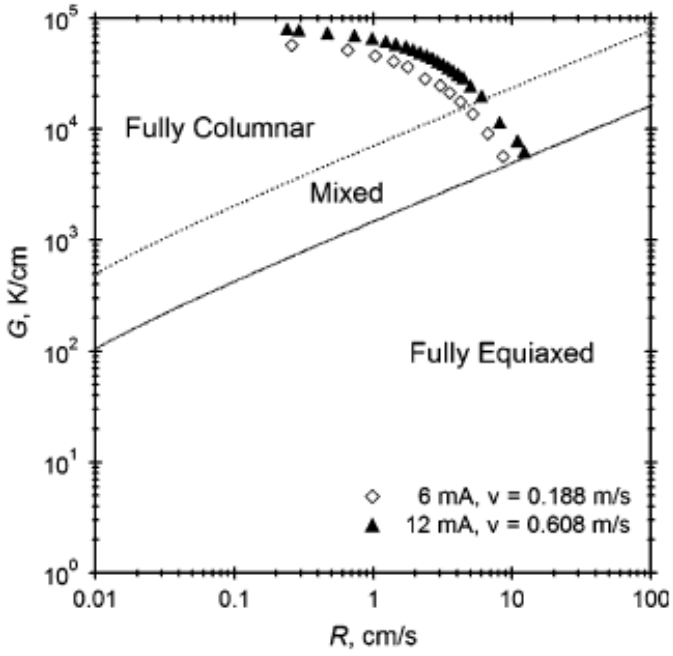

Figure 2.53*: Solidification map for the beam currents of 6 mA and 12-mA, showing the evolution of solidification conditions. η = 0.6 and T_0 = 923 K (650 °C) [112].*

Al-bermani et al. have used the equation, R=v.cosθ [44], to determine the solidification front velocity (R) and have calculated the thermal gradient (G) in the direction perpendicular to the beam motion during welding from the Rosenthal solution. The authors went on to show that, according to the solidification map proposed by Kobryn and Semiatin [29], the solidification conditions were marginal for columnar growth. Figure *2.53* shows the solidification map (G vs R) for the beam currents of 6 mA (0.188 m/s) and 12 mA (0.608 m/s) respectively [112]. As solidification begins the melt pool size diminishes, and the thermal gradient decreases while the

solidification velocity increases; the thermal model predicted a transition from fully columnar to a mixed (columnar and equiaxed) regime. However, the mixed morphology was not seen experimentally and Al-Bermani et al., suggested that during such a short solidification time, the already established columnar growth takes place preferentially. The authors also proved that the criterion for plane front stability during solidification was not met [112] in the Ti6Al4V alloy.

SLM technique: Srekanth et al., have used a similar approach to demonstrate (Figure *2.54*) that the formation of a columnar structure is unavoidable in the powder blown laser AM process, with a thin-wall Ti6Al4V alloy part, even after varying the travelling speed to a large extent (from 2.12 to 10.6 mm/sec) and the heat input (350 W to 850 W). This is because of the steep thermal gradient associated with the solidifying S/L interface always. Furthermore, the nature of the Ti6Al4V alloy, which has a low partition co-efficient during solidification, favours the formation of columnar structures rather than equiaxed grains [29, 48, 118].

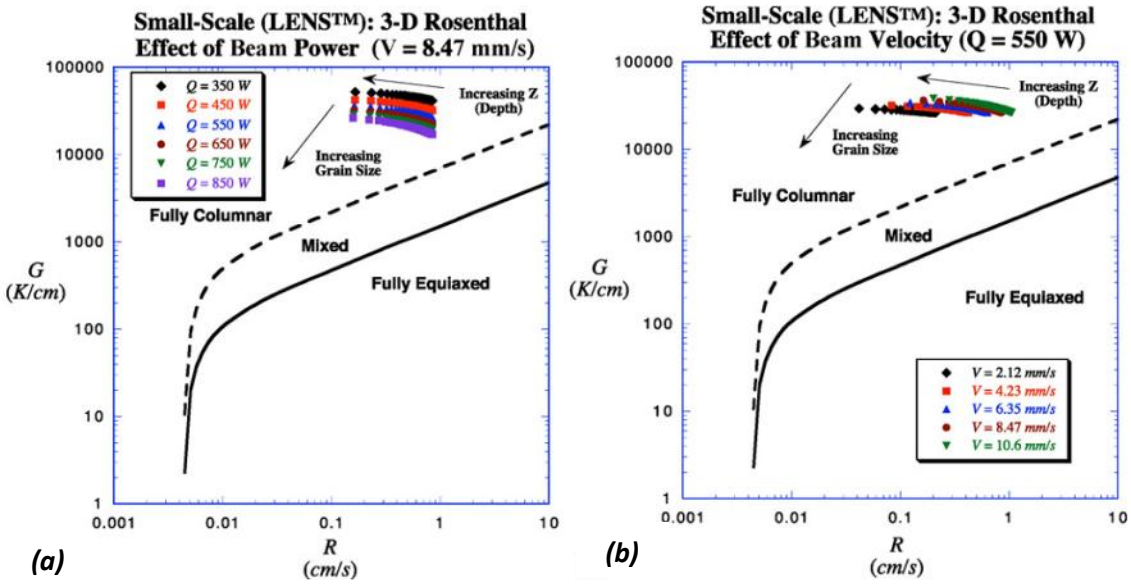

***Figure 2.54**: Solidification map showing the influence of the process parameters on G_L and R for the blown powder laser deposition process; (a) the variation of power and (b) the variation of laser velocity [48].*

More recently, F. Verhaeghe et al., have modelled the depth of the melt pool produced during the 'powder bed deposition of Ti6Al4V via the SLM technique' using a finite element code based on solving the enthalpy formation of the heat transfer equation in the steady state condition [121]. The model was partitioned to take into account the lower conductivity of the surface layer of loosely-packed powder. The efficiency of the laser beam was considered to be 36 % [121] and a similar efficiency has been reported for laser beam deposition by other authors [29, 48, 118, 122]**.** The apparent density of the loosely-packed powder was assumed to be 59 % of the solid material [30, 121]. F. Verhaeghe et al., have also calculated the energy flux along the Z direction (build

direction) with the powder bed partition on the solid substrate. It has been reported that for a 30 µm layer of powder on a substrate, approximately 20 % of the incoming laser energy is absorbed by the substrate and about 50% by the powder bed [121]. A Gaussian heat source with a beam radius of 26 µm was used in this work. In the model shrinkage due to evaporation were also considered [121].

To validate the model, four single tracks with four laser powers of 20, 40, 60 and 80 W were produced on a solid substrate with a powder layer of about 30 µm, and the laser beam scanning velocity of 200 mm/s. Figure *2.55* shows melt pool cross section for every value of the power inputs. Whereas, the Figure *2.56* shows a comparison of the melt pool size (width and depth) form the simulation against the experimental results for different laser powers. An increase in heat input increased the width and depth of the melt pool, with and without the consideration of evaporation. However, agreement of these model results with experiments was better when evaporation was taken into account, as shown Figure *2.56* [121].

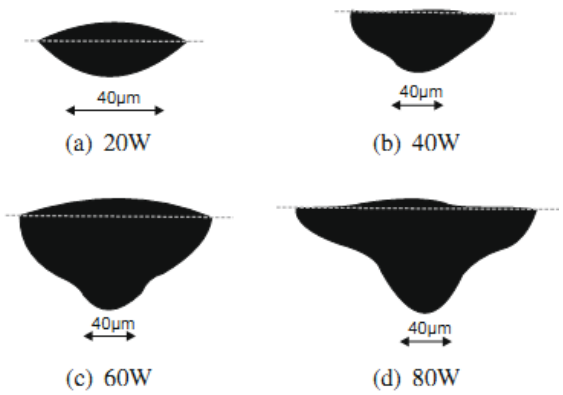

Figure 2.55: *Experimentally observed cross-sections of laser melt tracks for the different values of the power input [121].*

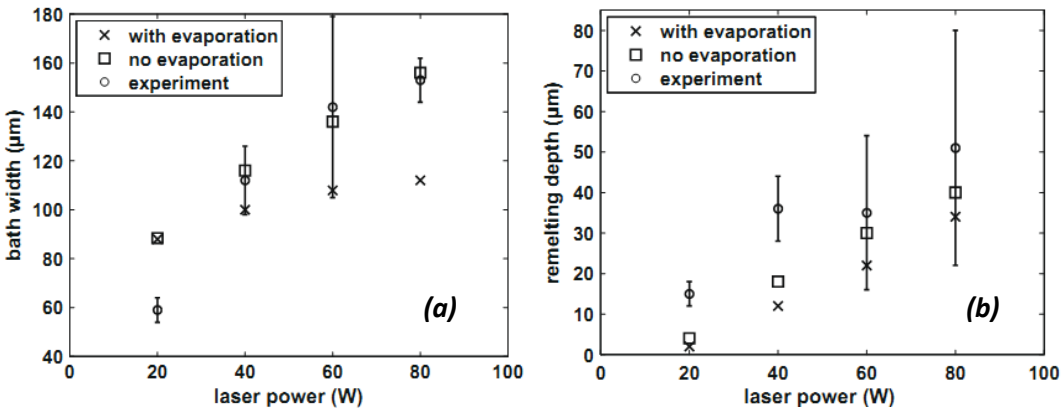

Figure 2.56: *Comparison of (a) the melt pool width, and (b) the remelting depth, in simulations and experiments by Verhaeghe et al. [121].*

2.9.6 Mechanical properties of AM deposits

2.9.6.1 Powder bed – EBSM and SLM processes

Murr et al., have reported the tensile properties of Ti6Al4V alloy samples produced by the Electron Beam deposition additive manufacturing technique [20, 111]. A set of cylindrical specimens were fabricated from Ti6Al4V Grade 5 powder material in an EBSM system. These samples were used to machine tensile specimens and were tested along with two other similarly prepared wrought specimen, type one from a billet forged at 1040°C to produce a coarse plate-like α with some intergranular β and the other from a billet forged and solution treated 1 h at 950 °C, air-cooled and then annealed 2 h at 700 °C to produce an equiaxed, α/β microstructure. Table *2.9* compares the mechanical properties of the samples. The selective electron beam melted AM Ti6Al4V specimens, showed comparable strengths (UTS) and elongation to the best wrought Ti–6Al–4V products [20, 111]. The tensile strength and hardness values reported by other authors in the literature are also shown in the Table *2.9*.

Effect of build temperature: In EBSM variation of the preheating current allows the user to increase, or decrease, the energy input for heating and sintering each powder layer before the melting cycle. It has been reported by Al-Bermani et al. that a change in preheating temperature will significantly change the microstructure and resulting mechanical properties [112]. Figure *2.57*a shows the variation of mechanical properties and microstructure with respect to build temperatures in the as-built and HIP'ed condition (hot-isostatically-pressed condition). The yield strength was consistent over the preheat temperature range of 899 K to 951 K (626 °C – 678 °C), but there was a significant decrease in yield strength observed at 973 K (700 °C). The reason for this can be seen in Figure *2.57*(b-c), both the α lath width and α colony scale increased as a result of processing at higher build temperature of 973 K (700 °C). Thus, the drop in mechanical properties for 973 K (700 °C) is clearly attributed to coarsening of the microstructure.

Table 2.9: *Mechanical properties of Ti6Al4V AM samples produced by the EBSM technique in comparison with wrought products reported by different authors.*

Sample & microstructure	HV (Gpa)	HRC	YS (Gpa)	UTS (Gpa)	A (%)	Reference
ISO 5832-3 (min for wrought and annealed material)	-	-	**0.78**	**0.86**	**10**	
Ti6Al4V ASTM Grade5 nominal (spec)	-	**37**	**0.90**	**1.00**	**15**	
EBM-1 (top) (coarse α-plates)	3.6	37	1.15	1.20	25	[111]
EBM-1 (bottom) (finer α-plates)	3.9	42	-	-	-	[111]
EBM-2 (top) (fine/coarse α-plates)	3.6	49	1.10	1.15	16	[111]
EBM-2 (bottom) (finer α-plates)	4.6	50	-	-	-	[111]
very fine lamellar with g.b α- phase – average of 5 samples	3.2 ±20	-	0.83±5	0.915± 10	13.1 ±0.4	[90]
Fine Widmanstätten α+β	-	-	0.883± 10	0.993± 6	13.6 ±0.9	[112]
Wrought-1 (coarse α-plates)	3.8	48	1.17	1.23	12	[111]
Wrought-2 (equiaxed α/β)	4.3	52	1.22	1.29	14	[111]

HV (Vickers hardness) for 25 gf (0.25 N) load at 10s dwell (1 HV=0.01 GPa). YS (0.2% offset yield stress), UTS (Ultimate tensile strength), and A (Elongation in %)

Hot isostatic pressing (HIP) of powder metallurgy and cast components is often used in post processing to eliminate any porosity that may initiate premature failures. HIPing of EBM Ti6Al4V is observed to cause a drop in yield and tensile strength, across all build temperatures with a slight increase in elongation as shown Figure *2.57* [112]. The same trend were also observed by Luca Facchini et al. [90]. Once again, this drop in strength can be associated with microstructural coarsening, brought about by the high temperature 1193 K (920 °C) used in the HIPing treatment.

Table 2.10: *Mechanical properties in as-built and HIP'ed EBSM Ti6Al4V samples [112]*

Build Temperature, K (°C)	Yield Strength (±1σ), MPa	Tensile Strength (±1σ), MPa	Elongation (±1σ), MPa
973 (700)	883.7 (±10.6)	993.9 (±5.6)	13.6 (±0.9)
951 (678)	932.4 (±3.2)	1031.9 (±2.6)	11.6 (±1.5)
917 (644)	928.8 (±5.5)	1028.9 (±4.3)	13.0 (±0.7)
899 (626)	938.5 (±10.9)	1029.1 (±14.9)	13.2 (±0.4)
973 (700) HIP	841.4 (±7.8)	938.8 (±7.1)	13.6 (±1.3)
951 (678) HIP	868.4 (±8.6)	974.2 (±10.8)	13.4 (±1.7)
917 (644) HIP	865.6 (±9.1)	969.2 (±8.0)	14.0 (±1.6)
899 (626) HIP	875.2 (±2.2)	977.6 (±3.0)	13.6 (±0.5)

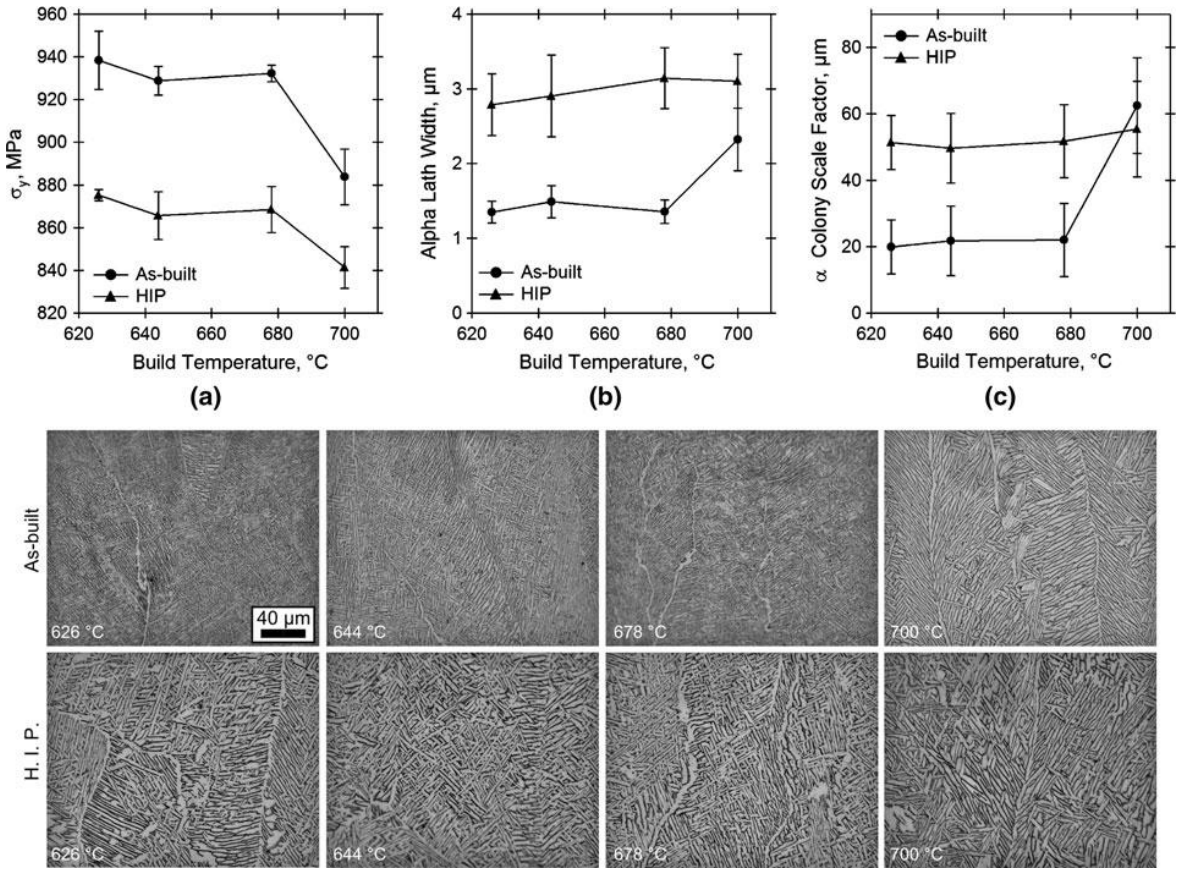

Figure 2.57: *Variation in mechanical properties with respect to build temperature; (a) Yield strength, (b) α-lath width, (c) α-colony scale factor along with the corresponding micrographs in the as-buit and HIP'ed (hot-isostatically-pressed) samples [112].*

Recently, Brandl et al. [31], have compared the tensile properties of additive manufactured Ti6Al4V alloys (Figure *2.58*) with different processes like Electron beam selective melting (EBSM), Selective Laser Melting (SLM), and the Laser Cladding (LC) technique to forged material properties, as tabulated in Table *2.11*. They reported that all the static tensile samples produced show poor properties perpendicular to the building direction. In addition, it was reported that although SLM samples showed a low elongation, the poor mechanical properties could be improved to a reasonable level by annealing and hot isostatic pressing. Overall, it has been widely reported that

the static tensile properties of the AM samples are equivalent with the design values of forged materials and, with ASTM standards after post processing [31].

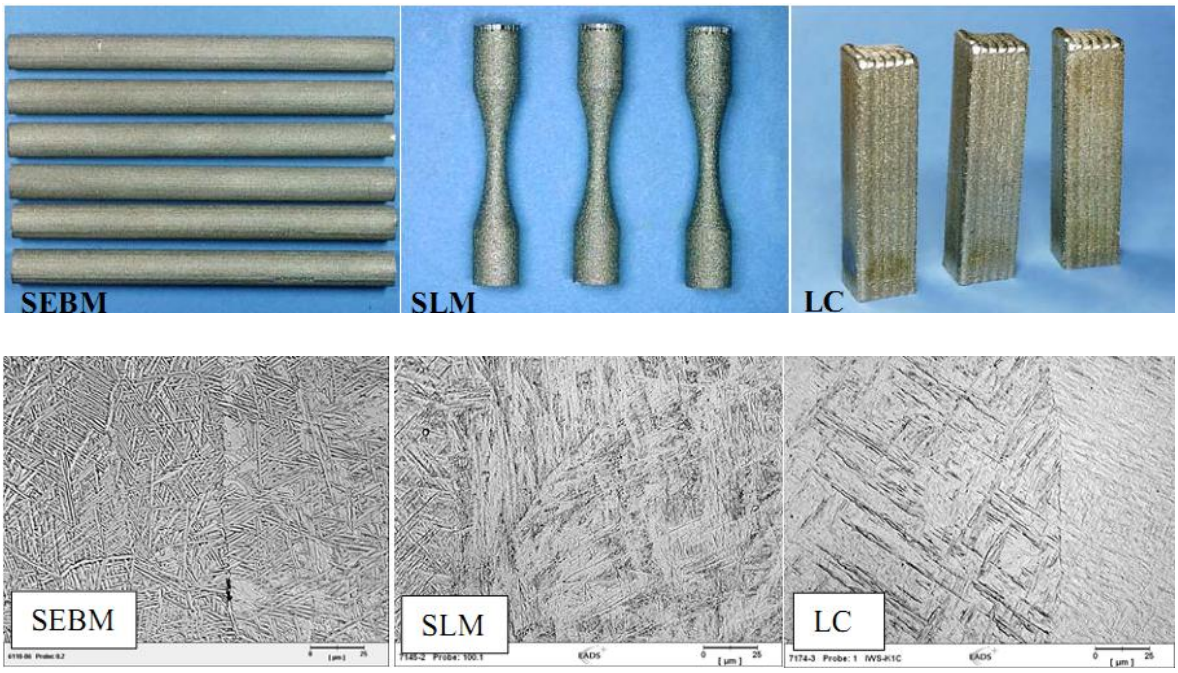

Figure 2.58: *Manufactured Ti6Al4V samples in the as-melted condition through EBSM, SLM and LC with their corresponding microstructure [31].*

Brandl et al. [31] have also reported the dynamic performance of e-beam, and laser beam AM test pieces under high cycle fatigue, as shown in Figure *2.59*. The samples for fatigue testing were tested with a load ratio of R=0.1. In Figure *2.59*, the EBSM and LC (laser cladding) materials showed a fatigue limit of around 600 MPa for 10^7 cycles. It has been reported that SLM products show low fatigue strength, due to their lower yield strength and large number of local defects like porosity and cracks [31]. It was also reported that the SLM mill annealed (MA) condition and the SLM hot isostatic pressed (HIP) samples have similar fatigue life. The samples with a rough surface (without machining in the as deposited condition) show a strongly reduced fatigue strength of about 200 MPa at 10^6cycles [31]. Amsterdam and G.A. Koolhave [123] have also reported that the laser beam deposited Ti6Al4V had a minimum high cycle fatigue strength of about 550 MPa for 10^7 cycles. They also mentioned that the presence of pores act as crack initiation points (as shown in Figure *2.60*) significantly reduce the fatigue life of components [123]

Table 2.11: *Static tensile properties for EBSM, SLM and LC Ti6Al4V AM deposits in the as produced condition, compared to those of forged bar [31].*

Condition	**Forged bar (Solution treated and aged)**	**EBSM**	**SLM**		**LC**
		7kW EB + powder bed (Vacuum)	**0.25kW laser + Powder bed (Argon atmosphere)**		**3kW Nd: YAG laser (Argon)**
		As-deposited	**843°C/4h as deposited**	**843°C/4h at 1000 bar- Hipped**	**As-melted**
Y.S	>861	950	848	816	1010
UTS	>931	1020	964	956	1090
A [%]	>10	14	12.5	13	12.2
R A [%]	>20	40	30	27	21
Y.M [GPa]	110	120	113	107	116

***** YS (0.2% offset yield stress), UTS (Ultimate tensile strength), R.A (reduction in cross-sectional area), A (Elongation in %) and Y.M (Youngs Modulus)

Murra et al. [20] have also compared the mechanical properties of powder bed EBM and SLM of Ti6Al4V builds in the as-deposited condition, as shown in Figure *2.61*. The SLM builds exhibited poor ductility compared to the EBSM builds, due to the presence of more pores and the more brittle martensite phase. Hence, the samples were heat treated to 843 ˚C/2h and furnace cooled before testing. The features of the fracture surface of the EBSM build (with 12% of elongation) were almost the same as that of the wrought α-phase billet (with 16% of elongation) as shown in the Figure *2.62*. The EBSM fracture surfaces illustrated the expected ductile-dimple behaviour with no evidence of preferential failure, at the layer interface or within transition zones (Figure *2.62*a).

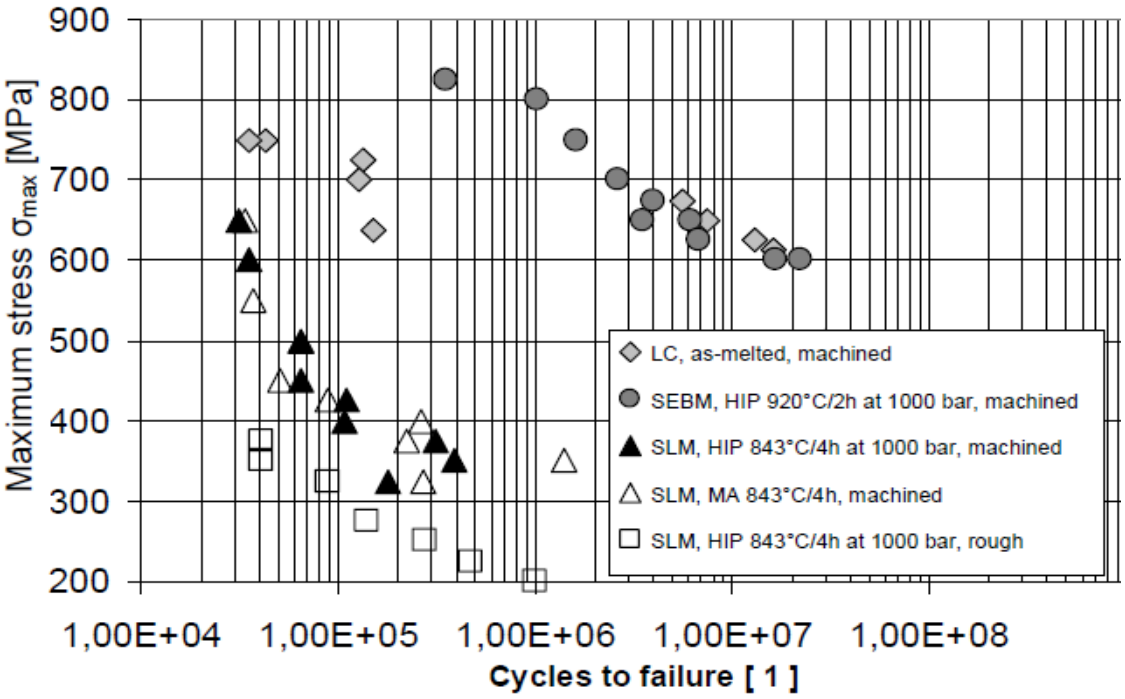

Figure 2.59: *Comparison of high cycle fatigue properties of Ti6Al4V samples produced by EBSM, SLM and LC additive manufacturing process [31].*

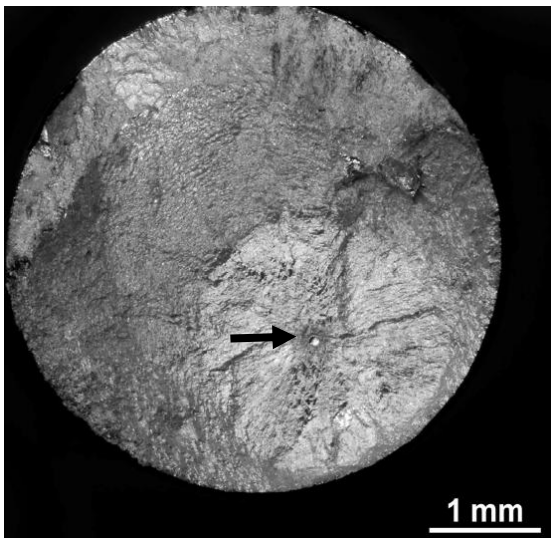

Figure 2.60: *Fracture surface of the Ti6Al4V fatigue sample is tested at 800 MPa. A circular crack initiated and grew from a pore with a diameter of 102 µm [123].*

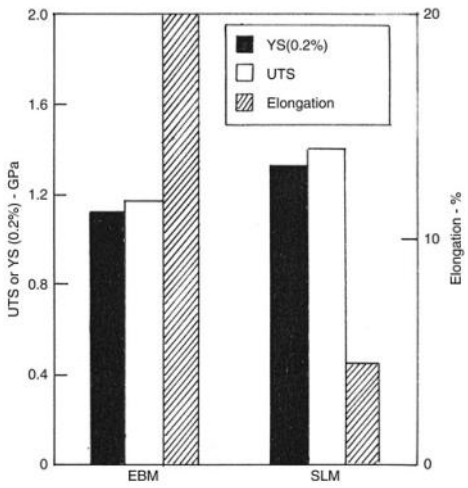

Figure 2.61: *Ultimate tensile strength (UTS), 0.2% engineering offset yield stress (YS) and elongation (%) for EBM samples compared with SLM Ti6Al4V by Murr et al. [20].*

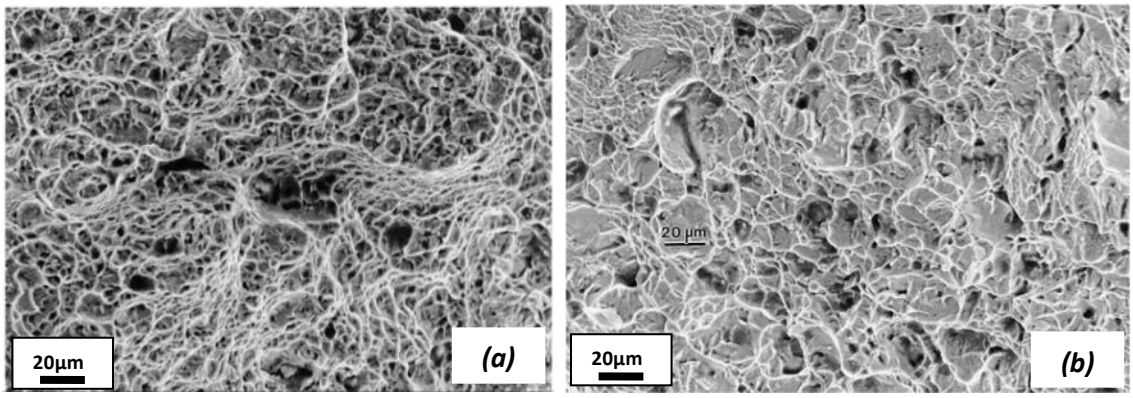

Figure 2.62: *Comparison of the fracture surface of (a) EBM manufactured Ti6Al4V samples with 12% ductility to (b) wrought billet with 16% ductility [111].*

2.9.6.2 Wire + arc AM or SMD (shaped metal deposition) technique:

Baufeld et al. [103] have produced square Ti6Al4V components with single wire beads using the shaped metal deposition (SMD) as shown in the Figure ***2.63***(a). The chosen coordinate system was the direction of the torch travel (x), the direction of the wall width (y), and the direction of the wall height (z). Tensile tests were performed on cylindrical dog-bone specimens cut from the wall in the X and Z directions. The tests were performed on three sets of samples; (i) in the as fabricated condition, (ii) a stress relieved condition (600 ˚C for 4 h) , and (iii) in an annealed condition (843 ˚C for 2h). Figure ***2.63*** (b-d) shows the stress-strain curves for these three different sets of test specimens [103].

The stress–strain curves showed a more limited amount of work hardening behaviour (plastic deformation) in the x direction compared to the z-direction and larger elongations to failure were

observed for testing along z- than in the x-direction which lead to a anisotropic mechanical behaviour in the build [103]. Similar observations have been reported for laser wire deposited AM by other authors [37, 101] and in SMD with other parameters [116, 124]. The specimens tested along the x-direction were perpendicular to the elongated prior β-grains. It was suggested by Baufeld and Van der Biest [116], that the transverse grain boundaries, acted as potential sources of failure, and were the reason of the anisotropic behaviour. Heat treatment at 600 ˚C (for residual stress) did not change the elongation to failure significantly. However, heat treatment at 843 ˚C (annealing) increased the strain to failure significantly, as shown in Figure ***2.63***. Figure ***2.64*** summarises the ultimate tensile strength (UTS) Vs elongation to failure of the SMD deposits with the minimum requirements for wrought (AMS 4928) and for cast (ASTM F1108) materials indicated by solid lines. Only the z- oriented specimens, with and without different heat treatment, and the x- oriented specimens after heat treatment at 845 ˚C fulfilled the requirements of the wrought products.

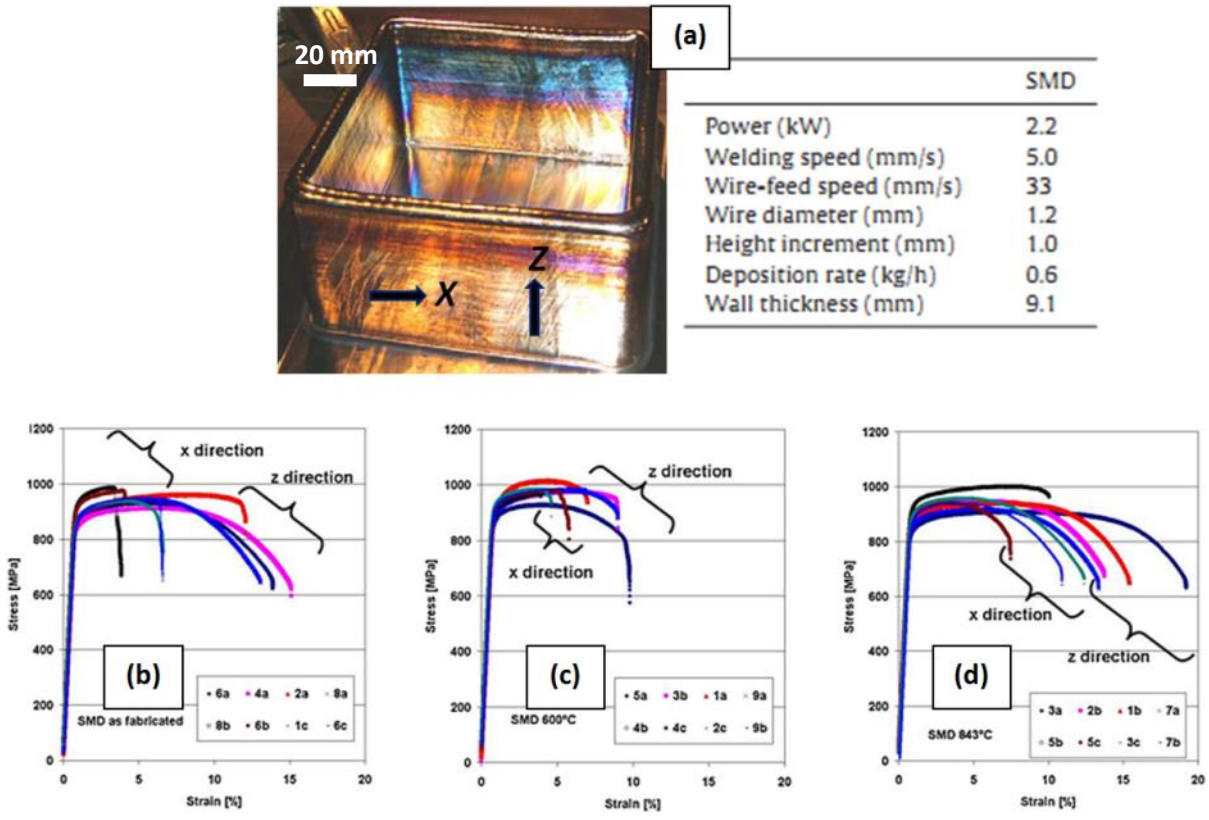

Figure 2.63: *Tensile stress-strain curves for SMD built Ti6Al4V samples (a) with the process parameters, (b) in the as-fabricated state, (c) after heat treatment at 600 ˚C (d) and 843 ˚C [103].*

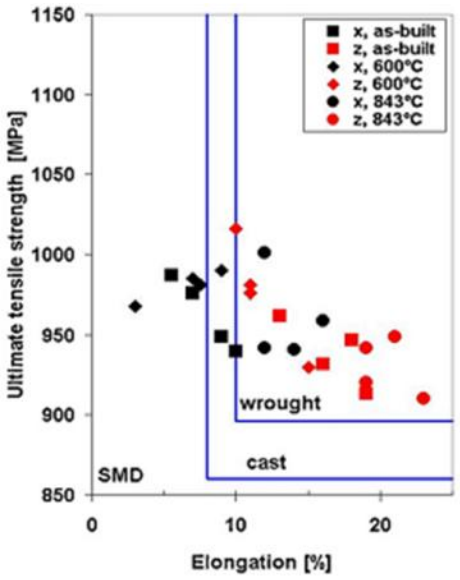

Figure 2.64: *Plot of ultimate tensile strength (UTS) versus elongation to failure in tensile tests on specimens from SMD AM samples, in the as-fabricated state, and after heat treatment at 600 ˚C and 843 ˚C. The minimum requirements for cast and wrought material are indicated by lines [103] .*

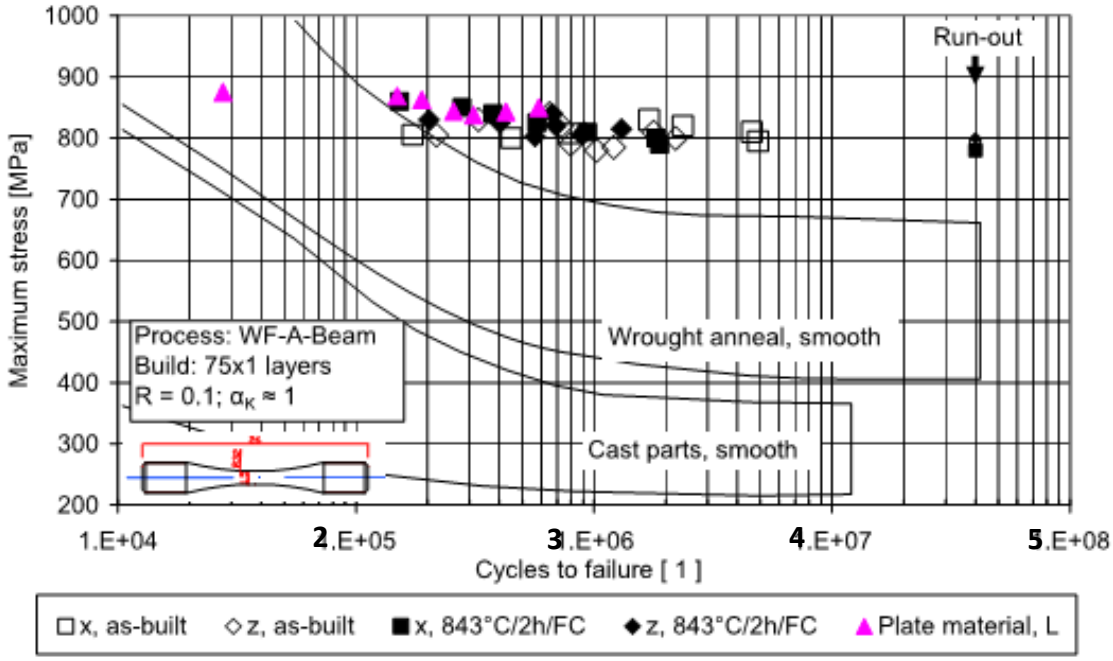

Figure 2.65: *High cycle fatigue properties of SMD AM specimens, tested along x- and z-directions in the as-built and heat treated at 843 ˚C/2hr/FC conditions. The line represents the upper fatigue limit required for cast and wrought annealed material with smooth machined surfaces [101].*

High cycle fatigue data obtained by Brandl et al. for the SMD specimens is shown in Figure *2.65* with a solid line indicating the upper fatigue limit required for cast and wrought products in the annealed condition[101]. The maximum stress for the fatigue tests was in the range of 750 to 913

MPa. This range was selected with an upper limit given by the yield strength and the lower limit by run out within reasonable testing time. It has been reported that the materials produced by SMD shows a clusters of data points in the area between 2 x 10^5 to 2 x 10^6 cycles and with a narrow stress range of 780 – 860 MPa. Hence, determination of a fatigue limit in this case is not meaningful, but the dynamic properties are approximately comparable to conventional plate material. Furthermore, the SMD deposits showed similar dynamic strength trends in both as-built and 843˚C/2h/furnace cooled conditions (Figure *2.65*). The dynamic properties of the materials tested along the X-direction were similar to those along the Z-direction [101].

It has been reported that the fracture surfaces of AM fatigue samples are very rough and, sometimes trans-granular fracture occurs along colonies, as shown in Figure *2.66*a. Figure *2.66*b shows the failure of a test piece due to crack initiation at a pore along the x-direction with a life cycle of 1.7 x 10^5. Cracks originate at the pore near the surface then propagate preferentially along the α/β interface omitting to cut the α-lamellae [103].

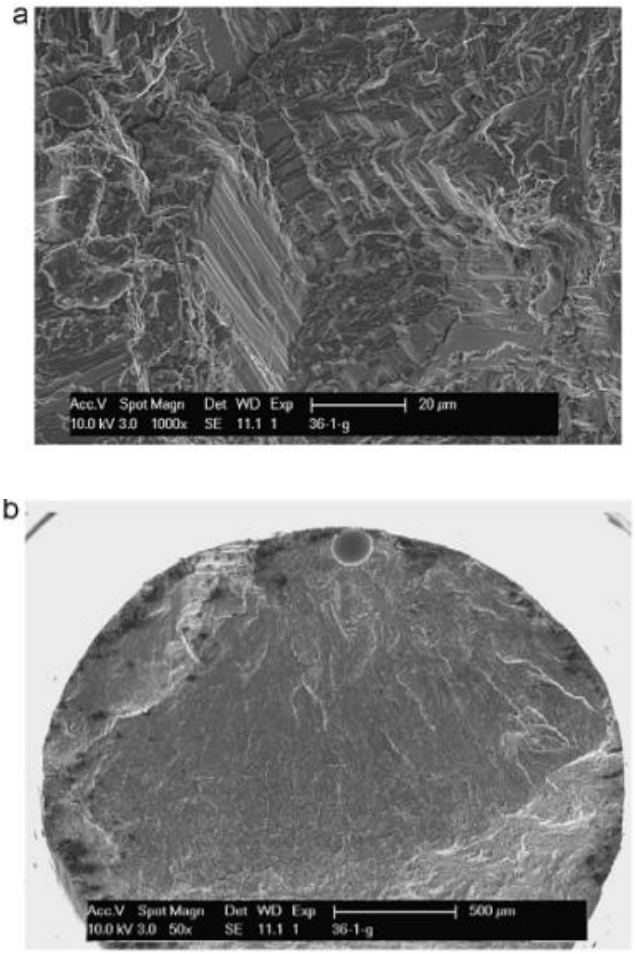

Figure 2.66: *Fracture surface of a SMD x-specimen failed after 1.7 × 105 cycles with a maximum load of 800 MPa [103].*

2.10 SUMMARY AND POTENTIAL FOR FURTHER STUDY

A detailed literature review of the typical microstructures and texture formed during AM of Ti6Al4V aerospace alloy using electron, laser and electric arc melting and deposition has been performed, including prediction from thermal modelling of the processes. The microstructure seen in all of the AM techniques with Ti6Al4V show a common columnar β grain structure, after an initial transient region at the base of the build. The coarse columnar β-grains start to grow perpendicular to the layers in the powder bed process, but their growth direction can also be related to the shape of the base of the melt pool in some cases. This structure is clearly linked to the high thermal gradient in the liquid (G_L>10^5 k m^{-1}) resulting from the focused heat source and the high partition coefficient of the Ti6Al4V alloy, which is close to one, and prevents nucleation in the liquid. The β grains were found to have irregular square cross-sections at the top view (along Rx-Ry) and develop a wavy natured columnar morphology (along the build direction in Nz-Rx) caused by the solidification front of the melt pool and an alternating rastering directions used in the AM process, which perturbed the growth direction.

In EBSM, the bulk microstructures in the build were also made-up of columnar prior β grains delineated by grain boundary α. Within the prior β grains, transformed α+β lamella structures are seen with both colony and Widmanstätten morphologies. Whereas, the SLM is primarily characterized by martensite (α') plates with no grain boundary α and apparent layer features.

Literature review on the AM technique shows that the columnar β grains adopt a strong fibre and cube texture, with a common <001> axis aligned approximately with the build direction as well as alignment with the two orthogonal raster directions.

The macrostructure of the SMD or WAAM deposits also showed huge columnar β grains in the mm to cm range, which grow epitaxially upon each layer deposition against the maximum heat extraction direction. Microstructural banding was observed much more clearly along the length of the deposits in arc weld deposits in comparison to the EBSM and SLM processes. This is mainly due to the HAZ upon the deposition of further layers, which caused the deposited layers to undergo a cyclic heat treatment in the α-β phase field. This resulted in a significant change in morphology across the bands.

The static and dynamic mechanical performance of Ti6Al4V produced via a range of AM techniques confirms that their properties can be superior to as-cast and wrought annealed products, but there are severe problems with porosity in some case.

2.10.1 Potential for further study

Overall a very limited amount of data was published on microstructure evolution during powder bed EBSM and Arc-wire deposition of Ti6Al4V, compared to SLM, at the start of this project. A lot of this work was published very recently. However, the amount of published work on texture with AM of Ti6Al4V alloy is still very limited. Despite the rapid rise in publications, the following important questions have not been adequately dealt within the literature and still need to be resolved,

(1) Whether the geometric design freedom of AM has any significant effect on microstructure and texture components of Ti6Al4V.
(2) A better understanding of the evolution of texture, variant and grain selection during AM of Ti6Al4V is still required.
(3) How to improve the microstructure, and in particular how to refine the large columnar prior β-grains seen in AM builds, by the following systematic study,
(4) The relationship between the microstructure, texture and key build parameters is still poorly understood.
(5) Residual stress also could affect the build performance especially when AM is used to repair the existing components.

Therefore, in the current study, the aim of the project considers most important key aspect of afore mentioned challenges as it was mentioned in the introduction chapter in section 1.7.

3 EXPERIMENTAL AND CHARACTERIZATION TECHNIQUES

3.1 INTRODUCTION

This chapter describes the experimental procedures used to produce the electron beam, laser beam and TIG Arc melted AM Ti6Al4V samples studied in this project. It also describes the setup and the experimental parameters used for each AM platform, as well as the specific experimental conditions and variables considered in building the AM samples analysed. The chapter then describes the samples types evaluated and the methods used to analyse them. It also discuss the mechanical testing carried out both in, and that feed into, this study as well as the thermal modelling methodology employed.

3.2 FEED MATERIALS

The powder or wire used in an additive layer manufacturing technique is the material that is consolidated in the final component. Therefore, attention has to be given to the processing of the powder, since the powder size, shape will affect the flow behaviour, which might influence the process stability, and any contamination may result in voids in the final component. Good quality pre-alloyed titanium powders with the size range of 30 to 80 µm and, 10 to 45 µm were used in this project as the initial feed powders for the EBSM (Arcam A12 Machine) and SLM (EOS MT270 machine) techniques, respectively. The initial powder was produced via two main production routes namely, gas atomisation (GA) [125] and the plasma rotating electrode process (PREP) [126]. The powder suppliers for the powder bed deposition were kept confidential by EADS and unfortunately could not be named here. However, it was mentioned that the initial oxygen content in the powder was about 1200 ppm for both the EBSM and SLM processes.

Gas Atomisation: The gas atomisation involves melting the feed stock, which is then injected through a nozzle into a perpendicular high speed cold inert gas jet, resulting in a spray of rapidly solidified particles that are collected in chamber. Gas atomisation is a relatively simple and widely-used process that yields good quality, clean powder suitable for most powder metallurgy applications. Particles produced by gas atomisation are approximately spherical, often with smaller satellite particles attached (as shown in Figure 3.1a) and sometimes containing entrapped bubbles of the inert atomisation gases.

PREP process: This technique uses a plasma arc to heat the end face of a circular bar that it is rotated about its axis at high speed. Droplets of molten material are thrown outwards by the centrifugal force, cool and solidify as they travel, and are collected in an annular container. The entire process is carriedout in a vacuum. In comparison to gas atomisation, PREP produces more spherical, better separated particles free from entrapped gas and with a smoother surface than gas atomisation (see Figure 3.1b), giving the powder better handling and flow characteristics. However, there are fewer manufacturers, and PREP process is more difficult to control, resulting in a higher cost of PREP powder than the gas atomised.

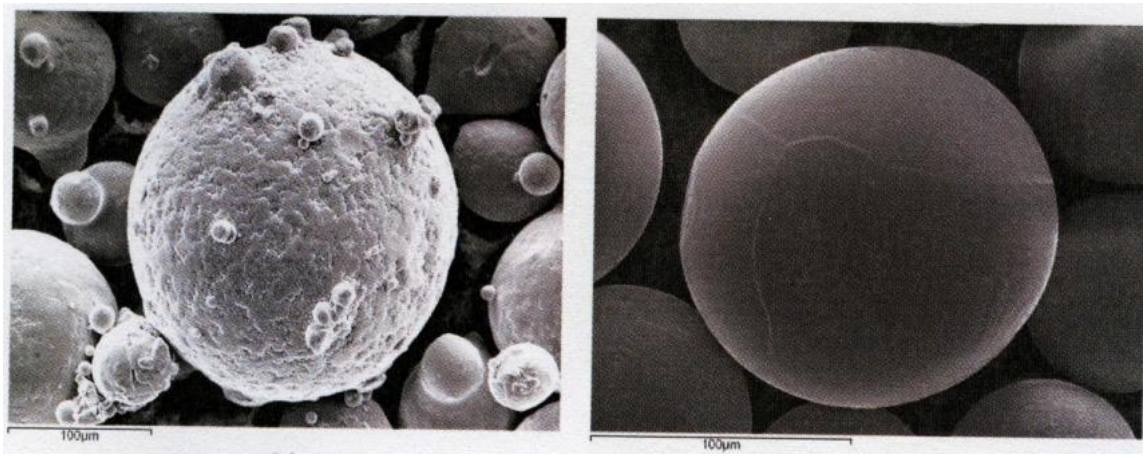

Figure 3.1: Morphology of typical powder particles produced by using gas atomisation and PREP atomisation using SEM second electron images [107].

A bare welding consumable Ti6Al4V wire, of 1.0 or 1.2 and 1.5 mm diameter, was used for the arc wire deposition process, with precise control over the interstitial elements like Oxygen and Nitrogen. The wire material used in this study was supplied by the VBC group and had the specification AMS 4945G. The initial oxygen and nitrogen content in wire was reported to be around 1400 ppm and 100ppm, respectively (from the wire suppliers). Hot rolled Ti6Al4V plate, with a thickness of about 7 mm, was used as a substrate material, and was ground with 400 grit SiC paper, and then degreased with acetone and ethanol before being used.

3.3 AM PROCESSING CONDITIONS

3.3.1 Electron beam selective melting (EBSM) - Powder bed technique

The selective electron beam melted AM samples were produced with an ARCAM EBM S2 machine, at EADS Airbus UK, which works based on the powder bed principle, as discussed in 2.8.3. Figure *3.2* shows a schematic representation of key components of the ARCAM EBM S12 system, which allows solid parts to be directly manufactured from metal, or alloy powder. The electron gun column houses a 3.5 kW thermionic tungsten filament under a vacuum of approximately 10^{-7} mbar (A). The build chamber (B) is initially evacuated to approximately 10^{-4} mbar before the introduction of helium gas raises this to 2×10^{-3} mbar. Powder is held in powder hoppers (C) and uniform 100 µm layers are spread across the build table using the traversing rake (D). Components (E), are built on a base plate (F) which is stainless steel, and sits within the build chamber (G). After completing a layer, the bed is lowered by an increment of 100 µm, using the z-axis assembly shown in (H), then, a new 100µm thick layer of powder is spread in the build chamber, and the cycle repeats to make the complete components from the 3D CAD model file.

The EBSM system is an electron optical system essentially identical to an EB welding unit, or a scanning electron microscope (SEM) where an electron gun (A) generates a focused Electron beam which can be systematically scanned (by deflection coils) across the building part; directed by the CAD design. The electron gun operates nominally at 60 kV and can develop an energy density in excess of 102 kW/cm^2. In addition, the build table (F) is normally heated to between 600 to 750°C (in this study to ~740 °C). Figure *3.3* shows a sequential representation of the additive layer manufacturing processes. After spreading and raking, powder preheating is performed by rapidly rastering the beam. Local melting of the powder is then carried out in two stages; firstly, the perimeter of each component, or contour, is melted using a continuously moving beam before the bulk of the component section is then consolidated using a regular raster pattern (hatching) [127].

Figure 3.2: *(a) Key components of the Arcam S12 e-beam AM machine, and control system; electron gun column (A), build chamber (B), powder hoppers (C), rake arm (D), component (E), base plate (F), build chamber (G), z-axis assembly (H), (b) photograph of the EBM build chamber and, (c) exterior of the Arcam S2 EBM machine [23, 112].*

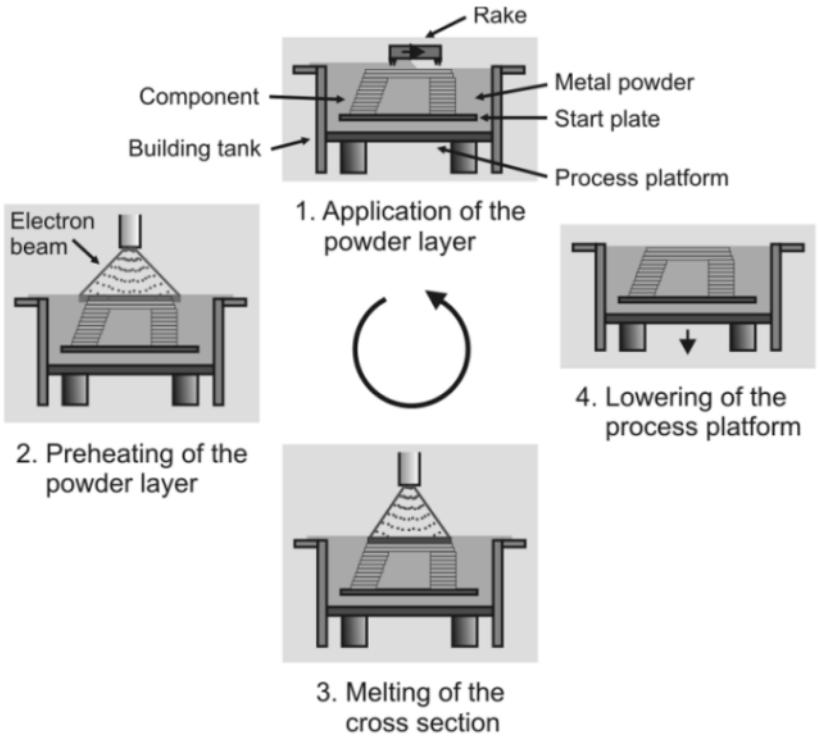

Figure 3.3: *Sequential representation of the process stages used in selective electron beam melting, additive layer manufacturing [10].*

Themes in the ARCAM Machine: The themes in the EBM Arcam machine are parameter sets used for specific purposes in the process and are accessible on the control page of the EBM software. Themes contain all of the properties of the electron beam including speed, power and focus of the beam. Four main themes are typically used to build a part in the following order [92],

(i) Base plate heating: used to raise the base plate to a pre-defined temperature. Standard practice is to raise the plate to 740 °C.

(ii) Powder pre-heating: used to pre-heat and sinter each layer of powder.

(iii) Wafer supports: used to generate supports beneath overhanging surfaces.

(iv) Melt: used to melt the perimeter of a component (contours) and for bulk melting (hatching) in between contours.

Figure 3.4: *Photographs of the key processing steps in EBM; (a) powder preheating, (b) melting of component perimeter (contour) using a multi-beam mode and (c) hatching [92].*

Figure ***3.4*** shows the application of three of the key themes. Figure ***3.4***(a) shows the powder pre-heating stage using an orthogonal raster pattern, while Figure ***3.4***(b) shows the melting of the component section outline, or contour, using the multi-beam contour method and Figure ***3.4***(c) shows hatching, using an orthogonal raster pattern. The orthogonal hatching raster pattern is rotated by 90° after every layer and, thus, rastering alternates along the Rx-(along X-) and Ry-(along Y-) axes [92, 112]. Table ***3.1*** shows typical settings for the key processing themes [92]. The power of the electron beam is determined by the value of the beam current. The focus offset is the value of current used by the focussing coils to focus the beam. It should be noted that beam speed is not constant for the melt themes and its value depends on a parameter called the speed function (SF).

The Speed function: The speed function is defined as a relationship between beam speed and current that is built into the EBM control software. The objective of the speed function is to ensure that a constant melt depth is maintained regardless of the current used. An increase in current is thus accompanied by an increase in speed to negate the effect of the increased beam power to and keep a constant depth of melt pool. Table ***3.2*** shows that the contour and hatch themes are defined by a range of currents, rather than a specific value. The beam speed, always varies within the stated range, according to the speed function. Figure ***3.5*** shows the relationship between speed and current for five different speed functions. A detailed working procedure and schematic diagram of this machine can be found in references [8, 10, 19, 20, 23, 88, 90, 92, 111, 112].

Table 3.1: *shows typical beam settings for the key EBSM processing themes [92].*

Theme	**Beam Current, mA**	**Beam Speed, mm/s**	**Focus Offset, mA**
Pre-heat	15	14600	45
Wafer support	2.2	275	8
Melt (contour)	5-8	40.5-93.8	22
Melt (hatch)	6-15	187.8-802	17

Table 3.2: *Electron beam settings for the contour and hatch themes with speed function [92].*

Theme	Beam Current, mA	Speed function (SF)	Focus Offset, mA
Contour	5-8	4	22
Hatching	6-15	19	17

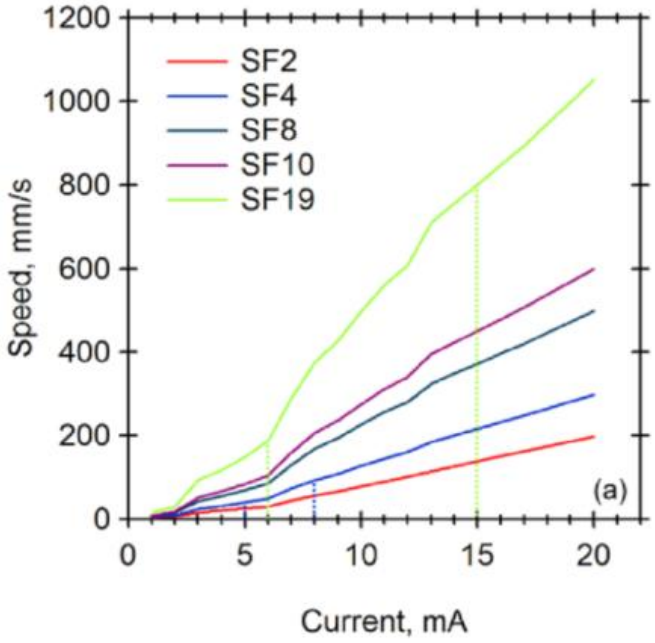

Figure 3.5: *The relationship between speed and current for five different speed functions. The vertical lines indicate the typical range of currents used for speed functions of 4 and 19 [92].*

3.3.1.1 EBSM samples

The operating conditions used to produce the samples investigated were the standard optimum settings recommended by Arcam (Arcam AB, Sweden [23]). The standard optimised parameters used to produce the Ti6Al4V samples using the Arcam machines are tabulated in Table *3.3*. In general, the speed function is used to attempt to maintain a stable melt pool depth of about 0.2 mm, when the beam slows down to reverse its path, or draws corners, etc. A target build temperature of 740 ˚C was maintained by control of the preheat scan stage. The parts were built on a stainless steel base plate, in which the temperature was monitored.

Table 3.3: *Standard settings used to produce the Ti6Al4V samples with the Arcam EBSM machine.*

Parameters	**Actual values**
Accelerating voltage	60 kV
Layer thickness	100 µm
Contour theme condition	Beam current of 5 - 8 mA, and a beam speed of ~ 0.15 - 0.3 m/s
Hatching theme condition	Beam current of 6 - 15mA and a beam speed of ~ 0.5 – 1.0 m/s
Beam offset thickness	0.24 mm
Build temperature	740 ˚C

In order to understand the influence of geometry on the formation of the primary β-grain structures and the related β- and α- textures, a set of 6 sample types was manufactured to represent common design elements seen in components (Figure *3.6*). The samples are described below,

(i) **Wall thickness vertical transition** (Figure *3.6*(a)): Vertical walls of different thickness (1 to 5 mm) were produced, after first depositing a wide 5 mm high base - to study the influence of wall thickness and a transient change from a thick to a thinner section. The 1 mm wall was the thinnest that can practically be achieved in the Arcam machine.

(ii) **Wall thickness inverse transition** (Figure *3.6* (b)): Vertical walls of different thicknesses (1 to 5 mm thick) were produced from the base plate before depositing a 5 mm thick, horizontal, capping layer - to understand the influence of wall thickness on a transient change from a thin to a thick section.

(iii) **Wall inclination** (Figure *3.6* (c)): 3 mm thick walls were built tilted at angles of 30°, 45°, and 60° relative to the build direction (N_Z) to investigate the effect of wall inclination angle.

(iv) **'V'- transitions** (Figure *3.6* (d)): The juncture between a V- cross-section from a flat plate, as well as a triangular section (internal angle 60°) reducing in width, were used to study the transition from a steady-state wide section through a constriction (1 mm wide), or where there is a progressively reducing section thickness.

(v) **'X'- transition** (Figure *3.6* (e)): Samples with two walls meeting at 90° were used for studying the behaviour within webbing intersections, exemplified here with a 1.0 and 1.5 mm wall thicknesses.

(vi) **Support structures** (Figure *3.6* (f)): A typical part with attached supports (required in AM to prevent collapse of some components) was used to study the effect of the transition from a supporting web through the point of contact into the component.

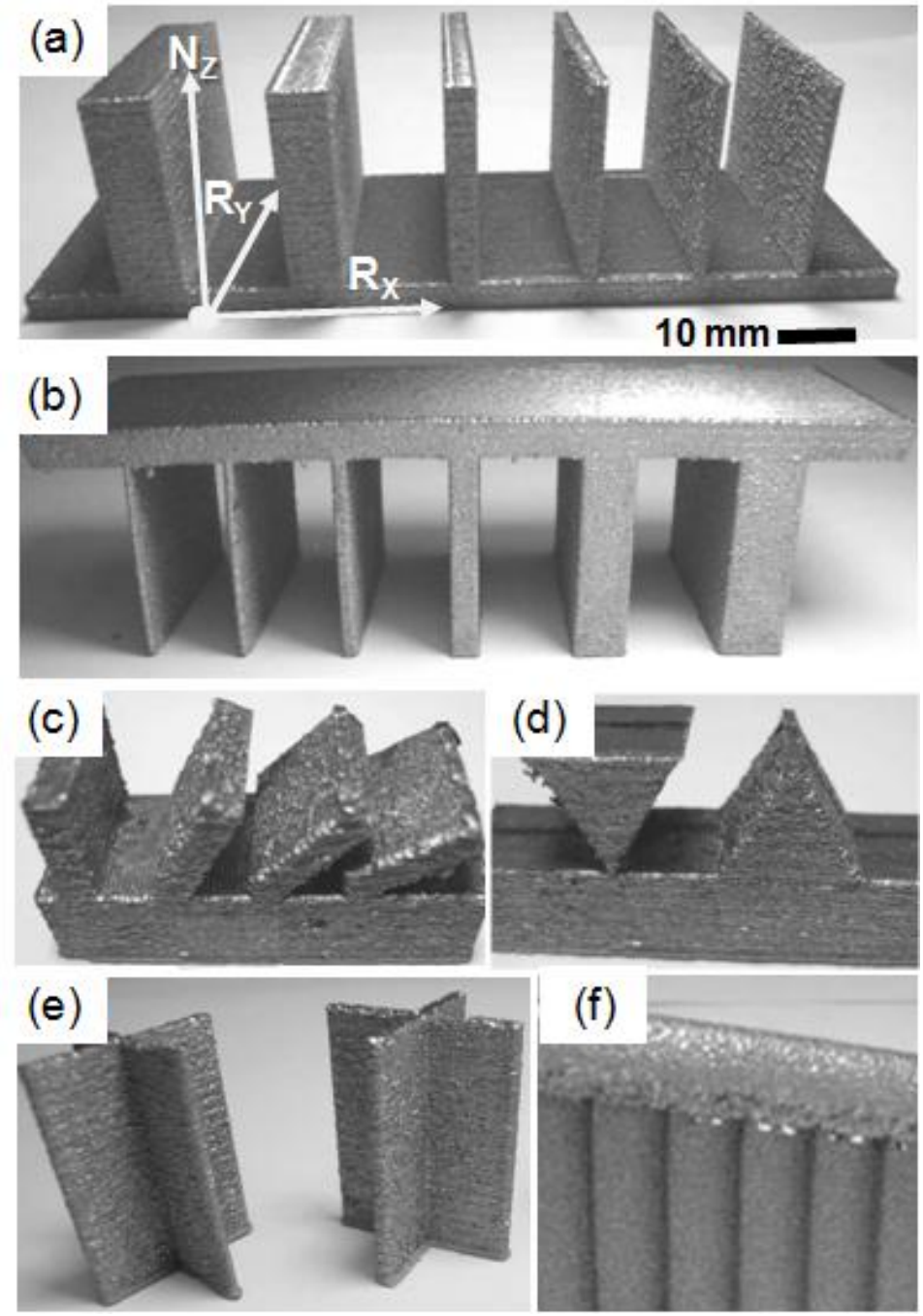

Figure 3.6: *The Sample set produced to investigate the influence of different generic build features on the formation the primary β-grain structure and related textures using Arcam A2 machine; (a) wall thickness vertical transitions, (b) wall thickness inverse transitions, (c)wall inclination angle, (d) 'V'-shaped transitions, (e) 'X' transition and (f) Support structures.*

3.3.2 Selective laser melting (SLM) - Powder bed technique

The SLM technology works in the same principle as that of EBSM powder bed deposition, except the source of heat is obtained from a Laser beam and the scanning strategy, as discussed in the

section 2.8.4. Figure ***3.7*** shows the exterior of the EOSINT M270 selective laser melting (SLM), or direct metal laser sintering (DMSL), system used in this study. In EBSM, contour pass was used first, to fuse the outer edge/section of the component and then infill hatching was used which rotates orthogonally 90˚ upon every new layer. Whereas, in SLM process, infill hatching was used fist and then a contour pass was used to melt the components outline sections. In addition to this, the infill hatching raster pattern is rotated by 30° after every layer *[30, 99]***.** The build chamber is purged with Argon and the oxygen sensor attached to the build chamber ensure to have a better control over the oxygen content in the build chamber.

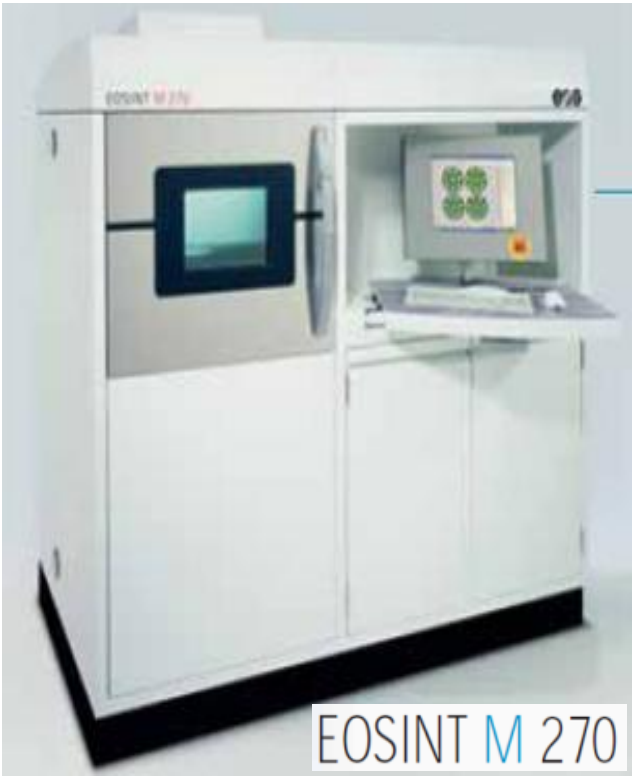

Figure 3.7: *The exterior of the EOSINT M270 SLM machine [30, 99]***.**

3.3.2.1 SLM samples

The specimen was built directly onto a Ti6Al4V base plate at room temperature using an EOSINT M270 selective laser melting (SLM) machine made by Electro Optical Systems, Germany. The samples were produced using the SLM facility available at the Additive Layer Manufacturing Centre, EADS Innovation Works (UK) with high purity, plasma-atomized powder, using the build parameters given in the Table *3.4*. On completing the build, the specimen was removed from the base plate by wire Electrical Discharge Machining (EDM). The process parameters used to produce the SLM specimen are listed in Table *3.4*. In order to understand the influence of geometry on the formation of the primary β-grain structure and the related β- and α- textures, a sample with

different wall thickness was manufactured to represent common design elements seen in components (Figure *3.8*).

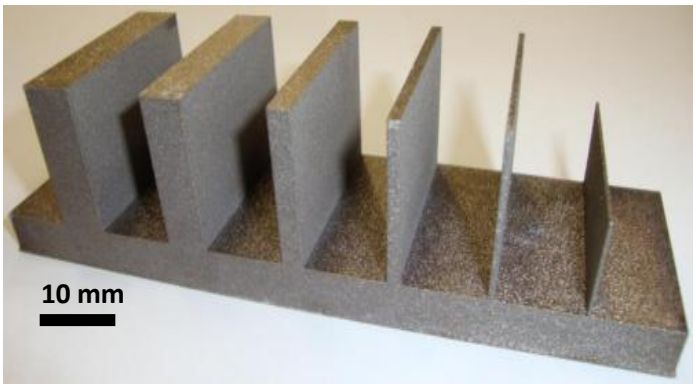

Figure 3.8: *The Sample set produced to investigate the influence of different wall thickness vertical transitions on the formation the primary β-grain structure and related textures using EOSINT M270 SLM machine.*

Table 3.4: *The process parameters used to produce AM specimens using the SLM technique.*

Standard parameters	
Power	170W
Powder Bed Layer thickness	30 µm
Scan Speed	1250 mm/s
Beam diameter	0.2 mm
Hatch space	0.1mm

3.3.2.2 Stress relieving (SR) heat treatment of SLM samples

Generally SR treatments are carried out to remove the residual stresses from prior fabrication steps, or prior heat treatments, to avoid part distortion. Since SLM samples were produced on the cold powder bed with no preheating it was obviously expected to have a high residual stress in the component and hence, in order to have a better indexing during EBSD (only for EBSD analysis), SLM samples were stress relieved at a temperature of about 600 ˚C for 25 hours (soaking time) [113].

3.3.3 Wire + Arc AM deposition technique

In the SMD or WAAM, the wire is fed into the melt pool produced by an electric arc source, as discussed in the section 2.8.5. Hot rolled Ti6Al4V plates were used as a base substrate plate for the arc deposition samples. Samples were produced at the Welding Engineering Research Centre, University of Cranfield, UK (RUAM Technology group Project) using either GTAW or GMAW processes. For the initial microstructural studies, three different GTAW techniques were used to produce the preliminary samples. The wire feeder used was a Migatronic KT4 with a maximum wire feed speed of 4 m/min. A Fanuc Robot Arc mate 120i was employed to automatically position the welding need. All the samples were produced with out of chamber welding process with both GTAW torch shielding of 75 % He + 25 % Ar at the flow rate of 15 L/min, and an extra hood shielding of 100 % Ar at the flow rate of 30 L/min.

3.3.3.1 GTAW deposited samples

(i) **GTAW with constant (DC) current power source (Figure *3.9*(a)):** A Migatronic Commander 400 power supply was used to produce the specimens with a current in the range of 90 to 240 A (See Table *3.5*). This gave a large arc with a wide wall thickness and an extended heat affected zone (HAZ).

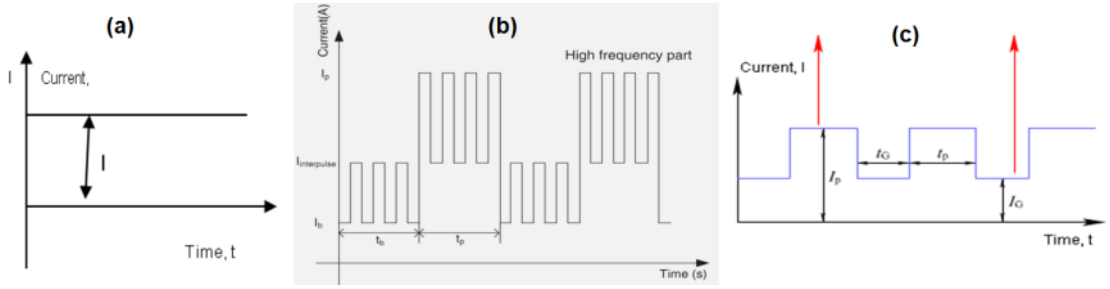

Figure 3.9: *Schematic views of; (a) direct current, (b) low + high frequency inter pulse and, (b) standard pulse current wave form with a TIG welding power sources.*

(ii) GTAW with different travel speed using VBC-HF Interpulse power source (Figure *3.9*(b)): A VBC Interpulse IP 150 power source was used to produce WAAM wall samples (See Table *3.5*). The VBC Interpulse IP 150 welding system has a constant pulse frequency of 20 kHz, when operated in the high-frequency mode. The VBC interpulse equipment is designed to supply direct current (a) high-frequency pulse TIG, (b) low-frequency pulse, and (c) a combination of low- and high- frequency pulse outputs. The power supply unit has a maximum current level of 150 A. The travel speed of 0.27 m/min was doubled to 0.54 m/min to study the influence of travel speed keeping constant line energy. The

average current can be calculated (Figure *3.9*(c)) by adding the pulse current to the interpulse current and multiplying by 0.45 from:

$$I_{average} = \frac{(I_{interpulse} + I_p)x0.45t_p + (I_{interpuse} + I_b)x0.45t_b}{t_p + t_b}$$

Where, I_p – peak current (A), I_b –base current (A), t_p –peak current, and t_b –base current. The interpulse Pulsed GTAW gives a constricted arc and smaller HAZ when compared to a standard DC power source. In addition to this, the combination of low and higher current-pulsing can create turbulence in the melt pool, which was thought might help to refine the grains in the final microstructure during solidification. Since this machine is not designed for the heavy duty use required to produce large walls, samples built with a conventional pulsed GTAW power source were also studied.

Table 3.5: *Process parameters used to produce the GTAW Ti6Al4V samples with DC and interpulse power sources.*

	ID	TS (mm/s)	WFS (mm/min)	Votage, V (v)	Current, I (A)	*Heat I/P (kJ/m)	Feed rate WFS/TS (m/m)
GTAW-DC	1	3	20.00	10	90	240	6.67
	2	6	26.67	11.7	180	281	4.44
	3	8	33.33	12.5	240	300	4.17
VBC-HF interpulse	4	3	20.00	10	I_p-120, I_b-60, I_{av}-90 + pulse freq.from 10 kHz to 20 kHz (t_p=t_b=0.05 s)	240	6.67
*Heat I/P= [(efficiency *V*I)/T.S]; Efficiency of GTAW process ~ 80 % [44, 46]							

(iii) **GTAW with change in wire feed rate using VBC interpulse: W**ith the pulse GTAW deposition technique, the wire feed rate was varied from 1.6, 2.0, 2.2 2.8 and, 3 m/min (with a constant travel speed of 0.24 m/min, 10 Hz low frequency, plus 20 KHz high frequency and, average current of 105 A were used).

(iv) **GTAW with standard pulsed current power source (Figure *3.9*(c)):** A Migatronic (TIG) Commander 400 power source was also used to produce AM specimens. Pulsed GTAW

should give less HAZ damage compared to a normal DC supply and can promote turbulence in the melt pool, hopefully encouraging grain refinement. *Table 3.6* shows the process parameters used to produce the samples with different peak to base current ratios (I_p/I_b) and pulse frequencies. During these variations the power input (η x $I_{average}$ x Voltage/T.S) kept constant for all the experiments in order to compare the morphology. The heat input efficiency for TIG welding considered to be η=0.7

Table 3.6: *Process parameters used to produce Pulsed GTAW Ti6Al4V samples with a systematic variation in peak and base current ratio (I_p/I_b) and pulse frequency.*

ID	TS (mm/s)	WFS (m/min)	Line Energy	V (v)	I_p (A)	I_b (A)	I_p/I_b ratio	I_{av} (A)	Frq. (Hz)	t_p (s)	t_b (s)
Variation of I_p/I_b ratio											
1	4.5	1.6	208.00	12	150	45	**3.3**	97.5	5.0	0.1	0.1
2	4.5	1.6	211.20	12	180	45	**4.0**	99.0	4.0	0.1	0.15
4	4.5	1.6	211.09	12	250	45	**5.6**	98.9	5.3	0.05	0.14
5	4.5	1.6	210.53	12	300	45	**6.7**	98.7	5.3	0.04	0.15
Variation of pulse frequency (Hz)											
7	4.5	1.6	208.00	12	150	45	3.3	97.5	**50.0**	0.01	0.01
8	4.5	1.6	208.00	12	150	45	4.0	97.5	**25.0**	0.02	0.02
9	4.5	1.6	208.00	12	150	45	3.3	97.5	**10.0**	0.05	0.05
1	4.5	1.6	208.00	12	150	45	3.3	97.5	**5.0**	0.1	0.1

3.3.3.2 GTAW arc deposited – Large walls 1, 2 and 3

Once an initial understanding of the influence of the process parameters on the build quality was developed, three large walls (Figure 3.10) were produced to allow mechanical properties measurement. The distortion in the WAAM (arrow marks in the build) is due the development of residual stress during the deposition process. Table *3.7* shows the process parameters used to produce these three different large builds. The location of the samples taken for microstructure analysis and mechanical property assessment are also shown in the Figure 3.10, where F, T and M stands for samples taken for fatigue, tensile and microstructure analysis, respectively.

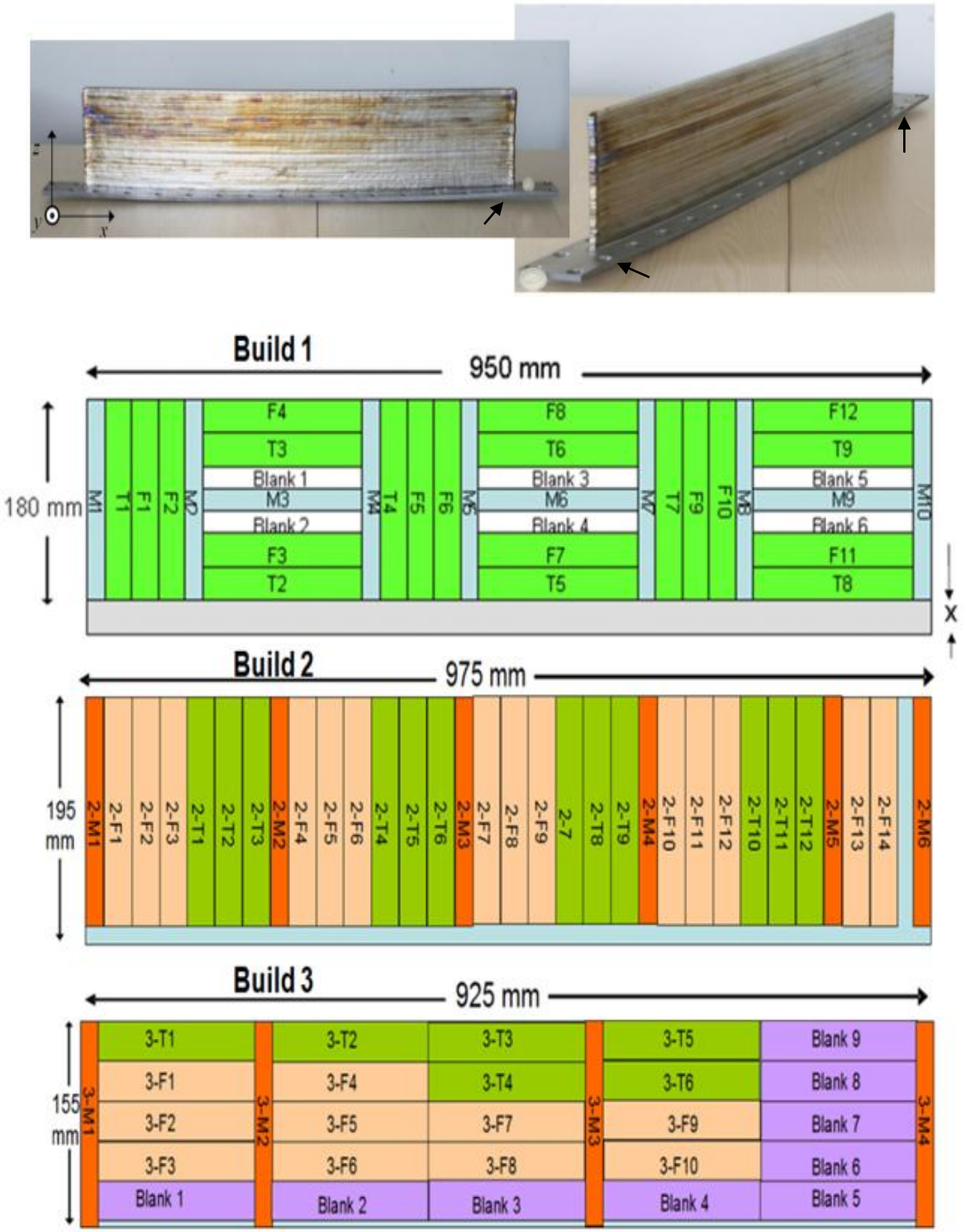

Figure 3.10: The WAAM large scale Ti6Al4V wall built in the RUAM project with the sample positions and orientation indicated for the analysis of micro-mechanical properties for the three builds. The distortion in the WAAM build is due the development of residual stress during the process (arrow marks in the build).

Table 3.7: *Process parameters used to produce the large WAAM wall builds.*

Paramters	**Build 1**	**Build 2 and 3**
Type of Machine used	VBC INTERPULSE TIG	MIGATRONIC COMMANDER 400
Wave form	High frequency TIG	Standard pulsed TIG
I_p -peak current (A)	150	180
I_b -base current (A)	70	45
Interpulse current	50	-
$I_{avarage}$ -Average Current(A)	75	99
t_p -peak time (s)	0.05	0.1
t_b -base time (s)	0.05	0.15
WFS (m/min)	1.6	1.8
Travel speed (mm/s)	3	4.5
Wire diameter	0.9	1.2
Step increment (mm)	1	1.2
Size of the wall in mm (length x height x width)	950 x 180 x 5	Build 2: 925 x 195 x 6 Build 3: 975 x 155 x 6.5
Shielding gas mixture	Torch shielding [75%He+25%Ar @ 15L/min]	Torch shielding [75%He+25%Ar @ 15L/min] + Extra hood shield [100%Ar @ 30L/min]

3.3.4 GMAW deposition technique

An innovative GMAW based solution, namely Cold Metal Transfer (CMT), was also used to investigate lower heat input deposition with higher deposition rates. CMT is a modified GMAW process based on a controlled dip transfer mode [128]. The process gives excellent quality in terms of defects, lower thermal heat input, and nearly spatters free welds. The CMT process overcomes common difficulties encountered during conventional short circuiting GMAW, like unstable process behaviour and severe spatter formation [106]. In CMT-GMAW, the mechanical motion of the wire is directly incorporated into the electrical process control. The reciprocated wire feeding system is synchronized with a high speed digital control that senses the arc length, short circuiting phase and thermal input transferred to the weld [106, 129]. When the wire moves forward and dips in the molten pool the digital control senses the voltage drop and that a short circuiting phase occurs where the current is reduced to a significantly lower level. A

feedback signal returns to the wire feeder in order to reverse the feeding direction. Then the wire back-drawing force assists the liquid bridge fracture and droplet detachment takes place. Metal transfer occurs by surface tension at near zero current. Arc re-ignition is initiated by an initial pulse of current that re-establishes the arc length and pre-melts a considerable amount of the wire volume [128].

3.3.4.1 GMAW wire samples

A constant layer height of approximately 1 mm was maintained until the end of the final deposit. 10 layers were deposited with 1.2 mm diameter wire to produce the final single wall specimen. An automatic robotic welding setup was used with a moving torch, and the walls were built on a base substrate plate of Ti6Al4V alloy of 7 mm thick, at room temperature (20°C), with the parameters shown in Table *3.8*.

Table 3.8: *The process parameters used to produce the Ti6Al4V microstructural sample with the GMAW-CMT process.*

Parameters	**Value**
Technique	MIG-CMT
I_{avg} -Average Current(A)	145.8
V_{avg}- Arc voltage (V)	14.6
WFS (m/min)	8.5
Efficiency	90 %
Travel speed (m/min)	0.567
Wire diameter	1.2
Step increment (mm)	1.2
Number of Layers	10
Shielding gas mixture	50% He+ 50 % Ar @ 15 Litre/min

3.4 EFFECT OF ROLLING ON TIG ARC WIRE DEPOSITION

In order to try to combine deformation with deposition, another experiment was conducted at the Welding Engineering Research Centre, University of Cranfield, UK (RUAM Technology group Project). As shown in the Figure *3.11*, immediately after the deposition of every layer, a roller was used to deform the deposited layer with a predefined load. The idea behind rolling after every layer of deposition was to induce deformation in to the deposited layers to reduce residual stresses (distortion shown in Figure 3.10) and promote recrystallisation of the large β grains during the deposition of subsequent new layers, i.e., rolling introduces deformation, stored energy and potential nucleation sites into the large β grains, thus inducing recrystallisation when layers are reheated during the subsequent deposition of new layers. It was hoped that this might favour the formation of the new fine grains in the final microstructure and improve the mechanical properties. Three samples were produced with 20 layers of deposition; (1) a control sample without rolling, (2) a wall rolled with a 50 kN load, and (3) a wall rolled with a 75 kN load. Table *3.9* shows the process parameters used for rolling deformation investigation. The amount stress could not be estimated directly, since the deformation is not uniform and, the contact area varies between the roll and the build. It is because, the roller used in this process is concave roller and the top surface of deposit is not perfectly flat (convex in shape). Hence, the contact area between the roll and build varies widely.

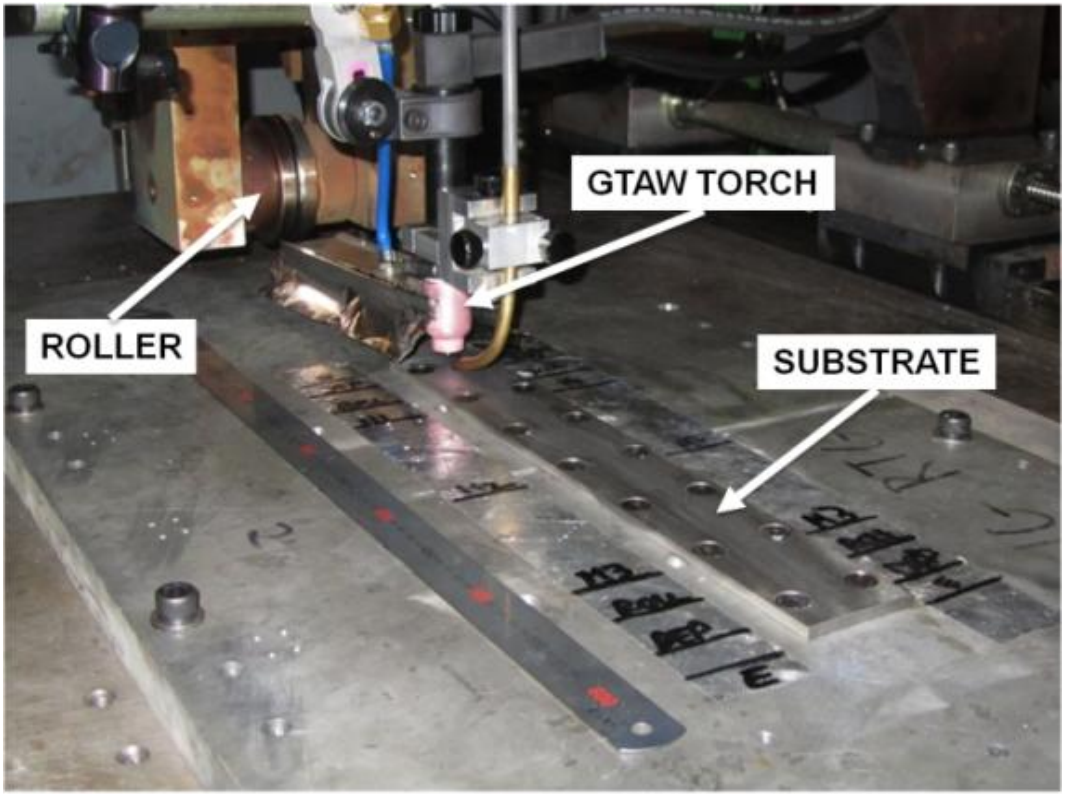

Figure 3.11: *The experimental setup used for wire additive manufacture with a rolling deformation stage at the Welding Engineering Research Centre, University of Cranfield, UK.*

Table 3.9: *Deposition parameters for the rolling investigation.*

Wire feed speed	1.6 m/min
Travel speed	4.5 mm/s
Ip	150 A
Ib	70 A
Pulse duration	110 A
Frequency	0.05 s
Gas flow rate	10 Hz
Trailing shield gas flow rate	20 l/min

3.5 THERMAL MODELLING

A finite difference (FD) code, TS4D, developed by Mackwood and Crafer [130], was used to estimate the solidification conditions found in the AM processes studied. This was achieved by simulating the standard operating parameters with a Gaussian heat distribution function. Full details of the TS4D - FD code can be found in reference [130]. The TS4D is based on a numerical solution of the enthalpy form of the linear heat conduction equation and, it assumes that there is no thermal expansion, distortion, vaporisation, or induced magnetic fields within melt pool, and also assumes constant thermo-physical properties for solid-liquid phases. TS4D modelling was carried out for 3 different AM processes, namely, SLM, EBSM and WAAM. The key process parameters used to simulate these 3 different processes are shown in Table *3.10*. Outputs obtained from the model include temperature contour plots, cooling rates, and the maximum thermal gradient, G_L, and growth rate, R, along the melting point isotherm. The model was applied in steady state conditions to a solid block titanium that was scaled to be much large than the thermal field size.

The material constants used were; the density of ρ =4305.72 (Kg/m^3), and Latent heat of fusion, $\Delta H_{Trans.}$ = 440 (kJ/m^3) [113, 121]. The Solidus (T_S) and liquidus (T_L) temperatures were defined as 1938 K (1665 ˚C) and 1988 K (1715 ˚C), respectively [113]. The laser beam and electric arc efficiency was assumed to be 35 and 80 %, respectively [46, 48, 118]. The sample was not preheated to simulate the room temperature laser and arc + wire deposition techniques, and hence, the room temperature thermal properties (specific capacity, thermal diffusivity and the density) were fed into the model. The model was preheated to the 1013 K (740˚C) build temperature to simulate the same preheating used in the EBSM process. The efficiency (η) of electron beam power absorbed has been reported to vary from 55% to 65% [48, 112] and for the

current EBSM model a value of 65% was assumed. The model was calibrated with the sample provided by the EADS using SLM process. In addition, the model was also calibrated using the results reported by Al-Bermani et al. [92] using EBSM process.

Figure *3.12* show a typical Ti6Al4V substrate block used to run the TS4D model to predict the solidification conditions. In EBSM, modelled block were - 10 to + 50 mm in length (X), -5 to +5 mm in width (Y) and 0 to 5 mm in depth (Z) with a mesh resolution of 0.6 mm, 0.1 mm, and 0.07 mm along x, y and z axis respectively. In SLM, block was - 5 to + 5 mm in length (X), - 2 to + 2 mm in width (Y) and 0 to 3 mm in depth (Z) with a mesh resolution of 0.1 mm, 0.04 mm, and 0.05 mm along x, y and z axis, respectively. In WAAM, the boundary conditions were - 50 to + 75 mm in length (X), - 40 to + 40 mm in width (Y) and 0 to 25 mm in depth (Z) with a mesh resolution of 1.25 mm, 0.8 mm, and 0.4 mm along x, y and z axis, respectively.

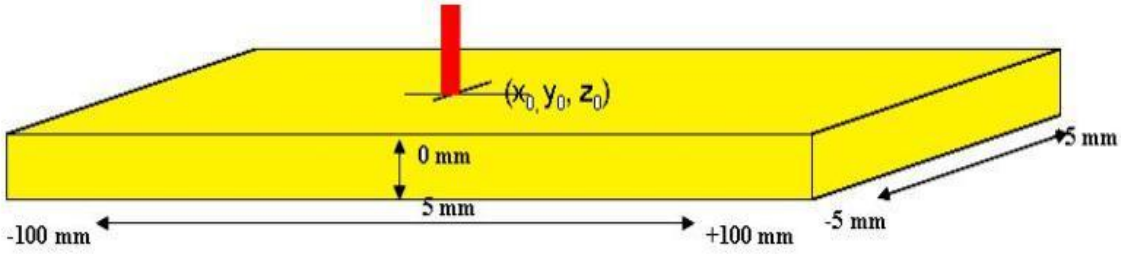

Figure 3.12: *Typical Ti6Al4V substrate block used to run the TS4D model to predict the solidification conditions.*

Table 3.10: *The standard process parameters used to simulate the thermal modelling for three different AM using TS4D.*

Substrate Temp. (K)	Beam Dia. (mm)	Travelling speed (m/min)	Density (Kg/m^3)	Specific heat capacity (J/Kg/K)	Conductivity (W/m/K)	Thermal efficiency (%)
EBSM						
1013	0.5	30	4305.7	678.5	19.5	65
SLM						
300	0.2	75	4430.0	526.3	6.7	35
GTAW + wire AM						
300	6	0.25	4430.0	526.3	6.7	80

3.6 CHARACTERIZATION OF MICROSTRUCTURE, TEXTURE AND FRACTOGRAPHY

The electron beam deposited samples were removed from their substrates and sectioned in the transverse Rx-Nz and the Normal Rx-Ry planes. Rx, Ry and Nz are the co-ordinate axis used for the specimens, as shown in the Figure *3.6*, where Nz is the build direction and Rx-Ry are the two orthogonal sample directions. These also coincided with the main hatching directions of the beam path in powder bed processing and Rx was aligned with the torch travel direction for the arc processes. Macro- and microstructure analysis was carried out by optical microscopy and, SEM (Scanning Electron Microscopy) in both the SE and BSE mode.

3.6.1 Optical microscopy

Optical microscopy was used to analyse the macro and microstructure of the as-deposited specimens. A *Zeiss Axiophot* equipped with an *Olympus* camera was used to investigate the unetched and etched microstructures. Mirror-smooth specimens for metallographic studies were prepared by first grinding with SiC abrasive papers at 150 rpm, for 1 to 2 minute, at each stage. The following grinding papers were used: 180 → 320 → 600 → 1200 → 2500 → 4000. For the polishing stages, the samples were polished with 6, 3 and 1 µm diamond solution for 10 minutes with an applied load of 10 N followed by polishing with OPS solution for 20 minutes. Subsequently, the samples are cleaned with ethanol and then dried in hot air. A solution of 2.5 Vol.% HF + 5 Vol.% HNO_3+ 92.5 Vol.% H_2O was used as etchant for optical microscopic studies.

3.6.2 Scanning electron microscopy

The samples used for optical microscopy were further examined with the help of a scanning electron microscope (SEM) to reveal fine microstructural and fractography details and to do EDX analyses if necessary. Both secondary electron (SE) and back-scattered electron (BSE) imaging modes were used to yield topographic and compositional information about the specimen. Scanning electron microscope analysis was carried out using *FEG-SEM Philips XL30 and Sirion FEI* with an accelerating voltage of 20kV–25kV and a working distance of 10 mm-15 mm. For the EDX analysis a *Phillips XL 30 FEG* equipped with an *EDAX* unit was used. In addition, to the regular optical metallographic procedure, samples for SEM were prepared with extra 2 hrs of Vibromat polishing using colloidal silica (as a media), for SEM analysis.

3.6.3 EBSD analysis

For EBSD analysis, un-etched samples were additionally polished using a Vibromat for 2 hrs before examination under FEG-SEM made by Sirion FEI or Phillips XL 30 or CamScan. Electron backscattered diffraction (EBSD) maps were performed both over a large area of (3x3 mm^2 or 10x15 mm^2 or 20x15 mm^2) with 10 µm as the step size to obtain the macro texture, and on a fine scale (200x200 μm^2) with small step size of about 0.15 µm to obtain microtexture and high resolution microstructural information. EBSD is carried out on highly tilted crystalline samples (generally at 70˚) as shown in Figure *3.13*(a-b). The specimen is illuminated with a stationary focused primary electron beam. The backscattered electrons are captured on a phosphor screen, positioned close to the sample and then recorded by a highly light sensitive camera. The camera images are transferred to a computer where the orientation and crystallographic phases [73, 131] of the irradiated crystal were automatically determined by an HKL-EBSD system operating Channel5 software [70].

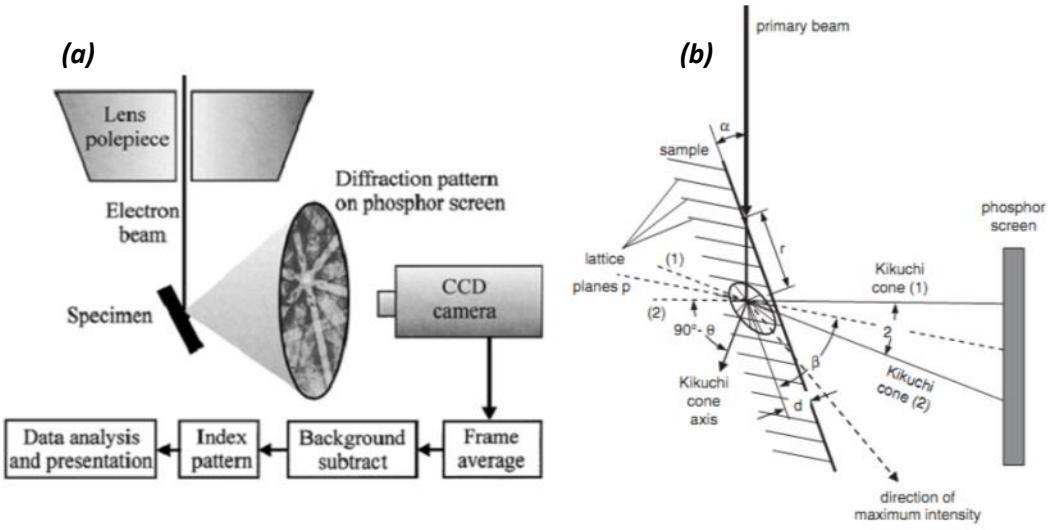

Figure 3.13: *(a) The experimental set up for EBSD inside the FEGSEM [70] and (b) Schematic representation of formation of backscatter Kikuchi lines [71, 131].*

In EBSD, the primary beam enters the sample at an angle of, α as shown in Figure *3.13*. It travels a distance r/cosα inside the material until it reaches a maximum depth, d, below the surface; r indicates the approximate spatial resolution of the technique. The primary electrons are incoherently scattered with an intensity distribution indicated by the ellipse. The incoherently scattered electrons are subsequently coherently scattered by the lattice plane, p, into pairs of Kikuchi cones (1) and (2) with an opening angle 2*(90°- θ) (θ: Bragg angle) around the cone axis. The cones leave the surface at an angle β. The path length which the electrons undergo for coherent scattering is t=d/sinβ. For β=α (angle between the sample and primary beam**)**, a

maximum electron intensity is obtained on the screen of Kikuchi pattern with the pair of lines for EBSD set of planes [70, 71, 73, 131].

The following are definitions used in the interpretation of Texture from the EBSD data;

Band contrast: Band contrast maps are grey scale images, which give a measure of the pattern quality for all the points in a map. A lighter shade of grey indicates a higher band contrast value and hence better EBSP quality (Figure 3.14a). All points have a band contrast value even if they have not been successfully indexed. The band contrast is influenced by a number of factors, including local crystalline perfection, grain boundary, sample preparation, surface contamination and the phase and orientation being analysed. The band contrast map often resembles an etched micrograph, revealing features such as grains, grain boundaries and surface scratches where poor indexing occurs.

Inverse pole figure (IPF) colouring: IPF represents the intensity of orientation with respect to a single axis; can also be used to depict other types of texture symmetry. IPF colouring scheme enables crystallographic orientations to be quickly interpreted with respect to the specimen coordinate system (Figure 3.14b).

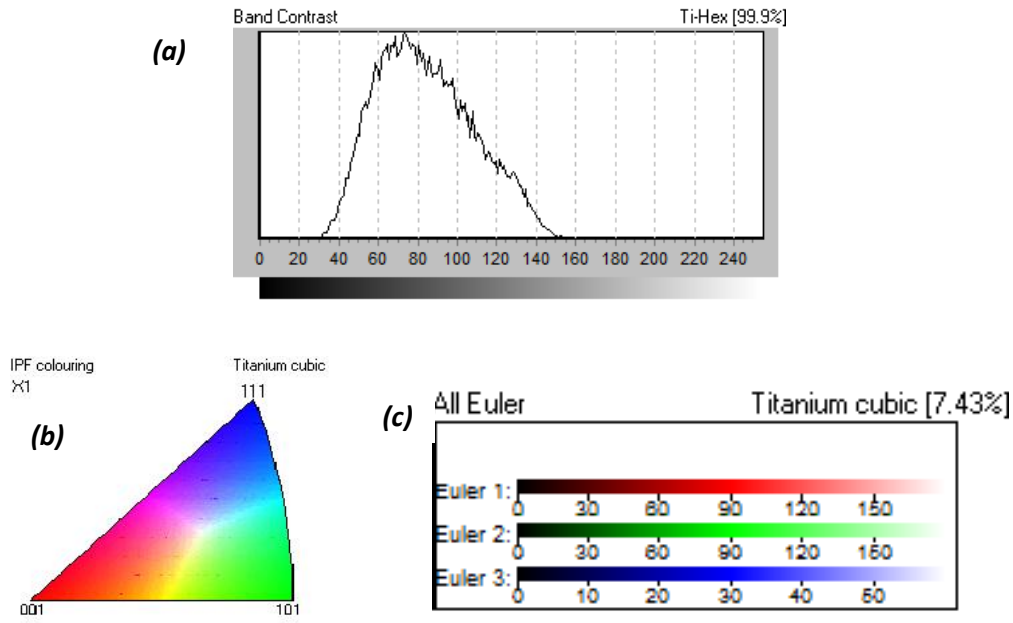

Figure 3.14: Shows the representation of quality of band contrast map (a), IPF colour key with orientation (b), and Euler map colour key with Euler 1, 2 and 3 (c) using Channel 5 software [70].

Euler map: Euler map are used to define the orientation of the grain with respect to the specimen geometry by the rotation using three Euler angles ϕ1, ϕ and ϕ2 (Figure 3.14c). Unlike IPF

colouring, this colouring scheme displays a unique colour for each crystallographic orientation referred to in rolling geometry. However, the crystallographic orientations cannot be interpreted as easily from the colours.

Misorientation map: This colouring scheme colours the points based on the misorientation with neighbouring points according to a user defined colour scheme. Misorientations between 2° and 15°, and greater than 15°, can be represented in different colours in the map. This type of map is useful for displaying grain boundaries based on the misorientation angle.

Kuwahara filter: It is used as noise-reduction filter that preserves edges of the grains with a smoothing angle of 5˚ (considering 1˚ misorientation as artefacts angle) [70].

3.6.4 β - Grain reconstruction

As pointed out in 1.1.1 (literature review), titanium exhibits an allotropic transformation at 882˚C (for pure Ti). When the alloy is cooled from the high temperature β phase to room temperature, each β-bcc grain transforms to room temperature α-hcp platelets of 12 different possible orientations (variants) with respect to the parent β-grain. In general, the transformation of β→α obeys the Burgers orientation relationship of $(110)_\beta//(0002)_\alpha$ and $[111]_\beta//[11\bar{2}0]_\alpha$. Theoretically, 12 possible variants, or orientations, can be found during the β → α transformation, according to the Burgers relationship, due to the symmetry of both phases. Inversely, the individual orientations of the room temperature α-platelets inherited from β grain can be used to calculate the most probable high temperature parent β-grain orientation. There are 6 possible variants during an α → β transformation, according to the Burgers relationship [5, 52-54, 132, 133].

Based on the above, a computer programme has been written by Wynne et al., at IMMPETUS (Institute for Microstructural and Mechanical Process Engineering: The University of Sheffield) to automatically reconstruct the high temperature β phase from room temperature α EBSD data [134, 135]. This programme automatically reconstructs the high temperature EBSD map of a parent β-grain from the 6 possible variants of β, during the α → β transformation from the room temperature α. Each variant is reconstructed individually using the misorientation with its adjacent variants. Firstly, the EBSD orientation data file for the α room temperature phase is cleaned to remove unindexed points. An algorithm is then used which calculates all the possible β orientations, by applying the Burger's relationship to each data point. From this data the most probable β orientation is obtained for each α variant using a minimum misorientation cut-off of ~3°. To do this, the average orientation of each variant is calculated first to give a set of 6 possible parent β orientations ($G_1^\beta, G_2^\beta, G_3^\beta, G_4^\beta, G_5^\beta$ & G_6^β). These 6 orientations act as the reference set, against which the solutions derived from the misorientation analysis can be compared, using the

misorientation analysis proposed by Humbert et al. [68, 136-140]. This gives between 1 to 3 potential solutions for each pair of points. However, in reality, for most misorientations there is only one solution for the parent orientation. Each time a solution from an analysed misorientation is close to one of the 6 orientations in the reference set, a coincidence number for the reference orientation is incremented by 1. For each variant, the reference orientation with the highest coincidence number is selected as the correct solution and by repeatedly doing this the high temperature parent β-grain EBSD map can be reconstructed. Misorientations across boundaries that do not coincide with a recognised variant misorientation are assigned to be β-grain boundaries (Variant misorientations of more than 4° during the reconstruction are recognised and assigned as separate prior-β grain boundaries [76, 132, 141]).

Texture data was extracted from the original measured α, and reconstructed β, EBSD orientation maps and presented in standard pole figures. The non-spatially correlated random α transformation texture was also calculated from the spatially correlated, reconstructed, β-phase EBSD data, using code developed by Bate [53, 142], by assuming a random distribution of habit variants. These calculated results were then compared to the α-texture measured by EBSD. In all the orientation maps presented, unless otherwise stated, inverse pole figure orientation contrast will be used with respect to the build direction (N_Z) and high angle boundaries (HAGBs) >15° are depicted by black lines.

3.7 MECHANICAL TESTING

Fatigue and tensile tests performed on the AM deposits were conducted at Westmoreland Mechanical Testing and Research, Ltd, UK as a part of AVLAM (Added-Value Layer Additive Manufacturing) Project Collaboration between EADS-UK, Bombardier Aerospace-Northern Ireland, and TWI-UK. The fractured specimens were sent to Manchester for further analysis to correlate the mechanical properties, to their microstructure and fractography.

3.7.1 Tensile testing

When a tensile load is applied to a material the degree of deformation depends on the applied stress. At lower loads, the stress (σ) is directly proportional to the strain (ε) and, the deformation is said to be elastic, obeying Hook's Law. The proportionality constant between (σ) and (ε) is called as Young's modulus (E) which is a direct indication of how stiff a material is. After a critical stress level, the material starts to deform plastically. The stress level at which this transition from elastic to plastic deformation occurs is called the yield stress (σ_y).The maximum tensile stress a

material can withstand before fracture is called its ultimate tensile strength (UTS) and ductility quantifies the amount of plastic deformation that has sustained before fracture .

(1) **EBSM tensile samples:** Cylindrical tensile specimens according to ASTM E8/E8M or EN 10002-1/2002-1 standard were prepared. The first and second test speed during tensile testing was about 0.005/min and 0.05/min respectively. As shown in the Figure *3.15*, three sets of samples from each location were produced to analyse the tensile properties of the EBSM Ti6Al4V builds. Figure *3.16* shows the dimensions of the samples prepared for tensile testing according to ASTM E8. The notations used are, BL - Back Left Corner of build chamber, BR - Back Right Corner, FL - Front Left Corner, FR - Front Right Corner and, C -Centre in the build chamber as shown in the Figure *3.15*. Whereas, X - represents coupon extracted in X-direction (powder re-coating direction - left/right axis of build chamber), Y- represents coupon extracted in Y-direction (powder transverse to re-coater – front / back axis of build chamber), and Z-represents coupon extracted in Z-direction through layer thickness direction, vertical axis of build chamber.

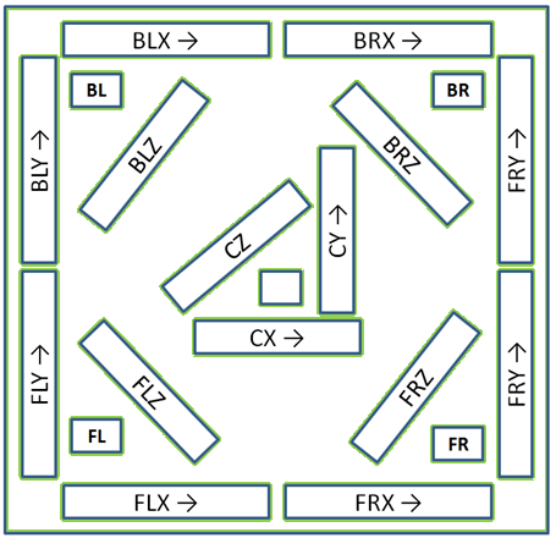

Figure 3.15: *The build layout of tensile and fatigue test samples manufactured in EBSM machine.*

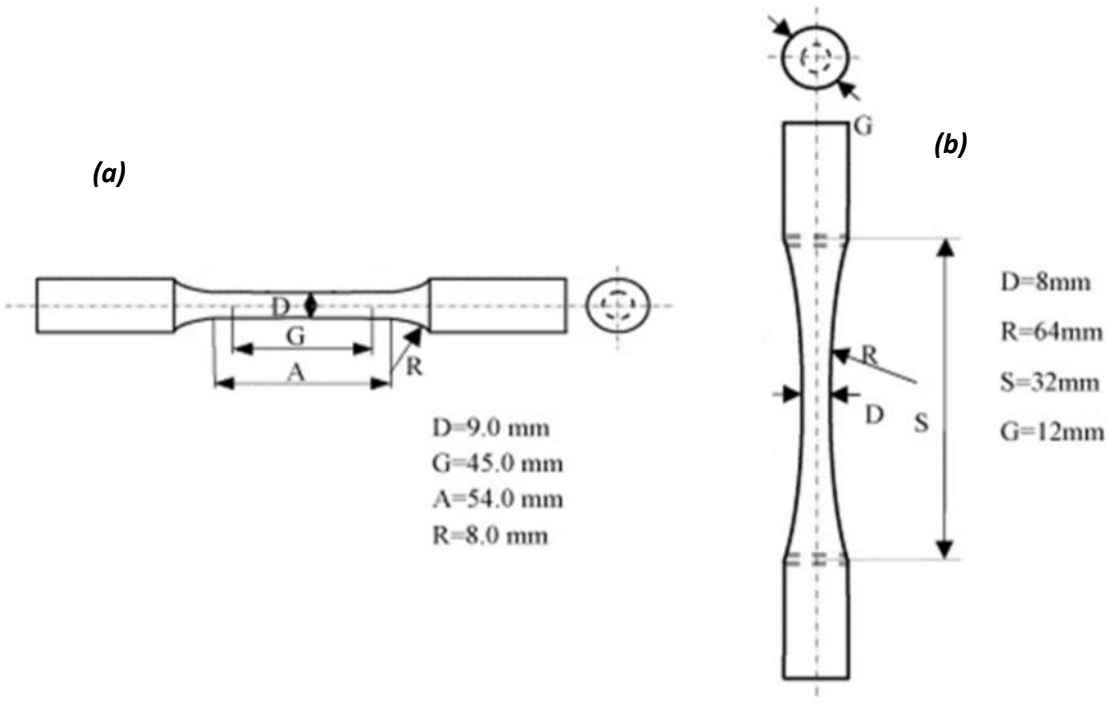

Figure 3.16: *Specimen dimensions for (a) tensile test (ASTM E8M) and (b) fatigue test (ASTM E466) performed on the EBSM builds.*

(2) **SLM tensile samples:** Samples for this build platform were not tested in this project.

(3) **TIG-Arc tensile samples:** The location of the specimen taken from large walls taken for tensile testing from the Arc welded deposits are shown in Figure 3.10. The Tensile specimens parallel and perpendicular to the build direction were extracted according to the requirements of EN 2002-001. The tensile specimens have a dog-bone shape with a gauge length of 75 mm and a 12.5×2.5 mm^2 cross-sectional area as shown in Figure *3.17*. Three control specimens were extracted from Ti6Al4V Bar (MIL-T 9047) and tested to provide a baseline comparison. Eighteen tensile specimens were tested; twelve in the vertical and six in horizontal directions were cut from the builds 1 and 2 with the process parameters shown in Table *3.7*.

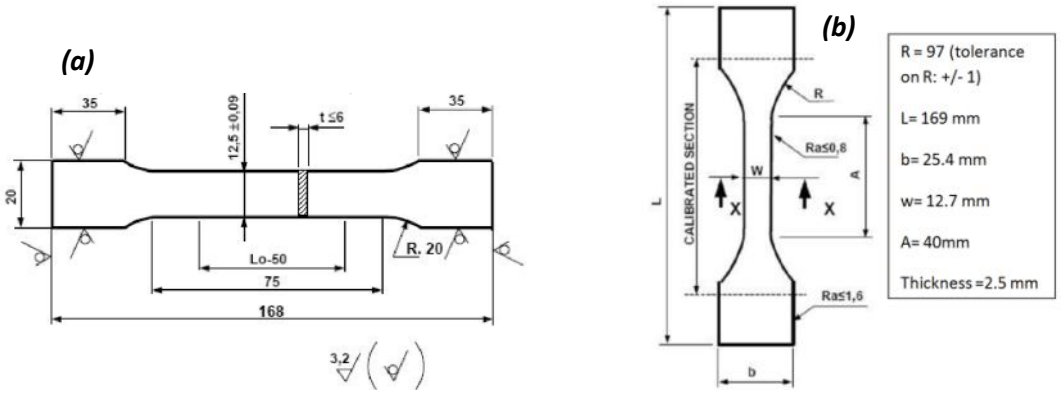

Figure 3.17: *Specimen dimensions for (a) tensile test and (b) fatigue tests performed on the arc wall deposits.*

3.7.2 Fatigue testing

When a material fails when subjected to a repeating, or fluctuating, stress over a period of time, even at load well below its yield strength, then a fatigue failure is said to have occurred. The degree of resistance to this type of failure refers to the fatigue strength of the material. In order to determine the high cycle fatigue life of the AM deposits the following tests were performed;

(1) **EBSM fatigue samples:** As shown in the Figure *3.15*, three sets of samples from each location were produced to analyse the fatigue properties of the EBSM Ti6Al4V builds. Figure *3.16*b shows the dimensions of the samples prepared for fatigue testing according to ASTM E466. The notations used are same as that of the tensile specimens. All the fatigue specimens were tested at ambient temperature with a maximum load of 600MPa, R=0.1 and sinusoidal wave form at 30Hz frequency. The test was stopped after 3,000,000 cycles.

(2) **SLM fatigue samples:** Samples for this build platform were not tested in this project as this work already has been done elsewhere.

(3) **TIG-Arc fatigue samples:** The locations of the specimens taken for fatigue testing, from the arc deposits, are shown in Figure 3.10. Figure *3.17* shows the dimensions of the samples prepared for fatigue testing, which had a thickness of about 2.5 mm. From build 1, 12 samples were tested with 6 numbers in vertical and 6 numbers in the horizontal direction of the same build. From build 2 and 3, Twenty-four fatigue specimens were tested with 14 numbers in vertical (build 2) and 10 numbe rs in horizontal (build 3) direction respectively according to EN6072 standard. Five control specimens (parent) were machined from Ti6Al4V rectangular bar (MIL-T 9047) and tested as a baseline comparison. These fatigue specimens are in the dog-bone shape with a gauge length of 40mm and a cross-sectional area of 12.7×2.5mm^2. All

the fatigue specimens were tested at a maximum load of 600MPa, R=0.1 and sinusoidal wave form at 30Hz frequency. The test was stopped after 10,000,000 cycles. Five baseline specimens were also tested under the same conditions for comparison.

3.7.3 Vickers micro-hardness tests

Hardness is a measure of a materials resistance to localized plastic deformation by a standard shaped indenter. The hardness distribution in the as deposited materials was examined using a Vickers *CSM micro indentation hardness* testing machine (CSM machine Indentation 4.03).

RESULTS AND DISCUSSION

4 THERMAL MODELLING AND MICROSTRUCTURE EVOLUTION DURING AM

4.1 INTRODUCTION

The microstructural factors which affect the mechanical properties of α+β Ti alloy like Ti6Al4V include the prior β-grain size, α-colony size, thickness of the grain boundary α and lamellar α, the size and shape of the primary α-grains, the volume fraction of α and β, and the presence of diffusionless transformation products such as martensite (α'). It is therefore important to study the evolution of microstructure during AM of Ti6Al4V alloy. In particular, in the context of solidification during AM, the size and texture of the primary β-grains strongly influences the texture in the finished product. For example, a large strongly textured β grain structure can lead to large α texture colonies, that are known to be very detrimental to fatigue life [38]. Hence, it is important to study the evolution of the β-grain structure and associated texture produced in AM as well as how this affects the transformation structure and α texture. Before going into more detail, on the evolution of the transformation structures and β-grain structures and textures seen in the AM products, it is important to first understand the solidification conditions that control the primary β grain structure and texture formed during production of AM components with this standard Ti alloy.

This chapter is aimed at comparing the general solidification conditions and typical microstructures and textures seen in AM across the three build platforms investigated. The chapter will first focus on predicting the solidification condition present in the AM processes studied. This was achieved by using a simplified finite difference model to estimate the solidification conditions expected in bulk sections for the three different AM (SLM, EBSM and WAAM) processes, under the standard operating conditions, shown in Table *4.1* and Table *4.2*. The chapter then focuses on comparing the evolution of the general microstructure, (including bulk β -grain structure) seen in the bulk deposits for all the three AM methods. The general texture evolution in the β-grains and, the related α transformation texture in each process will also be discussed. Finally, the chapter will finish by comparing the α-transformation microstructure seen in all three processes. Variation in the microstructure and texture with

geometry and non steady state conditions are also important but will be discussed in chapter 5. The microstructure and textures described will be from the centre of thick sections where steady state conditions have been established. In the case of the SLM and EBSM powder bed processes, this is from the centre of the thick sections, where the beam rastering is employed, and in the case of the WAAM process it is from the centre of a wall deposited by a single weld pass.

4.2 THERMAL MODELLING

4.2.1 Introduction

To better understand the solidification behaviour, seen in the 3 AM processes, a TS4D finite difference code programme was used to predict the solidification conditions, as described in section 3.5. The primary solidification parameters that control the morphology and scale of the solidified microstructure are the crystal growth rate and thermal gradient in the liquid at the solidification front [42-44]. As discussed in the literature review (in section 1.1) these parameter vary with position around the melt pool surface, as well as with the process parameters, and were the primary outputs determined from the model. The modelling results reported for the three different processes (namely, EBSM, SLM, and WAAM techniques) were obtained with the standard operating process parameters, shown in Table *4.1* and Table *4.2*, under steady state conditions (see Table *3.3* to Table *3.5*). Efficiency factors of 65 %, 35 % and 80 % were used for the e-beam, lasers and electric arc, respectively, with a circular Gaussian heat distribution function [44, 46, 112, 121]. These efficiency factors were observed by fitting the melt pool profile to measured data, where known [34, 48, 112, 121].

With the e-beam Arcam machine, a beam current of 10 mA was used to replicate the hatching stage, giving a nominal power of 600 W, and a travel speed of 0.5 m s^{-1}. The model was preheated to the 1013 K (740˚C) build temperature to simulate the actual preheating used in the EBSM process. For the laser beam process a power of 60 W was used and, for the arc process a power of 240 W was calculated from the voltage and current (see Table *3.10*). For the laser and wire arc deposition techniques, the metal block modelled was assumed to be at room temperature, since these techniques operate with no preheating. It should be noted that a source of error in the powder bed models arises because the base substrate was assumed to be fully solid and, the model did not take into consideration the fact that, when powder is first spread over the bed, it is loosely packed, leading to a lower bulk density, and reduced heat conductivity.

Table 4.1: *Standard settings used to produce the Ti6Al4V samples with the powder bed Arcam-EBSM and EOS-SLM machines.*

Arcam –EBSM machine	
Accelerating voltage	60 kV
Layer thickness	100 µm
Contour theme condition	Beam current, I : 5 - 8 mA, T.S : 0.15 - 0.3 m/s
Hatching theme condition	Beam current, I : 6 - 15mA, T.S : 0.5 – 1.0 m/s
Beam offset thickness	0.24 mm
Build temperature	740 ˚C
EOS-SLM machine	
Power	170 W
Powder Bed Layer thickness	30 µm
Scan Speed	1250 mm/s
Beam diameter	0.2 mm
Hatch space	0.1 mm

Table 4.2: *Standard preheating parameters used to produce the WAAM samples with the interpulse power source.*

Condition	TS (m/min)	WFS (m/min)	V(v)	Current (A)	Heat I/P (kJ/m)	Feed rate WFS/TS(m/m)
Pulsed GTAW	0.25	1.6	12	I_p : 150, I_b : 45, I_{av} : 90	300	6.67

4.2.2 Calibration

The models were used to give an approximate prediction of the solidification conditions, in order to provide a framework for discussing the microstructure developed in the AM deposits. Unfortunately, calibration samples were not provided by EADS Innovation works during this project. However, in Figure *4.1*a-b, the predictions from TS4D are compared to results reported for bead on plate experiments by Al-Bermani et al. [112] for the EBSM process using the same Arcam machine, with the same standard operating parameters. A very good fit to the melt pool shape can be seen with the efficiency factor employed. The SLM process is a very similar to EBSM and only differs by the smaller spot size, powder layer height, and lower substrate temperature and efficiency factor. Figure *4.1*c-d, shows an example comparison, between the size of an actual

melt pool at the base of the Ti6Al4V build that was produced using SLM compared melt pool that was predicted using the TS4D model. It can be seen that the efficiency factor adopted in this case also gave the right melt pool depth and width. However, the result obtained from this model was not validated sufficiently against the measurements using thermocouple or thermal imaging experiments or changes in hardness values from weld bead to substrate via HAZ.

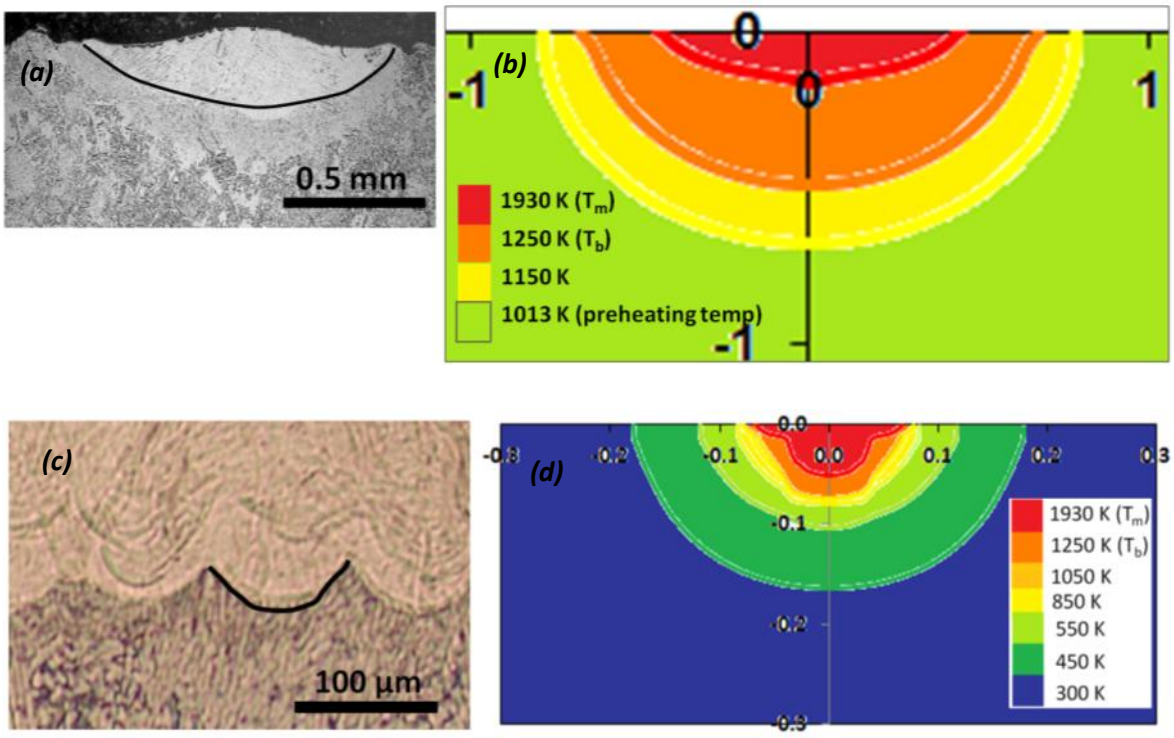

Figure 4.1: *Shows (a) the melt pool depth reported in bead on plate experiments by Al-Bermani et al. [112], and (b) the predicted results from TS4D model for the single contour-pass using EBSM technique in Ti6Al4V alloy for the standard operating conditions. In (c) and (d) an experimental sample showing the base of a SLM build is compared to predicted results from the TS4D model for the same standard operating conditions.*

The TS4D model was also used to try to give the approximate solidification conditions found with the wire + arc AM technique for the standard operating parameters (Table *4.2*). Although in this case the approximations increase, because this model is not specifically designed to simulate arc welding processes where there is a large volume of filler wire and there is an additional convective heat loss by the shielding gas. However, the model was still used to allow a 'ball park' comparison with the other techniques. For this process the efficiency factor was adjusted to give the correct melt pool width, as provided by Cranfied University for standard operating conditions. The approximate efficiency used of 80 % is quite high compared to that normally found in GMAW welding [44, 46] and reflects the high rate of filler addition.

4.2.3 Predicted melt pool shapes and sizes in AM using TS4D

Figure *4.2* to Figure *4.4* show temperature isotherms predicted in transverse (along Y-Z), top view (along X-Y), and longitudinal cross-sections side views (along X-Z), from the TS4D model, for the three different processes, under standard operating parameters in steady-state conditions. The red and orange colour fields depict the liquidus and β-transus isotherms. The figures could not be shown at the same scale for the three different processes, since the sizes of the melt pools were very different. However, Table *4.3* provides a quantitative comparison of the predicted size and shape of the melt pools for the three different AM processes.

In SLM, the melt pool is predicted to have a 'tear drop' shape with a smaller size of about 0.1 mm wide and 1 mm long (see Figure *4.3*), owing to the high raster speed and poor thermal conductivity of titanium [44]. The calculated depth of about 60 µm is approximately two layer thickness in the SLM deposits, since the depth of a single powder layer is about 30 micron thick and, its shape and depth agrees with other predictions for similar operating conditions (e.g. [98, 121]). In EBSM, the melt pool also has a 'tear drop' shape and was elongated with an approximate melt pool size of around 1 mm wide and 4 mm long (see Figure *4.3*). The calculated depth was ~ 0.2 mm (see Figure *4.2*), which is again approximately two deposited layers deep (a single layer thickness is 100 µm), and is used in the Arcam machine to ensure full remelting of the previous deposited layer. As can be seen in Figure *4.1*, in this case the model could be calibrated against the bead on plate melt tracks produced by Al-Bermani et al. [112] which gave very good agreement. It can be noted that the size of the melt pool is smaller for SLM when compare to EBSM. This smaller melt pool size is due to the smaller spot size and lower power input with this process. However, it is also affected by the lower substrate temperature, since SLM is a cold powder bed deposition technique, i.e., the powder deposition and fusion takes place with the substrate at room temperature. In comparison, the arc AM process was predicted to have a much lower aspect ratio elliptical melt pool shape, with a far larger size of about 4 mm wide and 5 mm length as shown in Figure *4.3*. The depth of the melt pool in arc AM process was modelled to be only about 0.5 mm. The actual depth of melt volume may vary from this, since wire is externally fed in to the melt pool during the process. However, the results are shown here for the comparison purposes and to illustrate the wide variation in the solidification conditions between the three processes.

Although, the efficiency factor (η) was not accurately known for the laser or EBSM processes, and the model was not partitioned to take into account the lower conductivity of the surface layer of

loosely-packed powder, the predictions gave good agreement to those of other workers for both the EBSM and SLM [112, 121] and are sufficient to provide reliable estimates of the solidification conditions. For example, in the SLM process, Verhaeghe et al. [98, 121] reported that the size of the melt pool, for 60 W power, was 60 µm deep and, 110 µm wide which is in good agreement with the results predicted here using TS4D with the same operating conditions. Whereas, In EBSM, the predicted size of melt pool of ~ 100 µm depth and 4.2 mm in length is almost equal to the values of a 100 µm by 5 mm, reported by Al-Bermani et al. [112] for the EBSM process**.** In case of the arc process, modelling gave a melt pool width and aspect ratio consistent with experimental observation [143], and this third process was more crudely modelled to provide a relative 'ball park' comparison with the other two powder bed systems.

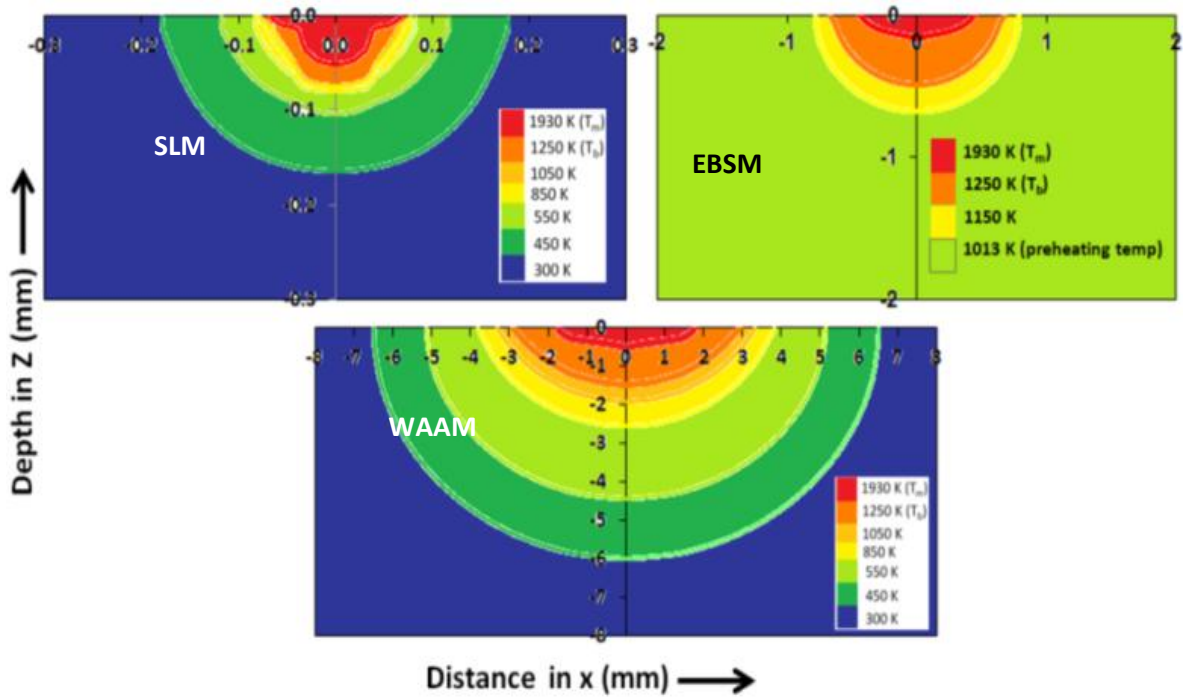

Figure 4.2: *Temperature isotherms predicted in transverse cross-sections in the R_y-N_z plane using the TS4D thermal model for the three different AM processes, at steady state conditions, using standard process parameters (note the different scales).*

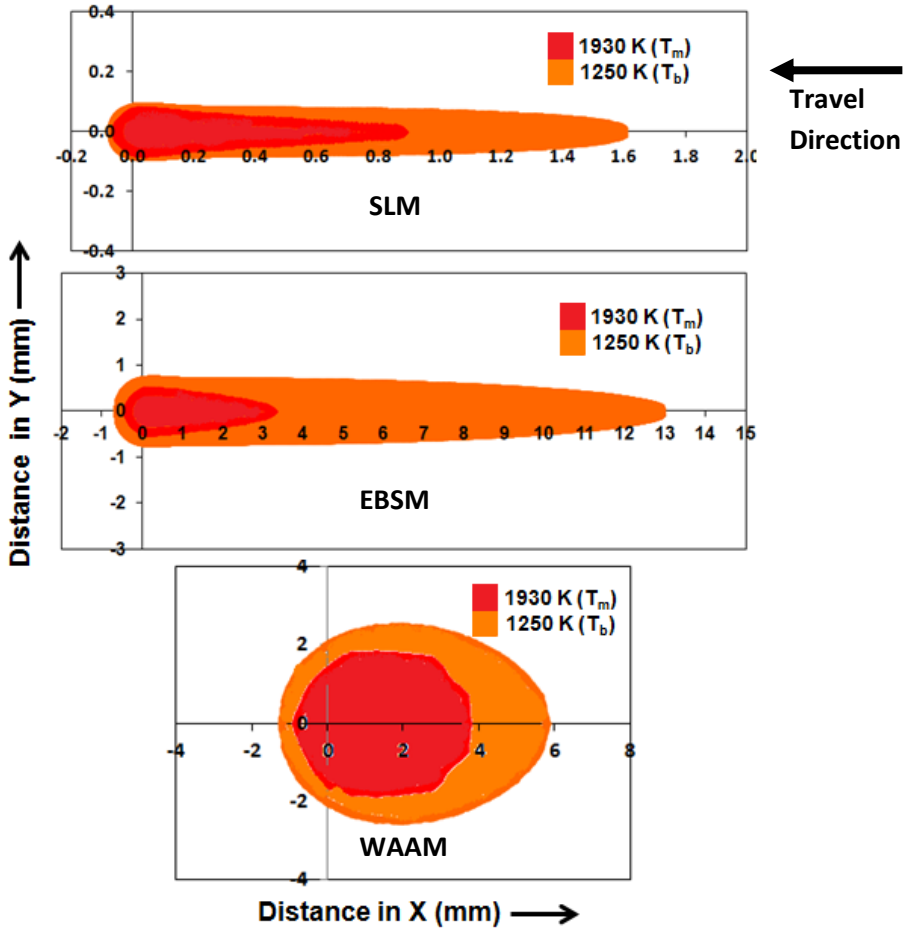

Figure 4.3: *Melting and β transus temperature isotherms predicted in the top view along the R_x-R_y plane using the TS4D thermal model for the three different AM processes at steady state using standard process conditions.*

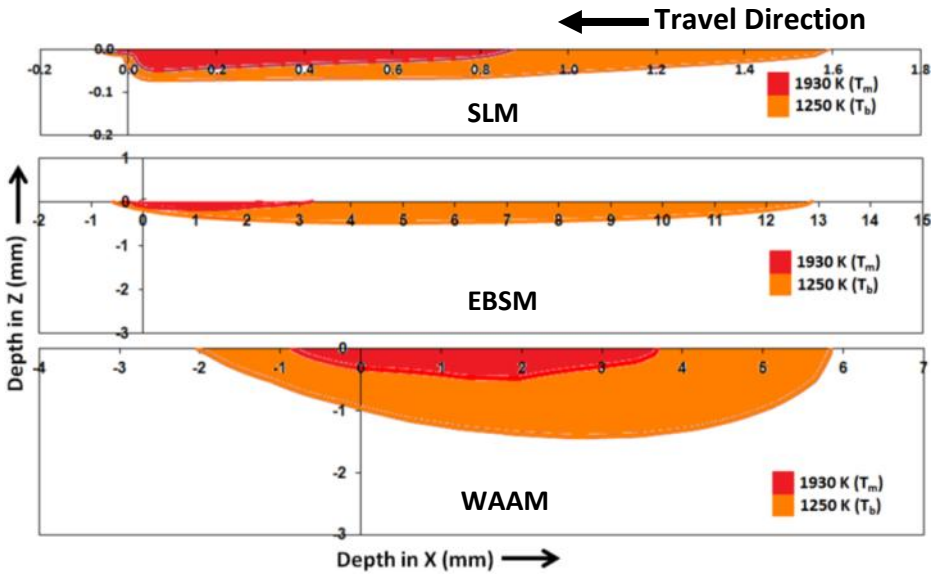

Figure 4.4: *Melting and β transus temperature isotherms predicted along the melt pool centre line in longitudinal cross-sections in Rx-Nz, using the TS4D thermal model for the three different AM processes at steady state using standard process conditions (note the different scales).*

Table 4.3: *Predicted steady state melt pool size and shape for the three different AM processes using TS4D, under standard operating parameters.*

Substrate temp (K)	T.S (m/min)	Size of the melt pool			Shape of the melt pool	Remelting depth
		Length (mm)	Width (mm)	Depth (μm)		
SLM						
300	75	0.98	0.12	58	Tiny tear-drop	~2 layers
EBSM						
1013	30	4.16	1.0	171	Elongated tear-drop	~ 2 layers
WAAM						
300	0.3	4.89	3.88	530	Large elliptical	-

4.2.4 Predicted solidification conditions in AM

In Figure *4.5* the thermal gradient, G_L, and growth rate, R, predicted at the melting point isotherm are plotted along the melt pool centreline, parallel to the raster direction (i.e. in the Rx-Nz symmetry plane) on the solidification diagram for Ti6Al4V presented by Kobryn and Semiatin [29]. Similar plots have also been calculated by Al-Bermani et al. [112] and Bontha et al. [48] for the EBSM and SLM, respectively, and can be compared in Figure *2.53* and Figure *2.54*.

In the SLM and EBSM power-beam processes, the thermal gradient in the liquid at the solidification front, G_L, can be seen to be very high (*Table 4.4*). The SLM process exhibits the highest thermal gradient, which is in the range 0.67-2.34 x 10^4 K cm^{-1}, decreasing to the rear of the melt pool. A similar range of thermal gradient of 1.5 to 2.5 x 10^4 K cm^{-1} has been estimated for the laser process by Bontha et al., using the 3D Rosenthal model [48] as shown in Figure *2.54* (for a power input of 350 W and travel speed of 9 mm/s). The growth rate R is closely related to the laser beam travel speed of 1.25 ms^{-1} [44], and along the centreline accelerates from zero at the base of the melt pool to a maximum of 1.25 ms^{-1} at the rear surface as solidification progresses.

In comparison in the EBSM process, the thermal gradient in the liquid at the solidification front, G_L, is in the range 0.32-0.66 x 10^4 K cm^{-1}, again decreasing to the rear of the melt pool. This range is lower than the thermal gradients (0.51 to 5.2 x 10^4 K cm^{-1}) reported Al-Bermani et al. [112] for the same power input of 600 W with a range of melting currents from 6 mA to 12 mA using EBSM

process. However, it should be noted that Al-Bermani et al. [112] used the simplified Rosenthal analytical model (shown in equation 18) and, calculated the thermal gradient at the S/L interface along the melt pool depth (in the R_y-N_z plane), instead of calculating it along the temperature isotherm in the R_x-N_z plane of the tear drop shaped elongated S/L interface of the melt pool.

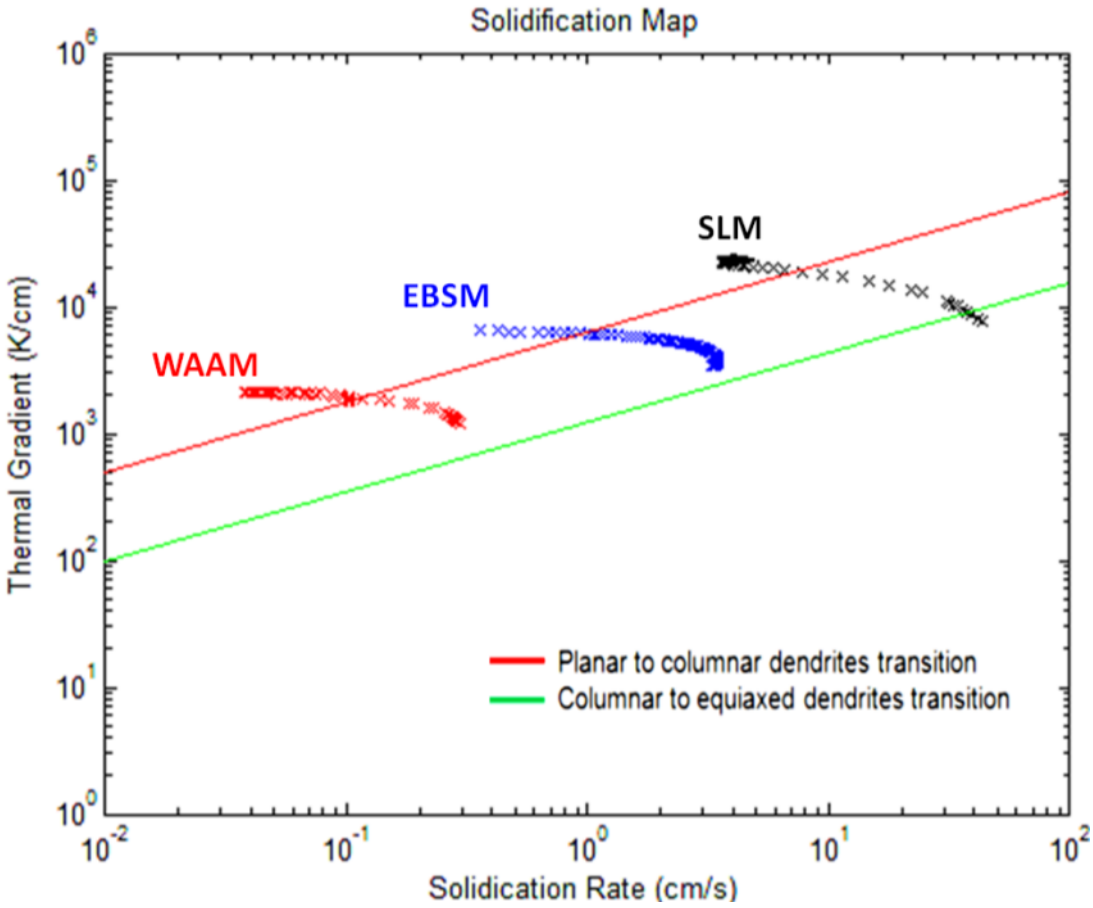

Figure 4.5: *Predicted thermal gradients (G_L) and growth rates (R) along the melt pool centre line in the Rx-Nz plane for the three different AM processes plotted on the solidification diagram for Ti6Al4V alloy proposed by Kobryn and Semiatin [29].*

Finally, for the Arc AM process a much lower thermal gradient of 0.15-0.22 x 10^4 K cm^{-1} was predicted. In addition, lower solidification rates of ~0.25 m/min were estimated at the rear of the melt pool. However, it should be noted that the predictions for the WAAM process must be considered to be the least reliable, because the addition of the filler material could not be taken into account. Nevertheless, it can be summarised that the SLM process provides by far the highest thermal gradient and solidification rate, owing to its small melt pool size and high travel speed, and these important parameters reduce greatly in order from the EBSM to the WAAM process.

Table 4.4: *Summary of the solidification conditions predicted for the three different AM processes with the Ti6Al4V alloy.*

Thermal gradient, G x 10^4 (K cm^{-1})			**Max. Solidification rate , R (m s^{-1})**			**Cooling rate, G*R x 10^5 (K s^{-1})**			**Min. G/R x 10^9 (K s m^{-2})**		
SLM	EBSM	WAAM	SLM	EBSM	WAAM	SLM	EBSM	WAAM	SLM	EBSM	WAAM
0.67-2.34	0.32 - 0.66	0.15-0.22	1.25	0.5	0.25	0.73-8.37	0.02-3.20	0.0009-0.375	0.08	0.22	0.73

The ratio of thermal gradient to growth rate (G_L/R) is an important quantity which dictates the level of constitutional supercooling and the associated instability of a planar front that results in formation of a cellular or dendritic structure [44]. The consitutional supercooling criteria (Equation 16) determines, whether columnar or cellular or dendritic growth will occur for a given set of solidification conditions. It has been reported by Rai et al. [144] and Al-Bermani et al. [112] that in Ti6Al4V, the freezing range ΔT_0 is equal to 50 K, and in most liquid alloys, the diffusion coefficient is approximately equal to 10^{-8} to 10^{-9} m^2 s^{-1} [112, 144]. Thus, the criterion for cellular and dendritic growth can be calculated as $G_L/R < \sim 5 \times 10^9$ K s m^{-2}. From Figure *4.5*, the ratio G/R, thus reduces to a minimum of ~ 0.08 x10^8 K s m^{-2} and, 0.22 x 10^8 K s m^{-2} at the rear, of the melt pool as material solidifies in the SLM and EBSM processes, respectively. The predicted solidification conditions thus fulfill the criterion for planar front instability. In EBSM the predictions also show that the solidification conditions would theoretically be expected to move very close to the mixed columnar/equiaxed region, identified on Kobryn and Semiatin's solidification diagram, in the latter stages of solidification and this observation is in agreement with that of Al-Bermani et al. [112]. In comparison the solidification conditions in the SLM process are predicted to enter the mixed region and then the equiaxed region at the end of the solidification. The solidification conditions from the thermal model thus suggest that SLM may favour the formation of fine prior β grains in the solidified consolidated powder. Finally, with the WAAM process, a minimum G/R ratio of 0.73 x 10^9 K s m^{-2} was predicted and despite the much larger melt pool, the solidification conditions show that solidification still begins in the fully columnar, and ends only in the mixed columnar dendritic morphology region.

In SLM, high cooling rates were predicted at the liquidus temperature of Ti6Al4V, in the range of 0.73 - 8.37 x 10^5 K s^{-1} (Table *4.4*) decreasing towards the melt pool rear which is in good agreement with values of cooling rate of 7 x 10^4 K s^{-1} reported by Qian et al. [34] in the same Ti6Al4V alloy deposited using the direct laser fabrication process. The EBSM process gave

predicted cooling rates in the range of about 0.02- 3.2 x 10^4 K s^{-1}, in good agreement with the value of 10^4 K s^{-1} reported by Al-Bermani et al. [112] for the same processing conditions. In comparison, the WAAM process gave cooling rates of about, 0.09 to 37.5x10^3 (K s^{-1}), which are much lower than for the other two process reported above and is in the range of values reported for GTAW process [44].

4.3 BULK β - GRAIN STRUCTURES IN AM

An important microstructural feature that can influence the mechanical properties in Ti6Al4V is the prior β-grain size as this can affect the α colony size and texture, as well as texture heterogeneity in the final product [38]. Most importantly, in Ti6Al4V alloys with a lamellar α+ β microstructure, is the colony size, which can be strongly influenced by the prior β-grain size and, is critical in determining the final mechanical properties in AM products[38]. Prior β grain structures in AM deposition with a Ti6Al4V alloy are known to be coarse and highly directional. However, little work has been conducted to evaluate their texture and compare β grain structures directly between processes [29, 112]. This section is thus focused on comparing the evolution of the typical β-grain structures seen in the bulk deposits for all three AM methods (namely, EBSM, SLM and WAAM) under standard operating parameters (shown in Table *4.1* and Table *4.2*).

4.3.1 Bulk β - grain structures in the SLM process

Figure ***4.6*** presents an example of the typical microstructural features seen by optical microscopy in a Ti6Al4V sample that was produced using the cold powder bed SLM process. The SLM samples were made by deposition of Ti6Al4V powder layers on to a forged Ti6Al4V plate substrate at room temperature. The overall microstructure shows fine columnar β-grains (see Figure ***4.6***a) which grow parallel to the build direction. The size of the columnar β grains was approximately 25 to 80 µm wide, and 0.5 to 1.5 mm in length. The base plate had a recrystallized α/β microstructure that was produced by working in the α+β phase field [5], with 90% primary α-grains and smaller β phase on the α-grain boundaries (see Figure ***4.6***c). As noted in 4.2, there is evidence of melt pool tracks, with a width of about 100 µm at the substrate deposit interface in Figure ***4.6***c.

Figure *4.7*b shows the reconstructed β grains obtained from room temperature EBSD α-orientation maps (Figure *4.7*a) using the method developed by Davies and Wynne [135], described in section 3.6.4 . Heterogeneously nucleated fine columnar β grains can be seen to develop (Figure *4.7*a) from the Ti6Al4V forged base plate. The un-reconstructed region near the bottom of SLM deposit, shown in Figure *4.7*b, corresponds to the base plate. This occurred because the α/β habit Burgers orientation correspondence relationship with the parent prior β phase has been lost during deformation and recrystallization of the forged base plate. The dashed line in Figure *4.7*a shows the boundary between the forged substrate and, the actual build.

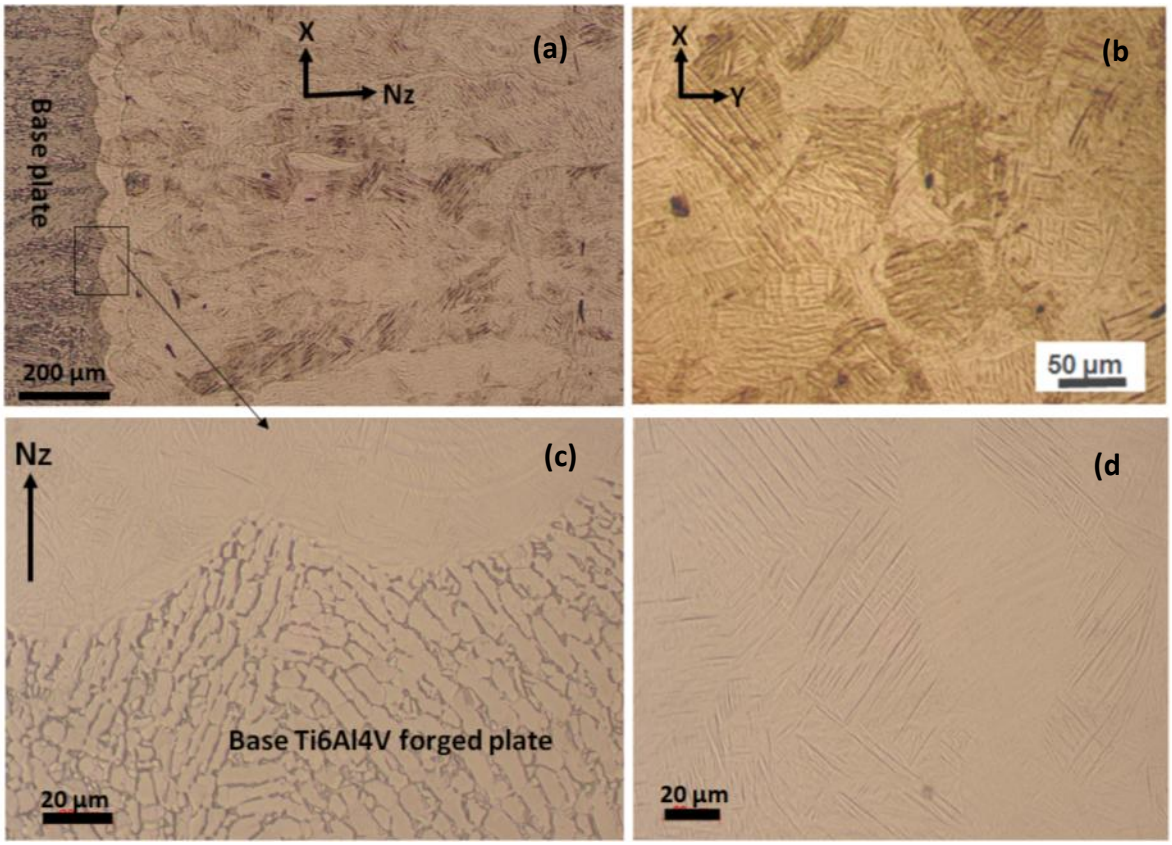

Figure 4.6: *SLM deposit seen by optical microscopy showing (a) an overview of typical columnar* β*-grains developed from the forged Ti6Al4V substrate along the build direction, (b) the* β *grains in the cross sectional top view, (c) evidence of the melt pool size at the forged Ti6Al4V substrate deposit interface and in (d) the martensitic α' plates within the prior* β *grains in a bulk AM section of the Ti6Al4V alloy.*

In EBSD maps from the centre of a bulk section shown in Figure *4.7*c, columnar <001>$_{\beta}$ grains can be seen to start to grow to a certain height and then stop, and, new columnar β grains begin to grow with a small volume fraction of fine more equiaxed grains. The columnar gains appear to develop against the direction of heat extraction, through the base plate. The columnar grains grow preferentially with a common <001> direction || Nz (build) in the bulk section (as shown in Figure *4.7*c). The measured length of the columnar β grains was from 1.0 mm to max of 3 mm, and these grains thus grow up through several deposited layers since a single layer height is about 30 to 40 µm.

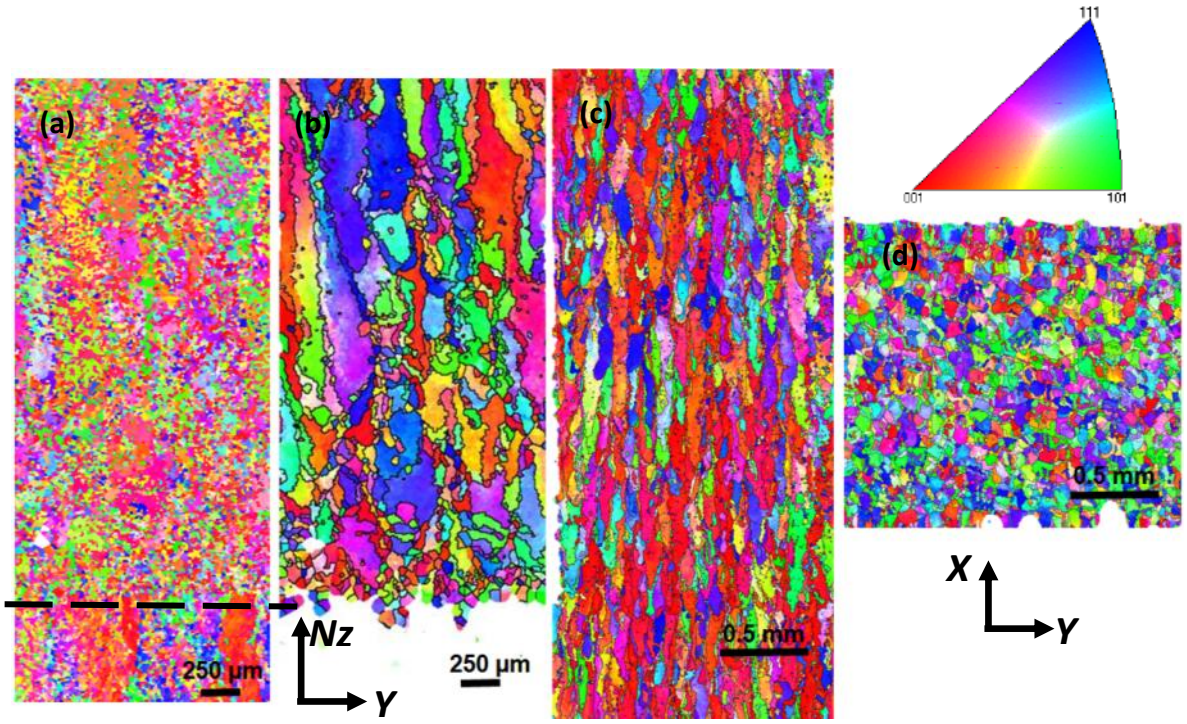

Figure 4.7: *EBSD orientation maps from a typical bulk SLM sample showing (a) the room temperature α-phase, (b) the reconstructed* β *grains immediately above the substrate, and (c) and (d) along the build direction (X-Nz), and in the transverse cross-section (X-Y) when steady state conditions are reached. The orientation contrast in the IPF maps is aligned parallel to the build direction (Nz) in all cases.*

4.3.2 Bulk β - grain structures in the EBSM process

Figure ***4.8*** presents an overview of the typical β grain structures developed in the samples built by the EBSM-AM process in the transverse Nz-Rx section. The prior β grains can be interpreted reasonably clearly from the optical micrographs, due to the presence of grain boundary α. After an initial transient region at the base of the build, a coarse columnar β grain structure can be seen to develop (Figure ***4.8***a). The measured length of the columnar β grains varied from 1.4 mm to more than 4 mm, with a width of 150µm to 300 µm. However, it was difficult to be certain of their true length in 2D sections because of their irregular width, and many of the grains appeared to extend across the whole length of the sample.

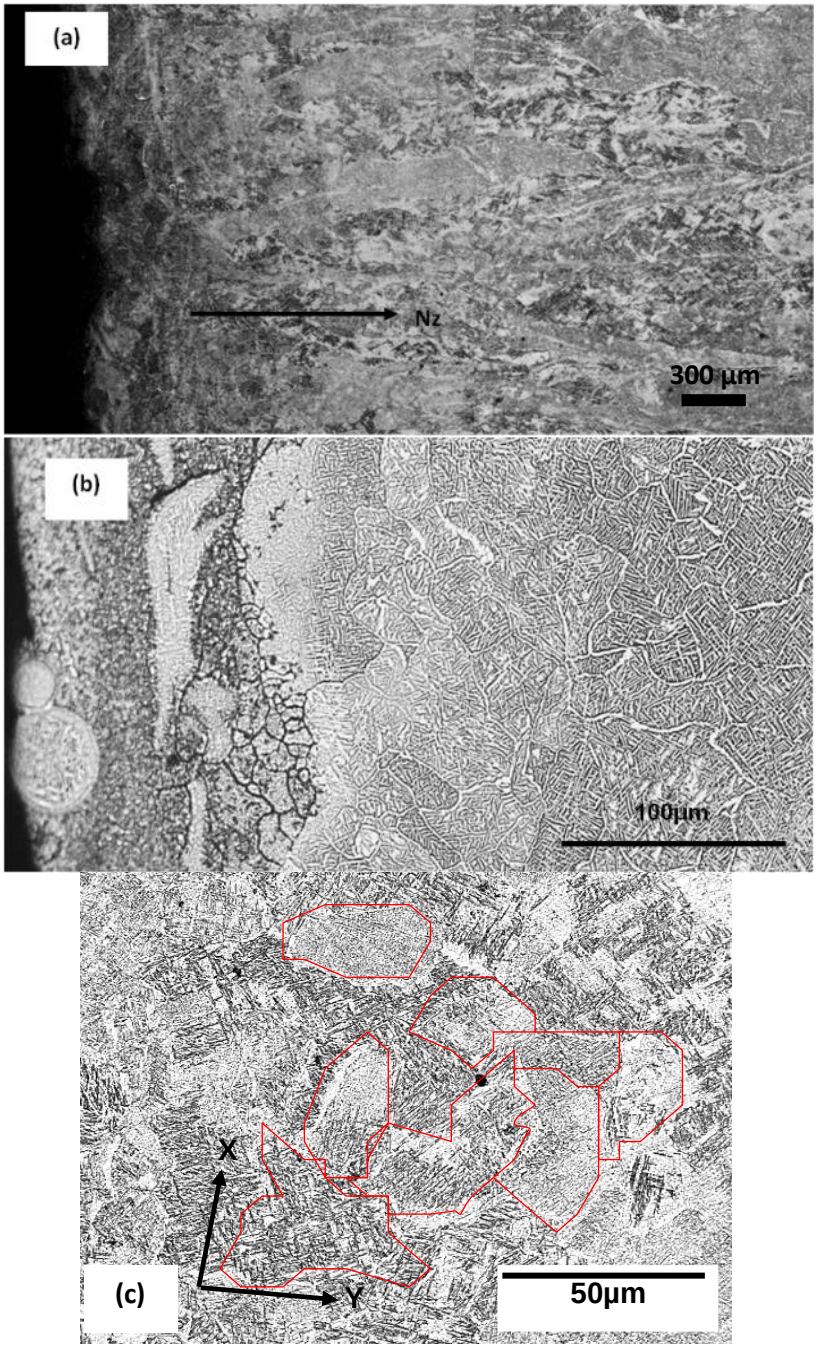

Figure 4.8: *Example overview of the typical microstructural features seen by optical microscopy in the EBSM-AM built samples, (a) macrostructural view from the base of a build along the Nz-Rx plane, (b) the initial transition region near the base of the build at higher magnification, and (c) a transverse section of the columnar grains showing irregular grain boundaries in the Rx-Ry plane.*

In Figure ***4.8***b, at a higher magnification, a transient microstructural region can be identified at the base of the sample. This consists of a ~ 500 µm thick zone contacting the base plate, which contains cracks, and small equiaxed grains (Figure ***4.8***b and Figure ***4.9***) with a large proportion of β-phase. This is caused because the composition has changed in this region by partial alloying with the stainless steel substrate [112]. This is followed by a further thin layer of fine equiaxed

primary β-grains that have not been affected by alloying [112]. Coarse columnar grains then develop by growth selection from this base layer with wavy grain boundaries. Figure ***4.8***c shows irregular columnar grain boundaries in the transverse section (Rx-Ry plane). From the base plate upwards, a typical EBSM bulk part thus contains an initial thin transient layer and a 'columnar zone', which grows until the top of the section.

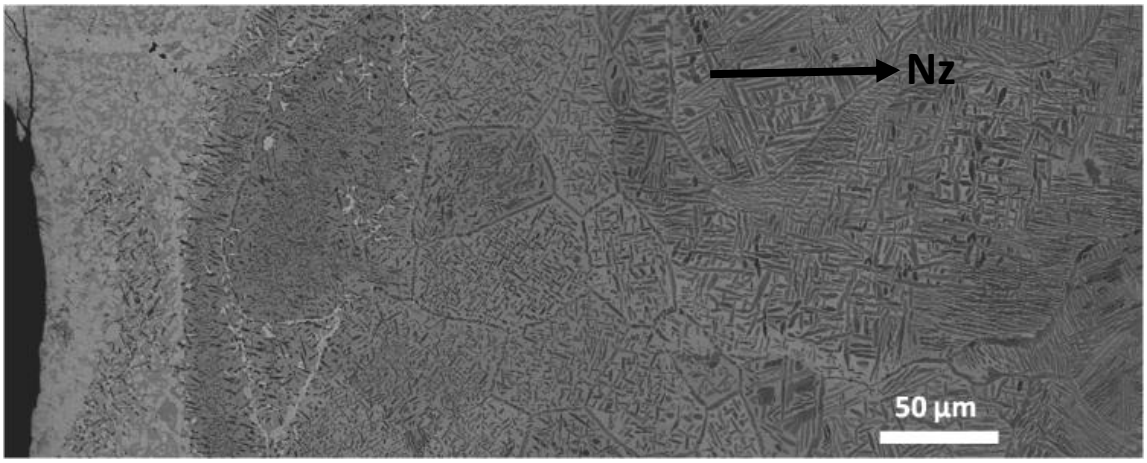

Figure 4.9: *Shows the presence of crack, and small equiaxed* β *-grains near the base of the Ti6Al4V build under SEM- BSE imaging mode. The change in contrast along the horizontal (along the build) direction in the micrograph is due to the initial comelting of Ti6Al4V powder and the stainless steel base plate.*

Figure *4.10* shows the EBSD orientation maps of the room temperature α phase along with the reconstructed prior β phase, obtained using the method developed by Davies and Wynne [135] (section 3.6.4). A 500 µm thick heterogeneously nucleated fine equiaxed β grains can be seen (Figure *4.10*a-b) at the base of the build due to the high cooling rate, and co-melting of the Ti6Al4V with stainless steel substrate. After the fine equiaxed region, large columnar grains start to grow along the build direction. These grains grow up through many deposited layers, and hence develop by epitaxial re-growth with no new nucleation. Figure *4.10*c shows that as more layers are deposited β grains oriented with an $<001>_{\beta}$ direction parallel to Nz (red), start to dominate the whole build section. The grains appear highly irregular in nature but have a predominant in <001> || Nz (red) orientation. However, other minor components are still present (green) (see Figure *4.10*c). Figure *4.10*d shows the reconstructed columnar β grains seen in the transverse section at the build height of approximately 15 mm.

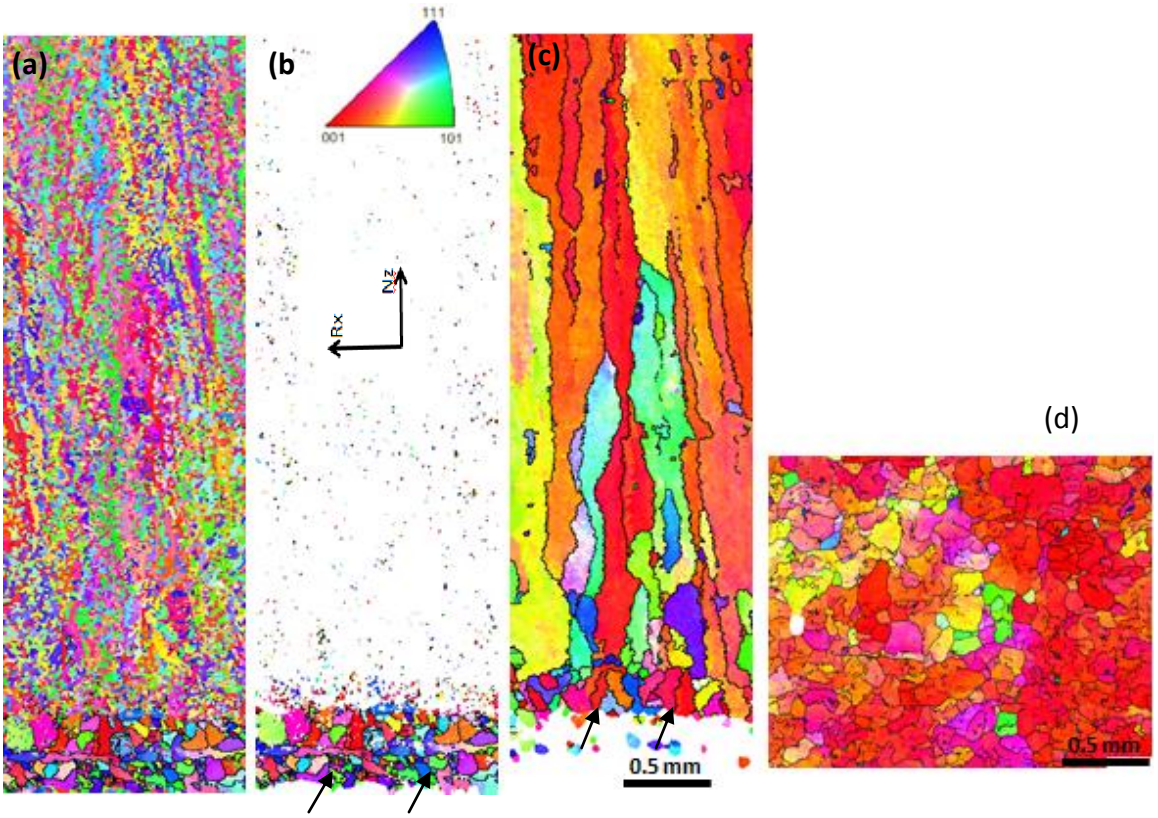

Figure 4.10: *EBSD data from the base the sample, (a) IPF map of both α+β phases at room temperature, (b) IPF map of β-phase at room temperature, (c) reconstructed high temperature columnar β grains along the build direction, which developed from the fine equiaxed grains at the base (arrow marks), and (d) reconstructed columnar prior β-grains seen in the transverse section at a height of ~ 15 mm. The orientation contrast in the IPF maps is aligned parallel to the build direction (Nz) in all cases.*

4.3.3 Bulk β - grain structures in the WAAM process

Figure *4.11* presents an example of the typical macrostructural features seen, by optical microscopy, in the wire plus arc AM (pulsed GTAW) deposited Ti6Al4V alloy under the standard operating parameters shown in Table *4.5*. It should be noted that, unlike in the powder bed samples, the wire arc process deposited the material with a single pass and the melt pool was the same width as the deposited 'wall'. At the base of the deposit a higher number of fine grained prior β-grains were observed, which might have heterogeneously nucleated from the substrate when the first layer was deposited. However, in the heat affected zone (HAZ) from the first weld bead the substrate will transform and will undergo β grain growth due to the high temperature reached [5, 38], so the exact interface is difficult to determine. Upon deposition of further layers, only a few grains are selected and grow aligned parallel to the build direction resulting in a coarse columnar grain structure. Since there is a higher thermal gradient conducted through the substrate plate, it is possible that these grains grow parallel to the heat extraction direction down

the deposited wall. However, this will be discussed in more detail later in section 4.3.4. The overall microstructure viewed in the transverse section, shows the presence of very large columnar prior β-grains ranging from 15 mm long to a maximum height of 35 mm, with a maximum width of 2.5 mm. The constrained columnar β grain growth shown in the macrostructure (Figure *4.11*) has also been observed and reported by Brandl et al. in laser Wire based AM [101]. The micrographs in Figure *4.11* show clear evidence of a HAZ before each deposited layer with microstructural banding due to reheating, with the exception that no banding can be seen in the last three layers, and this will be discussed later in section 4.5.

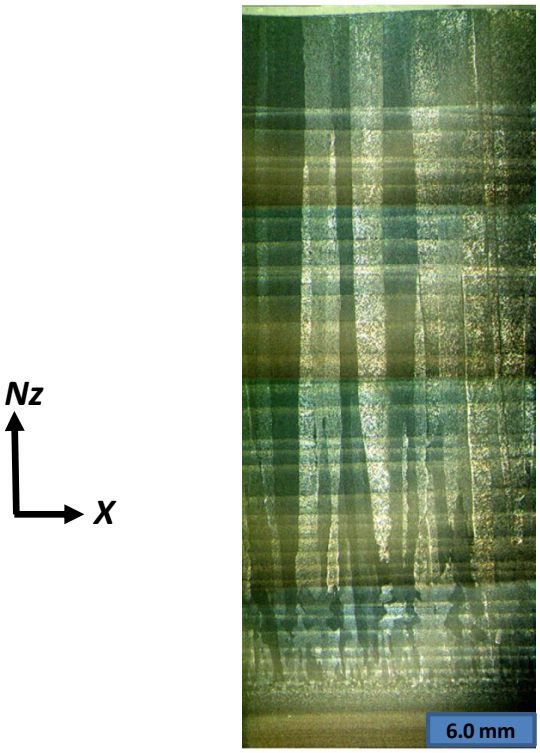

Figure 4.11: *The typical microstructure seen in the GTAW + wire deposited AM samples under standard conditions.*

Figure *4.12* shows the typical columnar β microstructure produced by pulsed GTAW deposition of Ti6Al4V alloy observed from reconstructed EBSD maps, for the standard operating parameters shown in Table *4.2*. From the reconstructed β IPF map, it is obvious that the <001> || Nz oriented β grains are rapidly selected near the base of the build and then spread to occupy almost the entire build height. In the higher magnification EBSD map near the base of the build (Figure *4.12*c), there is clear evidence that the grains are heterogeneously nucleating from the Ti6Al4V rolled substrate plate.

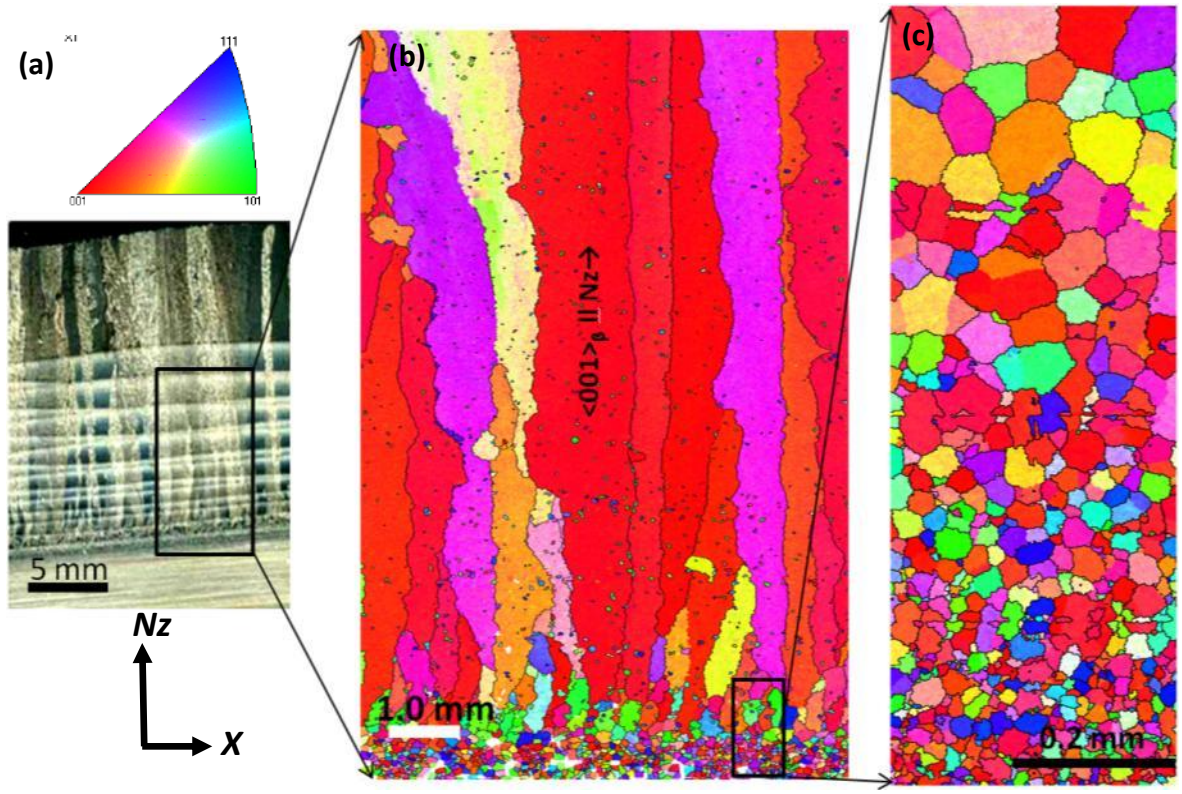

Figure 4.12: *(a) Macrograph of a typical pulsed GTAW + Wire deposited build and, (b) the prior β-grains reconstructed from the room temperature EBSD α-phase data, and (c) reconstructed β-grains near the base of the build at higher magnification.*

Table 4.5: *Standard parameters used to produce the high frequency (HF)- interpulse GTAW deposition samples shown in Figure* ***4.11*** *with an inter-pulse power source.*

Condition	TS (m/min)	WFS (m/min)	Arc V (v)	Current (A)	Heat I/P (kJ/m)	Frequency
GTAW HF-Interpulse	0.27	1.6	12	I_p = 150 I_b = 45-75 $I_{interpulse}$= 87-101 I_{av} = 99.	182	10 Hz low frequency + 20 KHz high frequency

4.3.4 Discussion of the bulk β grain structures seen across the 3 AM platforms

Development of columnar β-grain structures

The EBSD data presented here, and several other studies [8, 11, 19, 26, 28, 29, 31, 32, 37, 48, 111], have shown that a characteristic feature of AM with titanium alloys is the development of prior β grains with a coarse-columnar structure. This can result in very large grains relative to the component dimensions and an anisotropic microstructure, despite the rapid solidification rate and small melt pool size in AM processes (see 4.2).

All three processes showed columnar β-grains which developed by heterogeneous nucleation from the base substrates. In the EBSM and WAAM processes, once established from the base, columnar grains were able to grow through the entire section-height, but in the SLM process the columnar grains appeared to be more broken up, with a lower aspect ratio. Since, except near the stainless steel base plate in the EBSM process, the chemical composition and surface energy of the molten melt pool is same as that of the previous layer, in nucleation theory the wettability angle, θ, approaches 0˚ (Equation 9 and 10). This implies that there is no nucleation barrier during solidification and, hence, epitaxial re-growth readily occurs in each layer.

From the thermal modelling of both the EBSM and WAAM processes (Table *4.4* in section 4.2), it can be seen that there was a steep thermal gradient, G_L, perpendicular to the S/L interface of the solidifying melt pool surface (see section 4.2.4). In addition to this, the high partition co-efficient of Al and V in the Ti6Al4 alloy [115] leads to low constitutional supercooling ahead of the solidifying S/L interface as it was discussed in section 2.2.2. These conditions favour the continuous epitaxial growth of large β grains with no new nucleation ahead of the growth front. These results are also broadly in agreement with the modelling results which show that in all the processes solidification starts in the columnar region of the solidification diagram and it is only near the end of the melt pool where the conditions approach or cross the equiaxed /columnar boundary. In the centre of the bulk samples columnar grains thus developed by competitive growth from the base plate, and grew substantial distances upwards through many deposited layers, developing a strong preferred $<001>_{\beta}$ fibre texture, since the <001> is the easy growth direction in cubic metals. In the three processes, the preferred growth direction of the <001> β grains was parallel to Nz. Thus, most of the β grains seen in both the EBSM and WAAM processes, and to a lesser extent in SLM, had a red in colour in the IPF maps, which indicates an <001> direction parallel to the build direction. However, why this alignment should occur is not immediately apparent as the preferred growth direction should be aligned normal to the curved melt pool surface and the origin of the bulk <001> β || Nz fibre textures will be discussed in more detail in the next section 4.4.4.

In SLM, the columnar β grains grew to a certain height and stopped and then new columnar β grains starts to grow aligned approximately in the build direction. Such a discontinuous columnar grains structure is often referred to as a 'stray' grain structure in welding terminology [44, 145]. The formation of stray grains (SG) has also been seen during processing of Nickel single crystal alloys, where they are thought to form from disoriented dendrites [145-147]. Theories concerning the formation of stray grains include; limited re-nucleation from dendrite fragments in a slightly undercooled liquid, and disorientation by dendrite bending or twinning, but their origin is not well understood. Stray grains are known to be most likely to be formed in conditions where there are high thermal gradients and cooling rates in association with a moving welding heat source, such that the solidification front grows in an asymmetrical direction, relative to a crystal easy- growth direction i.e., the growth direction changes relative to the crystal direction during solidification [147].

Thermal modelling has predicted that the thermal gradient in the SLM process is higher compared to in the other two processes (Table *4.4*) but this is outweighed by the much higher growth rate, and the tail end of the melt pool reaches the solidification condition where it moves into the equiaxed grains region in the solidification map proposed by Kobryn and Semiatin (shown in Figure *4.5*). Thus, of the three processes, the solidification conditions with the SLM process are predicted to produce the highest level of undercooling ahead of the growth front. However, with the large positive thermal gradient, and high solidification rate ahead of the S/L interface, it is still not possible to obtain a high enough constitutional super cooled region ahead of the growth front for a high rate of nucleation to occur and cut-off the columnar growth. In the circumstance where G_L and R are very high, nucleated or fragmented dendritic tips can get trapped in between fast growing columnar grains, which are aligned, perpendicular to the melt pool solidification front, and this leads to the formation of broken up stray grains in the SLM process [44, 147]. When the cooling rate is high, the chances of formation of crystal defects due high solidification stresses are also very high; for example, some solidification thermal cracks were observed in the SLM process (see section 4.5.4). These crystal defects could also act as an effective heterogeneous nucleation site, which restricts columnar growth and leads to the formation of finer broken up columnar β-grains in the SLM process.

Irregular β grains structures

In the EBSM process, the vertical columnar grain boundaries were wavy in appearance and appeared to be perturbed by the rastering direction which alternates by 90˚ every layer [26, 92]. Whereas, in the SLM process wavy grains were not as apparent since the powder bed layer height is small, and the rastering sequence rotated 30˚ upon the every new layer deposited. In addition,

in the SLM process the columnar grains were broken up and only grew to a limited number of layers heights, which made the influence of the rotation of the rastering direction more difficult to determine. In comparison, in the WAAM process, the morphology of the large β-grains appeared to be less influenced by the rastering direction, which rotated through 180˚ each alternate layer.

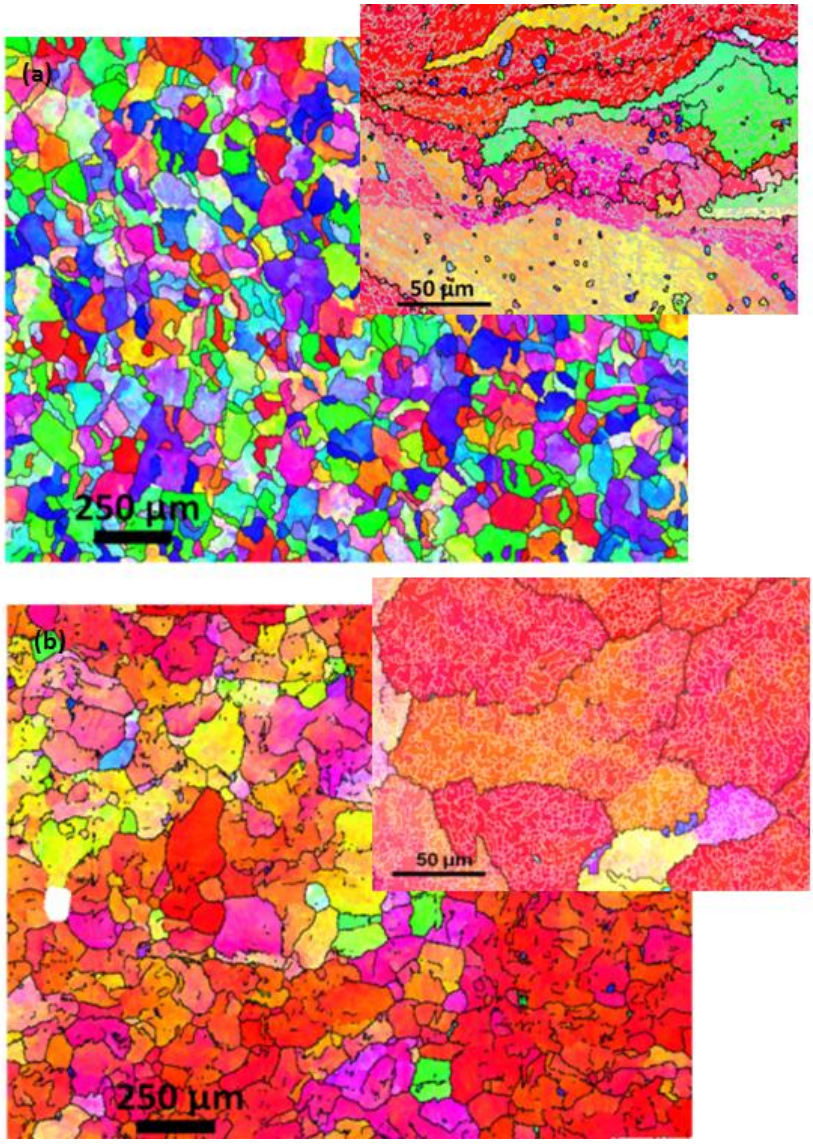

Figure 4.13: *High resolution EBSD map, showing (a) fine columnar grains in SLM and, (b) irregular columnar region seen in the EBSM, from the centre of bulk sections following Kuwahara filtering. The inset in the both the (a&b) shows substructure of a LAGBs of < 3˚ in grey colour and, HAGBs of > 15˚ in the black colour (in SLM process the inset shows the substructure in Rx-Nz plane).*

The grain structures produced in bulk samples produced by EBSM have been seen to consist of coarse highly-irregular columnar grains (Figure ***4.13***b). But SLM, the other powder bed method, did not show such irregular β grains in the final microstructure, as shown Figure ***4.13***a, since the

grains were much smaller and the layer height was much reduced (30 µm). The irregular bulk-grain structures in the EBSM deposits also showed large areas of similar IPF orientation contrast and contained discontinuous HAGBs, making the grain size difficult to reliably quantify. The origin of these irregular grains could be related to preferred growth directions becoming aligned with the raster directions, or there could be a geometrical effect of solidification by growth inwards from the edge of the melt pool with a tendency for grains of similar orientation to impinge at the weld centre line [44]. In addition to this, in both the SLM and EBSM powder bed processes, the β grains contained evidence of internal substructure comprised of low angle boundaries, as shown in Figure ***4.13***. Al-Bermani et al. [112] have also noted that the irregular β-grains produced in EBSM often contained substructure.

The irregular nature of the coarse columnar grains can be attributed to several factors. Firstly, the edge of the melt tracks is more uneven than in welding, due to variability in coupling with powder of varying packing density and particle sizes, which would result in local variations in the extent of melting. Secondly, and more importantly, the changes in the raster direction will disturb a grain's growth direction. For example, wavy columnar boundaries seen in the R_Y – N_Z sections have a wavelength related to the layer height [29, 112]. The orientation spread, and the presence of low angle boundaries within the columnar grains are also features of their irregular structure. Al-Bermani et al. have attributed this behaviour to the relaxation of internal stresses, and, or, impingement of imperfectly orientated cells, or dendrite arms, during solidification [112]. This can be compounded by the presence of solidification stresses [148]. However, it is also known that with a curved melt pool surface columnar grains can adjust their orientation to follow the maximum thermal gradient by two mechanisms; multiple branching of dendrites [44, 149], or the generation of crystal defects such as screw dislocations at the solid liquid interface [43, 150]. Thus, while on average a bulk <001> || N_Z fibre orientation is maintained against the melt pool surface for each individual melt track, it is likely that the orientation of a grain can be perturbed by the direction of travel and curvature of the melt pool surface, which locally varies the direction of the maximum thermal gradient at the solidification front.

Heterogeneity in the bulk β grains structures

The higher resolution EBSD maps (1µm step size) from typical bulk regions have been used to investigate heterogeneity in the bulk β grain structures. The maps were Kuwahara filtered to reduce misorientation noise before analysis. An example is given in Figure *4.14* with accompanying pole figures taken from individual grains. In EBSM, The irregular bulk-grain structure also shows large areas of similar IPF orientation contrast and contains discontinuous HAGBs in EBSM samples (Figure ***4.13***b).

In the first example set (Figure *4.14*b) it can be seen that in a given EBSD plan view section, individual grains exist that deviate significantly from the preferred fibre direction and, as well as being rotated relative to each other around N_Z, are off axis from the ideal <001> || N_Z fibre by up to 10°. Such grains appear with different colours in the IPF map. The second set of examples (Figure *4.14*c) is taken from the large red area in the map, where the orientations are all very close to the ideal <001> || N_Z fibre. The formation of <001> β ||Nz fibre texture will be discussed in more detail in section 4.4.4. In this case the individual grains are still randomly rotated around N_Z relative to each other. Within both sets of grains there is typically an orientation spread of ~ 10°, which mostly results from a rotation around N_Z. In addition, in Figure ***4.15*** an orientation line scan is shown from a small step size map of a large columnar grain, obtained parallel to the build direction. This grain exhibited a similar misorientation spread, but in the misorientation line scan it can be seen that there is a regular spacing of single, or clusters of, low angle boundaries of significant misorientation (3 - 5°) above background. The average distance between these boundaries is approximately 100 µm, which coincides with the height of each consolidated powder layer. The adjustment of the crystal growth direction would account for the higher misorientations seen within columnar grains along the build direction, at intervals corresponding to the layer deposition height (Figure ***4.15***), as this would coincide with a 90˚ change in the beam travel direction. This behaviour could also account for the spread in orientations seen within individual grains in high resolution plan view EBSD maps (Figure *4.14*).

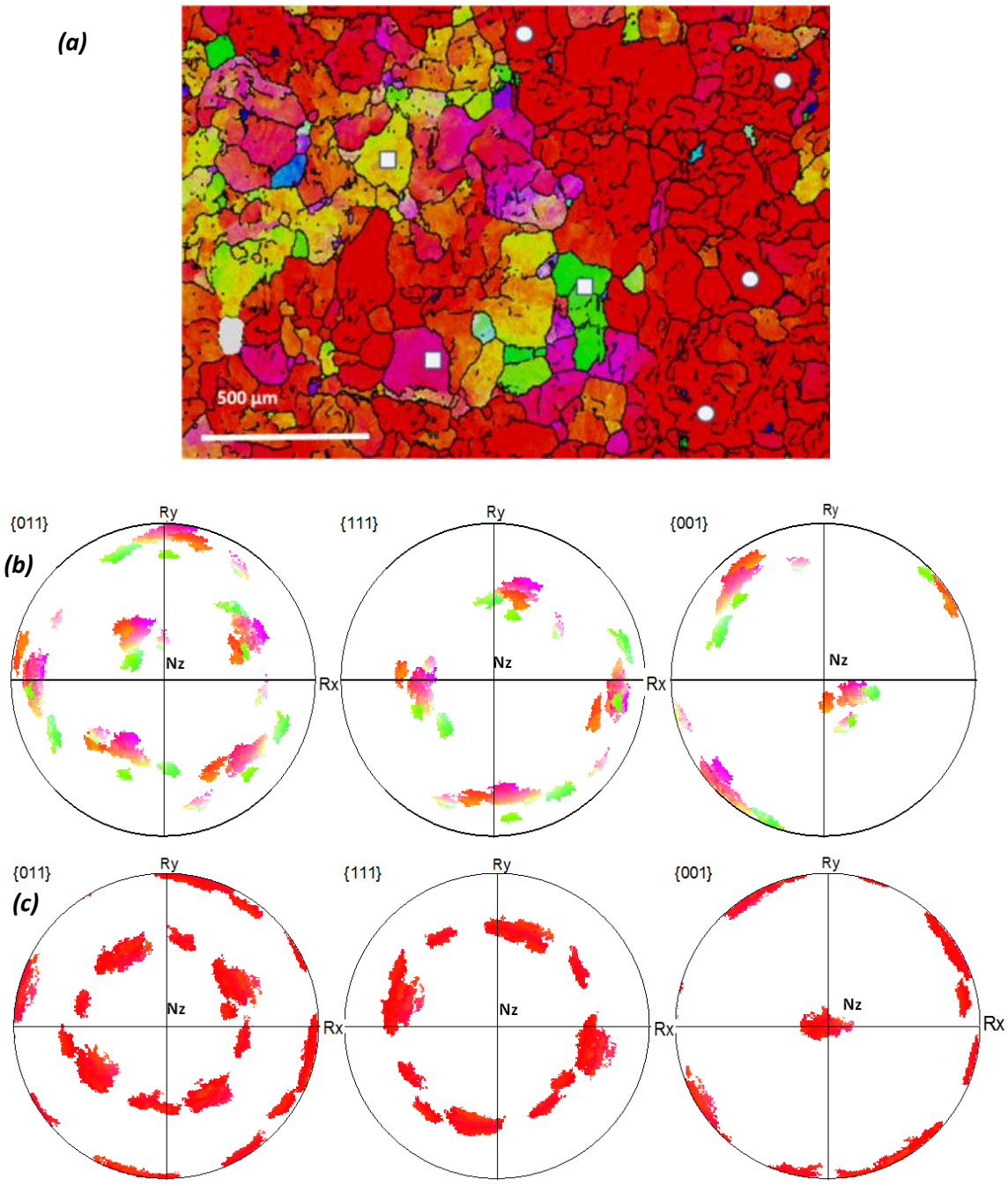

Figure 4.14: *(a) High resolution EBSD map from the irregular columnar region seen in the centre of bulk EBSM-AM sections, following Kuwahara filtering. Pole figures of families of grains that deviate (squares) or are aligned (circles) closely to the ideal <001> || N_Z fibre orientation are shown in (b) and (c) respectively.*

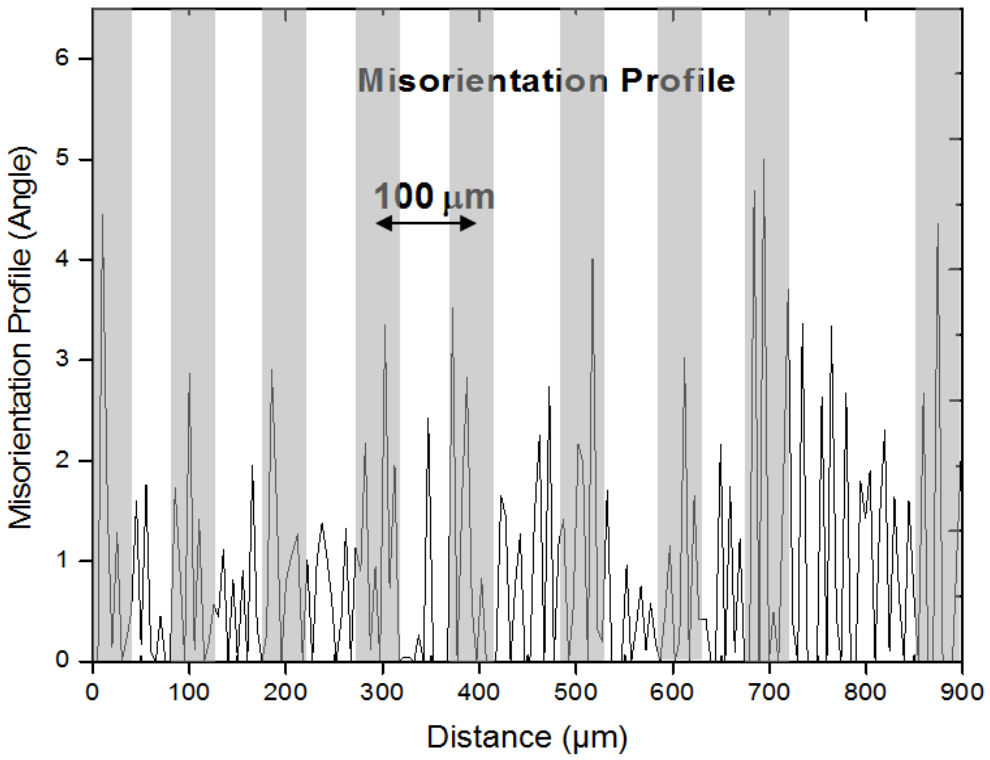

Figure 4.15: *Orientation line scan along the direction of build show a regular misorientation spacing of single or clusters of low angle boundaries at approximately 100 µm, which coincides with the height of each consolidated powder layer in the EBSM process.*

Prior-β grain size

Table *4.6* shows a comparison of prior β-grain sizes for the three different AM processes. Although the development of primary coarse columnar β grains is a characteristic feature of AM with titanium alloys, the grain size varied with respect to the different processes, depending primarily on the local cooling rate and solidification conditions, and the melt pool size may also have had an influence.

The SLM process exhibited the smallest grain size, due to the lower heat input, very small melt pool size and the unheated base substrate (see Table *4.3* and Table *4.4*). Consequently, the predicted thermal gradient within the smaller melt pool is very large and the resulting cooling rate in SLM is very high, which when combined with the formation of stray grains, leads to the formation of fine prior β-grains in the SLM process. The solidification map shown in Figure *4.5* also suggests that SLM should produce fine equiaxed grains, due to the fact that the rear end of the melt pool during solidification touches the CET line in the solidification map. However, a full equiaxed structure was not observed. In EBSM, although the melt pool shape is tear drop shaped, the same as in SLM, due to preheating to 740 ˚C and the larger melt pool size, the thermal gradient and the predicted associated cooling rate was less (Table *4.4*). Due to the fact that a

fairly uniform thermal gradient is maintained in the very long tear drop shape in the EBSM, the grains grow more equally along the interface and the lower cooling rate leads to a slightly coarser average grain size than in SLM. In the WAAM process, the melt pool is elliptical in shape and also the size of the melt pool is comparatively much larger than in the other two processes. The cooling rate is also a lot lower than that for the EBSM and SLM processes. This results in the formation of much larger columnar β-grains, which are also able to grow to a large size, as their size is not as restricted by the size of the melt pool. The grain size distribution in the high resolution reconstructed β grain EBSD maps for both the SLM and EBSM processes, determined in the Rx-Ry plane using the linear intercept method is shown in Figure *4.16*. Average grain sizes of 60 µm and 100 µm were observed for the SLM and EBSM processes, respectively. However, a far greater spread was seen for the EBSM process owing to the large <001> $_{\beta}$||Nz texture regions developed with this process.

Table 4.6: *Comparison of the prior β-grain sizes for the three different AM processes.*

β grains size || Nz		**β size || Rx-Ry**
Width (mm)	**Length (mm)**	**Diameter (mm)**
SLM Process		
0.03- 0.08	0.5 - 1.5	0.03 - 0.22
EBSM Process		
0.15-0.30	1.4 - 5.0	0.05 -0.56
WAAM Process		
0.50- 2.50	15.0 - 36.0	0.8 - 2.3

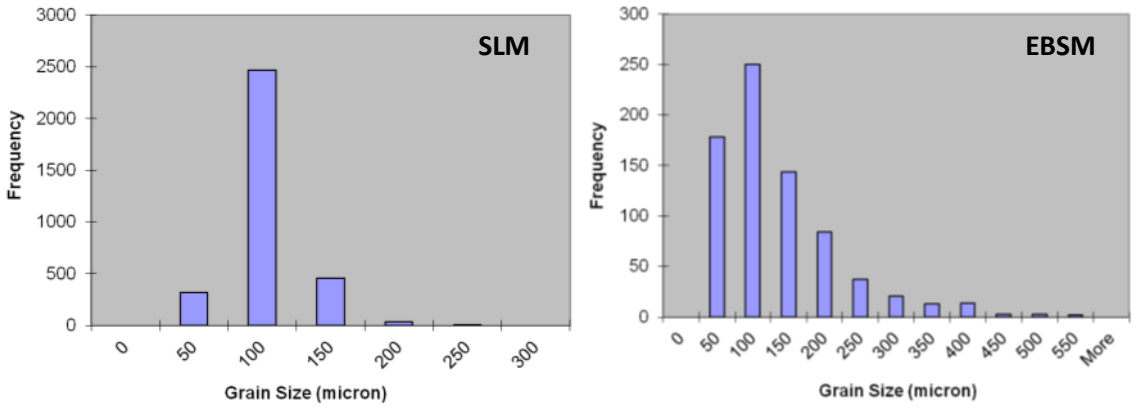

Figure 4.16: *Grain size distributions measured at high resolution in the Rx-Ry plane in SLM and EBSM bulk section built from the Ti6Al4V alloy.*

Metallurgical limitations of Ti6Al4V in columnar β-grain growth

According to the solidification map published by Kobryn and Semiatin's, and predictions of the solidification conditions in EBSM and WAAM processes, the ratio, G_L/R, is expected to just move into the mixed region in the latter stages of freezing; i.e. at the melt track centreline [29, 48, 112] (Figure *4.5*). Whereas, in SLM, the solidification conditions at the tail end of the melt pool are expected to fully cross the mixed region and move into the equiaxed grain region in the solidification map. However, except in the SLM process, fully columnar growth structures have been observed. This apparent contradiction may reflect over interpretation of Kobryn and Semiatin's solidification map which, although validated against laser glazed samples, is not well populated with data. In SLM, the G_L/R ratio crosses the CET line in the solidification map, and the deposits contained fine columnar stray grains.

Despite the high growth rates, which arise from the high translation speed in AM, the difficulty of entering the equiaxed regime clearly reflects the large thermal gradients seen in the melt pools with each process. However, it is important to note that the metallurgical characteristics of the Ti6Al4V alloy do not lend themselves to grain refinement. Firstly, the high solubility of aluminium and vanadium in titanium give rise to partition coefficients of close to one for both elements [115]; i.e. with respect to Al and V there is very limited segregation at the growth front. This also results in a very low growth restriction factor, which reflects the rate of development of a constitutional supercooled zone ahead of a solidification front. In fact, the presences of trace elements like iron are much more significant in terms of solute partitioning than Al and V [114, 115]. A further issue in preventing columnar growth is to ensure nucleation ahead of the growth front can take place at low undercoolings (ΔT ~1 K), which requires a supply of efficient heterogeneous nucleants. In weld pool solidification these are provided either by dendrite fragmentation, or through the addition of grain refiners [114, 115]. Unfortunately, in Ti6Al4V there are no artificial inoculants present and, due to the low level of solute partitioning and narrow mushy zone, detachment of dendrite fragments would be expected to be difficult. The strong tendency to develop columnar grain structures in AM with titanium alloys like Ti6Al4V can thus be attributed to the characteristics of the material, as well as the solidification conditions. Indeed, Wu et al. and Bermingham et al. [110, 114, 115, 151] have shown that equiaxed grain structures can be more readily produced in alloys that contain carbon, or boron, because they have a low solubility in titanium and the alloys consequently exhibit a larger freezing range.

4.4 BULK TEXTURES IN AM

In all the AM processes studied, it is apparent that the coarse columnar β-grains grow preferentially with a <001> direction aligned parallel to the build, or deposition, direction. Consequently, the final bulk microstructure in the AM of Ti6Al4V alloy deposits is highly anisotropic. As a result, it is import to study the solidification texture, i.e., distribution of crystallographic orientations of the β-grains, and the transformed α-texture with the three different AM processes, to see if there is likely to be any significance anisotropic behaviour in their mechanical properties. This section will focus on the evolution of the bulk primary β-textures typically seen in AM, and the corresponding α – transformation textures for the three different processes, including the texture near the base of the build, and will also investigate the possibility of variant selection during the β → α transformation [51, 142].

4.4.1 Texture in the SLM process

Pole figures depicting the reconstructed β and α-textures obtained from EBSD maps from an SLM deposit are presented in Figure *4.17*. The pole figures are orientated with the build direction, N_Z, normal to the plane of projection. The texture shown is the average found in the centre of bulk sections when the growth conditions had stabilised (at ~ 10 to 15 mm above the substrate), and a stray columnar β -grain structure was well established. To improve statistics, this data was stitched together form several maps to make sure there was at least 1000 grains for reliable texture analysis.

4.4.1.1 Primary β- texture in SLM

In the reconstructed β pole figure a $<001>_\beta$ fibre texture can be observed, with a maximum intensity of ~ 4 or 5 x's random as shown in Figure *4.17*a. The fibre axis has not been adjusted and it's aligned with Nz, the build direction. In the averaged data, the distribution of poles round the <001> || N_Z axis is fairly uniform with little strengthening of poles. A similar β-phase $<001>_\beta$ || N_Z fibre texture to that observed here, in bulk sections, has been inferred by simulation of the β-texture in laser deposited Ti6Al4V by Kobryn and Semiatin [29].

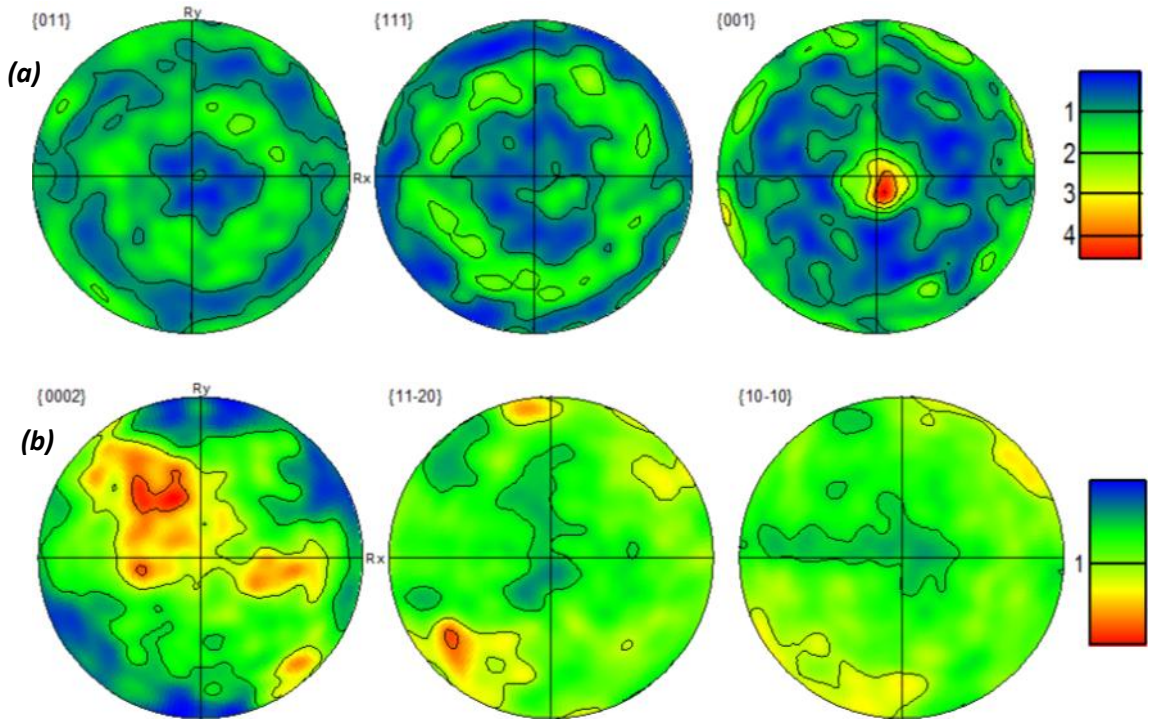

Figure 4.17: *Pole figures depicting the reconstructed* β *textures from the centre of a bulk component (a) and, the bulk* α*- texture (b) in the SLM components.*

4.4.1.2 Transformed α-texture in SLM

It can be seen that the α-phase pole figures indicate a very weak transformation texture, as shown in Figure *4.17*b. The transformed α-texture has a maximum intensity of only 2 x's random and has clearly been diluted by the large number of possible orientation variants in the β → α transformation. Because the texture strength is very low, it is difficult to assess, if any statistically significant variant selection has occurred, and this possibility will be discussed in more detail with the EBSM texture data.

4.4.2 Texture in the EBSM process

Pole figures depicting typical reconstructed β and α- textures seen in bulk section obtained from EBSD maps of the EBSM deposits are presented in Figure *4.18*. The pole figures are orientated with the build direction, N_Z, normal to the plane of projection. The pole figures presented in Figure *4.18*a are from the centre of bulk sections when the growth conditions had stabilised and a coarse-irregular columnar β -grain structure was well established. To improve statistics, this data was stitched together form several maps and included approximately 800 grains.

4.4.2.1 Primary bulk β-texture in EBSM process

In Figure *4.18*a, a <001>$_\beta$ fibre texture can be observed, which is stronger than in the SLM process with a maximum intensity of ~ 8 x random. In the averaged data, the distribution of poles round the <001> || N_Z axis is again fairly uniform. However, this was not always the case in specific individual maps which often showed a stronger cube component and this point will be discussed further in chapter 5. Figure *4.18*b, the texture in the transition zone near the base of the build is also shown, where heterogeneous nucleation took place from the partially melted powder fused with the base plate. Although the sampling statistics are poor (approximately 150 grains), because of the narrow width of this layer, the texture appears close to random.

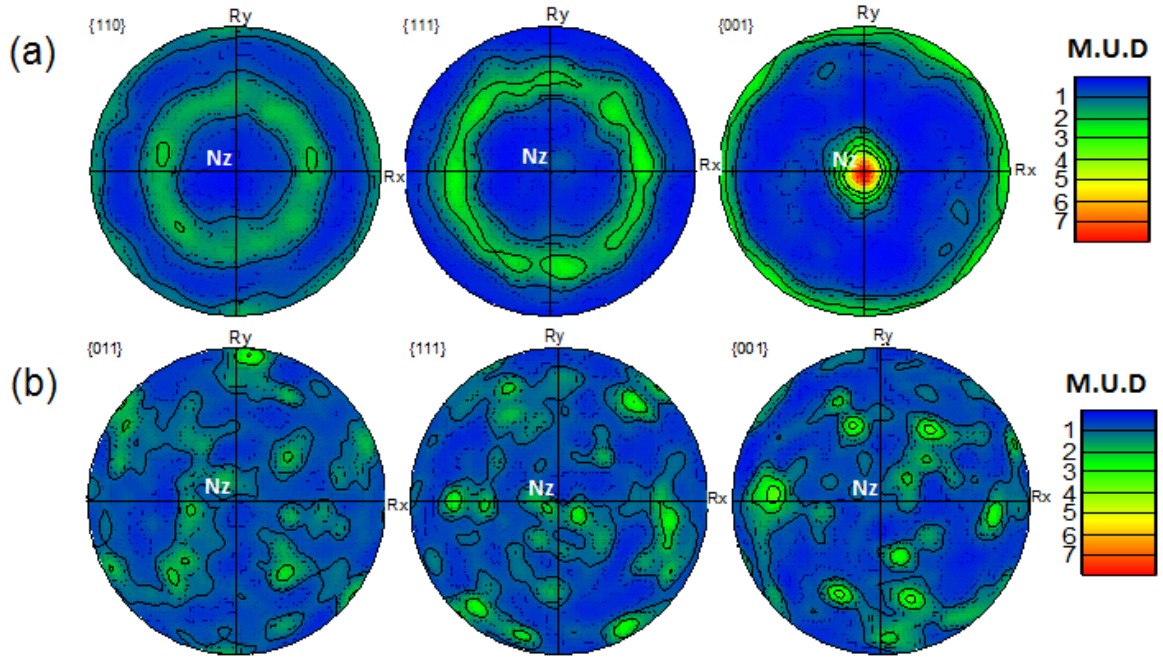

Figure 4.18: *Pole figures depicting the reconstructed* β *textures from centre of a bulk component with approximately 800 grains (a), and at the base of a build (b).*

4.4.2.2 Transformed α-texture in the EBSM process

Examples of α-textures, obtained by EBSD orientation mapping, from which the primary β-texture were reconstructed, are shown in Figure *4.19*. The bulk α-texture found in the centre of thick sections, corresponding to the reconstructed β-texture previously shown in Figure *4.18*a, is presented on Figure *4.19*. It can be seen that the α-phase pole figures also indicate a fibre texture, which is consistent with transformation from the <001> || N_Z β-phase fibre texture, while obeying the Burger's relationship [5, 49, 152]; i.e. the parallel habit planes depicted in the $(110)_\beta$ and $(0002)_\alpha$ pole figures show rings of intensity around N_Z in identical positions in the stereographic

projections. However, the α-transformation texture is considerably weaker than in the reconstructed β-texture, having a maximum intensity of ~ 3 x random (compared to ~ 8 x random for β). The ring in the α texture is also not as uniform in the intensity as seen in the β texture.

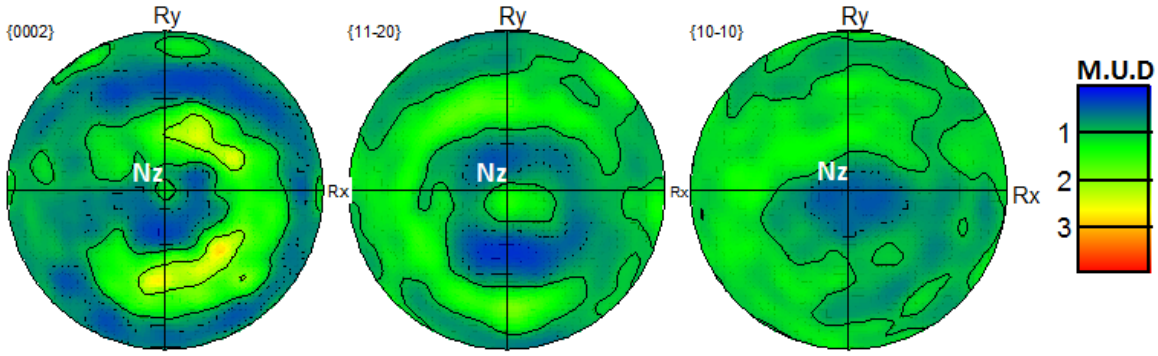

Figure 4.19: *Pole figures depicting the original α -phase texture measured by EBSD for form the centre of a bulk section.*

4.4.3 Texture in the WAAM process

Pole figures depicting the α-texture and reconstructed β-texture obtained from EBSD maps are presented in Figure ***4.20***. The pole figures are orientated in the same way as for the other two processes, i.e. the build direction, N_Z, is normal to the plane of projection. The average texture found in the centre of bulk sections, when the growth conditions had stabilised and a coarse columnar β -grain structure was well established, is shown in Figure ***4.20***a. A strong $<001>_\beta$ fibre texture can again be observed, with a maximum intensity of ~ 13 x random. However, despite stitching together 2 very large area maps of 15 x 10 mm^2, the numbers of grains taken for analysis was still only ~50, due to the fact that the β-grains size was very large in the WAAM process. Hence, although this map shows higher texture intensity than for the other processes, due to the poor sampling statistics, caution is required in making direct comparisons. In the averaged data, the distribution of poles round the <001> || N_Z axis is not uniform and, the poles are strengthening randomly around the Nz fibre axis. It can be seen that the α-phase pole figures again indicates a weaker fibre transformation texture. Since the sampling statistic were poor, it is difficult to draw a conclusion as to whether the transformation shows any preferred variant selection.

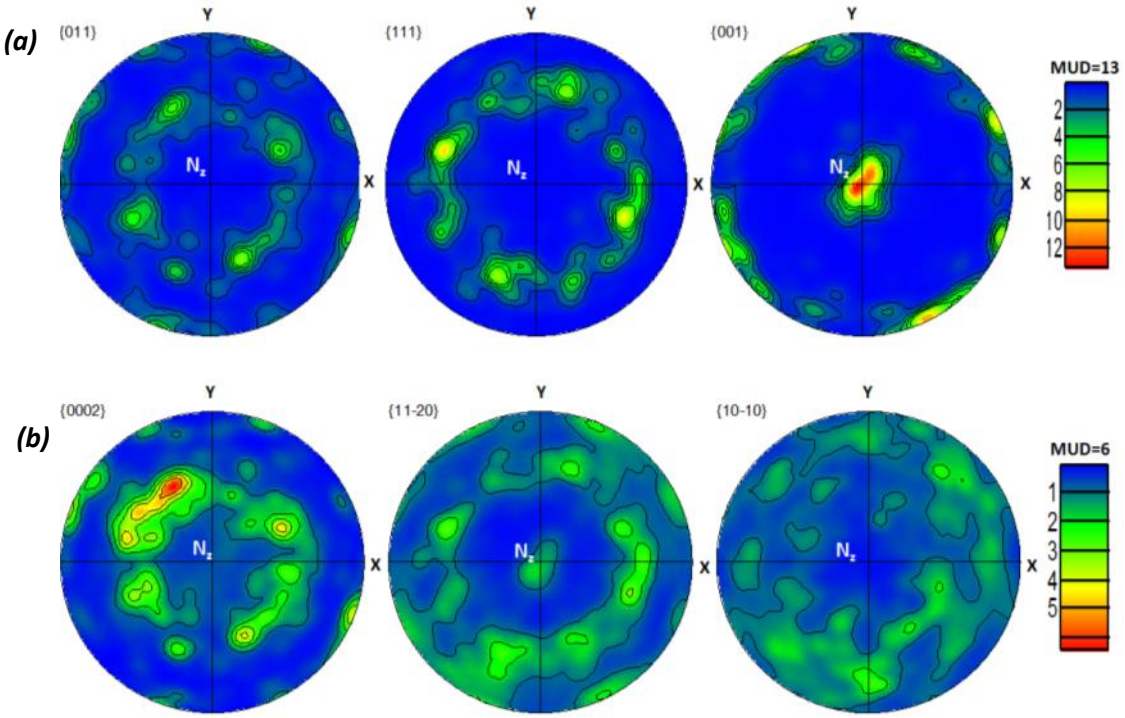

Figure 4.20: *Pole figures depicting reconstructed* β *textures (a), and the α- texture (b) from the centre of a bulk component in a WAAM Ti6Al4V build.*

4.4.4 Discussion of the bulk textures seen in the 3 AM platforms

Overall, a similar β-phase $<001>_{\beta}$ || N_Z fibre texture was observed in all three AM process, in bulk sections. However, subtle variations were seen between the 3 processes, and in particular, different texture intensity were observed for both the primary β and α- phases.

Primary β- textures

It is well know in solidification that metals with a BCC crystal structure have a preferred <001> growth direction [43, 44]. During columnar growth of the β-phase, grain selection occurs giving rise to a preferred $<001>_{\beta}$ orientation aligned with the maximum thermal gradient, which is normal to the solidification front. In directional solidification this can readily lead to an $<001>_{\beta}$ fibre texture, but in processes with a travelling melt pool, like welding, the maximum thermal gradient will vary locally with position because it is perpendicular to the solidification front at the melt pool surface [43, 44, 150]. This is because the melt pool surface is not flat and can be imagined as a 'bowl' shape, although this becomes more elongated, and changes shape from the WAAM to the EBSM and SLM processes. An idea of the different melt pool geometries can be obtained by examining the modelling results shown in Figure *4.2* to Figure *4.4*. The presence of an <001> fibre texture in AM has been previously observed by Moat et al. [117] in their work on laser metal deposition of Waspaloy, where reconstruction of the primary phase was not required.

However, in this study the <001> fibre axis was found to be tilted away from N_Z in the direction of beam travel, by an amount that varied with the process conditions. This effect was attributed to the scanning pattern used, that involved a single beam path that always moved in the same direction, and the curvature of the rear of the melt pool which changed with different beam parameters; i.e., the preferred growth direction was an average of the normal to the curved surface at the rear of the melt pool.

It is thus surprising that in all the processes studied here, texture alignment was found with the build direction and not the melt pool surface. However, this does not mean that there is an influence of heat flow down the wall, because solidification should still be controlled by the maximum thermal gradient normal to the melt pool surface, not the macroscopic far-field heat flow. For the powder bed processes examined, this difference can be related to the rastering pattern used to 'in-fill' the centre of bulk sections within a component. A simple 2 D model can be used to illustrate this point as shown in Figure *4.21*. If it is assumed that the rastering direction reverses each alternate layer. With SLM and EBSM, owing to its elongated shape, which results from the high travel speed, curvature of the melt pool is most pronounced in the transverse plane normal to the beam travel direction (see Figure *4.4* from thermal model). When the beam travel in one direction (-Rx), the <001> β grains starts to grow against the maximum thermal gradient from the base of the melt pool inclined towards -Rx (as shown in Figure *4.21*b). However, in the next layer, when the beam raster's in (+Rx) the maximum thermal gradient in the melt pool will change towards +Rx, and a grain aligned originally with a <001> direction parallel to the melt pool base will now be less favourably orientated as it will be titled away from the melt pool base surface normal (as shown in Figure *4.21*a). Thus, the most favoured average growth direction would be for grains orientated parallel to Nz. In reality, the situation is more complex because in the Arcam machine (EBSM) the rastering direction alternates in Rx and Ry, as well as in +Rx and –Rx and in the SLM process the raster direction rotates by 30˚ each layer. Thus, using the same argument shown schematically in Figure *4.21*, backwards and forwards rastering in orthogonal directions will favour on average selection of grains with a preferential growth direction aligned parallel to Nz. While this explains the Nz aligned fibre direction, in the EBSM process, the β grains showed a strong bulk $<001>_\beta$ fibre texture || Nz with an intensity of about 8, whereas, in the SLM process, the intensity of the bulk $<001>_\beta$ fibre texture || Nz was only ~ 4 to 5 x's random texture. This weaker texture is linked to the more stray columnar grain structure seen in the SLM process, due to the different solidification conditions (see Figure *4.5*).

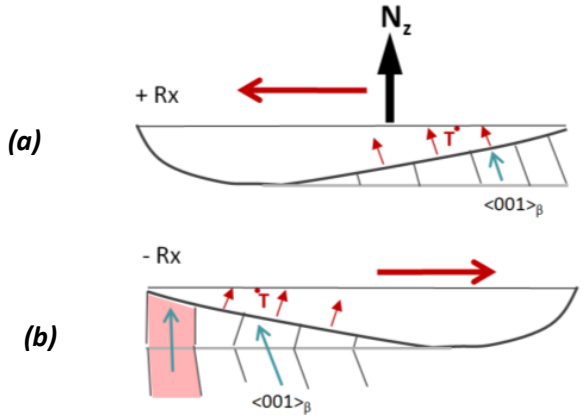

Figure 4.21: *Schematic diagram showing the influence of change in rastering sequence on the growth behaviour of columnar <001>$_\beta$ grains during AM.*

In the WAAM process the heat sources only travels in a parallel direction, but reverses by 180˚ every alternate layer. However, the β grains from this process still showed a strong <001> β || Nz fibre texture with an intensity of 13 x's random. This is more surprising because of the more 'bowl' shaped melt pool. However, the model showed that for this process the melt pool was very shallow (Figure *4.2* to Figure *4.4*) and had a relatively flat base, which with an alternating raster direction would encourage preferred growth in Nz.

α- texture and variant selection

Overall, the transformed α- textures were weaker than the primary β texture in all the AM processes and the α-texture strength decreased in line with the reduction in β texture strength from the WAAM to the EBSM and to the SLM processes. At first sight this suggests there is little variant selection [51, 53] in AM. The α-texture is therefore weakened because it is diluted by the large number of possible orientation variants in the β → α transformation, because there are 12 possible variants [49, 79]. In the EBSM process, the α-phase had a bulk texture, which can be described as a <0002>$_\alpha$ || N_Z fibre transformation texture with a texture intensity of approximately 3 to 4 x's random texture. When compared to the corresponding β- texture, the <0002>$_\alpha$ poles are aligned with the high temperature β texture, but a texture intensity of 8 x's random was observed in the β phase. In the SLM process, the α-transformation texture showed a weaker texture with a maximum intensity of about 2 x's random, since the primary β- texture was already weaker (4 x's random texture) due to the stray columnar grain structure. In the WAAM process, the transformation α- texture was again consistent with the corresponding high temperature β- texture, and the texture intensity was approximately 6 x's random due to the strong primary β fibre texture developed with this process during columnar grain growth.

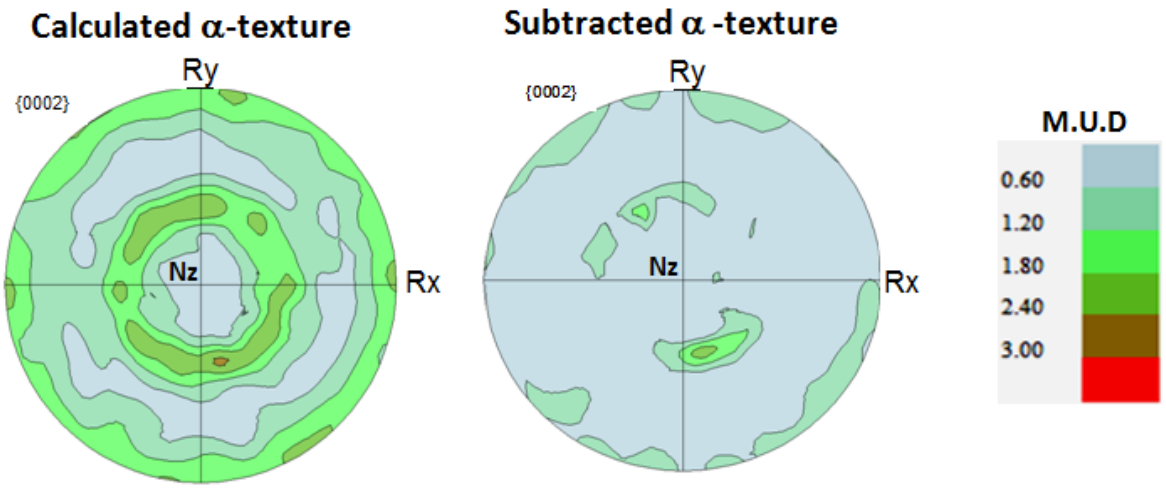

Figure 4.22: *(0001) pole figures: (a for the α-transformation texture calculated from the reconstructed β texture, assuming a random distribution across the 12 Burgers relationship variants; (b) the remaining intensities when the calculated orientations are subtracted from the original measured α pole figure (in the EBSM process).*

When thermo-mechanical processing titanium alloys, it is often observed that stronger transformation textures are observed than predicted from the Burger's relationship because a more limited number of α-plate orientations are formed due to '*Variant Selection'* [53, 54, 76, 133, 153]. An important question is, therefore, if variant selection is observed in AM. The possibility of variant selection was studied using Textan software developed by P Bate [154], which can calculate the theoretically expected transformation texture according to the Burgers relationship, between the α/β phases, without any constrains such as residual stress, or other memory effects. The software allows a random distribution to be assumed over the 12 possible habit variants during a β to α transformation, or conversely over the 6 variants possible when transforming from α to β. Variant selection was not studied in the SLM and WAAM deposits, since the intensity of the primary β texture was very weak in the SLM process and in the WAAM process the sampling statistics were too poor, owing to the very large grain size. Analysis of the possibility of variant selection was therefore carried out only with the EBSM texture data.

On initial inspection, the uniform distribution around the fibre axis in the bulk β and α-texture (Figure *4.18*a, and Figure *4.19*) suggests that there is not strong evidence of variant selection taking place in the EBSM consolidated material. Previous authors [112, 134] have also come to similar conclusions. To confirm if this was indeed the case here, the spatially correlated orientation data from the reconstructed EBSD maps were used to calculate the theoretical transformation texture expected. For this calculation a random distribution was assumed over the

12 possible habit variants in the Textan code. The calculated, non-spatially correlated, random transformation texture is shown in Figure *4.22*a. From comparison of the measured (Figure *4.19*) and calculated random α-texture pole figures (Figure *4.22*a), it can be seen that the two textures are very similar. However, when the calculated and measured orientation data sets are subtracted (as shown in Figure *4.22*b), they are not in complete agreement and the retained orientation spread suggests there maybe some weak alignment with one of the rastering directions (R_x).

Stanford and Bate [53] have provided evidence that at moderate cooling rates preferentially orientated nucleation of grain boundary α, between neighbouring β grains with a mutual parallel <110> direction, gives rise to Widmanstätten α colonies of the same orientation. This results in a stronger transformation texture than predicted with a random variant distribution [79]. However, because the cooling rate is high in AM, and the large β grain size, the nucleation of α colonies mainly occurs within the β-grains, where orientation selection would not be significantly influenced by the grain boundary structure. In support of this argument the colony size measured by Al-Bermani et al. [112] is ~ 20 – 50 µm compared to a grain width of 20 - 500 µm observed in EBSM build as shown in Figure *4.16*. Equally, this mechanism is not relevant in the case of a martensitic transformation. An alternative argument in favour of variant selection in AM is that internal stresses could bias nucleation of the α plates [68]. This has been shown to be theoretically possible for internal stresses greater than 100 MPa [55]. A correlation between variant selection and the sample reference frame (<0001> normal to TD) has also been observed in Ti6Al4V friction stir welds by Davies et al. [134] which was attributed to the presence of residual stresses. In fact, the residual stress in the SLM sample should be very high compared to the EBSM process, due to the higher cooling rate associated with the SLM. However, the effect of higher residual stress associated with SLM is difficult to observe in the texture due to the fine more randomly oriented stray grains. Overall, variant selection has not been observed to be a strong effect in the EBSM process and this has resulted in a weaker, diluted, α-texture. Because substantial internal stresses may be expected, due to the travelling heat source during AM; this is somewhat surprising but may be related to the alternating orthogonal rastering pattern used in beam ratcheting which would change the orientation of the stress field in each layer and the high build temperature, which would cause the residual stresses to relax [8].

4.5 TRANSFORMED MICROSTRUCTURES IN THE AM PROCESSES

It is important to be aware of the transformed α- microstructure typically seen in the AM processes studied, since the colony size, thickness of the α plates, grain boundary α, volume fraction of α and β phases at room temperature, and the presence of diffusionless transformation products, strongly affects the mechanical properties in the final build. This section will therefore focus on comparing the transformed microstructures seen in all three processes, including, their microstructural heterogeneity across the deposited layers with build height.

4.5.1 Transformation microstructure in the SLM process

The transformed bulk α-β microstructure typically seen in the SLM process consisted of a fine tempered martensite α' with a plate like, or acicular morphology, with a small area fraction (~3%) of very fine discontinuous β delineating the plate boundaries, as shown in Figure *4.23*. The volume fraction of β phase was determined from the SEM – BSE image using Image J software by the method proposed by Attallah et al. [155]. Due to the relatively very high cooling rate (>410 K/s) through the β transus after the solidification experienced by each layer, a diffusionless martensitic transformation is expected on cooling [41]. However, the presence of fine β suggest, it has been transformed by subsequent thermal cycles during deposition of subsequent layers and has partially decomposed, as has been reported by other authors [20, 41, 98, 121]. In the SLM process, there was no significant visible microstructural banding with build height, since the layer height and the melt pool is very small and the time at temperature very short compared to other two AM process.

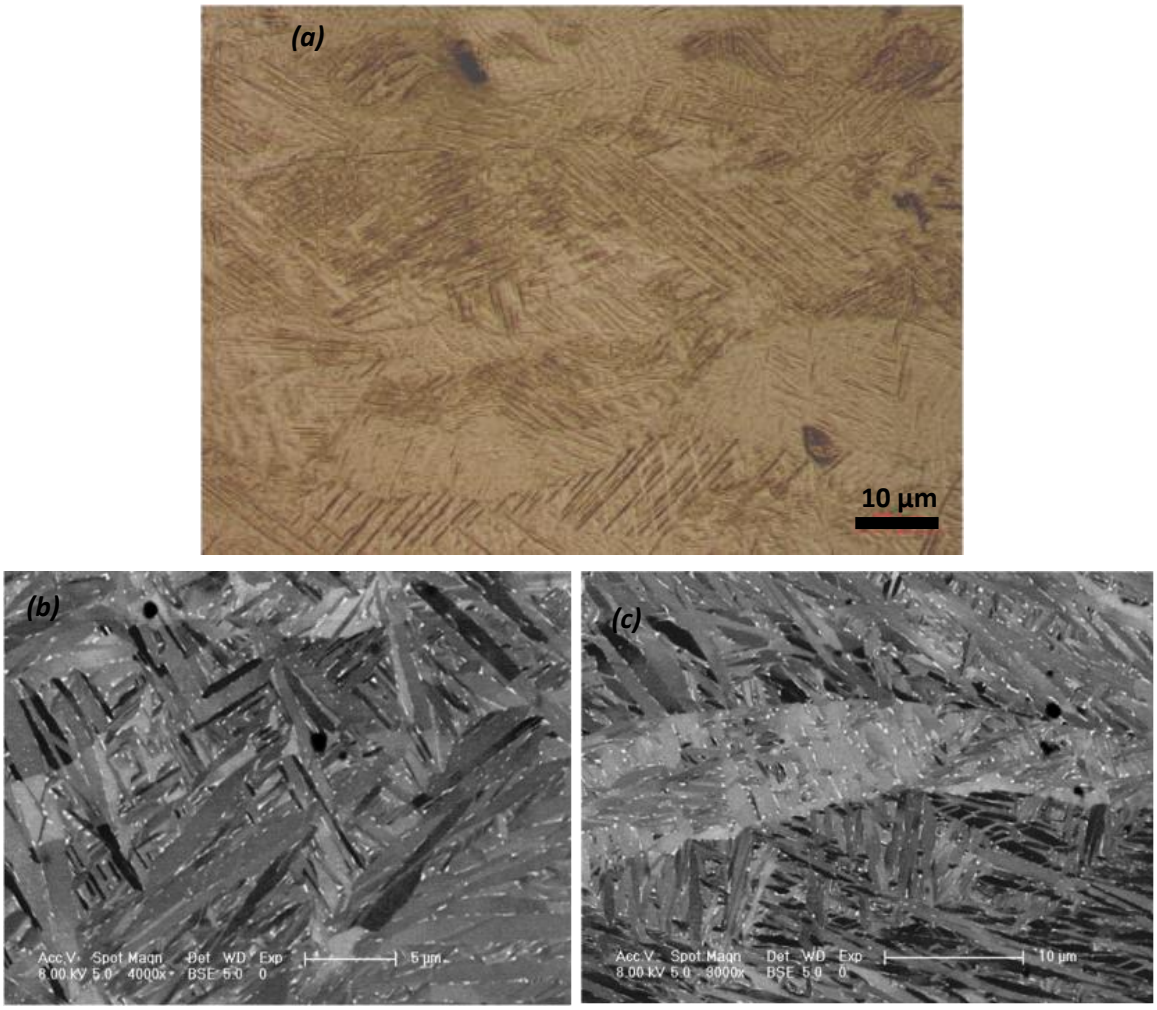

Figure 4.23: *Typical transformation microstructure seen in the SLM process (a) optical micrograph indicating the appearance of martensitic α', (b) SEM – BSE image showing the presence of discontinuous* β *in-between the α plates within the prior* β *grains, and (c) no evidence of grain boundary α between the prior* β *grains.*

4.5.2 Transformation microstructure in the EBSM process

The transformed bulk α-β microstructure typically consisted of a fine annealed Widmanstätten α, or basket weave morphology, with a small volume fraction (~ 5%) of discontinuous β delineating the plate boundaries (see Figure ***4.24***). A thin layer of grain boundary α of about 1.22 µm (thickness) was observed at the parent β-grain boundaries. The presence of fine Widmanstätten α (1.38 µm thickness) plates has been reported by other authors during AM of Ti6Al4Valloy [3, 6, 20, 112]. Overall, the α lamellar thickness suggested a cooling rate of order of 100 K/s, which is similar to that seen in a thin air-cooled component [41]. Grain boundary α is usually formed after long exposure to annealing temperatures (Figure *4.25*c) and may have developed due to the continuous build exposure at 740 ˚C , as reported by Ahmed and Rack [41].

Another noticeable feature of the transformed α-microstructure was banding due to the repetitive thermal cycling experienced by each layer. Banding in the Nz-Rx plane was consistent with the layer height, as shown Figure *4.25*. The inset in Figure *4.25* also shows clear evidence of banding from beam overlap during rastering in the R_x-R_y plane. The sample studied thus showed banding in both the Nz-Rx and Rx-Ry planes, as seen in Figure *4.25*, where systematic microstructural variation could be seen, consisting of a homogeneous grey and thinner light and dark etched bands, caused by the repetitive thermal cycles experienced at a given location and this will be discussed further in section (4.5.5).

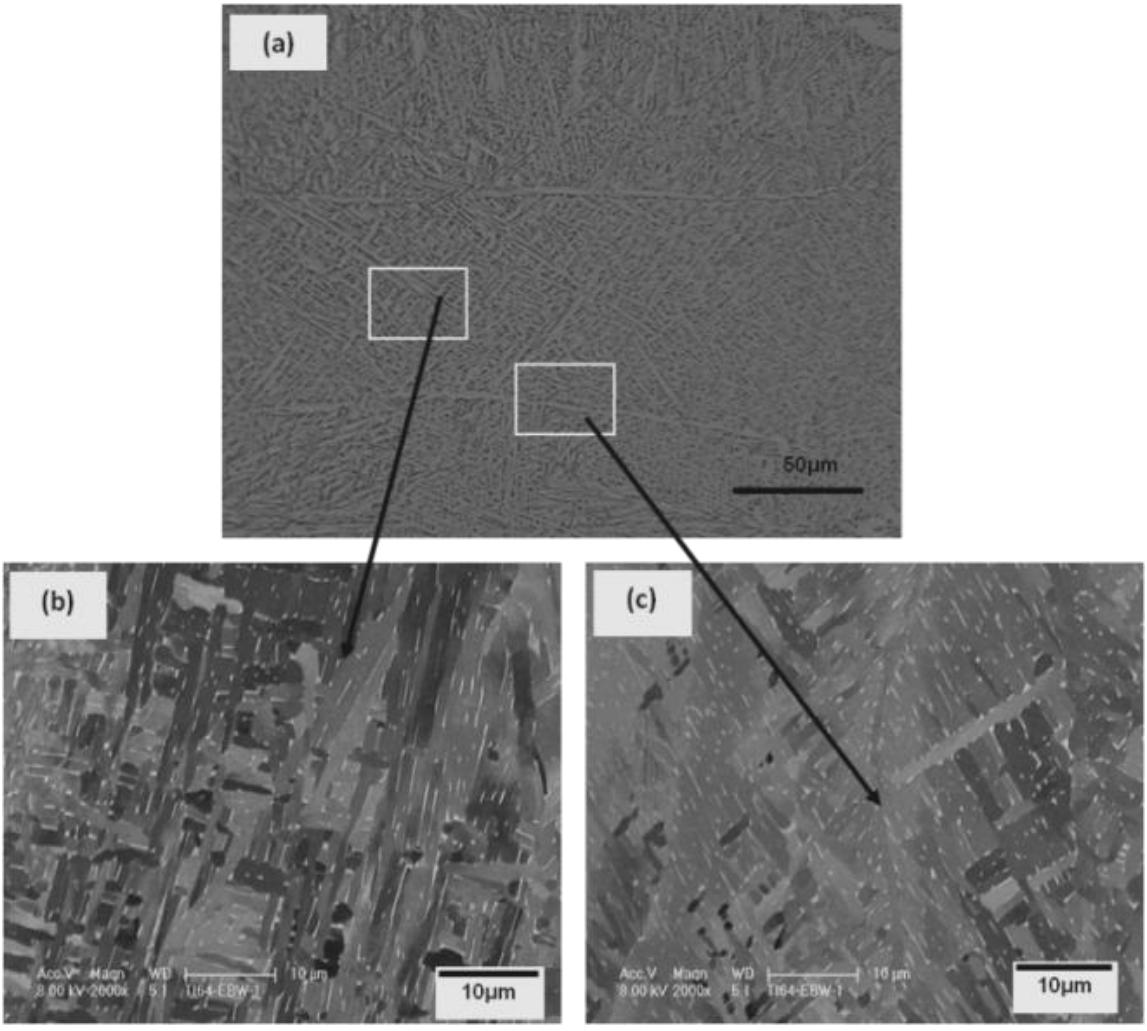

Figure 4.24: *Typical transformation microstructure seen in the EBSM process, (a) fine annealed Widmanstätten α with a basketweave morphology under optical microscopy, (b) the α plates in SEM- BSE imaging, (c) the presence of grain boundary α .*

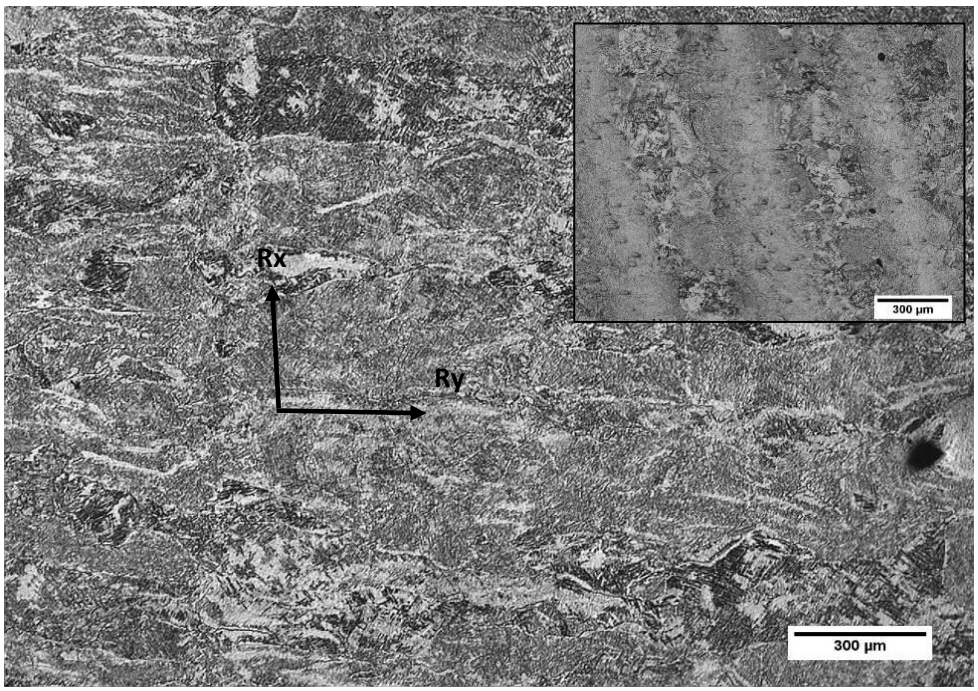

Figure 4.25: *The presence of strong microstructural banding in the R_x-N_z plane and in the R_x-R_y plane (inset) in the EBSM Ti6Al4V sample.*

4.5.3 Transformation microstructures in the WAAM process

In the WAAM process, within the prior β-grains, the typical microstructure consisted of a Widmanstätten α-morphology with a high volume fraction of very fine continuous, and rarely discontinuous β delineating the plate boundaries, as shown in Figure *4.26*. In addition to the presence of the Widmanstätten α within the β grains, coarse colonies of α-plates could be seen originating from grain boundary α with some grains (See Figure *4.26*d). Pronounced banding was also seen in this process. However, the final deposited layer showed the presence of the martensite phase, as shown in Figure *4.26*a. The formation of these different transformed microstructures as well the microstructural banding will be explained in the next section in 4.5.5.

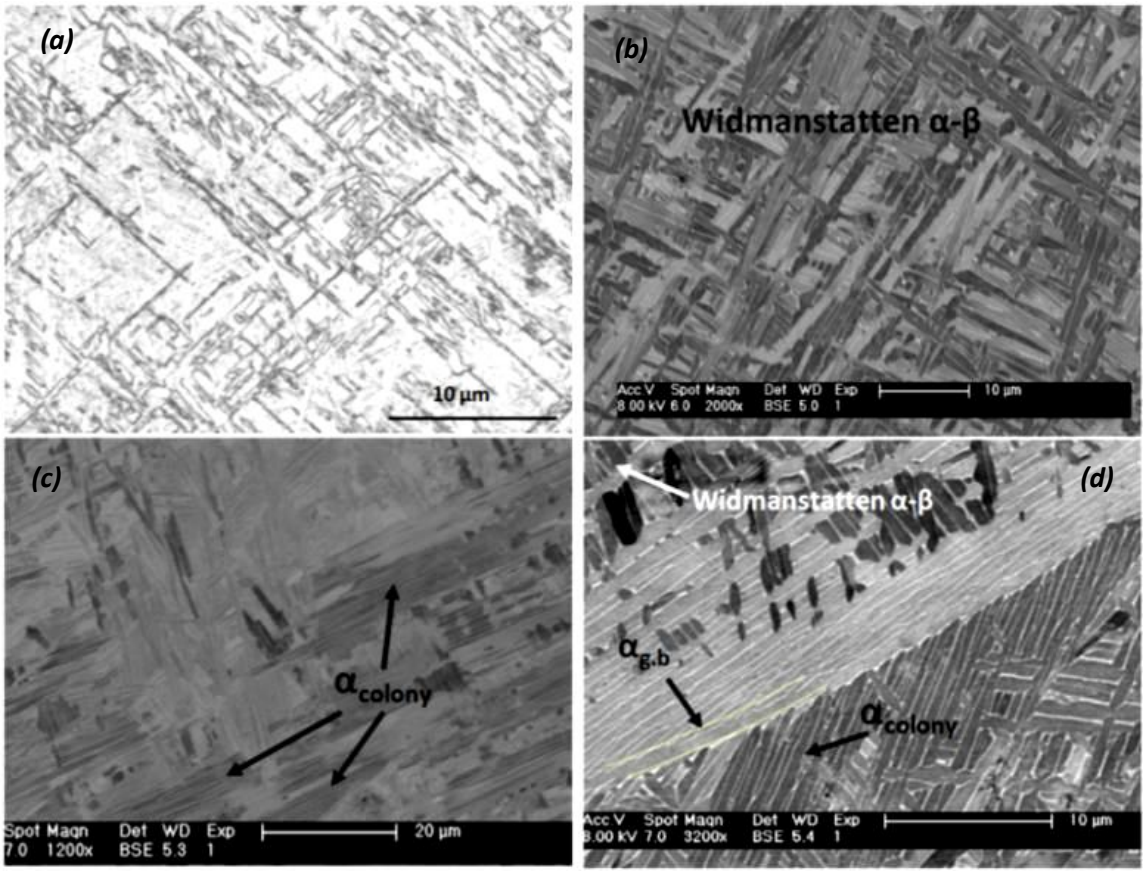

Figure 4.26: *Typical transformation microstructure seen in the WAAM process, (a) showing α' martensitic phase under optical microscopy in the last layer deposited, (b-c) the BSE images of Widmanstätten α+β within the prior β-grains, (b) α-colonies; (d) shows the presence of grain boundary α, and a colony α (near the boundary).*

4.5.4 Defects in the three AM processes

Defects such as lack of fusion, porosity and thermal cracks were observed in the cold powder bed process (SLM), whereas, porosity and lack of fusion were observed in the preheated powder bed EBSM AM processes. In the WAAM process very little porosity was observed. In the powder bed AM process, the powders are consolidated using an electron, or laser beam, to produce a final 3D component, and 100 % densification is difficult, so some porosity is expected in the final component. Figure *4.27* shows examples of the presence of the porosity in the Ti6Al4V sample produced by different AM processes.

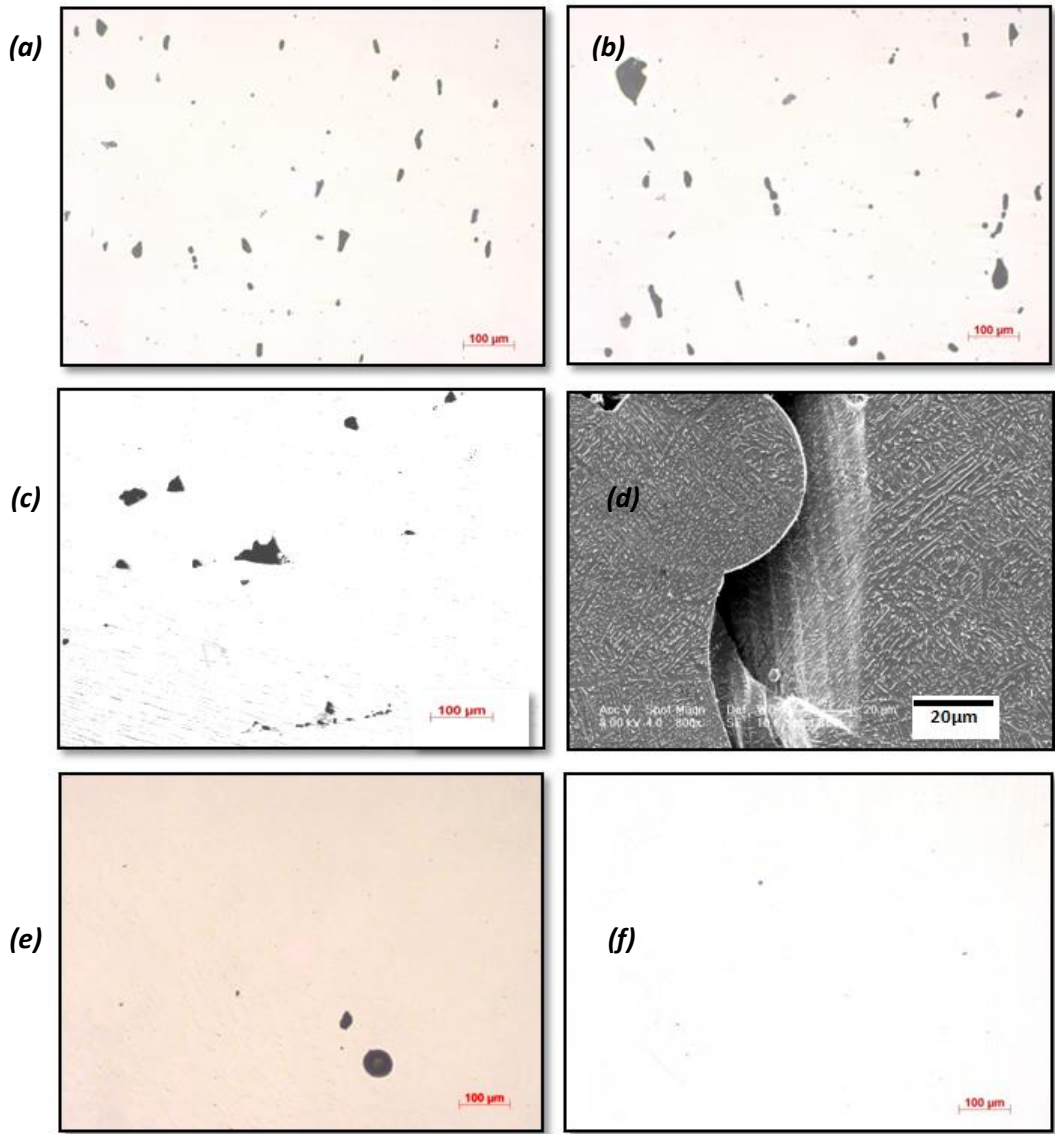

Figure 4.27: *Micrograph showing presence of porosity (a-b) in the SLM samples, (c-d) the presence of porosity and a lack of fusion defect in the EBSM samples and (e-f) the presence of the occasional random pore in WAAM samples.*

Further analysis of porosity was carriedout without etching under the optical microscopy using Image J software at 100 x magnification for all 3 processes (3 fields of view is analysed in each process). The SLM process exhibited a presence of porosity levels ranging from a min of 0.29 % to a max of 1.67 %. The EBSM build also exhibited some porosity (see Figure *4.25*), but the amount of porosity in the EBSM technique was less and, varied from no porosity to a max of 0.84%, which was less than that seen in the SLM process. In comparison to the powder bed AM processes, the WAAM process showed very little porosity, with the occasional randomly located pore. In some instances cracking was also observed with the SLM process (Figure *4.28*).

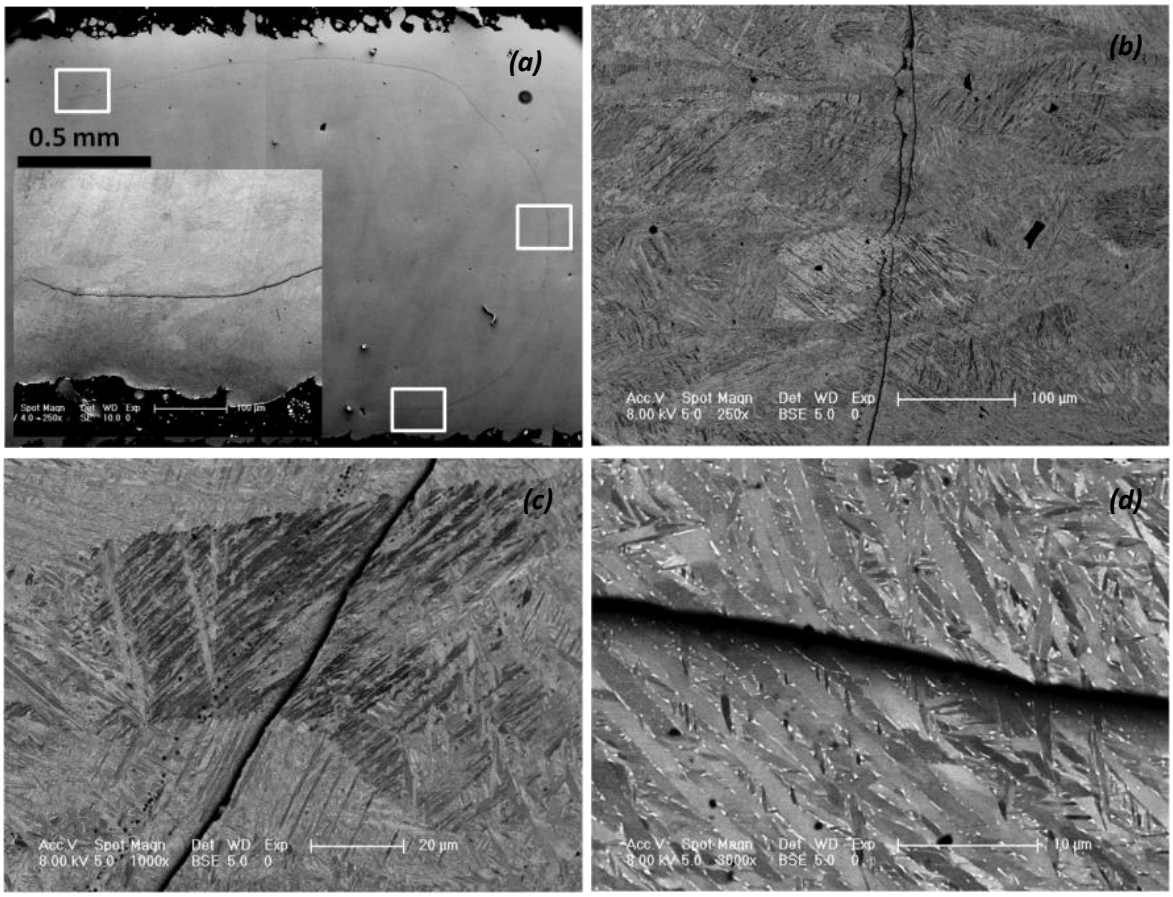

Figure 4.28: *SEM image showing the presence of thermal cracks in a SLM deposits (a) low magnification. (b-d) showing the crack path in relation to prior* β *grain structure and a plate orientation*

Figure *4.28* shows the presence of a crack formed due to the high thermal stresses associated during rapid solidification with a cooling rate of 0.67 to 2.34 x 10^4 K/s, seen in the SLM process. The SEM secondary electron image shown in the Figure *4.28*a confirms the presence of a thermal crack, and the inset in the Figure *4.28*a shows the crack front at a higher magnification. The propagation of the cracks can be seen to be deflected, when it crosses the prior β grain boundaries and had a tendency to follow the α-β interface in Figure *4.28*c.

4.5.5 Discussion on the α-microstructures and defects in the 3 AM platforms

α –transformation microstructure

In AM, on cooling, following solidification of the consolidated powder, the BCC β-primary phase transforms to HCP α with a small fraction of retained β. In fact, a given volume fraction of β may transform more than once, due to thermal cycling into the β-phase field caused by subsequent

heat source passes [25, 39, 156]. Table ***4.7*** shows a comparison of the transformed α-microstructural features, such as the presence of martensite, grain boundary α-thickness, α plate thickness, and area fraction of β including, the primary β grain size for all the three AM processes.

The SLM process showed evidence of martensite α' (see Figure *4.23*) forming during the first thermal cycle experienced within the HAZ from the initial beam pass due to the higher cooling rate associated with the process. The actual cooling rate at the β to α transus temperature (T_β) was not determined from the modelling work but for an approximate comparison, the cooling rate at the melting temperature (T_m) is shown in Table ***4.7***. Because of the very high cooling rates, the β-phase may first transform to martensite, α', (cooling rates > 400 °C/s [41]) and then decompose into tempered α and β on thermal exposure during the repetitive subsequent build cycle [90]. In EBSM, the high target temperature maintained at the top of the build (740 °C) was at the upper end of the reported range of martensite start temperatures of 600 to 800 °C for Ti6Al4V and the cooling rate is lower than in SLM [41, 92, 112, 157], the Widmanstäten microstructure and grain boundary α layer, noted in (Figure ***4.24***), also suggests a diffusional transformation. Nevertheless in both the β → α + β and β → α' transformations the α plates exhibit the same Burger's orientation relationship to the parent phase [5, 41, 79]. Because of crystal symmetry, this provides 12 possible α habit variants, that can form from a single β parent grain, which will dilute the texture in transformed microstructure compared to the parent. The grain boundary α of thickness 1.22 µm seen in EBSM process usually forms when the sample is heat treated for prolonged period of time just below the β-transus temperature and then cooled to room temperature at relatively low cooling rates [41]. There was no such grain boundary α phase in the SLM process.

In EBSM, during the entire build the sample is preheated above the 740 ˚C for prolonged periods of time, and hence, the EBSM builds are more prone to the formation of grain boundary α. In addition to this, the EBSM samples had a discontinuous, but more elongated β phase particles at the boundaries between the α-plates, due to the lower cooling rate in EBSM compared to SLM. In SLM, the entire sample was built on a room temperature substrate plate and cold powder bed system and a lower heat input is used; hence the cooling rate is very high. This lead to no formation of grain boundary α between the prior β grains and, discontinuous very fine β particles present in-between the α-plates in the SLM process.

The cooling rate in the WAAM processes was substantially lower in the powder bed processes. Grain boundary α was consequently observed in the bulk sections with the WAAM process, in addition to colony α plates originating from the boundary α and Widmanstätten α plates, as shown in Figure *4.26*. As has been explained in the literature review (section 1.1), during the solid-state phase β → α transformation, the α-plates initially nucleate from the β grain boundaries

at moderate cooling rate and then rest of the untransformed β phase within the β-grains, transforms into a Widmanstätten α-morphology [39, 41, 113, 156]. In the final layer in the WAAM process, martensite α' phase (Figure *4.26*a) was observed, due to the higher cooling rate at the top of the build, which originates from the application of a high flow rate of shielding gas.

Table 4.7: *Show a comparison of the transformed α-microstructural features for all the three AM processes.*

β grains size (mm)			**Transformed α-phase (μm)**			**β-area fraction in %**	**C.R at T_m x 10^3 K/s**
Rx-Nz Plane		**Rx- Ry**	**α'**	**$\alpha_{g.b}$**	**α_{thick}**		
W	**L**	**Dia.**					
SLM							
0.03- 0.08	0.5-1.5	0.03- 0.22	yes	No	1.11	3	73-837
EBSM							
0.15- 0.30	1.4- 5.0	0.05- 0.56	No	1.22	1.38	5	2-320
Arc AM							
0.50- 2.50	15 - 36	-	final 2 layers	0.82	1.86	8	0. 09-37.5

The thickness of grain boundary α in the WAAM process was ~ 0.82 μm, which less than that of the 1.22 μm larger seen in EBSM. The reason for this could be that wire AM is a cold process with no pre-heating used, and the heat conduction through the base substrate reduces thermal exposure of a particular single layer. The α thickness was therefore less, since the deposited wall substrate plate was not continuously preheated, like in the case of EBSM, where a build temperature of 740˚C is maintained during the entire build. Depending upon the cooling rate, and time of exposure of a particular layer above the β transus temperature, the volume fraction of β phase varied widely. It can be seen from Table ***4.7***, that the SLM process resulted in the least amount of β (3 vol. %) with a very fine discontinuous β morphology in-between the α- plates. Whereas, the EBSM process gave 5 % of discontinuous β phase in-between the α plates. Finally, the slower cooling rate in the WAAM process resulted in an 8 % β volume fraction with a thin continuous β between the α-plates.

Microstructural banding in AM

Microstructural heterogeneity, or banding in the titanium AM has been previously discussed by Kelly and Kampe [25] in the Laser + wire AM process and is a result of the repeated thermal cycles

experienced by the solidified material, with a reducing peak temperature, as the heat source is rastered across the surface each time a new powder layer is consolidated. This was not observed in the SLM process, since the layer height is very small (in the rage of 30 to 40 µm). Whereas in both the EBSM and WAAM processes, a white layer delineating bands of width equivalent to one layer height were seen (Figure *4.25* and Figure *4.11*). These white bands are thought to coincide with a peak temperature isotherm just below the β transus temperature [25].

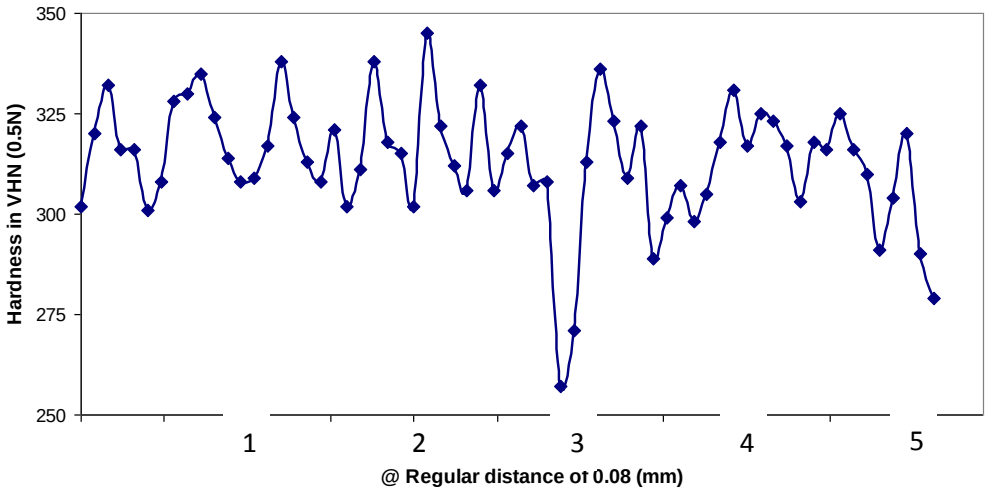

Figure 4.29: *Shows the cyclic changes in the hardness value at a regular interval of 0.08 mm across the Rx-Ry plane using a Vickers microhardness testing machine for the EBSM process.*

The microhardness traverse in Figure ***4.29*** shows that banding also results in a modest cyclic variation in yield stress within the build, due systematic variation in the α lamellar plate spacing. While the microstructure banding was clearly evident in optical microscopy, it was very difficult to capture by SEM, in both SE and BSE mode, since the observed level of contrast was less and not very reproducible. The Figure *4.30* shows that the light band probably contains coarser α plates with a more irregular appearance, which have partially spheroidised during cyclic reheating of the build during overlap of the thermal field from each raster track. This suggests that this region has reached to a high temperature in a range just below the β transus. With distance, into the grey light region, the α-plate size became progressively finer and contained more defined plates, which have thus not experienced such a high temperature after transformation.

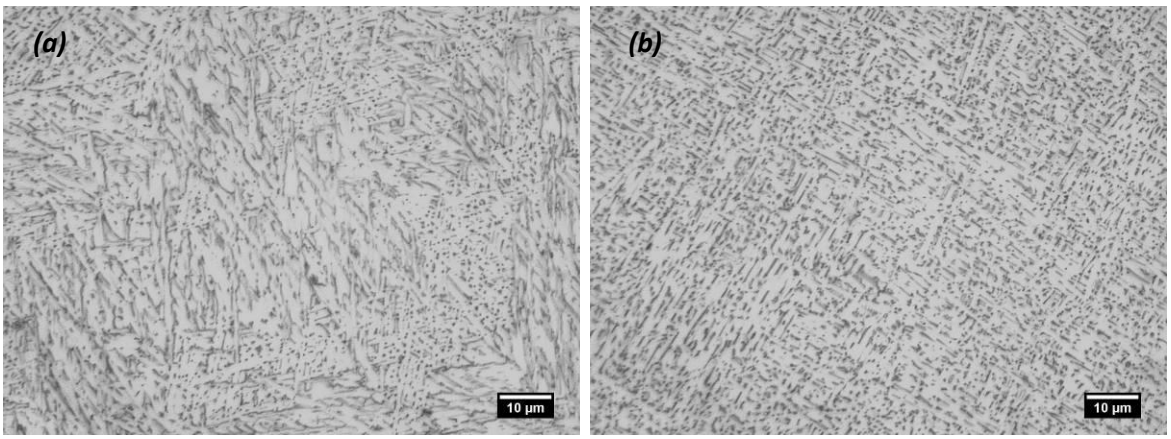

Figure 4.30: *The typical morphology of α phase in the dark region of a band (a), and with a light band region (b) in the EBSM process.*

In WAAM, the optical micrographs also showed clear evidence of a Heat Affected Zone (HAZ) with layers of microstructural banding, due to reheating upon further deposition (Figure *4.11*). The overall structure showed banded large columnar prior β grains with the exception of no banding in the last three layer of deposit. Apart from at the top of the build, the overall microstructures in the banded layers consisted of coarse colony and Widmanstätten α. Whereas, the nominal microstructure in between the layers showed mainly a Widmanstätten α morphology, with a gradient in the α plate thickness, with respect to the temperature reached and cooling rate on re-heating, during the cyclic heat treatments each layer receives. The formation of banding in Wire plus arc AM will not be discussed further here, since Kelly and Kemp [25, 122, 156] have already explained this phenomenon in a Wire pus laser AM process, which is similar to that of banding seen in the WAAM process and this work has been discussed in the literature review (see 2.9.3). Figure ***4.31*** shows the variation in Vickers micro-hardness measured with a 500 gm load at of 0.5 mm intervals along the direction of build for a whole 25 mm height wall in the WAAM process. The hardness varies from a minimum of 287 to a max of 384 (HV) with an average of 350 HV. The hardness reduces from bottom to top, due to the reduction in cooling rate as the build height increases, owing to the greater distance for heat flow to the larger substrate plate. The local variation in hardness seen is again due to banding caused by the cyclic thermal effects and the inhomogeneous distribution of microstructure with change in morphology across each layer. The microstructure layer banding can be completely removed by application of a normalising heat treatment to a TI6Al4V alloy build. Figure *4.32*(a-b) shows an optical micrograph before and after a normalising heat treatment, where the build was solutionised, above the β transus at 1050 ˚C for 30 min (soaking time), then air cooled to room temperature.

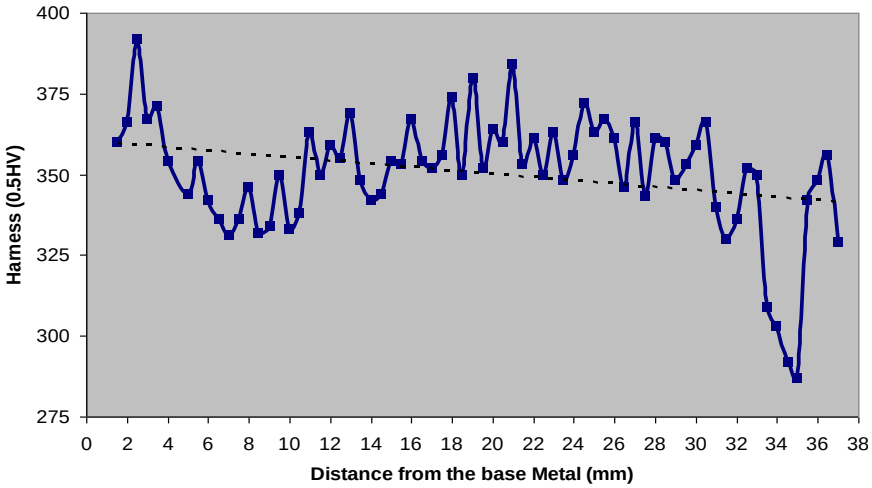

Figure 4.31: *The variations of Vickers hardness along the entire build height in a WAAM deposited wall.*

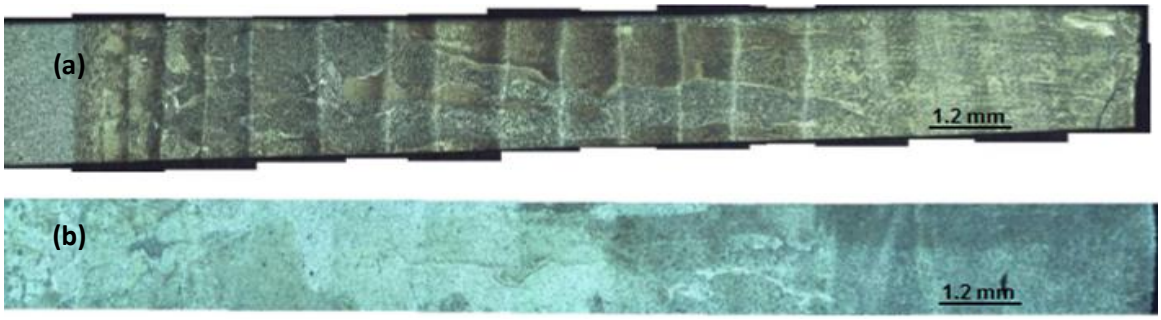

Figure 4.32*: Optical micrographs of a WAAM wall deposit before (a) and after (b) a normalising heat treatment (solutionised, above the* β *transus to 1050 ˚C with 30 min soaking and then air-cooling).*

Defects in AM

Overall, three types of defects were observed in the AM deposits, namely fusion defects, gas porosity and cracking. The amount of porosity in the SLM samples ranged from 0.29 % to 1.67 %. Whereas, within a fixed field of view samples produced via the EBSM technique showed no porosity to max of 0.84 %. In comparison, in the WAAM walls porosity was seen only occasionally and this is possibly caused by moisture on the welding wire. The higher porosity observed in the SLM process is agreement with bulk density values of 98 to 99 % reported by other authors [30, 33, 98, 108]. This value is lower than the bulk density of 99 % reported for the EBSM samples [8, 20, 23, 31, 90, 93, 107]. Entrapped argon gases, variability of coupling between the laser and powder surface, cleanliness of the used powder, and rapid melting at room temperature, tend to increase the level of micro-porosity associated with the laser powder bed technique, and are

reported to be the key reasons for the increased amount of porosity in SLM components. In addition, to the presence of a more brittle martensitic α' phase, thermal cracks can be seen to develop due to the higher cooling rate and low build temperature associated with the SLM techniques, unlike in EBSM where preheating reduces the thermal mismatch between the melt sintered layer and previous layer. The presence of thermal cracks in SLM is probably mainly due to solidification cracking [44, 128, 145]. Solidification cracking generally occurs during solidification, where the surrounding cooling material can exert a tensile stress on the liquid, which results in crack initiation and, the high solid fraction inhibits the backfilling of interdendritic regions, which act as crack initiation points [128, 145].

4.6 CONCLUSIONS

A detailed analysis has been performed on bulk sections from all the three AM build platforms (namely, SLM, EBSM, and WAAM processes) along with the thermal modelling work, to study the evolution of the bulk β grain structures, primary β and transformed α-textures, and the transformed α-microstructure found during AM of a Ti6Al4V alloy. The results and trends obtained can be summarised as follows.

4.6.1 Summary of thermal modelling of AM

The TS4D FEM model with a Gaussian heating source was successfully used to predict and compare the solidification conditions in the three different AM. A summary of the melt pool sizes and shapes, and solidification conditions are shown in Table *4.3* and Table *4.4*. The size of the melt pool increased from the SLM to the EBSM and WAAM process. The melt pool size for EBSM is nearly 9 x's wider than for the laser process. Both SLM and EBSM processes show a 'tear drop' melt pool shape. However, the EBSM process exhibited a comparatively more elongated tear drop shape, compared to the smaller melt pool seen in the SLM process. In comparison, the WAAM process had a much larger melt pool size with a low aspect ratio elliptical shape. The thermal gradients at the solidification front in the melt pools decreased from the SLM to EBSM to the WAAM process. The maximum solidification rate R, at the tail end of the melt pool was observed to be almost equal to the travel speed of the heat source in each process. Owing to the low heat input and high travel speed, the cooling rate was very high in SLM compared to EBSM and, was much lower in the highest heat input WAAM process. Of all three processes, the high cooling rate observed in SLM was due to the fact that the melt pool size was very small owing to the low heat input and the fact that no preheating was employed of the substrate plate, unlike in EBSM. Of the three processes studied, modelling the solidification conditions suggests that the SLM technique most favours formation of fine equiaxed grains as the solidification path just crossed the CET (columnar to equiaxed transition) boundary on the solidification diagram.

4.6.2 Summary of the bulk β grain structures in AM

All the AM processes produce columnar β-grains which grow by epitaxial re-growth up through each melted layer. However, the size of the grains varied with the relative size of the melt pool and the cooling rate observed in each processes. Columnar growth can result in very large grains relative to the component dimensions and an anisotropic microstructure, despite the rapid solidification rates. The size of the melt pool increases and the cooling rate reduces from SLM to EBSM and to the WAAM process, and the prior β grain size also increases from a finer size in the SLM to a moderate size in EBSM and to huge grains in WAAM that can be seen by eye (Table *4.6*). Of all the AM processes, it was found that the SLM process produced the smallest β grains (size of

about 0.03 mm to 0.08 mm in width and 0.5 to 1.5 mm in length). The EBSM process developed β-grains that were bigger than in the SLM process (with a max size of 5 mm in length and 0.33 mm in width). In the arc AM process, the grains size was observed to be very large with dimensions of 2.5 mm wide and 35 mm long, due to the lower cooling rate and large melt pool size than the EBSM and SLM.

The morphology of the columnar β grains can be influenced by the sequence of the heat source rastering in each process. The EBSM process exhibited 'wavy' columnar grains, but in SLM this was not apparent due to the smaller layer height and stray grain structure. Whereas, in the WAAM process, the morphology of the large columnar β grains was less influenced by rastering direction owing to the large melt pool size and the simpler rastering pattern. In the SLM process the columnar growth was intermittent due to the solidification conditions favouring the formation of a stray grains structure. The grain structures produced in bulk samples produced by EBSM have been seen to consist of coarse highly-irregular columnar grains. In comparison, in SLM process, the other powder bed method did not show such irregular β grains in the final microstructure, since the grains were much smaller. The irregular nature of the coarse columnar grains in the EBSM process can be attributed to several factors; variability in coupling with powder of varying packing density and particles size, relaxation of internal stresses, and, or, impingement of imperfectly orientated cells, or dendrite arms, solidification stresses, multiple branching of dendrites, and the generation of crystal defects such as screw dislocations at the solid liquid interface during solidification.

4.6.3 Summary of bulk textures observed in AM

All the AM platforms showed primary columnar β grains with a $<001>_{\beta}$ || Nz fibre texture of different strengths. The primary β-texture strength decreased from the WAAM to the EBSM and SLM processes. The bulk primary β grain size, bulk β texture and the corresponding α-texture for different processes are compared in Table *4.8*. In all the AM processes, the fibre texture was found to be parallel to the build direction (Nz), which at face value is surprising as it should be linked to the maximum thermal gradient normal to the curved melt pool surface during solidification, and not the macroscopic far-field heat flow down the substrate. This discrepancy can be explained by the influence of the rastering pattern employed in AM. The backwards and forwards rastering each alternate every layer changes the direction of maximum thermal gradient in solidifying at the S/L interface in the melt pool. Therefore, after several layers have been deposited, melt-track axial-centreline bulk β grains are preferentially selected that have a <001> direction aligned normal to the base of the melt pool, i.e. $<001>_{\beta}$ parallel to Nz. This occurs because, although grains with orientations closer to the maximum average thermal gradient of the curved melt pool surface have a growth advantage in individual beam passes, they will be more poorly aligned in the next beam pass when the travel direction changes. While this explains

the Nz aligned fibre direction, in the EBSM process, the β grains showed a stronger bulk <001>$_{\beta}$ || Nz fibre texture than in SLM, with an intensity of about 8. It can be seen that of the three AM processes, the SLM process had the best β grains structure, with an almost random final texture due to the broken up fine β columnar grains seen. This is due to the solidification conditions predicted for the SLM process which indicated the highest potential for constitutional super cooling and thus allowed the formation of stray grain structures in the melt pool. In the WAAM process, the primary β grains also showed a very strong <001> β || Nz fibre texture with an intensity of 13 x's random. The strong alignment with build direction is more surprising in this case because of the more 'bowl' shaped melt pool. However, the model showed that for this process the melt pool was very shallow (Figure *4.2* to Figure *4.4*) and had a relatively flat base, when combined with an alternating raster direction this would encourage preferred growth in Nz. In all the AM processes, the room temperature α-phase showed a weaker texture compared to the primary β-texture and the transformation texture strength decreased in line with the reduction in β-texture strength, from the WAAM to the EBSM and to the SLM process. It has been shown that this occurs there because little variant selection operates during AM, and therefore, the α-texture is weakened since it is diluted by the larger number of possible orientation variables in the β → α transformation by 12 possible variants.

Table 4.8: *A comparison of the primary* β*-grain size bulk texture with size, and shape of the melt pool and solidification conditions for all the three different AM processes*

β grains size || Nz		**β grain size || Rx-Ry**	**Bulk texture intensity (MUD)**	
Width (mm)	**Length (mm)**	**Diameter (mm)**	**β- texture**	**α-texture**
SLM Process				
0.03- 0.08	0.5 - 1.5	0.03 - 0.22	8	3
EBSM Process				
0.15-0.30	1.4 - 5.0	0.05 -0.56	4	2
Arc AM Process				
0.50- 2.50	15.0 - 36.0	-	14	6

4.6.4 Summary of the transformed room temperature α-microstructures in AM

The SLM process showed transformed microstructure consisting predominantly of a fine tempered acicular martensite α'-phase. Whereas, the EBSM build showed fine basket weave Widmanstätten α plates within the β matrix. Continuous grain boundary α was also observed in the EBSM, due to the high build temperature (740 ˚C), more moderate cooling rate, and long time

at temperature. Whereas, in the WAAM process a transformed microstructure with a mixture of primary colony α plates and, basket weave Widmanstätten α plates was observed. A thinner grain boundary α layer was also seen between the prior-β grains, with fine martensitic plates in the top layer of the build. The SLM builds did not show grain boundary α due to the very high cooling rates seen in this process, compared to in the other two EBSM and WAAM processes. The thickness of the α plates increased from finest in SLM, to coarser in EBSM and coarser in the WAAM samples, since the cooling rate reduced from SLM to the WAAM process. The volume fraction of β phase at room temperature also increased from SLM to WAAM, since the cooling rate reduces from SLM to WAAM.

Microstructural banding was not visible in the SLM process, owing to the very smaller layer height and melt pool size. However, in the EBSM process, banding was readily seen with careful observation. In the WAAM process the banding was more obvious and clearly visible by the naked eye. In other words, the microstructural banding increased with layer height, or melt pool size, from SLM to EBSM and WAAM. Of the all AM processes, the SLM process showed the largest amount of defects, such as porosity (~1.67 %) and thermal cracks, due to the higher cooling rate, entrapment of shielding gas and variability in coupling with the powder bed. In comparison, EBSM showed less porosity in the final build (~0.8 %). Compared to the other two processes, the WAAM samples exhibited the least porosity with only the occasional gas pore detected.

Following the above analysis of the microstructural and texture behaviour seen in bulk AM sections, it is obvious that the following areas need more understanding and these will be discussed in more detailed in the next two chapters: Firstly, an important question is whether the geometric design freedom of AM has any significant effect on the local microstructure and texture (chapter 5). Secondly, it is vital to know how to improve the microstructure of particular importance is to develop techniques to refine the large columnar prior β-grains seen in AM builds. The possible methods that could be exploited to change this include, by changing the operational parameters, or introducing additional process steps (chapter 6).

5 EFFECT OF GEOMETRY ON β GRAINS IN AM

5.1 INTRODUCTION

This chapter mainly focuses on studying the effect of build geometry on the β grain structures in AM. As a consequence of the complex component designs possible in AM, the β-grain structure and texture are likely to be affected by the local geometry (e.g. different wall thicknesses, section changes, inclination angle etc) because, for example, such features may vary the local direction of heat flow. Such local effects could result in microstructural heterogeneity in critical areas in AM components. It is therefore very important to investigate the effect of component geometry on the heterogeneity of the grain structure and texture in AM.

The EBSM and SLM powder bed processes can both fabricate parts with a high degree of design flexibility. However, in this project most work was carried out on EBSM fabricated samples and equivalent SLM samples were only provided towards the end of the research, by EADS. Hence, the results presented, on the effect of build geometry, concentrate on the EBSM process and will be described first, before a more limited comparison is made to the behaviour of equivalent SLM samples. In this chapter, the influence of different generic geometries that are common features of component designs, on the development of the primary β-grain structure and the local texture will be discussed using EBSM and SLM processes. The influence of geometry on the primary β-grain structure and its texture will be studied using the EBSD reconstructed β phase maps and, its influence on the final room temperature transformation α-texture will also be examined.

5.2 INFLUENCE OF BUILD GEOMETRY ON GRAIN STRUCTURE

5.2.1 Effect of wall thickness in EBSM

To understand the influence of wall thickness and vertical thickness transitions on the formation of the primary β-grain structures and the related β- and α- textures, samples were produced with a thick base on which thinner section walls were built (as shown in Figure *3.6*), using the Arcam EBSM machine with the standard process parameters (shown in Table *3.3*). Figure *5.1* shows cross sections parallel to the build direction (Rx-Nz plane) of reconstructed β-grain structures seen in the EBSM process through the transition from a wide section base to vertical walls of increasing

thickness, from 1 to 5 mm. The base section was built first to a height of 5 mm to ensure a coarse-columnar structure was fully established before adding the thinner walls. Sections through the walls parallel to the build direction (Nz-Rx) and to the deposited layers (Rx-Ry plane) are shown in Figure *5.1* at a height of 5 mm, once the grain structure was no longer influenced by the base.

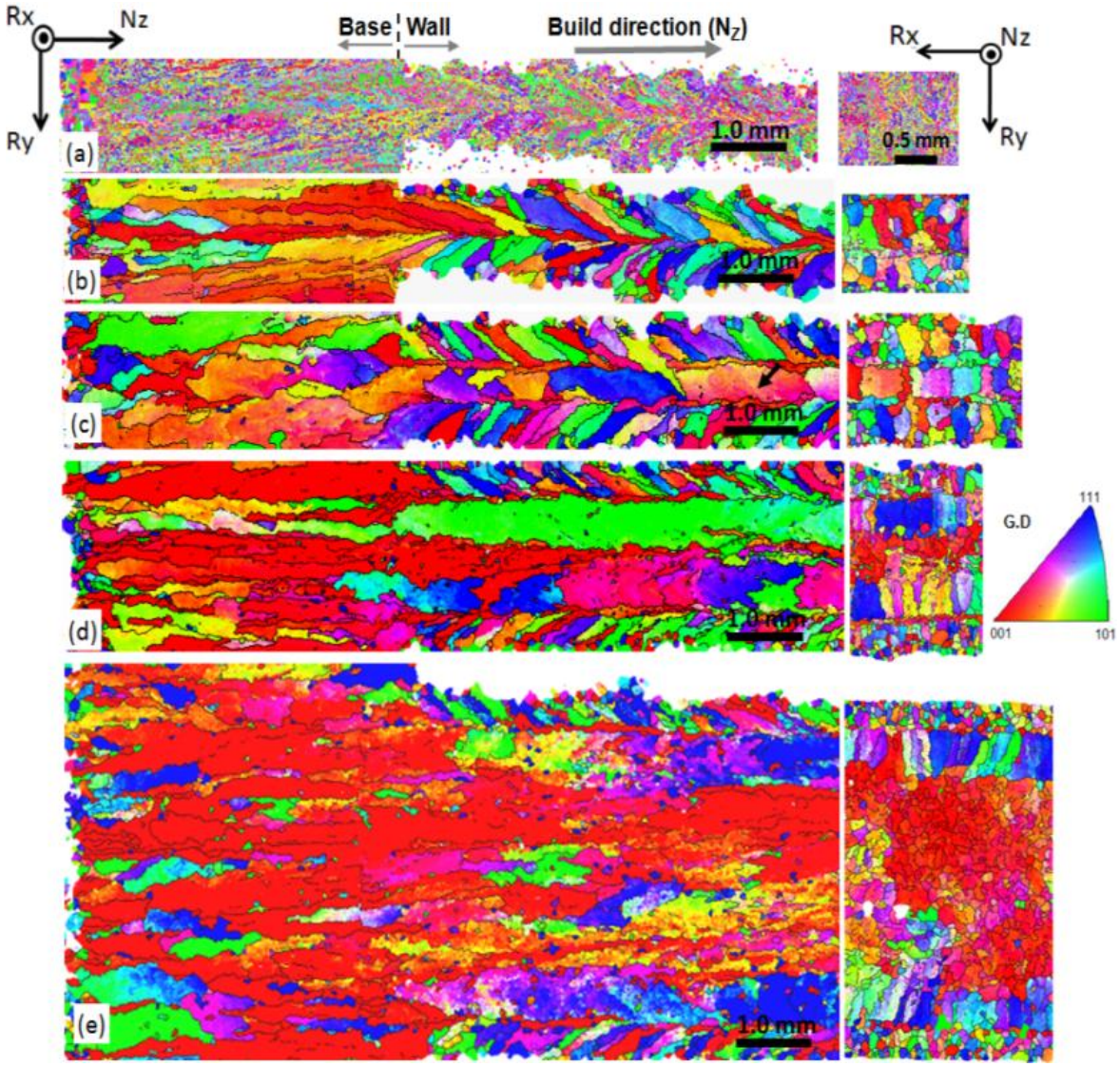

Figure 5.1: *EBSD maps of vertical (R_X–N_Z) cross sections through the transition from a continuous thick section to different wall thicknesses in EBSM samples; (a) showing an example of an original α phase map and (b) – (e) reconstructed* β *grain structures for 1 mm, 1.5 mm, 2.0 mm, and 5 mm, wall transitions, respectively. The accompanying plan view cross sections (R_X–R_y) are from half way up the vertical walls. The black lines delineate boundaries greater than 15° in misorientation. Orientation contrast is according to the inverse pole figure aligned parallel to Nz.*

An example of a typical original α-phase map from which the β-grain structure in Figure *5.1*b was reconstructed is given in Figure *5.1*a. The thinnest 1.0 mm wall was produced with a single contour pass, with no in-fill hatching. In Figure *5.1* it can be seen that there is a significant effect of reducing the section thickness of the walls. In the thinnest 1 mm wall (Figure *5.1*b) growth inwards can be seen from both wall faces, cutting off the coarse grains from the base plate and this leads to a defined centreline boundary in the melt pool track.

The thickness of the next wall was increased to 1.5 mm (Figure *5.1*c), and this wall was produced by two contour passes (~ 1 mm wide) overlapping by ~ 50%. In this case, inward growth of the fine columnar grains did not cross the whole section and vertical columnar growth of extremely long grains was able to continue up the wall's centre from the base section, leading to a "sandwich-like" grain structure. Indeed, all the thicker walls were observed to have a skin of inward-growing fine columnar grains, of ~ 0.5 mm thick, or about half the width of the contour pass melt pool (Figure *5.1*c - e). Once the wall thickness became greater than ~ 2 mm, consolidation in the centre of the cross sections required cross-hatching. This produced the coarse irregular vertical columnar grain structure already discussed in 4.3.4 within wall centres that continued up from, and looked similar to, that seen in the base slab. As noted previously for the bulk sections 4.3.4, in thicker walls uninterrupted growth of most of the coarse columnar grains was seen across the entire EBSD maps and often carried on to the top of the component sections.

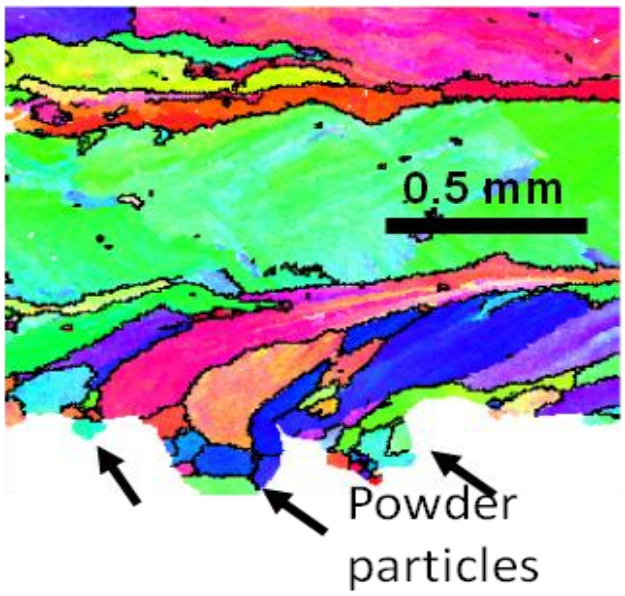

Figure 5.2: *Higher magnification view of reconstructed* β *grain structure showing the nucleation of grains from the powder bed at the component surface in the EBSM process.*

In the coarse scale EBSD maps (Figure *5.1*) data was missing from near the wall surfaces, because of the difficulty of indexing close to the sample edge. More careful mapping at a higher resolution with the EBSM samples revealed the surface layer from which the surface skin of curved columnar grains developed. In Figure *5.2*, heterogeneous nucleation, or epitaxial re-growth, can be seen to occur from the partially-melted powder particles contacting the wall surface in the surrounding powder bed. This nucleation layer was confined to the powder contacting the immediate component surface and was thinner than the equiaxed zone found at the base of the build, above the stainless steel build plate, where partial alloying with the substrate also occurred (see section 4.3).

5.2.2 Effect of wall thickness transitions in SLM

To understand the effect of wall thickness and vertical thickness transitions on the formation of the primary β-grain structures and related β- and α- textures in the SLM process, a similar sample with a thick base and added thin wall sections was produced (as shown in Figure *3.8*) with the standard process parameters shown in Table *3.4*. Figure *5.3* shows reconstructed β-grain structures seen in this sample through the transition from the wide section base to vertical walls of increasing thickness, from 0.4 to 2 mm. With the SLM sample, the base section was also built first to a height of 10 mm to ensure a coarse-columnar structure was fully established before adding the walls. Sections through the walls parallel to the build direction (Nz-Rx plane) and to the deposited layers (Rx-Ry plane) are again shown in Figure *5.3*, once the grain structure was no longer influenced by the base.

The thinnest wall produced with the SLM process was about 0.4 mm which involved two over lapping contour passes. Once the wall thickness became greater than ~ 0.4 mm, consolidation in the centre of the cross sections required cross-hatching. The thickness of the next wall was increased to 1.0 mm (Figure *5.3*c), and this wall was produced with a contour pass around the edge of component and then infill cross-hatching. With the SLM process, this cycle repeats with a 30˚ rotation of infill hatching upon the deposition of every new layer. All the walls, including thicker ones were observed to have a skin of fine inward-growing columnar grains, of ~ 0.15 mm to 0.20 mm thick, which is approximately equal to the half the melt pool width. However, this was only obvious in the Rx-Ry plane and the SLM powder bed process showed a much less significant skin effect when compared to the EBSM process, where the skin thickness was about 0.5 mm.

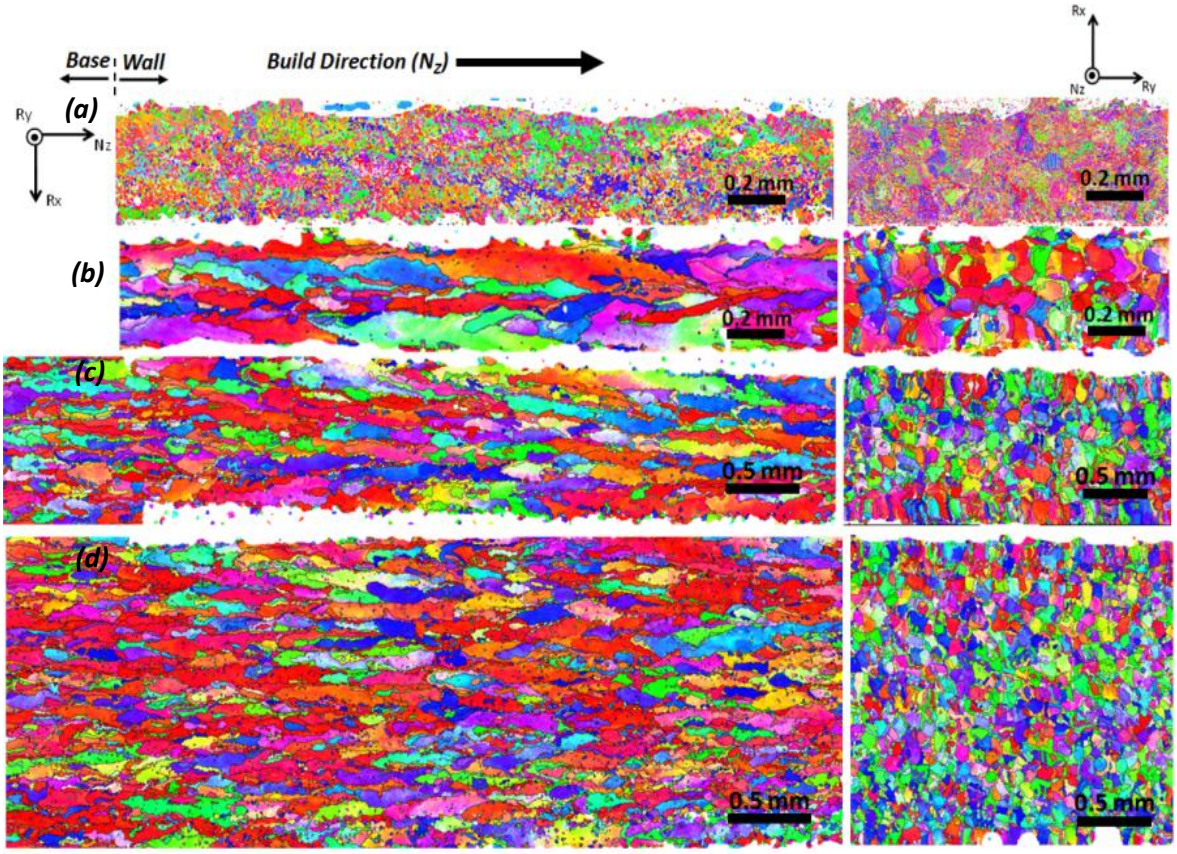

Figure 5.3: *EBSD maps of vertical (R_X–N_Z) cross sections through the transition from a continuous thick section to different wall thicknesses in the SLM process; (a) showing an example of an original α phase map and (b) – (d) reconstructed* β *grain structures for 0.4 mm, 1.0 mm, and 2.0 mm, wall transitions, respectively. The accompanying plan view cross sections (R_X–R_y) are from half way up the vertical walls.*

In the centre of thicker walls, where in-fill hatching and contour hatching with a 30 degree rotation every new layer is employed, fine columnar grains can be seen with a predominant <001> fibre orientation (red colouring in Rx-Nz plane of the Figure *5.3*), as has been discussed in 4.3.4. The bulk grain structure has been previously described and exhibited a fine stray β-grain structure with a size of about 0.25mm to 2 mm in length and, a width of 0.3 mm.

5.2.3 Effect of wall thickness inverse transitions in EBSM

The effect of a capping section, or inverse wall transition, was also studied with the EBSM process using the sample design shown in Figure *3.6*. In Figure *5.4* examples are shown of the primary β-grain structure (Rx-Nz plane) across a section transition from the two thinnest walls to a wide capping section, or horizontal wall (see Figure *3.6*b). In this case the walls were first built directly from the stainless steel base plate to a height of 30 mm, to obtain steady state conditions, before

adding the horizontal section. These two walls can be seen to have a similar structure to those in Figure *5.1*.

In the horizontal capping section, distant from the vertical wall junctions, a similar structure is seen to that previously described for bulk sections, but without the influence of alloying, or the chill, from the steel substrate base plate. At the base of the horizontal section, fine equiaxed grains are seen in the first melted layer originating from partially melted powder contacting the wall bottom surface. The different grain structure of the grains nucleated from the surface of thin walls can be seen to grow into the horizontal capping section as coarse, irregular-columnar grains (as shown Figure *5.4*) creating a local heterogeneity in the horizontal section. However, red grains with a <001> β || Nz orientation that nucleated from the wall skin, or from the bottom of the powder bed, continued to grow as large grains, whereas the other grains were cut-off or overrun by these faster growing grains, as shown in Figure *5.4*b.

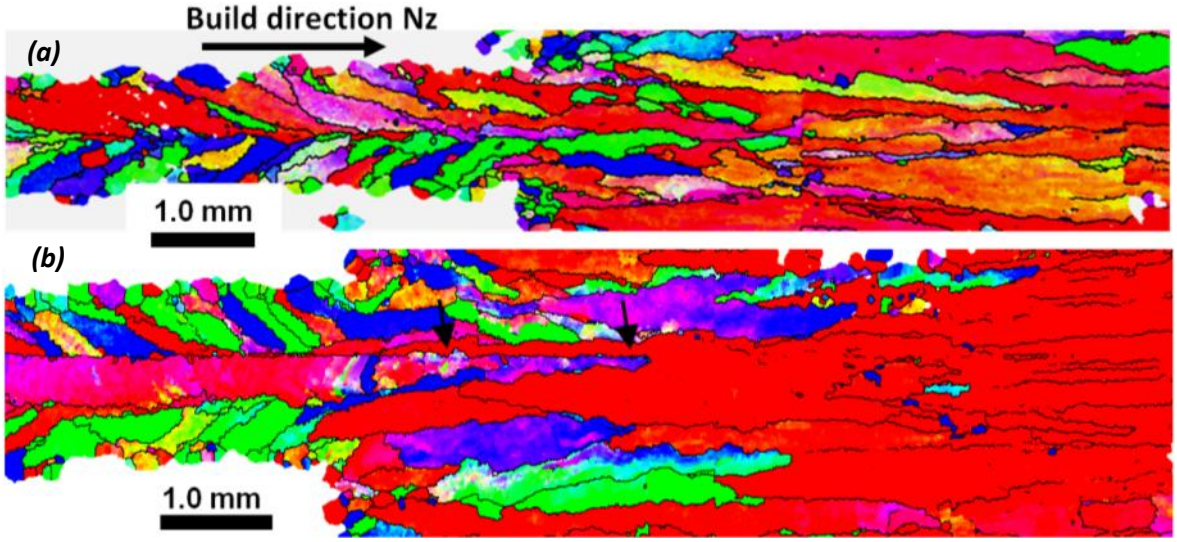

Figure 5.4: *Reconstructed β grain structures showing longitudinal cross sections (through the wall thickness inverse transition sample from (a) a 1mm and (b) 1.5 mm vertical wall to a thick horizontal capping slab.*

5.2.4 Effect of wall inclination angle in EBSM

The effect of building inclined walls on the β grain structure was studied again with the EBSM process. Figure *5.5* shows examples of sections through 3 mm thick walls, built at inclined angles of 30˚, 45˚, and 60˚ relative to the build direction N_Z. The primary β-grain structure can be seen to develop vertically upwards, normal to the powder deposited layers irrespective of the wall

inclination angle once columnar β grains become established. The columnar β grains again develop from a skin layer nucleated from the powder bed, within the contour pass.

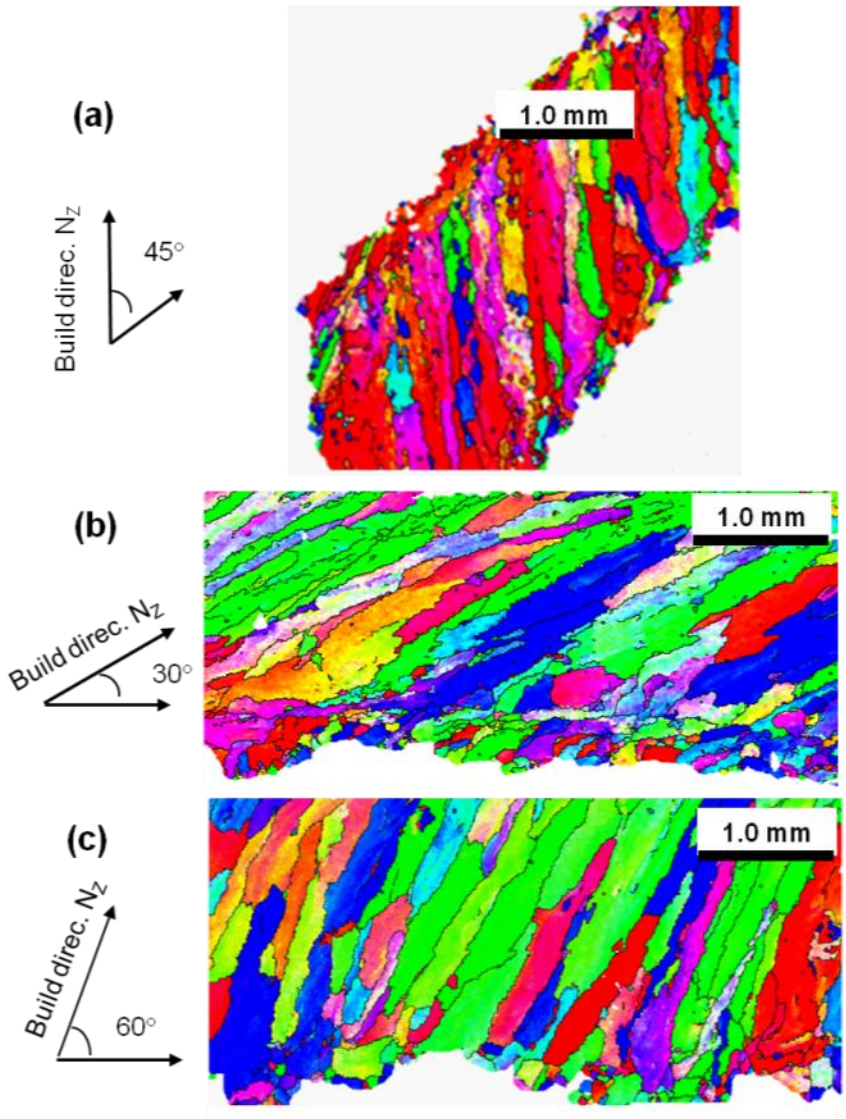

Figure 5.5: *Reconstructed β-grain structures from 5 mm thick inclined walls (a) 45° macro view, and the bottom of walls inclined at angles of (b) 30° and (c) 60°, to the vertical.*

5.2.5 'V'- transitions in EBSM

A 'V' shaped section attached to a bulk horizontal base was used (shown in Figure *3.6*) to study the effect of a transition from a steady-state, thick section through a narrow constriction (1 mm wide). In the EBSD image, shown in Figure *5.6*a, a single grain with a <001> || N_Z orientation can be seen to be selected by the constriction. This grain initially expands as it carries on growing upwards through the subsequently deposited layers. However, columnar grains also develop from the contour skin layer contacting the powder bed at the base of the V-section, either side of where it is attached, which prevent this grains talking over the entire section width.

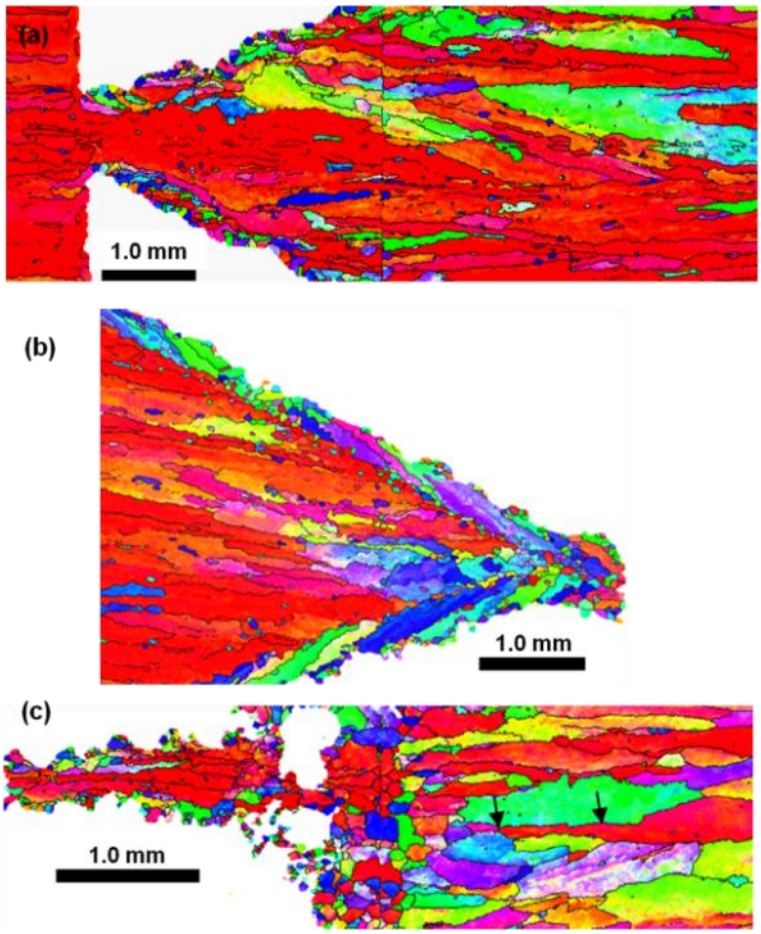

Figure 5.6: *Reconstructed β grain structures showing longitudinal cross sections through the V-transition samples (a) from a flat plate to a V-section and (b) the tip of an inverted V-section (c) through the attachment point of a support web.*

It is also of interest to observe what happens when a V section is inverted, with respect to the build direction (N_Z). In this case there is a continuously reducing section width. The tip of this sample is shown in Figure *5.6*b, where it can be seen that the large <001> || N_Z orientated (red) columnar grains within the bulk section are simply terminated by a thin skin layer of fine inward growing columnar grains formed in the contour pass.

5.2.6 Support structures in EBSM

Support structures are thin webs which are used to prevent collapse of more complex geometries during manufacture using the powder bed method [127]. These thin webs are attached to the component by a small point. This geometry was studied in the EBSM process using a sample where a typical support had been used (see Figure *3.6*), and as can be seen from Figure *5.6*c, in

this case the effect on the β-grain structure in the supported part is negligible. The red <001> || N_Z fibre orientated columnar grains seen in Figure *5.6*c from within the support web do not, grow significantly into the attached part.

5.2.7 'X' – transitions in EBSM

Finally, the typical behaviour of the β-grain structure within the 90° crossover region of two vertical walls, 1.0 mm and 1.5 mm thick, was studied with the EBSM process (see Figure *3.6*). In Figure ***5.7***, examples are given of the 1.0 mm and 1.5 mm thick sections produced by a contour pass that drew round the profile, with no in-fill hatching. In this case, the grain structure can be seen to be similar to that seen in the straight walls of the same thickness, but followed the contour pass beam track, as it turned through 90˚ to follow the corners created by the cross-over section.

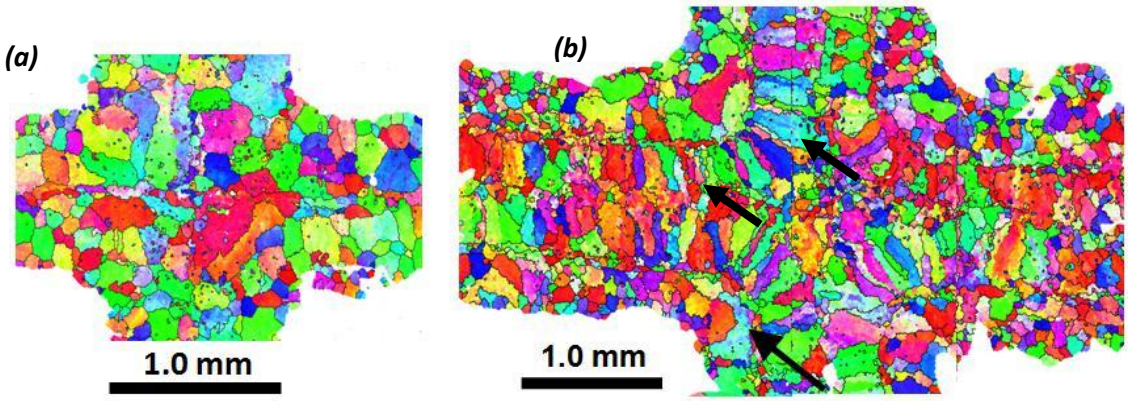

Figure 5.7: *Reconstructed* β *grain structures showing transverse Rx-Ry cross-sections through 'X' – cross over transitions between two thin 1.0 mm and 1.5 mm vertical walls.*

5.2.8 Discussion of the influence of build geometry on β grain structures in AM

The EBSD data presented and the observations made show that the local grain structure can be significantly influenced by the geometry of the component design, partly as a result of the effect this has on the heat flow, but more importantly, because of skin effects, caused by the outline contour pass and interaction with the surrounding powder bed.

Effect of skin layers

Skin effects are caused by surface nucleation that occurs from the surrounding powder bed, as shown in Figure *5.2*. It can be observed that there is a significant effect of changing the wall

thickness with the EBSM process. In the thinnest 1 mm wall the columnar structure growing up from the base was cut-off near the wall root, by finer curved-columnar, grains growing in from the wall faces, which meet in the middle of the wall. This was the minimum wall thickness that could be produced by the EBSM process and was built using only a single contour pass with no in-fill hatching. This 1 mm wall showed heterogeneous nucleation of β grains from the partially melted powder in the powder bed, which grew inwards from both wall faces, cutting off the coarse grains from the base plate, as shown in Figure *5.1*b. In this case the fine columnar grains grew clearly following the maximum thermal gradient, normal to the curved melt pool surface. The inward growths from both wall surfaces lead to the formation of a centreline boundary which is similar to that seen in a fusion weld bead if there is no nucleation ahead of a solidifying S/L interface during solidification [44, 128].

When the wall thickness was increased to 1.5 mm, two contour pass that overlapped by 50 % were used. In this case, inward growth of columnar grains did not cross the entire cross-section, because the vertical columnar grains from the base were able to continue to grow in the centre of the 1.5 mm wall and this led to the 'sandwich-like' grain structure shown in Figure *5.1*c. This occurs because, when the wall width was too wide to be produced by a single pass, the inner half of the melt pool does not contact the powder bed, except at the top surface where the powder is spread over the solid build section. Hence, on the inner side of the melt pool track there was no new supply of nuclei, so that epitaxial re-growth takes place up from bottom of the melt pool, from the previously consolidated layer, resulting in the formation of long, coarse, columnar grains growing vertically up from the base plate. Whereas, in the outer-half of the outline contour pass curved columnar grains still grow inwards towards the centreline of the melt pool nucleated from the powder contacting the surface. In the cross-section view parallel to the EBSM deposited layers (Rx – Ry) shown in Figure *5.1*c, it can be seen that the transverse boundaries for these grains are regular in appearance and aligned, which is consistent with one side of the "herring bone" columnar grain structures seen in welds when there is an elongated tear drop shaped weld pool [44, 128]. These grains thus have a regular lathe morphology aligned with their long axis parallel to N_Z, but appear with a blue tint in the EBSD-IPF maps and are tilted away from <001> || N_Z towards <111> || N_Z (see Figure *5.1*c-e). Furthermore, at the centreline of the contour pass, individual *inward*-growing grains from the fine curved-columnar structure were noted to bend round and start growing up the wall, as thin grains sandwiched between the outer curved-columnar and inner growing coarse-vertical columnar grains, which meet in the middle of the melt pool (Figure *5.8*; arrow). These grains always appeared red in the IPF orientation contrast maps and had a <001> direction closely aligned with the build direction (N_Z). Their behaviour is similar to the centreline 'axial' grains sometimes found in weld pool solidification [44, 150].

A further increase in wall thickness to > 2 mm, or, greater, required both the contour pass and 'infill' cross hatching rastering which resulted in a different bulk grain structure generated in the centre of thick sections. This structure has already been discussed in chapter 4.

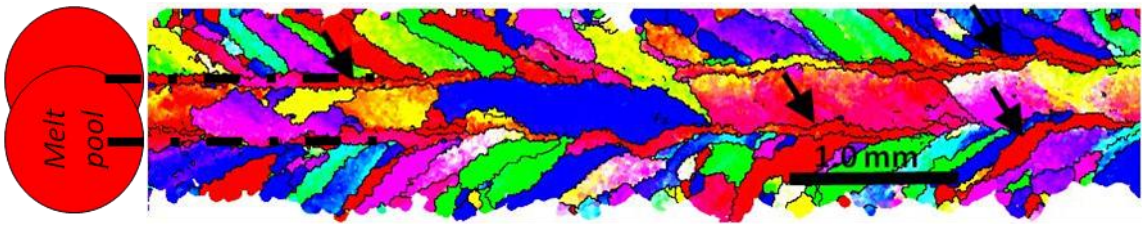

Figure 5.8: *The EBSD reconstructed β grain structure map showing centre line axial grains at the melt pool centre line, between inward and columnar vertical growth in the contour pass in the 1.5 mm wall using EBSM process.*

In EBSM the contour pass, that outlines a component's section perimeter, is drawn first in each newly spread powder layer. As discussed above, this gives rise to a surface skin that has a significantly different grain structure and texture to that seen in the bulk of thick sections, where 'in-fill' hatching is required. This skin effect is shown in the Rx-Ry section in Figure *5.9* and was observed in all the thicker walls which had a skin of inward growing fine columnar grains of approximately 0.5 mm thick, or about half the widths of the contour pass melt pool track on both sides. In addition to this, regular vertical columnar grains (with a herringbone structure) were observed growing upwards from the inner half of the contour pass. The 'red' central line axial <001> β grains seen in Figure *5.8* between the regular and inward growing columnar grains can also be seen in Figure *5.9*. Finally, in the bulk section, over many deposited layers, selection of favourably orientated grains lead to the development of large irregular columnar grains as discussed in section 1.1. EBSD orientation measurements showed that in the contour pass the grains in both the outer and inner skin layers, tended to be tilted away from the Nz orientation, due to the direction of maximum thermal gradient not being vertical (shown in Figure *4.2*), but normal to the curved solidification front. Whereas, in the bulk sections large columnar grains aligned with a <001> || Nz fibre orientation (Figure *5.9*, red in colour) developed. As discussed previously in section 4.3, the <001>||Nz bulk fibre texture develops by average selection of a preferential <001> || Nz growth direction over many layers, due to the altering rastering pattern used in in-fill hatching..

The complex skin and core grain structures produced by the contour and in-fill hatching passes in the EBSM process are highlighted and summarised schematically in Figure *5.10* to Figure *5.12* for the 1.0 mm, 1.5 mm and, > 2 mm thick wall samples, respectively.

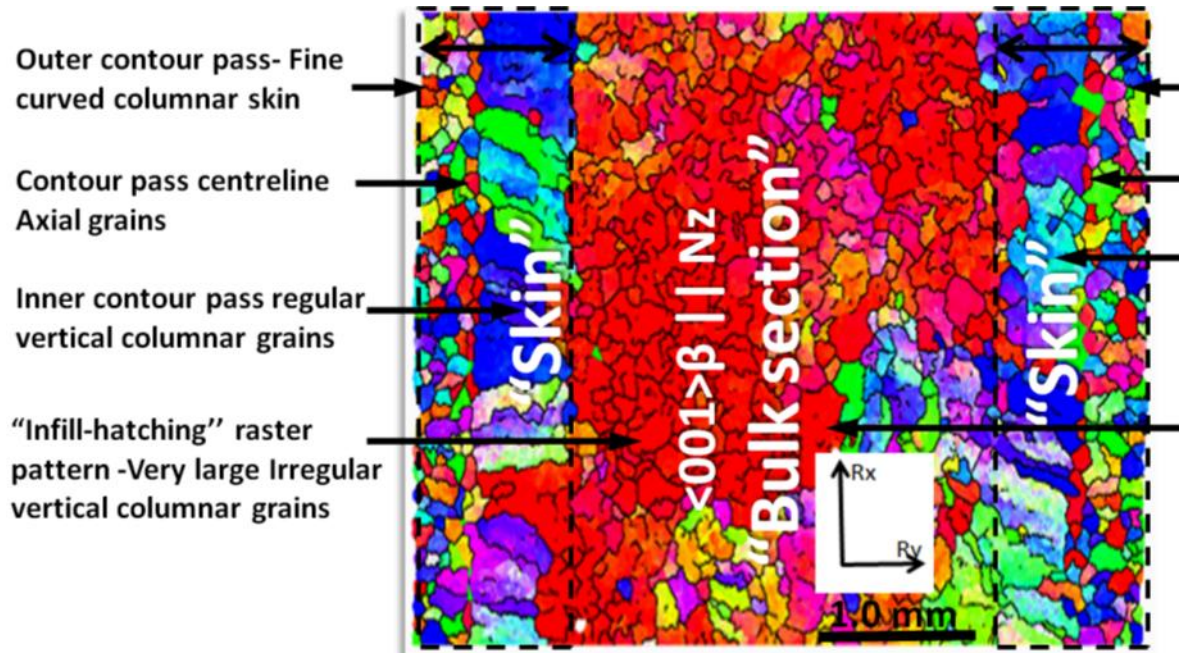

Figure 5.9: *EBSD reconstructed β grain structure map (in Rx-Ry plane) showing the evolution of different microstructural features generated a thick Ti6Al4V wall that was produced using both the contour and infill-hatching rastering) by the EBSM process.*

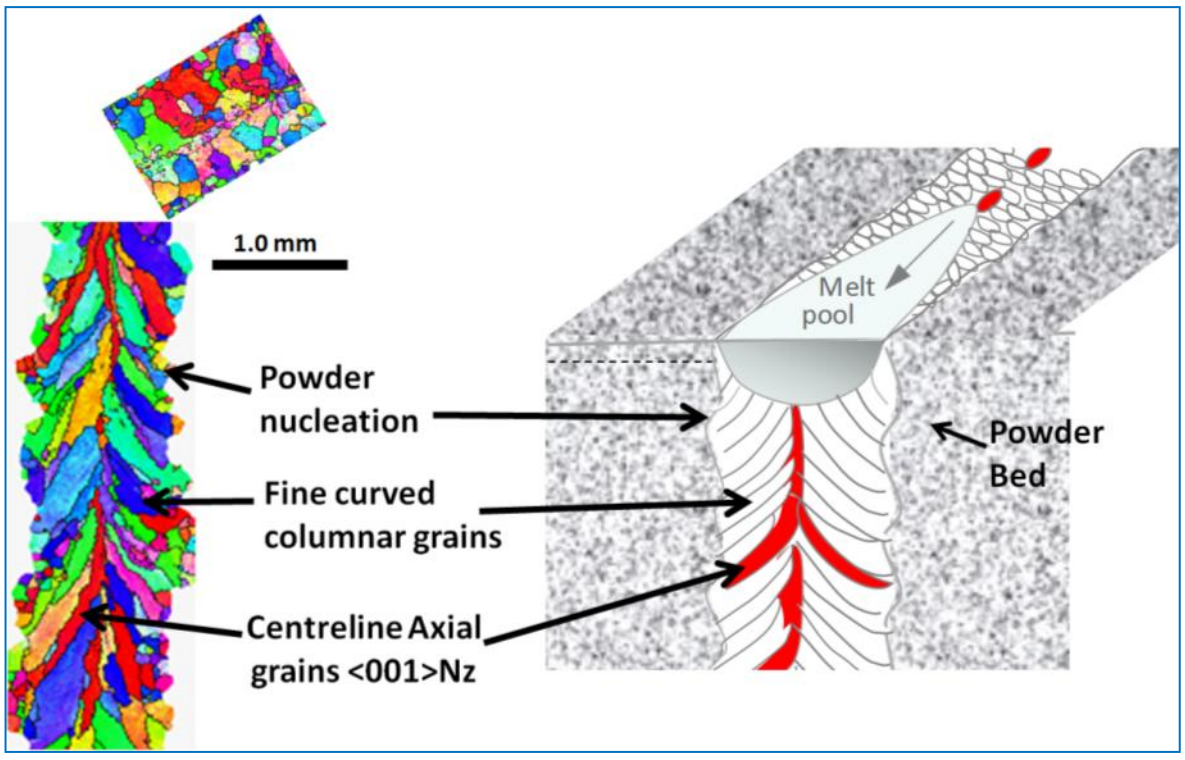

Figure 5.10: *Schematic diagram showing the β-grain structures generated by a single beam contour pass in the 1 mm wall produced by the EBSM process.*

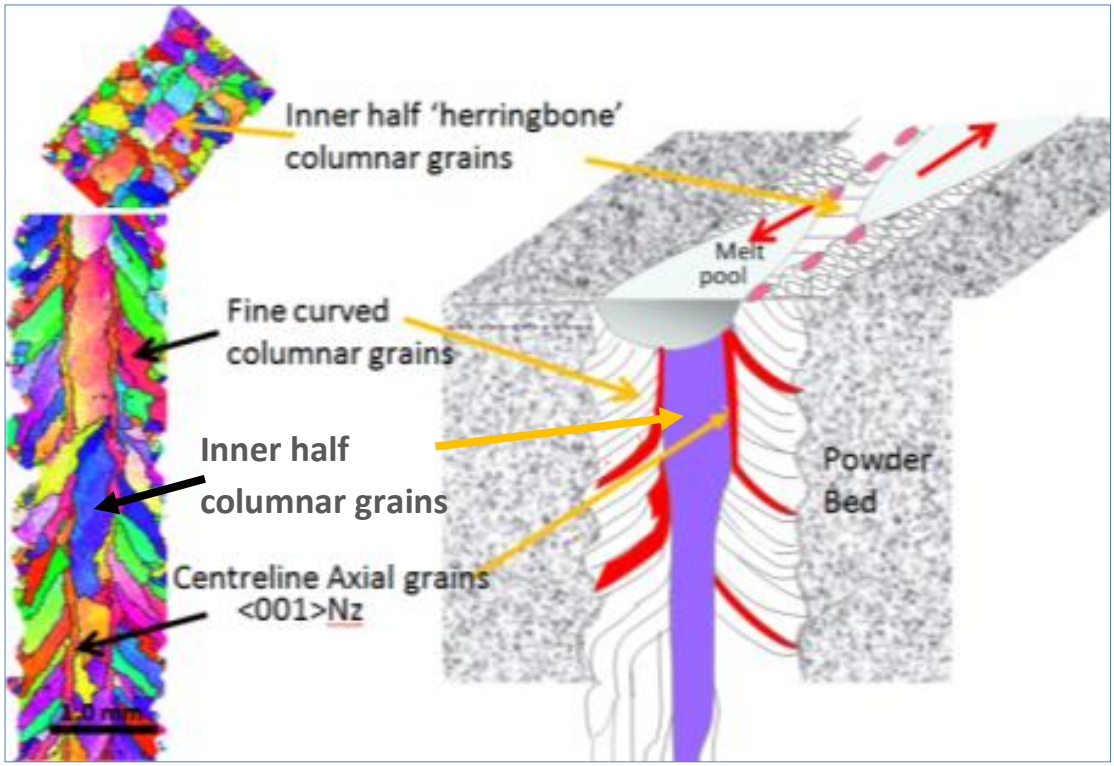

Figure 5.11: *Schematic diagram showing the β-grain structures generated by the double beam contour passes (with 50 % overlapping) in the 1.5 mm wall produced by using EBSM process.*

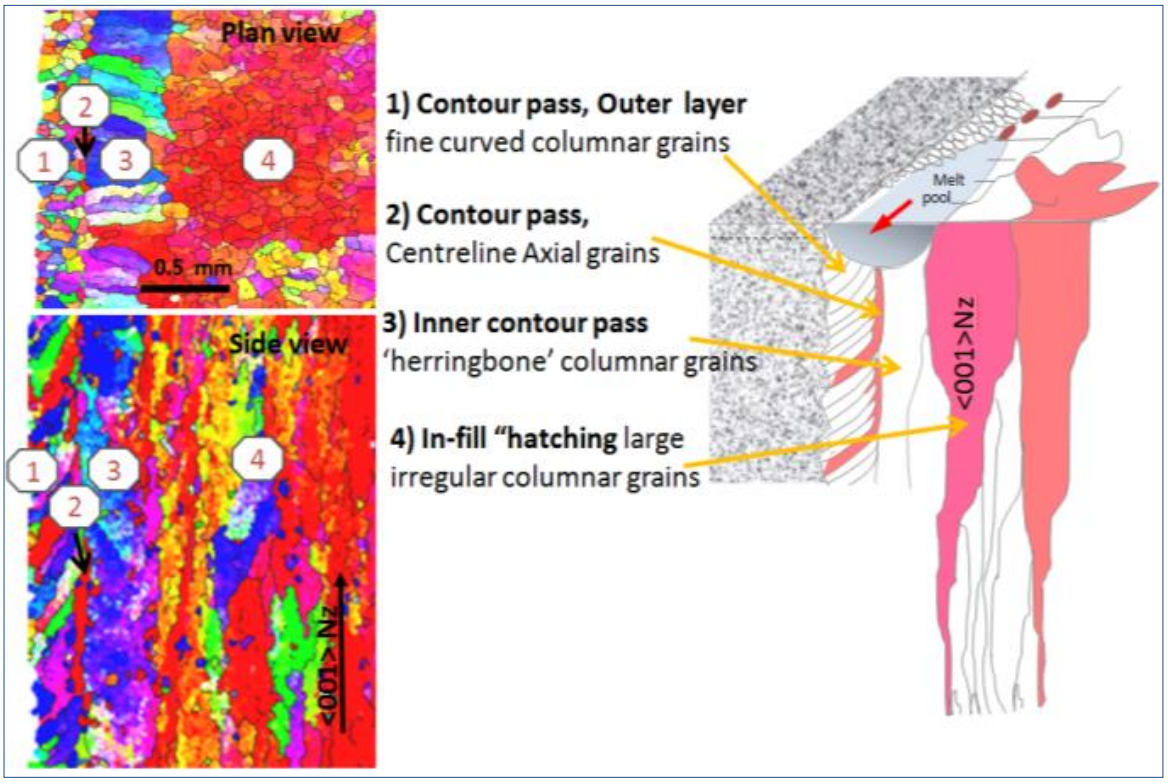

Figure 5.12: *Schematic diagram showing the skin β-grain structures generated by the contour pass with 'in-fill' hatching in > 2 mm thick wall sections produced by the EBSM process.*

The presence of a skin effect was also observed in the SLM process. However, the thickness of the skin layer in SLM is smaller (~ 0.15 mm) than in EBSM (of about ~0.5 mm) due to the small size of the melt pool in the SLM process. The thinnest wall produced with the SLM process studied was 0.4 mm wide, which involved two over lapping contour passes and is therefore equivalent to the 1.5 mm wall seen in Figure *5.11*. This contour pass is produced with a different speed function and typically a larger melt pool than for the standard operating condition for the bulk section hatching shown in the thermal modelling (where, the width of melt pool was ~ 100 micron). For the 0.4 mm wall, the EBSD maps in Figure *5.3*b suggest a slight overlap and a melt pool width of ~0.3 mm. The thickness of the next wall was increased to 1.0 mm (Figure *5.3*c), and this wall was produced with infill cross-hatching, as well as a contour pass around the perimeter of edge of the component section similar to in EBSM. All the walls were observed to have a skin of inward-growing fine columnar grains of ~ 0.15 mm to 0.20 mm thick, which is approximately equal to the half the melt pool width. With the SLM process, inward growth from the powder in the skin was a lot harder to identify because of the much finer scale and difficulty of obtaining high indexing up to the build surface, but this can be inferred to occur, all be it on a more local scale, by comparison with the EBSM results. The bulk microstructure within the SLM build showed columnar β-grains more weakly aligned with a $<001>_{\beta}$ || Nz fibre orientation, which is similar to that of the EBSM techniques, except for the smaller size of the broken up columnar grains (or stray grains) as has been discussed in 4.3.4. This is due to the solidification conditions in SLM most favouring constitutional supercooling, resulting in stray grain structures in bulk sections.

Vertical transitions and wall inclination

In the EBSM process, in the section transition regions the local microstructure could be explained by competitive growth of different skin and bulk columnar grain structures. Figure *5.4* showed the development of the primary β grain structure during transition from the two thinnest vertical walls to a wide capping section, or horizontal wall. In the horizontal capping section (Figure *5.4*), at the base, fine equiaxed grains are seen in the first melted layer originating from partially melted powder granules contacting the wall bottom surface. Then the vertical growth of coarse, irregular-columnar grains continued to develop, from the surface powder nucleated grains, as discussed in section 4.3.4. However, where they were attached to the horizontal section, the vertical walls locally altered the grain structure into the capping slab for a considerable subsequent built height (~1.5 mm). This effect results from the presence of the skin structure on the surface of the vertical walls. The finer grains from the wall skin can be seen to try to grow into the capping slab. Depending on the orientation of the powder nucleated grains, they either develop into new coarse columnar vertical grains, or are progressively cut-off by faster growing, more favourably <001> || Nz orientated neighbouring columnar grains. The grains that survive and go on to develop to become large grains again have an orientation close to <001> || N_Z

(coloured red). These more favourably orientated grains expand more, from both the surrounding horizontal section and, when present, from within the walls themselves, as shown in Figure *5.4*b. These grains eventually over-grow the finer grain structure originating from the skin layer in the transition region. The grain structure then reverts to the same coarse-columnar structure typically seen within bulk sections.

In comparison to the above, in the case where walls of different thickness were built on a thick base layer, the coarse columnar bulk structure was cut-off at the wall surfaces by the skin structures, as discussed above (Figure *5.1*). In thin walls the skin structure completely cut-off the bulk grain structure, but in thicker walls the different microstructure was confined to the thin skin layer and the coarse columnar bulk grain structure continued to grow up the centre at the wall sections.

When the effect of wall inclination angle was studied, 3 mm thick walls were built at an angle of 30˚, 45˚, and 60˚ relative to the build direction. These walls did not show any significant change in grain structure with orientation, i.e., in all samples, the grains continued to grow normal to the powder deposited layers from the base, irrespective of the build angle. Once nucleation was established at the base of the tilted wall, columnar β grains grew by epitaxial re-growth until the end of the final layer, as discussed in 4.3.4.

V- and inverted V- Transitions

Figure *5.6* (a-b) showed the β grains structures developed in the 'V' shaped and, inverted 'V' shaped sections after a steady-state condition was achieved. With this geometry, it can be expected that there is potential to select a single grain in the V-section, in a similar manner to that observed in a Bridgeman furnace for growing single crystals [158]. In the 'V' transition with 1 mm thick narrow constriction (shown in Figure *5.6*a), a single β grain grew through the constriction and continued to grow by epitaxial re-growth until the end of the build upon the deposition of further layers. This single large β grain, with a <001> || N_Z orientation (red), was selected by the local geometry restriction. The grain initially expanded as it carried on growing upwards through the subsequently deposited layers. However, columnar grains also developed from the contour skin layer contacting the powder bed at the base of the V-section, from both sides of where it was attached. Growth competition with these surrounding columnar grains prevented the grain selected by the V-transition expanding into the build. After, the addition of about 2 mm more material, the grain structure thus settled down to that seen in a normal bulk section.

When the V section was inverted with respect to the build direction (Nz), there was a continuously reducing section width and the tip of this sample was shown in Figure *5.6*b. It can be seen that in this case the large <001> || N_Z orientated columnar grains (red) within the bulk

section were simply terminated by the restriction of the diminishing section geometry by the skin layer of fine inward-growing columnar grains, produced by the contour pass, as described above.

Supporting structures

At the attachment point support webs could potentially locally affect the part they support in a similar manner to the thin wall inverse transition sample, or the 'V' section transition described above (Figure *5.4*a). However, in this case it can be seen that the effect on the β-grain structure in the supported part was negligible, as shown in Figure *5.6*c. This is because the width of the contact point is very small and consists largely of partially fused powder, which again provides a source of new nuclei. The red <001> || N_Z fibre orientated columnar grains seen in Figure *5.6*c from within the support webs thus did not grow significantly into the attached part and were rapidly cut-off by the surrounding columnar structure.

X- Transitions

The typical behaviour of the β-grain structure within the 90° crossover region of two vertical walls was studied with 1.0 mm and 1.5 mm thick sections produced by a contour passes, with no in-fill hatching (Figure ***5.7***). Here, the grain structure behaves as might be expected from the observations of single wall sections of similar thickness, and shows the presence of the same structures shown in Figure *5.1*(b-c), and described above. In the 1.5 mm wall cross-over region the effect of the beam path tracking the outline of the section can be seen with the boundary alignment in the inner half of the contour pass 'herringbone' columnar zone rotating through 90° (arrowed) around the corner, where the two walls meet, as shown in Figure ***5.7***b.

5.3 EFFECT OF BUILD GEOMETRY ON TEXTURE DEVELOPMENT

Orientation contrast in the reconstructed EBSD maps show that changes in build geometry, not only influence the β-grain structure, but also affect the local texture. The significance of this was analysed by examining the primary-β and α transformation textures, locally within microstructural transition regions present in the test sample geometries produced by the EBSM and SLM process.

5.3.1 Primary β Texture

Example pole figures depicting examples of reconstructed β-textures seen in geometry transition regions, obtained from EBSD maps, are presented in Figure *5.13*.

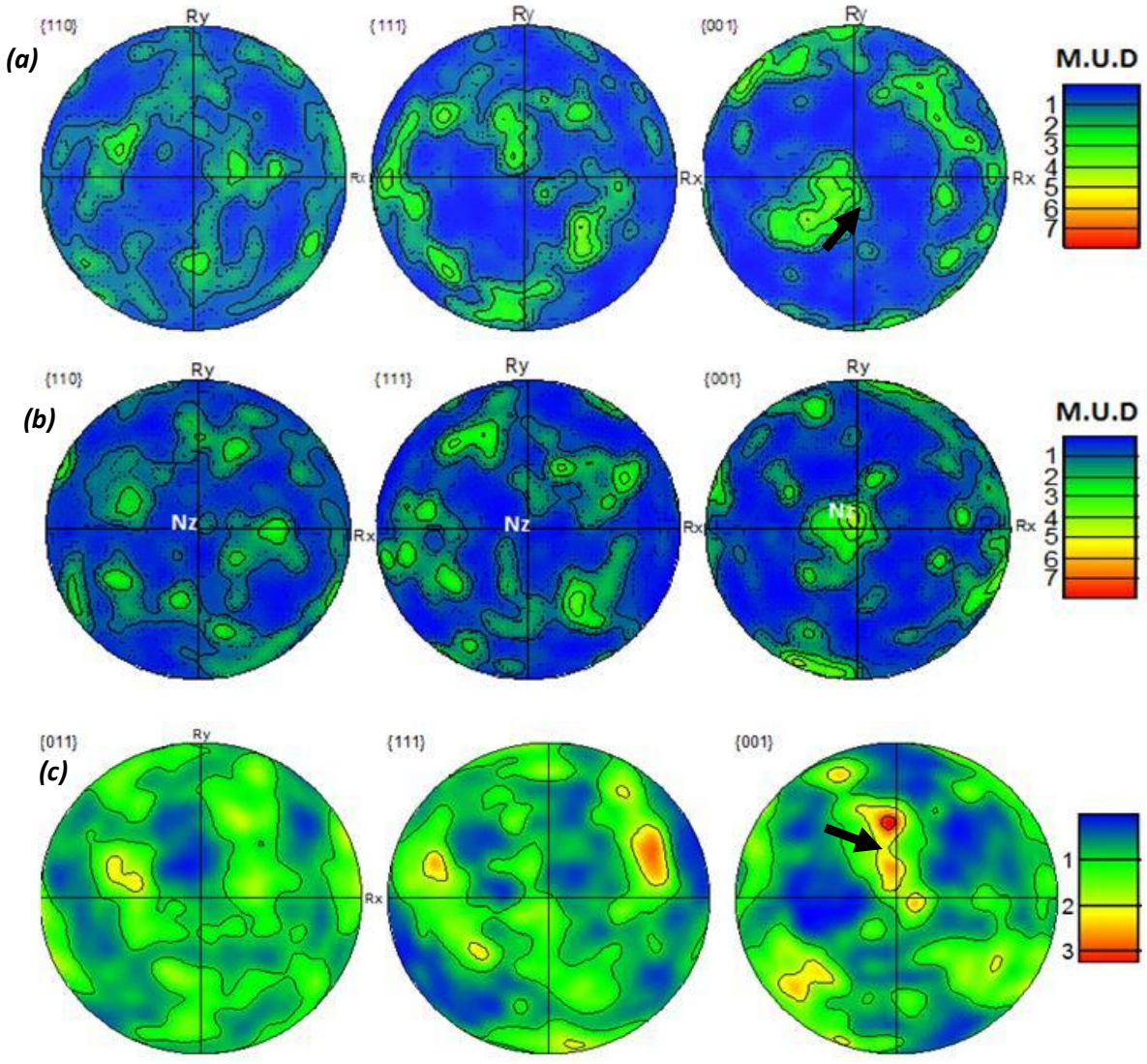

Figure 5.13: *Pole figures depicting reconstructed* β *textures from (c) a 2.5 mm wall surface skin, (b) the transition area between a 1.5 mm thick vertical thin wall and a horizontal capping slab from EBSM and, in (c) a 1.0 mm wall surface skin produced by the SLM method.*

Figure *5.13*a depicts the reconstructed β-phase texture of the fine inward growing columnar grain structure from the outer contour-pass of a 2.5 mm thick wall. The pole figures show a weaker texture of maximum strength ~ 3 xs random, compared to the bulk texture reported above in Figure *4.18*a (~8 x random). The pole figure shows increased intensity in a weak $<001>_{\beta}$ fibre, which rotates from around 45° away from N_Z, towards the N_Z direction seen in the bulk textures in the wall interior (Arrow in Figure *5.13*a), rather than a pure <001> β || Nz fibre texture.

In Figure *5.13*b pole figures show the data from the region where there was a transition from a thin wall 1.5 mm, to a thick horizontal section, to illustrate an example of an area where there is a likely to be a local texture heterogeneity. When investigating such regions sampling statistics become a significant issue, but the pole figures can be seen to contain both elements of the bulk $<001>_{\beta}$ || Nz fibre texture and a weak Nz-Ry, mirror symmetry $<001>_{\beta}$ 45°-Nz fibre texture. In comparison, Figure *5.13*c depicts the reconstructed β-phase texture of the fine inward growing columnar grain structure from the wall skin contour-pass of a 1.0 mm thick wall in the SLM process. The pole figures show a weaker texture of maximum strength ~2 to 3 x random, compared to the bulk texture of ~ 5 x random (in Figure *4.17*a). Here also the pole figures show a weak intensity $<001>_{\beta}$ fibre texture, which again rotates toward Nz similar to in the EBSM skin pass.

5.3.2 Transformed α-textures

The α-phase pole figures measured from geometric transition regions indicated a very weak transformation texture, since the original β texture strengths were less (~ 3 x random) in such local regions. For example, α- textures are shown for wall skins in both EBSM and SLM processes in Figure *4.14*. The intensity of the transformed α-texture is very weak with a maximum texture intensity of only 2 x random.

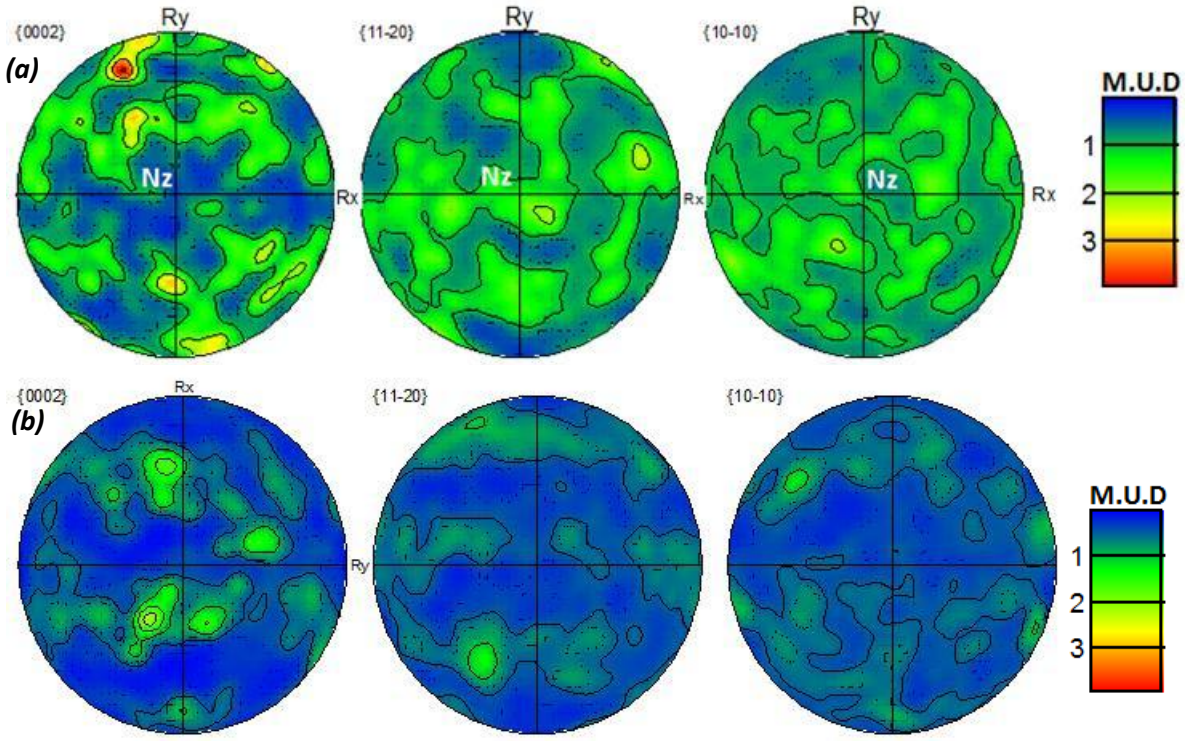

Figure 5.14: *Pole figures depicting the room temperature measured α texture in wall skin grain structures from (a) a 2.5 mm wall in the EBSM process, and (b) a 1.0 mm wall in the SLM process.*

5.3.3 Discussion on the effect of build geometry on texture development in AM

Primary β texture

Examination of heterogeneities in the local β-texture at surfaces, in thin walls, and section thickness transitions showed that in such regions the local texture was always weaker than in the bulk texture in both the EBSM and SLM processes. This observation is not that surprising since a strong solidification textures require growth under stable, directional, heat-flow conditions [42, 44].

EBSD orientation measurements showed that for the contour pass the β grains in the outer skin layers, tend to be tilted away from the <001> || N_Z orientation seen in the bulk sections, with a texture intensity of 3 xs random, due to the direction of maximum thermal gradient not being vertical, but normal to the curved solidification front of the melt pool in the contour pass. This weaker texture arises from the nucleation of randomly orientated grains on the sintered powder particles in the surrounding bed that were partially melted at the edge of the outline melt track. However, the pole figure shows increased intensity in a weak $<001>_\beta$ fibre, which rotates from around 45° away from N_Z, towards the N_Z direction seen in the bulk textures in the wall interior (Arrow in Figure *5.13*a). This behaviour is consistent with some preferential growth selection, as

the fine columnar grains grow inwards from the wall faces, following the direction of the maximum thermal gradient at the solidification front. A stronger texture does not develop because of the short distance the grains grow, before they meet the coarser vertical columnar grain structure solidifying from the inner edge of the melt pool. Figure *5.13*b show the pole figures in the transition area between a 1 mm thick vertical thin wall and a horizontal capping slab in EBSM process, where the <001> direction of the powder nucleated grains tends to bend around by 45 ˚ and also strengthen towards Nz from both sides of the skin in the 1 mm thin wall. i.e., in such regions, the pole figures can be seen to contain elements of the bulk $<001>_{\beta}$ || Nz fibre texture and a weak N_Z-R_Y, mirror symmetry $<001>_{\beta}$ 45°-Nz fibre texture, showing a progressive transition between the two cases described above for the bulk texture and contour pass skin effect from side walls (Figure *4.18*a and Figure *5.13*a). In other transition areas, such as the "V" transition shown in Figure *5.6*a, a single orientation dominates the texture because the geometry change encourages the preferential growth of a large single β-grain.

Figure *5.13*c depicts the reconstructed β-phase texture of the fine inward growing columnar grains from the contour-pass of a 1.0 mm thick SLM wall. The pole figures again show a weaker texture of maximum strength ~ 2 to 3 x random, compared to the bulk texture of ~ 5 x random shown in Figure *4.17*a. This weaker texture arises from the nucleation of randomly orientated grains on the sintered powder, as explained above. The pole figures again show a weak rotation of the $<001>_{\beta}$ fibre, which follows the melt pool curvature and moves from Rx around 45° towards the N_Z direction (Arrow in Figure *5.13*c).

α - Transformation textures

In local areas of both the EBSM and SLM samples, where geometric transitions and the original β-texture was less well defined, the α-transformation texture appeared to be very weak, or close to random. Examples of this behaviour were shown in Figure *5.14*, for both the EBSM and SLM processes. This occurs because, variant selection has not been observed to be a strong effect during AM (See section 4.4.4), and in such regions when starting with a weak β texture, the β → α transformation has resulted in even weaker, diluted, α-textures.

Texture homogeneity along the build height in the EBSM process

In the EBSM process, it was reported Al –Bermani et al. [112] that they observed a strong cube texture during processing of the Ti6Al4V alloy. However, in the analysis carried out here, on average a near fibre texture was observed in bulk sections once steady state conditions were established (see 4.3.4). In order to check whether the texture was consistent at different positions in the build height, further EBSD analysis was carried out at different distances from the base of a build in the EBSM process. The EBSD data in Figure *5.15* and Figure *5.17* reveals a systematic

variation in the bulk β grain structure and texture with height from the build base. Whereas Figure 5.16 shows the EBSD map of the measured α phase which was used to reconstruct the β grains shown in Figure *5.15*. At distance above the base of the wall, rather than a fibre texture, a strong <001> β cube component is observed, as shown in Figure *5.17*a. Whereas, when the build height is increased, the cube texture progressively reduces in intensity and a more random fibre texture is observed (Figure *5.17*), but there is still has some cube strengthening.

Near the base of the build, the fine heterogeneously nucleated equiaxed β-grains can be seen to initially develop with a strong <001> cube texture || Nz. These grains are strongly aligned with the two orthogonal rastering direction, Rx and Ry as shown in *Figure 5.17*a, where the <001> poles are aligned in the rastering direction of Rx and Ry with an intensity of around 5 x's random. At a 5 mm build height, where there was a transition in section width, the large columnar β grains were well established and they show a fully red colour in IPF map which indicates a strong $<001>_{\beta}$ || Nz fibre texture. The corresponding poles figures (*Figure 5.17*b) showed a stronger texture with an intensity of 8 xs random. However, the cube component is now weaker and the <001> poles show a more random distribution around the Nz fibre orientation, when compared to the base of the build. Further analysis at build heights of 25 mm and 35 mm (near top of the build), showed a strong fibre texture || Nz with a texture intensity of 6 xs random in both locations, with an even weaker cube component.

The reason for the strong cube texture at the base can be explained. In the initial layers, grains were heterogeneously nucleated at the base. But, in the subsequent layers, their growth direction during solidification is controlled by the maximum thermal gradient, which is normal to the solidifying melt pool surface. The <001> β grains preferentially grow along the build direction since the S/L interface is the base of an elongated tear drop melt pool in the powder bed (shown in thermal modelling section 4.2). When the build height was increased, to large distances of 25 mm and 35 mm, the grain growth direction repeatedly changes, due to the complex beam rastering pattern. This is because the maximum thermal gradient direction changes every time the beam changes direction as discussed in section 4.4.4. In such a circumstance, the β grains grow across many deposited layers by selecting the most favoured average growth direction (among the grains from base) and this would be for the grains which are oriented parallel to Nz as was discussed in section 4.4.4. It can, therefore be concluded that the cube texture observed near the base of build is a result of grain growth influenced by the maximum thermal gradient against the base melt pool. But, the fibre texture observed with greater build height is developed by selecting the averaging growth direction against the complex moving melt pool surface across many deposited layers. The cube strengthening still noticed in the maps produced at heights of 25 and 35 mm could also be attributed to the poorer sampling used. In each of these cases an area of only ~ 10 x 10 mm^2 areas were mapped and hence, the number of grains analysed here was much

less than that of the bulk β- texture (shown in section in 4.4.4) where, approximately 1000 grains was considered.

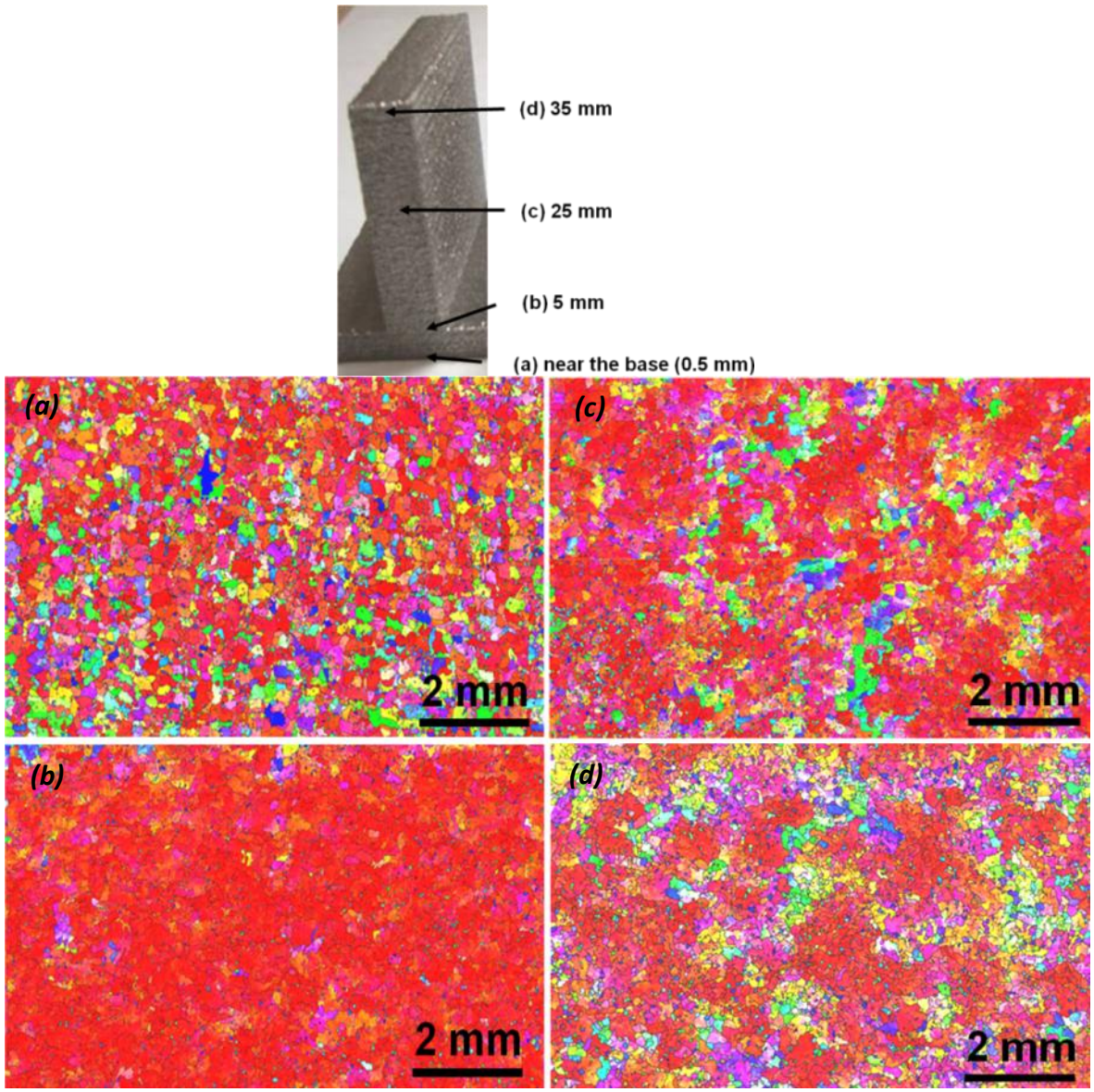

Figure 5.15: *EBSD maps showing the heterogeneity of β grain structures with build height from the base (a-d) during processing of a Ti6Al4V alloy using the EBSM process. The IPF orientation of the map is aligned || Nz.*

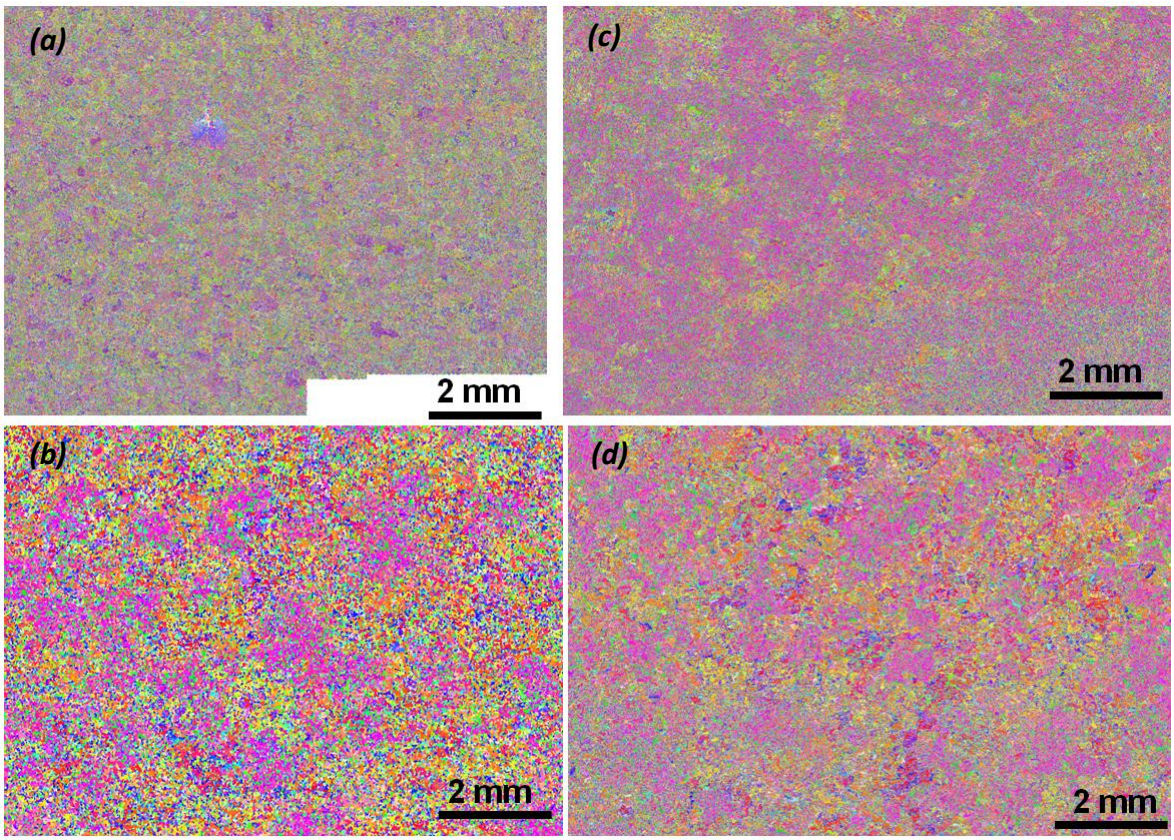

Figure 5.16: *EBSD maps of the transformed α phase with build height from the base (a-d) which was used to reconstruct the high temperature β grains shown in Figure* ***5.15*** *. The IPF orientation of the map is aligned || Nz.*

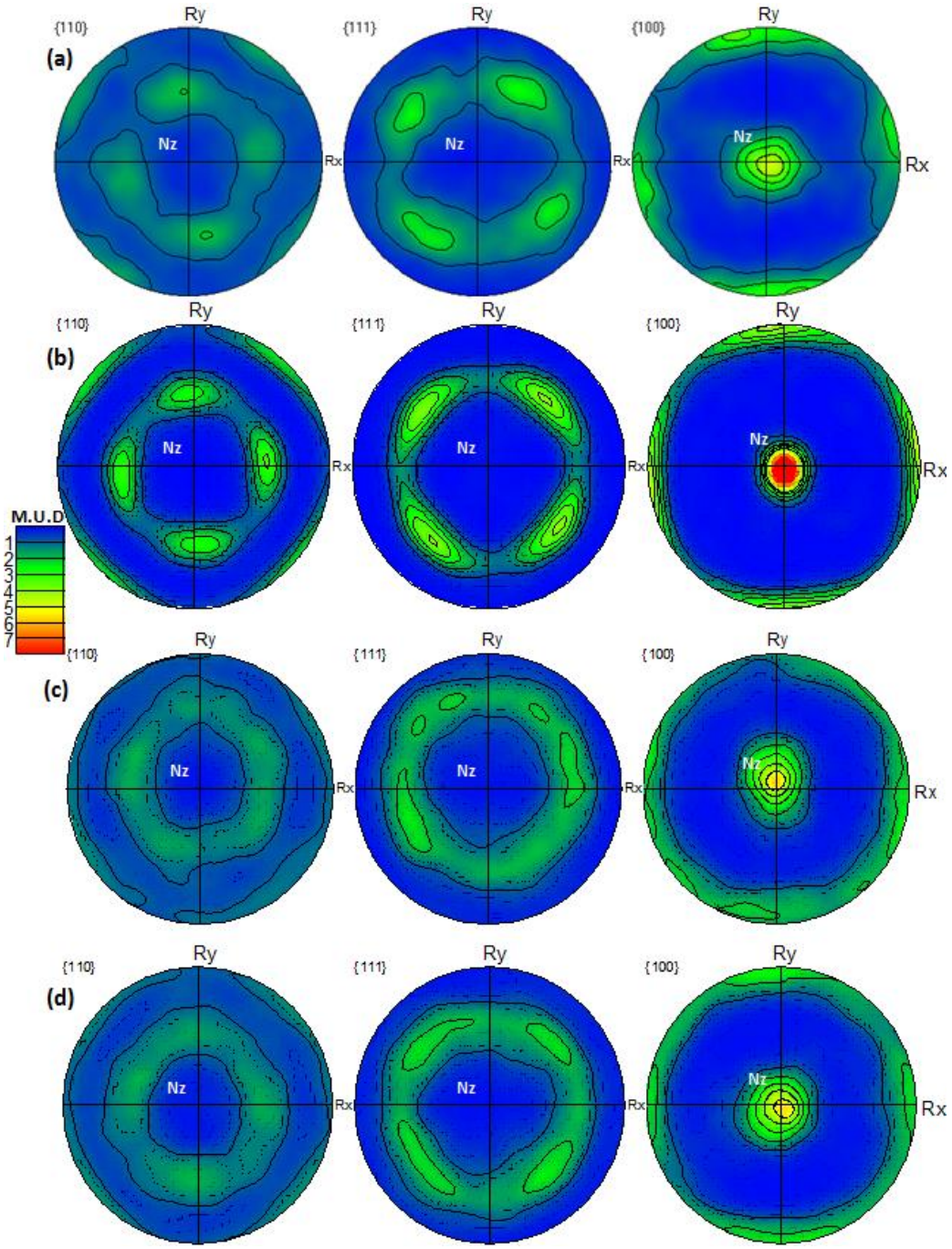

Figure 5.17: *Variation in bulk β texture along the build direction; near the base of the build (a), at the cross section changeover (5 mm) (b), at the middle height (25 mm) (c), and at the top of the build (35 mm) as shown in Figure* ***5.15****.*

5.4 CONCLUSIONS

The main conclusions made in this work concerning the effect of build geometry in powder bed EBSM and SLM on the grain structure and texture are summarised below.

5.4.1 Summary of the influence of build geometry on β grain structures in AM

Detailed analysis has been performed of the effect of changes in build geometry on the primary β-grain structures found in Ti6Al4V AM components, produced by the EBSM and SLM processes. Reconstruction of the β-phase has helped the development of the primary β grain structure to be unambiguously determined.

Overall, in the EBSM process, large columnar β-grains nucleate heterogeneously either from the base, or, partially melted powder contacting the side walls and constrained columnar grains then grow against the heat extraction direction by epitaxial re-growth to occupy the majority of the entire build microstructure. However, there is a distinct difference between the grain structure produced by the contour pass and in-fill hatching. In bulk sections, where infill hatching was used, coarse irregular columnar grains grow parallel to the build direction, with a $<001>_{\beta}$ || Nz fibre orientation, due to selection of a preferred average grain growth direction as was discussed in section 4.3.4. In comparison, the contour beam pass produced a double layered skin structure. This consisted of an outer layer of fine columnar β-grains that are surface nucleated and grow inwards, following the curved bottom of the melt pool to the melt track centreline. These grains meet a coarser herringbone structure growing, from the inner side of the contour track, where powder nucleation is not possible.

Moving in from the surface, four distinct regions of different β-grain structures were identified in the EBSM process, but owing to the smaller scale and the stray bulk grain structures such layers were harder to identify in the SLM process. Firstly, (i) a surface layer of randomly orientated partially melted powder was seen, from which (ii) fine inward-growing curved columnar grains developed, as far as the centreline of the outline pass (~0.5 mm in the EBSM process and 0.15 mm in SLM). In EBSM, some of these grains were seen to be favourably orientated and continued to grow long distances as 'axial grains' up the wall at the contour pass centreline. This was followed by (iii) regular "herring bone" columnar grains growing upwards in the inner half of the outline pass and, finally, (iv) where cross hatching was used large, irregular, vertically-growing, large columnar grains were seen within the centre of thick sections in EBSM. Just structures i) and ii) are seen in the thinnest 1 mm wall produced, with a single contour pass, where solidification occurs symmetrically from either side of the melt pool (Figure *5.1*b), whereas in EBSM i) ii), and iii) are seen in walls less than 2 mm thick (Figure *5.1*c. d), and all four structures are seen in sections thick enough (>2 mm) to require in-fill by cross-hatching (Figure *5.1*e). The same phenomenon

applies to the SLM process for powder nucleated outer skin grains. However, compared to the EBSM process, the SLM process produced more broken up fine columnar grains in the bulk section (Figure *5.3*) as discussed in section 4.2.4 and hence such clearly defined skin layers were not observed. In SLM, only layers (ii) and (iv) were positively identified.

The EBSM process was also used to study grain structure transition regions in a selection of generic geometries typical of design elements in components. In such regions heterogeneities in the β-grain structure were found to be relatively localised. As discussed above, the contour pass forms a different finer grained skin grain structure on thicker sections, or across entire wall widths in very thin sections (1 mm). This skin structure can also alter the microstructure in transition regions, where there is a change in section thickness, because it can continue to grow on into a bulk section. However, its influence was short lived because it was rapidly overgrown by the coarser $<001>_{\beta}$ || N_Z fibre bulk-grain structure. As a result, heterogeneities in grain structure caused by geometry were found to be relatively localised. In all cases the dominant coarse-columnar bulk grain structure became rapidly re-established, or overran, local microstructure variation where section changes occurred. For example, where a vertical wall met a horizontal wall, finer curved-columnar grains from the skin of the vertical wall quickly developed into coarse-vertical columnar grains, or was overgrown by the vertical columnar grains growing from nuclei in the powder bed in the surrounding material (Figure *5.4*).

Equally, in the extreme case of the 'V' transition sample, the growth of a single β-grain, selected by a local section constriction, was restricted by competition from surrounding vertical columnar grains nucleated from the powder bed (Figure *5.6*a). Only in the case of a transition from a thick to very thin sections did the 'skin' grain structure take over (Figure *5.1*b). In the EBSM process, β grains were also observed to grow normal to the powder deposited layers irrespective of the wall angle. The β grains seen in support webs did not grow significantly into the attached part and were also rapidly cut-off by the surrounding columnar structures.

To conclude, the EBSM process showed a pronounced local heterogeneity in the microstructure in the local transition areas, when there is a change in geometry. i.e., The grain structure was strongly affected by changes in build geometry, such as skin effects, section thickness changes, support structures, build angle, cross over's in lattice structures etc. However, this effect was less significant in the SLM process, due to the smaller melt pool and more refined bulk stray grain structure.

5.4.2 Summary of the influence of build geometry on texture in AM

A detailed study has been performed on the effect of changes in build geometry on the primary β and transformed α texture found in Ti6Al4V powder bed AM components, produced by EBSM and SLM processes. Overall, both the β solidification texture and α transformation texture was weakened, in such a transition region. There was a distinct difference between the texture produced by the contour pass and in-fill hatching. The contour grain structures had a $<001>_{\beta}$ fibre texture that was tilted away from Nz due to the curvature of the melt pool surface. This was also apparent from the skin grain structure, which consisted of an outer layer of fine columnar β-grains that are surface nucleated and grow inwards, following the curved bottom of the melt pool to the melt track centreline. In comparison, in bulk sections, where infill hatching was used, a strong $<001>_{\beta}$ || Nz fibre texture was seen since coarse irregular columnar grains developed in the thick sections, as discussed in the section 4.3.4.

The previously reported strong cube texture component seen in bulk sections of EBSM samples [112] was only observed near the base of a build in the current study. I.e. at 5 mm above the base, a strong $<001>_{\beta}$ cube texture developed which was aligned with the two orthogonal rastering directions (Rx and Ry). However, with an increase in build height the cube texture changes into $<001>_{\beta}$ fibre texture || Nz. The cube texture observed near the base of build is a result of grain growth influenced by the maximum thermal gradient against the tear drop shaped melt pool base. In comparison, the fibre texture observed at greater build heights is developed by selecting the averaging growth direction against the complex moving melt pool surface across many deposited layers, as discussed in section 4.4.4.

The contour pass formed a different fine grain skin structure on thicker sections, or across entire wall widths in very thin sections (1 mm), and the skin grain structure also altered the microstructure in transition regions, where there was a change in section thickness. However, its influence was short lived because it is locally different structure were rapidly overgrown by the coarser $<001>_{\beta}$ || N_Z fibre bulk-grain structure. As a result, heterogeneities in texture caused by geometry were found to be relatively limited. Examination of heterogeneities in the local texture near surfaces, in thin walls, and section thickness transitions, showed that in such areas the texture was weaker than for the bulk, because the preferred growth direction changed with distance.

The α -phase had a transformation texture closely related to the β <001> fibre texture. However, its texture was considerably weaker than that of the parent, because of the dilution that occurs during transformation with almost no variant selection. Thus, in transition regions, where the primary β texture was already weakened the α texture was close to random.

6 EFFECT OF PROCESS VARIABLES ON β GRAIN STRUCTURES IN WAAM

6.1 INTRODUCTION

As well as the effects of build geometry (chapter 5), process parameters can also affect the final microstructure, or be altered to potentially improve the undesirable coarse large β grains developed in the AM processes, as was discussed in chapter 4.3 (section 4.3). This chapter will mainly focus on the influence of process parameters on the primary β grain structures seen in the WAAM process. This is because the solidification conditions (e.g. melt pool shape, growth rate, and growth front thermal gradient, and cooling rate, shown in the thermal modelling (section 4.2) will control the primary β grain structure and α transformation microstructures developed in an AM process such parameters are parameters linked to the power density and travel speed of the heat source, but in addition in AM (as has been noted above) the beam travel path, or raster pattern, and build sequence can also influence microstructure and texture. Furthermore, in the WAAM process, material is added using a filler wire which can also influence the temperature in the melt pool.

In powder bed AM the process parameters such as the amount of heat input, travelling speed of the heat source, height of the powder bed, scanning sequences, etc., can affect the final microstructure, but are controlled within a narrow envelope by the machine software, since these processes are mature. In comparison, the WAAM process is a newer technology still under development and considerably immature, in terms of the current understanding of the influence of the process variables on microstructure. In WAAM the parameters are more flexible and the arc current, travelling speed, type of power source used (e.g. DC or Pulsed or Interpulse GTAW), wire feed rate, etc., can have a significant effect on the final microstructure. Samples with different build parameters will, therefore, only be discussed here produced by the WAAM process, since there are more possibilities for varying the process variables and EADS did not provide samples with different process parameters using the EBSM and SLM processes during the period of this project.

In addition to the process variables mentioned above, additional methods can be combined with AM to try to improve the coarse β grain structure. One method that was studied in this project was to combine WAAM with a deformation step, involving rolling each deposited layer. This novel hybrid-AM and thermomechanical process was used to attempt to recrystallise the deposited material when it was heated by the deposition of the next layer.

In this chapter, the effect of different process parameters on the β grain structures produced by the WAAM process with the Ti6Al4V alloy will be examined. The effect of common different key process parameters (for e.g. in the GTAW), on the development of the primary β-grain structure and texture will first be discussed. Secondly, the benefits of a novel approach of combining deformation with arc AM, to modify the coarse β-columnar grain structure seen in AM, will be reviewed.

6.2 INFLUENCE OF PROCESS PARAMETERS ON β GRAIN STRUCTURES IN THE WAAM PROCESS

The influence of the following process variables were studied in the WAAM processes; (i) constant current GTAW, (ii) HF interpulse GATW, (iii) standard pulse GTAW, and (iv) CMT GMAW. The results obtained using these different power supply configurations will be discussed in the same sequence below. In addition the effects of changing parameters such as the energy input and travel speed will be examined for specific arc processes. In all the cases, Ti6Al4V walls were built using external wire feed and deposition was performed layer-by-layer with an alternating forward and backward travel direction of the welding head along the X direction.

6.2.1 WAAM using a constant current GTAW-DC power source

In an initial study, the effect of heat input and travel speed was investigated with a constant DC current power supply. In this case, a constant wire feed rate was maintained, which means that the layer thickness reduced with travel speed. In this experiment it was originally requested that a constant line energy should be maintained (q/v) as the travel speed increased, but as can be seen in Table *3.5*, the heat input increased with travel speed, leading to a wider wall thickness. A constant current Migatronic GTAW commander 400 DC power supply was used to produce specimens with a current range of 90 to 240 A and a travel speed range of 3 to 8 mm/s (see Table *3.5*). Figure *6.1* shows longitudinal and cross-sectional micrographs of WAAM builds produced using the GTAW - DC power source. The three samples were produced with DC current values and line energies of 90 A - 240 kJ/m (a), 180 A - 281 kJ/m (b), and 240 A – 300 kJ/m (c) respectively. Full experimental details are given in 3.3.

The travel speed of the heat source and the heat input are shown in the Figure *6.1*. With the lowest heat inputs and travel speed, just above the substrate, the β-grains were still fine and then large irregular columnar β-grains with the size of up to 13 mm in length, and a maximum width of 7 mm, were seen to develop from the base plate, as shown in Figure *6.1*a. In contrast, the higher heat input and travel speeds (Figure *6.1*b-c) led to the formation of 4 different microstructural regions in the walls with distinct grain morphologies, namely; (i) a fine equiaxed grain region at the base of the build (at the interface between substrate and the deposited wall), followed by (ii) a columnar grain region, (iii) an equiaxed grains region and, (iv) a final fine more regular columnar grain region seen during solidification of the last layer, which is titled slightly in the direction of heat source travel. The microstructures seen in the transverse section were in good agreement with the longitudinal cross sections (Figure *6.1*). It should be noted that the process conditions that produced higher heat input wider walls were not used subsequently, because they did not produce consistent stable wall geometries.

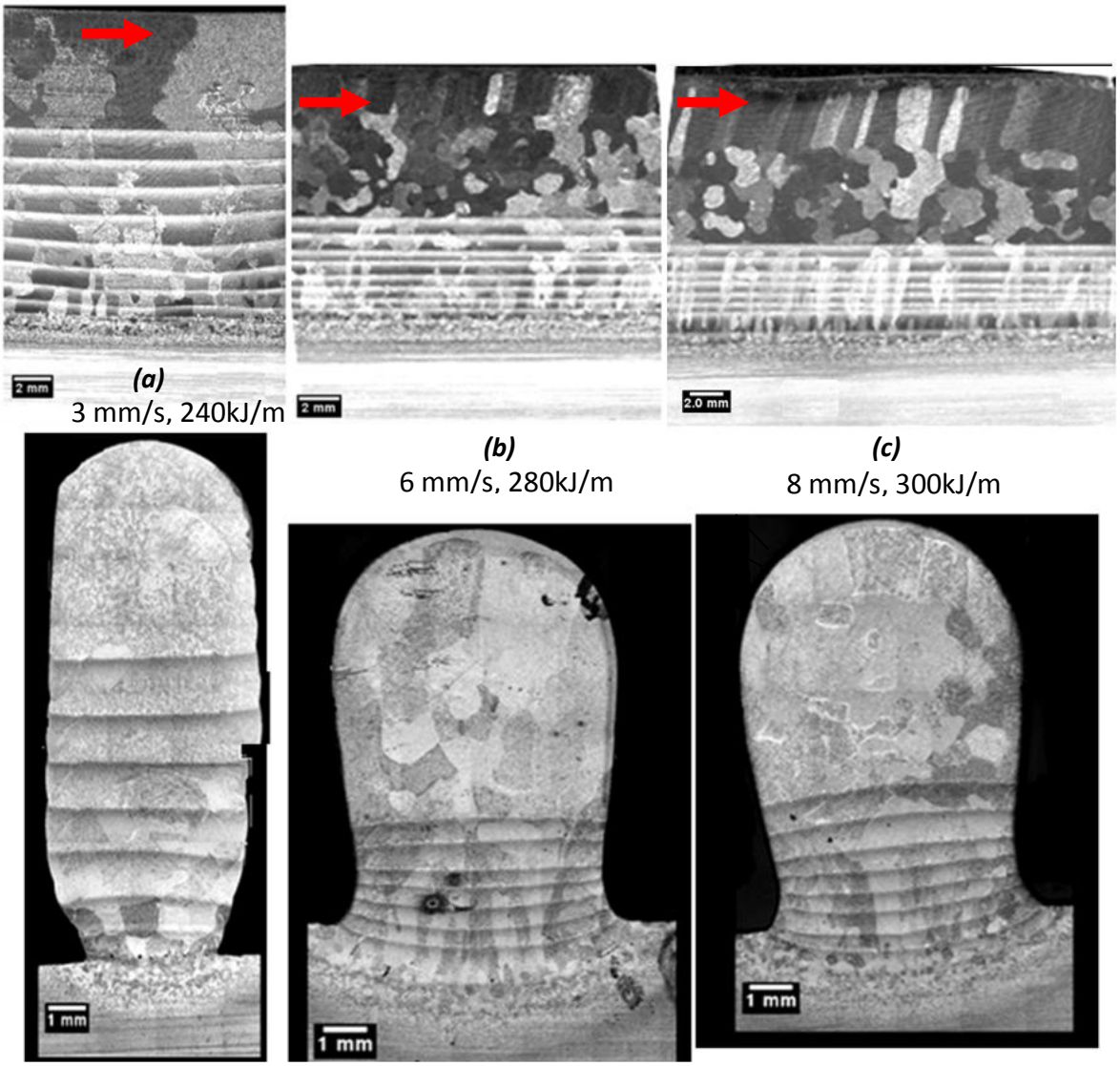

Figure 6.1: *Longitudinal, down the wall centre line, and transverse cross-sectional micrographs of Arc +Wire AM samples produced using a GTAW - DC power source, with current values of 90 A (a), 180 A (b), and 240 A (c). The travel speeds and corresponding line energies are given in each image. The red arrow mark shows the direction of the movement of heat source during the deposition of the final layer.*

6.2.2 Influence of change in travel speed using the HF interpulse power supply

To try to refine the large grains sizes seen in constant current power source, deposits were produced using a VBC-HF interpulse IP 150 power source with a high frequency interpulse power system (see Figure *3.9*). In addition, to see the influence of travel speeds on microstructure, two samples with different travel speeds of 0.27 m/min, and 0.57 m/min were produced with a constant heat input of 182 (kJ/m). The other process parameters used to produce these deposits were a high frequency power supply that alternated between frequencies of 10 Hz and 20 KHz in 0.05 s**,** I_p=120 (A) and I_b=60 (A) pulses, and a W.F.S = 1.6 (m/min), as shown in (Table *4.5*).

The effect of increasing the travel speed was studied because during solidification the travel speed is directly related to R and this could change the G/R ratio in the solidification map (see Figure *4.5*), which controls the morphology of the final microstructure. In addition, the VBC-HF (interpulsed) process provides a constricted arc and a more focused heat source [159] compared to the GTAW-DC process, which could also affect the thermal gradient in the melt pool. The VBC-HF interpulsing current with a constricted arc could also possibly increase turbulence in the melt pool and thus provide a lower thermal gradient, and promote dendritic fragmentation at the S/L interface.

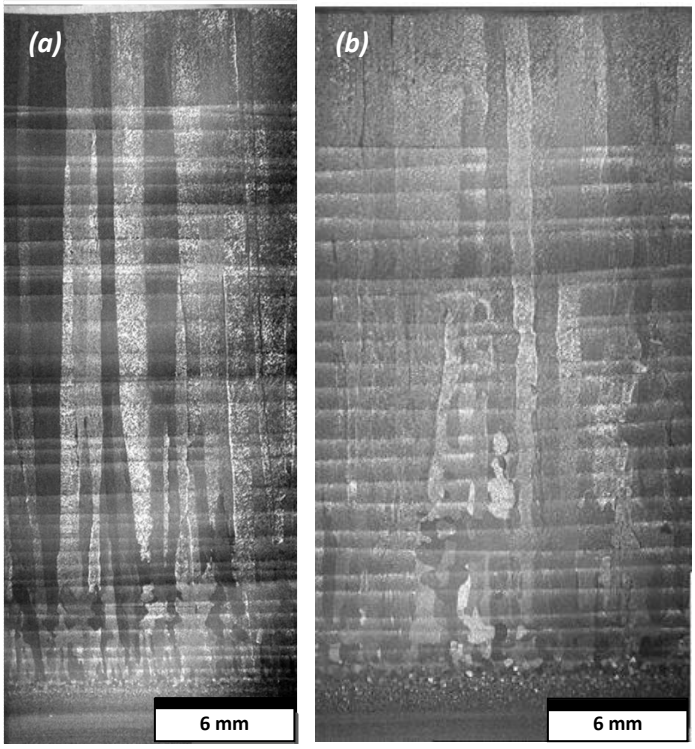

Figure 6.2: *Section along the centre of a GTAW deposited Ti6Al4V wall with a travel speed of 0.27 m/min and 0.54 m/min, respectively using VBC Interpulse power source with the same line energy of ~ 180 kJ/m.*

Figure *6.2*(a-b) shows the cross sections of deposits produced with travel speeds of 0.27 m/min and 0.57 m/min. Both samples showed the presence of large columnar β grains (35 mm in length and 2.5 mm in wide) after nucleation at the wall base, although a few random equiaxed grains were seen in the middle of the build. The interpulsed frequency and change in travel speed had no significant influence on the size and shape of the β grains.

6.2.3 Influence of wire feed speed (WFS) using the VBC interpulse power source

A multilayer Ti6Al4V wall with dimensions of 50 mm in height x 180 mm in length x 5mm in width was produced, while the wire feed rate was progressively increased (shown in Figure ***6.3***a). A higher wire feed rate can reduce the thermal gradient by cooling the melt pool, which might favour fine grains. The wire feed speed was increased from 1.6 m/min at the base to 3 m/min near the top of the build. The deposit was produced using the VBC high frequency power supply that alternated between 10 Hz and 20 KHz frequencies in 0.05 s, other process parameters are low, $I_{average}$ = 105 A, T.S= 0.24 m/min with an line energy of 210 kJ/m. The role of power supplies will be discussed further below 6.2.6 (see experimental section 3.3.3).

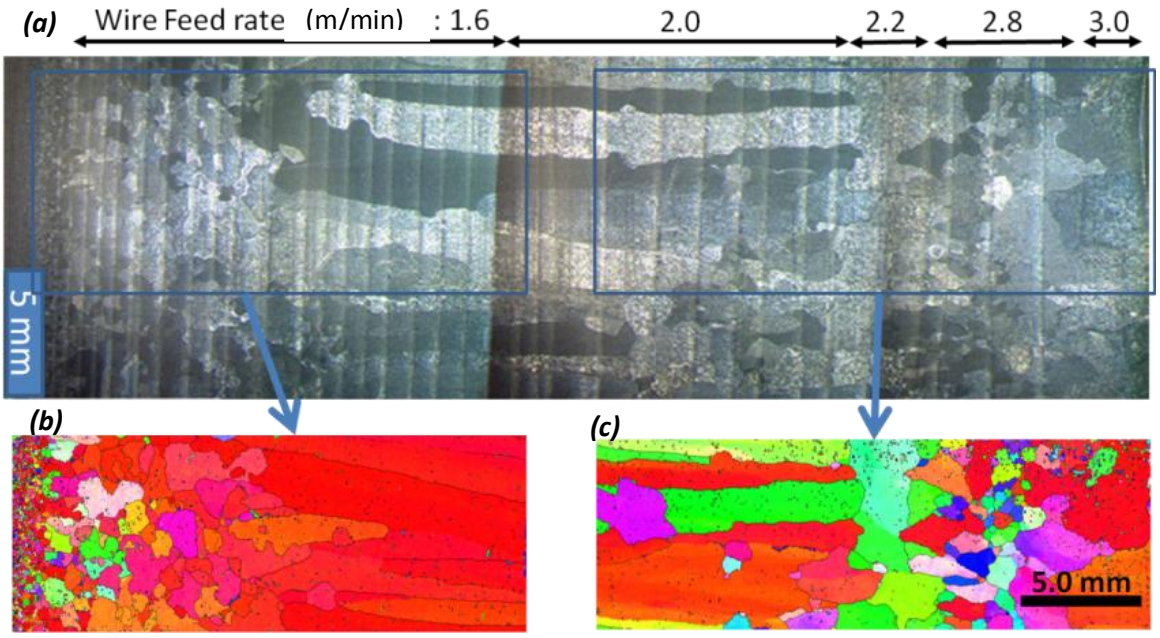

Figure 6.3: *Centre the cross section though of GTAW Ti6Al4V wall with a interpulsed power supply, and average current is 105 A, travel speed of 0.24 m/min, when the wire feed speed was varied from 1.6 to 3 m/min, showing a transition from large columnar to equiaxial prior β grains when the wire feed speed is 2.2 m/min (a), and their corresponding reconstructed* β *grains in (b) and (c).*

Initially, a normal columnar grain structure developed from the base of the build. But, the morphology of the large columnar β grains changed to equiaxial, when the wire feed speed reached 2.2 m/min. This is clearly visible in the reconstructed β grains IPF map shown in Figure ***6.3***(b-c), which was reconstructed using room temperature α-phase EBSD data. When the WFS increased to 2.2 m/min, the red <001> β grains were terminated and, new grains were nucleated (size varied from 0.52 mm to 3.9 mm). The machine was stopped when the WFS

reached 3 m/min, since the arc could not melt the extra wire fed into the molten pool. Based on this investigation, optimised process parameters were chosen, to attempt to produce equiaxed β-grains in an entire build which was successful, as shown in Figure ***6.4***. The optimised WFS used was a minimum of 2.2 mm/min. while this approach was successful in developing an equiaxed grain structure, the grain size was still very large with an average diameter of 1.47 mm.

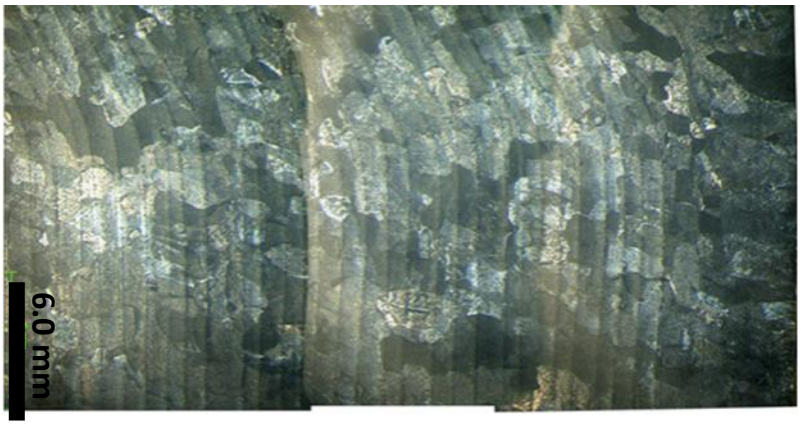

Figure 6.4: *The equiaxed grain structure seen throughout an entire wall produced with a high wire feed rate of 2.2 mm/min and processing parameters of low frequency 10 Hz plus high frequency of 20 KHz, pulsing ($I_{average}$ = 105 A), and a T.S= 0.24 m/min.*

6.2.4 WAAM using a GTAW- Standard pulsed current power source

Since the 'VBC Interpulse IP 150 power source' machine was not designed for heavy duty use, to produce large walls a conventional standard pulsed GTAW system was studied. The effect of pulsing was examined by altering the base to peak current (I_p/I_b) ratio's and pulse frequency. The aim of pulsing the current was to stir the melt pool to promote dendrite arms to fragment at the S/L interface and, encourage the formation of equiaxed grains [44] rather than large continuous epitaxial re-growth of columnar grains.

6.2.4.1 Influence of (I_p /I_b) ratio on the grain size

Figure *6.5* shows micrographs of the samples that were produced with different peak to base current (I_p /I_b) ratios of 3.3, 4.0, 4.4, 5 .6, and 6.7 and an AC square wave power supply with a frequency of 5 Hz (see experimental section 3.3.3). The average current (I_{av}) and heat input were kept constant at 99 A and 210 kJ/m, respectively, as shown in

Table *3.6*. From Figure *6.5*, it can be seen that changes in the (I_p/I_b) ratio did not have any significant influence on modifying the large columnar grains developed during the WAAM process.

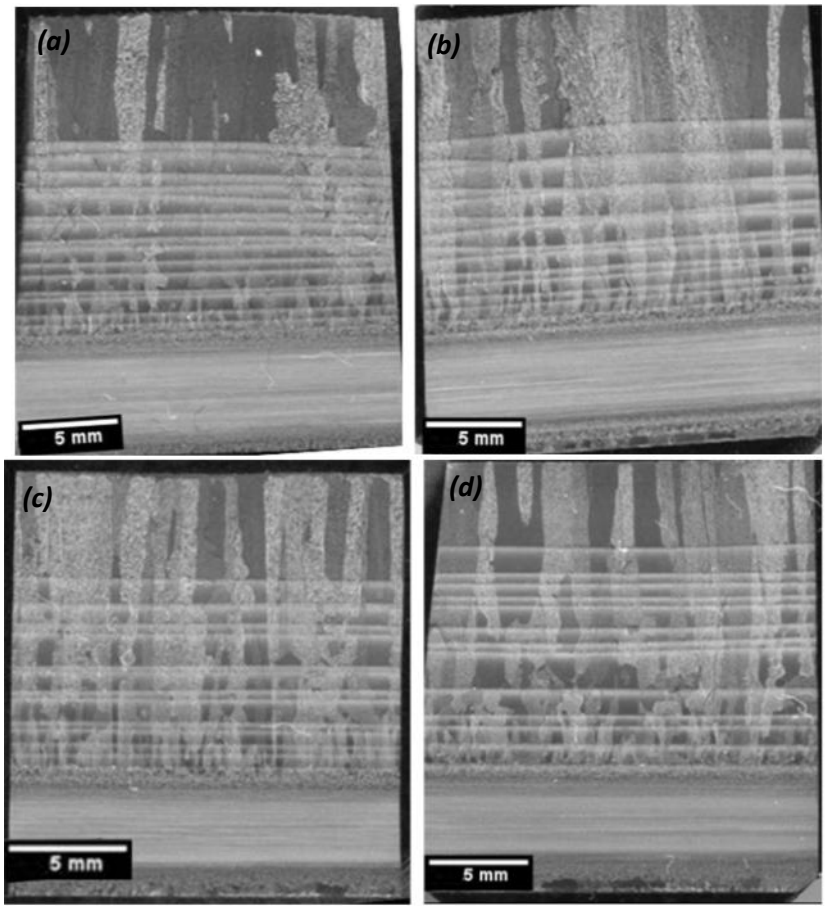

Figure 6.5: *Micrographs showing the effect of different current pulse (I_p/I_b) ratio's from 3.3 (a), 4.0 (b), 5.6 (c), and 6.7 (d) during WAAM of the Ti6Al4V alloy using a pulsed power source.*

6.2.4.2 Influence of pulse frequency on the grain size

To study the influence of the pulse frequency on the β grain structure, samples with pulse frequencies of 5, 10, 20, 25, and 50 Hz were produced using a Migatronic GTAW power supply, while the average current and heat input was kept constant at 99 A and 210 kJ/m. The microstructure of all the deposits, produced with the different frequencies, showed the presence of large columnar β grains (Figure *6.6*). It can be clearly seen that changes in the pulse frequency did not influence the large columnar β grain structure.

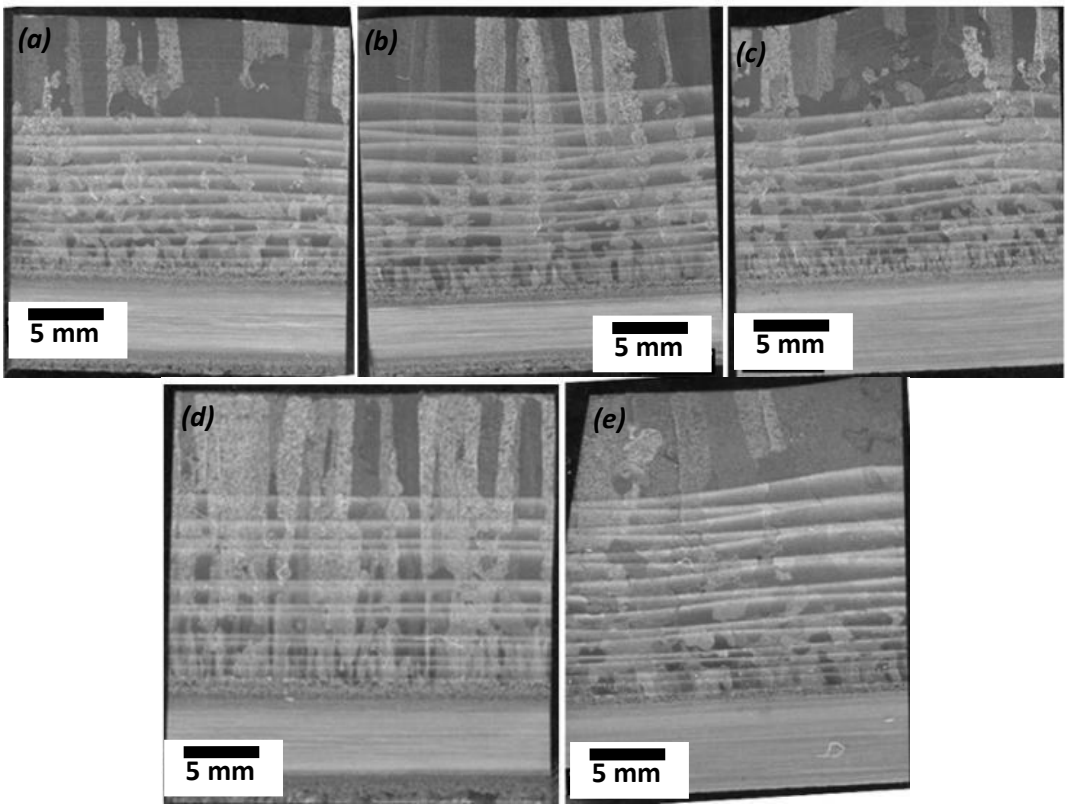

Figure 6.6: *Micrographs showing the effect of changes in pulse frequency from (a) 50 Hz, (b) 25 Hz, (c) 10 Hz, and (d) 5 Hz during the WAAM process with the Ti6Al4V alloy.*

6.2.5 WAAM using the GMAW - CMT process

To see if a cold metal transfer (CMT) GMAW process could help with the formation of a fine equiaxed grain structure, and to compare this process to builds with the normal GTAW power supply, an additional sample was investigated that was produced using a lower heat input CMT–GMAW process, with the process parameters shown in Table *3.8*. In the CMT- GMAW process the wire is moved forward and dips in the molten pool with a controllable frequency. The digital control then senses the voltage drop when short circuiting occurs, and the current is reduce to a significantly lower level. The wire is then retracted and the wire withdrawal force assists liquid bridge fracture so that droplet detachment takes place, and metal transfer occurs by surface tension. Hence, the overall amount of heat input in the process is very low, which should give a lower thermal gradient in the melt pool, when compared to a standard GTAW processes. A single wall specimen with ten layers was deposited with this method using a 1.2 mm diameter wire and a constant layer height of ~ 1.5 mm.

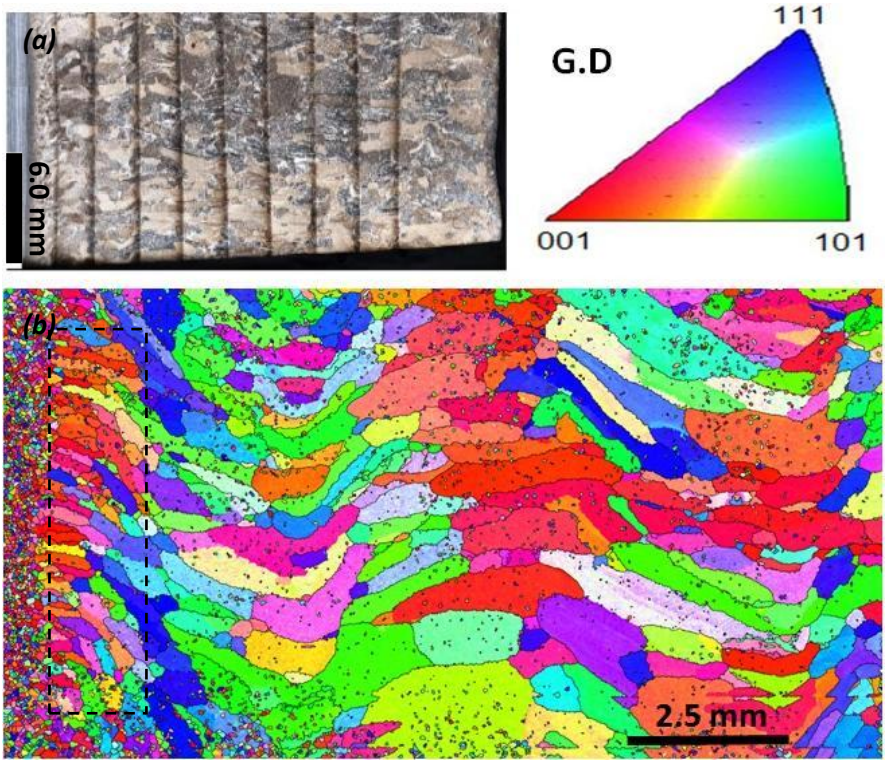

Figure 6.7: *Macrograph (a) and an EBSD map (b) of the reconstructed high temperature* β *grains in a Ti6Al4V sample that was produced using the CMT-GMAW WAAM process (EBSD IPF map oriented || Nz build direction). The horizontal direction is the direction of the build.*

The Figure *6.7* shows a centre line cross section macrograph and reconstructed EBSD β grain map of the Ti6Al4V wall built using the CMT process. With the CMT process the backwards and forwards movement (+X and –X axis) of the torch, resulted in clear evidence of grains bending to follow the heat source, in a zigzag fashion, in the X-Nz plane. It can be seen from the reconstructed β grain EBSD map that the size of the columnar grains was approximately 4 mm in length, and the width varied from 0.16 to 1.12 mm, which is smaller than the grain size in the normal GTAW process.

6.2.6 Discussion on the influence of process parameters on β grain structures in the WAAM process

In the deposits built with the WAAM process, under all conditions fine hetrogenously nucleated equiaxed β-grains could be seen to develop at the base of the walls, due to the high cooling rate from the base plate. Rapid β grain growth also occurred in the HAZ below the first deposited layer, which led to an equiaxed coarser β grain structure being seen at the base of each wall compared to in the rolled substrate plate. In general, coarse columnar grains then developed by epitaxial re-growth from this initial equiaxed layer (similar to in the bulk grain structure discussed in

section 4.3) as was predicted from the solidification map and thermal modelling discussed in 4.2 (see Figure *4.5*). This occurs due to the lower growth rate associated with the WAAM process, which prevents the G_L/R ratio crossing into the mixed grain structure field on the solidification diagram, despite the lower thermal gradients seen with this process. However, in some instances, a coarse equiaxed grain structure was produced in the WAAM builds.

In the WAAM walls deposited with the DC GTAW process, when a low heat input and travel speed (240 kJ/m and 3 mm/s) was used, a large columnar β-grains (Figure *6.1*a) developed by epitaxial re-growth, as was discussed above. Whereas, when the heat input and travel speed was increased (> 280 kJ/m and > 6 mm/s), the formation of 4 distinct microstructural regions was noticed, as shown in Figure *6.1*(b-c): namely (i) a fine equiaxed β grain region at the base, followed by (ii) a constrained columnar grain region, (iii) a coarse equiaxed grain region and, (iv) then a fine aligned columnar grain region at the top of the final layer. The reason for this transition from epitaxial columnar growth to equiaxed grains, seen when the process parameters were changed (transition from the 2^{nd} to 3^{rd} region), is probably because a higher heat input and travel speed reduces the G_L/R ratio, which would help in allowing some limited nucleation in the melt ahead of the growth front, as discussed in section 2.2.2. In favour of this argument, the melt pool size and wall width increased with increasing heat input which would reduce the thermal gradient at the solidification front [128]. The effect of a higher G_L/R ratio can also be seen on the solidification diagram presented in Figure *4.5*. Although the higher heat input generated an equiaxed grain structure with these conditions, the wall width was not consistent (Figure *6.1*b-c). Whereas, the lower heat input (Figure *6.1*a) sample produced a more consistent wall thickness and achieved the expected wall height at the end of the process. Thus, these high heat input conditions were found to be outside of the range of the process parameters that gave stable build conditions.

The more regular finer columnar grain region found at the top of the final layer of the deposits was seen to be aligned with the concave surface of the melt pool in cross-section view micrographs (Figure *6.1*b-c). This suggests that these grains were nucleated from the melt pool surface and grew downwards to meet grains growing up from the bottom of the melt pool (Figure *6.1*b-c). This occurred because the convective heat loss through the top surface is very high in the WAAM process, when forced cooling occurs from the high shielding gas flow rate used, and this can locally dominate the heat extraction through the wall by conduction. It was also noted that these columnar grains, seen at the top of the final layer, were inclined to align themselves with the maximum thermal gradient (depending up on the direction of GTAW torch movement). This same phenomenon was also noticed in nearly all the wall sections, irrespective of the process conditions, and is clearly caused by the chill effect at the high gas flow rate required for effective shielding in an out of chamber WAAM process, combined with the travelling heat source.

The initial results with the DC GTAW power supply thus demonstrated that, in the WAAM process, an increase in travel speed and heat input (see Figure *6.1*b-c) favours the formation of equiaxed grains, since the G_L/R ratio reduces with a higher heat input and travel speed, which promotes constitutional supercooling and some limited nucleation in the melt pool.

It was expected that the use of VBC- HF process would help promoting dendrite fragmentation at the S/L interface for the equiaxed grains, since interpulsing can increase the turbulence in the melt pool and also the constricted arc providing more focused heat source [159]. However, the two different walls produced with a travel speeds of 0.27 m/min and 0.54 m/min (with a constant heat input of 182 kJ/m) using VBC-HF interpulsed power source, did not show any significant reduction in the large grain size noticed in the DC-GTAW process for almost the same energy (see Figure *6.1*a and Figure *6.2*a). Although the increase in travel speed was expected to reduce the (G_L/R) ratio [44, 46], which could possibly help in the formation of equiaxed grains, changing the travel speed also did not show any significant reduction in grain size using the VBC interpulse GTAW process (Figure *6.2*). However, it might be that the limited change in travel speed possible (from 0.27 m/min to 0.54 m/min) while maintaining stable process conditions was not enough to have a significant effect on the large columnar β grains seen in the deposits (Figure *6.2*).

Increasing the wire feed speed (WFS) was expected to affect the thermal gradient at the growth front by cooling the melt pool and consequently promoting undercooling, by altering the G_L/R ratio. At the base of the build it can be seen from the EBSD reconstructed β-grain map in Figure ***6.3***b that, when a low wire feed rate was used, initially columnar β grains start to grow with their easy $<001>_\beta$ growth direction aligned parallel to Nz, as was discussed before in section 4.3. However, when the WFS increased to 2 and 2.2 m/min, the nucleation of new equiaxed grains could be seen in Figure ***6.3***c. Changes in the IPF colour key also show evidence that the new grains had more random orientation (see Figure ***6.3***c). When the WFS was increased to 2.2 m/min from 1.6 m/min the extra cold metal fed into the melt pool was therefore sufficient to reduce the thermal gradient, and the resulting G_L/R ratio at the S/L interface enough, to allow nucleation to occur in the melt pool.

In the GTAW process it has been reported by other authors [160-162] that the arc pressure changes with current and pulsing the arc will increase melt pool turbulence and fluid flow. This enhanced fluid circulation, or convection, in the melt pool could encourage the formation of equiaxed grain structures by reducing thermal gradients and causing dendritic fragmentation, which can then act as a source of nuclei for equiaxed grains, provided some undercooling is achieved ahead of the growth front [44, 163]. However, in the current study all the builds produced with a standard pulsed GTAW power source still showed large columnar β grains (as indicated in Figure *6.5*). Although the peak to base current (I_p/I_b) ratio was varied from 3.3 to 6.7,

it did not produce any significant changes in the microstructure. However, it has been reported in the literature that an increase in (I_p/I_b) ratio can show a beneficial effect in terms of a reduced grain size. This behaviour has been reported in welding a Ti6Al4V alloy with a pulsed GTAW, but with different process parameters [160, 164, 165]. It can also be seen from the Figure *6.6* that the pulse frequency had no significant effect on the prior β grain size. i.e., the large columnar prior β grains were not affected by low or high frequency of pulsed current and in each case columnar β grain growth was still seen until the end of the final layer. This lack of change in grain structure in response to an increase in melt pool turbulence can be related to the metallurgy of the Ti6Al4V alloy. The Ti6Al4V alloy has a very low freezing range and, Al and V exhibit negligible solute partitioning [39, 115, 151]. As a result, the Ti6Al4V alloy would be expected to have a very narrow mushy zone and to develop only short dendrites, which have a high mechanical strength and are unlikely to fragment even if there is increased fluid flow in the melt pool.

In the CMT-GMAW process it can be clearly seen that the β grains first hetrogenously nucleate from the substrate plate and, similar to in the standard arc process, coarse columnar grain structures then developed in the deposit (Figure *6.7*). Despite the CMT technique cooling down the melt pool, by reducing the heat input, this process was not as effective as using a high wire feed rates with GTAW and columnar grain structures were still observed. However, the columnar grains were seen to bend towards the direction of torch movement and, when the next layer was deposited, the opposite movement of the torch was seen to causes grains to re-nucleate better aligned with the opposite torch travel direction. This behaviour was not observed with the standard GTAW power supply where columnar growth was always aligned with Nz. However, this effect is not unexpected since the melt pool has a bowl shape and the average maximum thermal gradient at the rear of the melt pool is inclined and would reverse in direction when the torch travel direction reverses. This effect is probably caused because the CMT process produces a different shaped melt pool and had a reduced thermal gradient at the S/L growth front. A combination of marginally more constitutional undercooling and a shallower melt pool probably causes closer alignment of the β grain growth with the base of the melt pool, because alignment can be maintained in the next raster path in the reverse direction, by new nuclei, or dendrite fragments surviving that are better aligned with the new growth direction of the melt pool surface. Dendrite branching or bending in a wider mushy zone could also produce a similar effect [44, 148]. It can also found from the reconstructed β grains that, although the size of the columnar grains was still very large, with an average of 3 mm in length, and 0.6 mm in width, this was smaller than seen in the standard GTAW process (35 mm in length and 0.5 to 3 mm in width). This reduction in grain size occurs as a result of the lower heat input with CMT and because large columnar grains were not able to become established due to the realignment, facilitated by the dendrite branching or fragmentation that occurs in each layer.

6.3 INFLUENCE OF PROCESS PARAMETERS ON TEXTURE IN WAAM

In the WAAM process the bulk Ti6Al4V sample, produced under standard conditions, had a coarse columnar grain structure with a strong primary β phase $<001>_{\beta}$ || Nz fibre texture and weaker related α transformation texture, as was discussed in chapter 4.4. However, this strong texture is related to the β grain growth behaviour during solidification and potentially can be modified with changes in the process parameters. This section focuses on the effects of changes in the process parameters on the texture development in the WAAM process. More limited samples were analysed by EBSD measurement than in chapter 4 and 5, owing to problems arising from the large grain sizes observed in the WAAM processes. The example texture examples evaluated here were from two samples produced, with (1) change in WFS using GTAW process and (2) sample produced with CMT- GMAW process.

6.3.1 Primary β textures

Pole figures depicting reconstructed β-textures obtained from the EBSD maps shown in Figure ***6.3*** and Figure *6.7* are presented in Figure 6.8. The pole figures are orientated the same way as for the other EBSM and SLM processes, where the build direction (N_Z) is normal to the plane of projection. The texture found in the bulk microstructure (Figure 6.8a) show again here the standard bulk texture pole figures shown in chapter 4 under the standard process conditions using a GTAW power supply, when a coarse columnar β-grain structure was well established. As discussed previously (section 4.4) a strong $<001>_{\beta}$ || Nz fibre texture can be observed, with a maximum intensity of ~ 21 xs random. However, the sampling statistics were poor, since the observed β-grains were too large to map a reasonable number of grains. This texture is compared to that shown in Figure 6.8b for the increasing wire feed rate sample, from the position in the wall when the wire feed rate was above 2.2 m/min and an equiaxed grain structure was observed (see Figure ***6.3***c). Despite the coarse grain size, it can be seen that the texture is much more random than that of the texture seen in the bulk wall produced with a standard WFS of about 1.6 m/min. However, the pole figures still show the present of some <001> || Nz alignment associated with a cube component. Again because of the large grain size and poor sampling statistic, it is hard to tell if this is more than a random event, but the presence of a weaker <001> || Nz related texture appears likely.

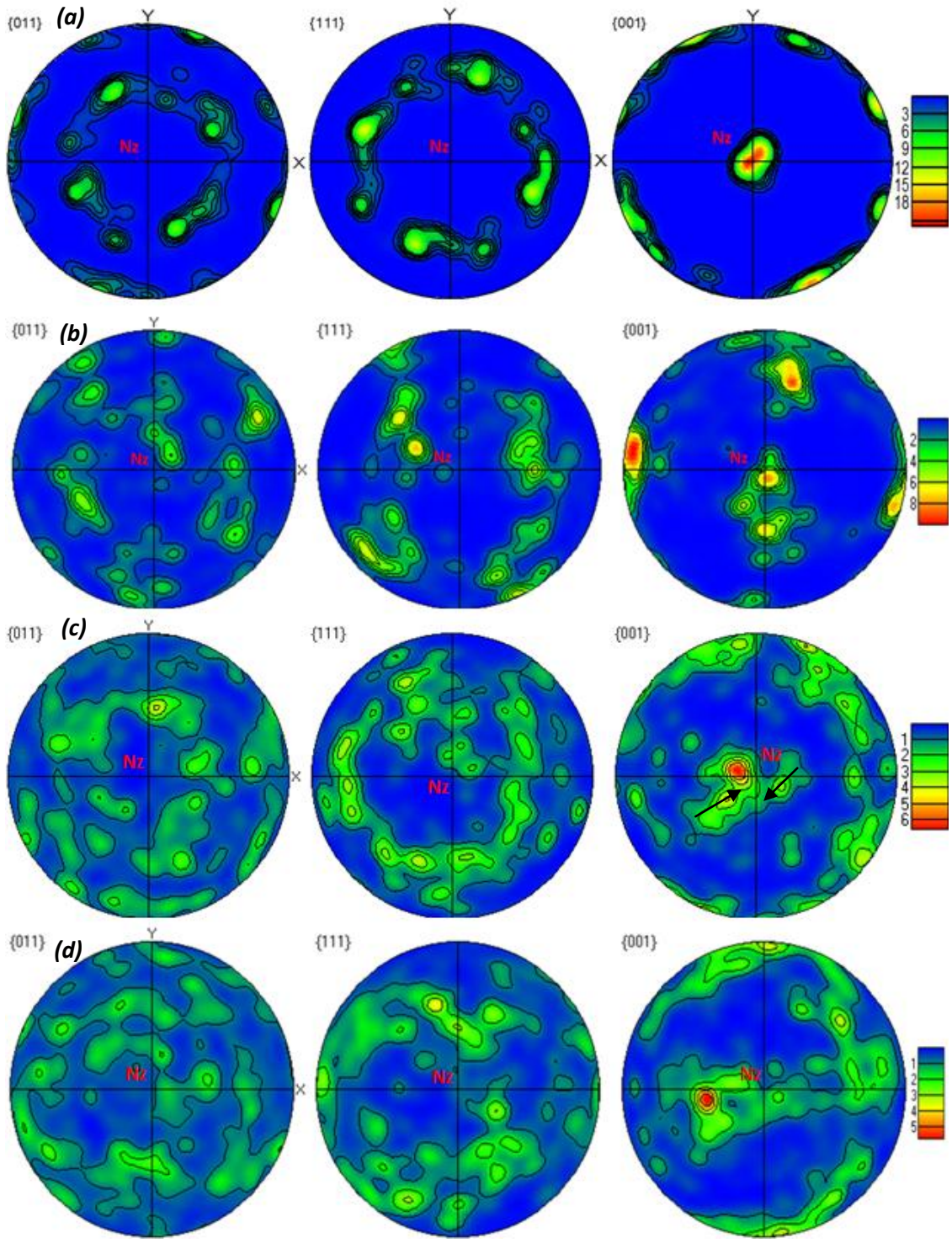

Figure 6.8: *Pole figures depicting primary β <001> || Nz fibre textures; (a) from a standard build after establishing steady state conditions with a WFS of 1.6 m/min, (b) the change in the primary β texture when the WFS was increased > 2.2 m/min in the GTAW process, as shown in Figure 6.3. (c) Shows the presence of a β fibre texture in the last layer of the CMT-GMAW specimen (highlighted area in the dotted line in Figure **6.7**), and (d) the presence of a tilted primary β fibre texture in the CMT-GMAW deposits.*

Finally, Figure 6.8c-d show the textures in the first layer and subsequent layers of the whole build in the wall produced with the CMT-GMAW process. Figure 6.8c shows the local texture in the first layer of the CMT- GTAW specimen, and this region is highlighted with a dotted line in Figure *6.7*. This again shows the presence of strong <001> β fibre texture with texture intensity of 7 xs random. However, this local texture is tilted slightly off axis from Nz by 5 - 10˚ towards the direction of the heat source travel (X). In comparison in Figure 6.8d, the same tilted fibre texture can be seen spread along X, in the backwards and forwards direction of the heat source travel.

6.3.2 α transformation textures

Pole figures measured from the bulk transformed α phase in the WAAM GTAW process, with the standard conditions and a typical WFS of 1.6 m/min is shown in Figure *6.9*a, after steady state conditions were established. This data was obtained from the corresponding α phase of the EBSD map shown in Figure ***6.3***. The bulk α phase showed a transformation α fibre texture of 7 xs random strength, corresponding to the respective primary β texture, shown in Figure 6.8a. In comparison, Figure *6.9*b shows how the transformed α texture changed, when the WFS was increased to above 2.2 m/min and an equiaxed β grain structure was produced. In this case, the α texture strength decreased to 4 xs random. Figure *6.9*c also shows the presence of a weaker transformed α-texture in the CMT-GMAW deposits, where the β grain structure was not as closely aligned with the build direction.

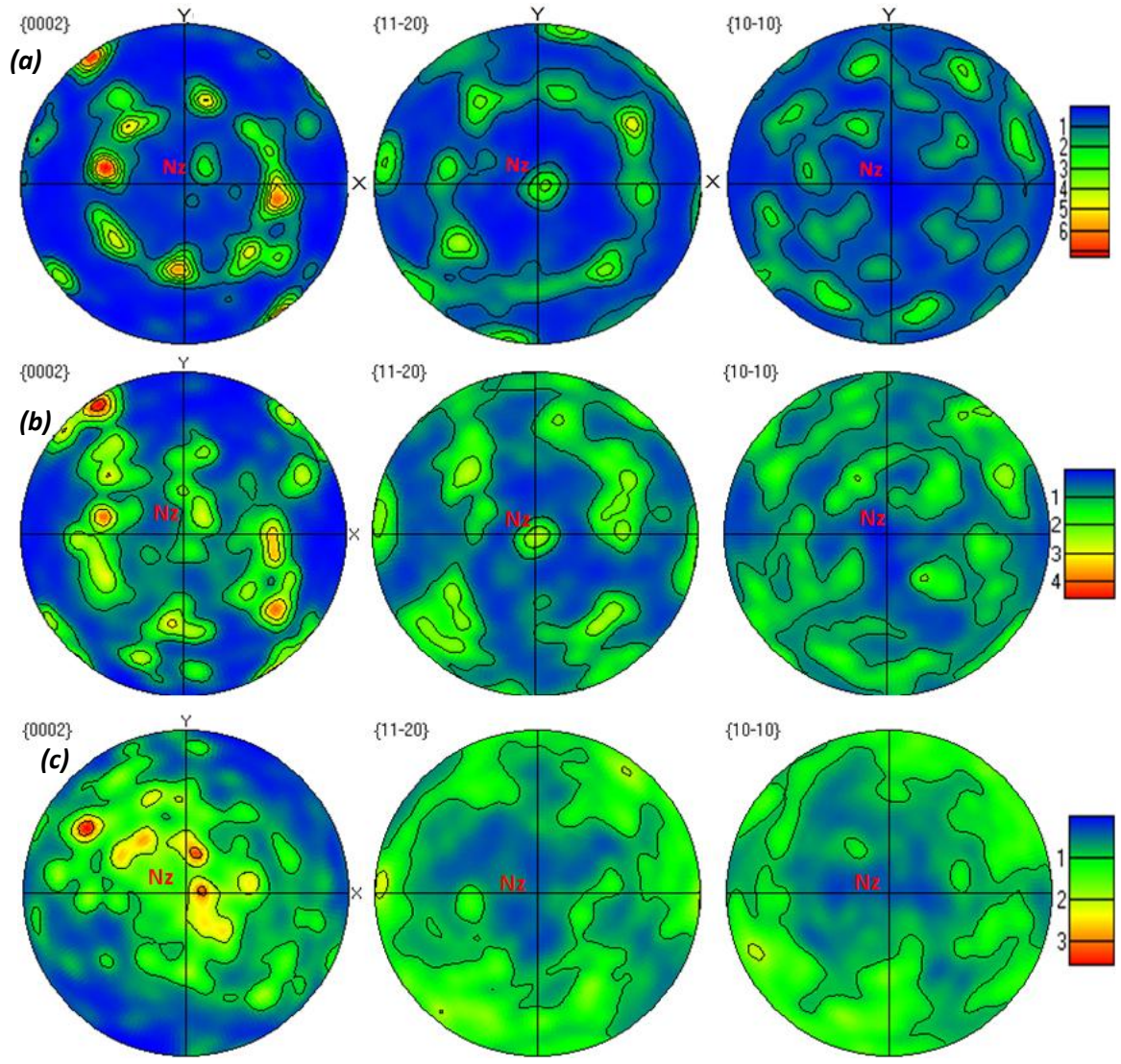

Figure 6.9: *Pole figures depicting transformed α textures (a) for standard GATW WAAM conditions with a WFS of 1.6 m/min, (b) the WFS > 2.2 m/min, and (c) the presence a weak transformed α-texture in the CMT-GMAW deposit.*

6.3.3 Discussion of the influence of process parameters on texture in WAAM

Primary β textures

The bulk primary β texture found in the WAAM build that was produced with high WFS was compared to the normal texture shown in Figure 6.8. For the standard WFS of 1.6 m/min, a strong $<001>_{\beta}$ || Nz fibre texture was developed in the bulk texture with a maximum intensity of ~ 21 xs random, as discussed in section 4.4. In comparison, Figure 6.8b shows the change in bulk primary β textures when the WFS increased > 2.2 m/min, where the texture becomes more random than that of the texture seen in the standard WFS of about 1.6 m/min. This occurred because the increase in wire feed speed affected the thermal gradient at the s/L interface, by cooling the melt pool down, which altered the G_L/R ratio and allowed nucleation ahead of the growth front,

resulting in an equiaxed grain structure. Hence, randomisation of the texture was observed when the WFS was increased to 2.2 m/min or more. However, the cube component still seen in this texture has not been satisfactorily explained and needs further investigation with more reliable statistics.

Figure 6.8 (c and d) showed the local texture in the first layer and in the bulk section of the CMT-GMAW specimen. This local texture analysis showed the presence of weaker <001> β fibre texture that was slightly titled away from Nz axis by 10˚ towards the heat source travel direction with a texture intensity of 7 xs random. This behaviour occurred because the grains nucleated tended to bend and grow in the direction of heat source movement, following the melt pool (see Figure *6.7*). In comparison, the bulk β texture for the CMT process presented in Figure 6.8d showed a <001> fibre texture which was aligned || to Nz (with the maximum intensity of 6), but spread along heat source travel direction with an maximum intensity of 6 xs random. The spread of <001> β texture along the direction of deposition (X) is due to the different alignment of the grain structures observed with this process, which followed the curved melt pool surface, and the forwards and backwards movement of the heat source.

α- transformation textures

The pole figures measured from the bulk transformed α phase, with a typical WFS of 1.6 m/min, showed a weak transformation α fibre texture with an intensity of 7 xs random (Figure *6.9*a), as discussed in section 4.4. In comparison, Figure *6.9*b indicated a change in the α texture, when the WFS were increased to above 2.2 m/min. In this case, a texture intensity of max 4 xs random was observed, which was weaker than seen in the bulk texture with a WFS of 1.6 m/min. This reduction in α texture intensity was associated with the randomisation of the primary β texture, because of the formation of newly nucleated required grains, as discussed above. The CMT-GMAW deposit also showed the presence of a weaker transformation α texture spread around Nz (Figure *6.9*c) and the maximum observed texture intensity was 3. Again, the presence of weakened α textures suggests there is little variant evidence of variant selection and that the texture becomes diluted by a random habit plane distribution on cooling down following solidification.

6.4 EFFECT OF ROLLING DEFORMATION IN THE WAAM PROCESS

6.4.1 Introduction

A preliminary study was performed during the course of this work to assess the potential for introducing an additional deformation step in AM, to refine the large columnar prior β-grain structures seen in the AM builds. The deformation step was applied in the WAAM process by using a roller to lightly deform each layer, before depositing a new weld bead. The aim of this hybrid manufacturing process was to introduce recrystallisation in the solidified alloy, during the re-heating stage that occurs when the next layer is deposited, and thereby improve the coarse β grain structure and strong texture described in chapter 4. In order to study the effect of rolling deformation on AM, immediately after the deposition of each layer, the single wall samples were deformed with predefined loads of about 50 kN and 75 kN by a roller. The results were compared to a control sample with no deformation. All the samples were produced with the process parameters shown in Table *3.9*. Full details of the set up used can be found in section 3.4. The results presented in this section are preliminary results and further understanding of the texture development requires additional systematic experiments, coupled with deformation and thermal modelling.

6.4.2 Deformation conditions

Table *6.1* shows the average change in layer height and wall width after every rolling each layer which allows an estimated of the net cold deformation between each pass. The compressed samples with different rolling loads are shown in Figure *6.10*. The sum of the total strain during deformation in all directions should be equal to zero ($\xi_{RD} + \xi_{ND} + \xi_{TD} = 0$). In conventional rolling wide plates, a plane strain condition applies in RD-ND and usually it is known that the $\xi_{RD} = -\xi_{ND,}$ and $\xi_{TD} = 0$ during the rolling deformation [65, 73, 166]. Here, the average strain introduced by the rolling load was calculated from the reduction in height (ξ_{ND}) and increase in wall width (ξ_{TD}). From these two strains, the strain in RD (ξ_{RD}) could also be obtained by assuming constant volume. These approximate average strains are shown in Table *6.2*. From the Table *6.2*, it can be seen that the strain in RD is minimal and deformation mainly occurs by plane strain in TD and ND. Therefore, because of the thin wall width the strain tensor is different to in rolling, i.e., although plane strain compression still occurs the main strain components are rotated 90˚ about ND compared to when rolling a wide sheet. Thus, although there is a decrease in layer height and an increase in wall width during deformation, the length of the sample along the rolling directions remains unchanged. The sample rolled with the load of 50 kN and 75 kN had undergone cold compression

of 8 % and 18 % in ND, respectively. However, the samples will not be deformed uniformly throughout the cross section; since the cross section width along the build direction was not perfectly constant, due to the curved shape of a single weld bead wall. Equally, the strain distribution produced by the roll will be concentrated below the surface, because the wall height is very large compared to the roll diameter [166]. This is not the case in a normal rolling process, where the deformation is usually more uniform throughout a cross section.

Table 6.1: *The change in layer height and wall width after rolling deformation in the Ti6Al4V builds using the pulsed GTAW process.*

Change in layer height after rolling		
ID	*Av. Layer height (mm)*	*Reduction after rolling (mm)*
Control	1.13	
50 kN	1.04	0.09
75 kN	0.93	0.20
Change in wall width after rolling		
ID	*Av. Total wall width (mm)*	*Increase due to rolling (mm)*
Control	5.71	
50 kN	6.17	-0.46
75 kN	6.71	-1.00

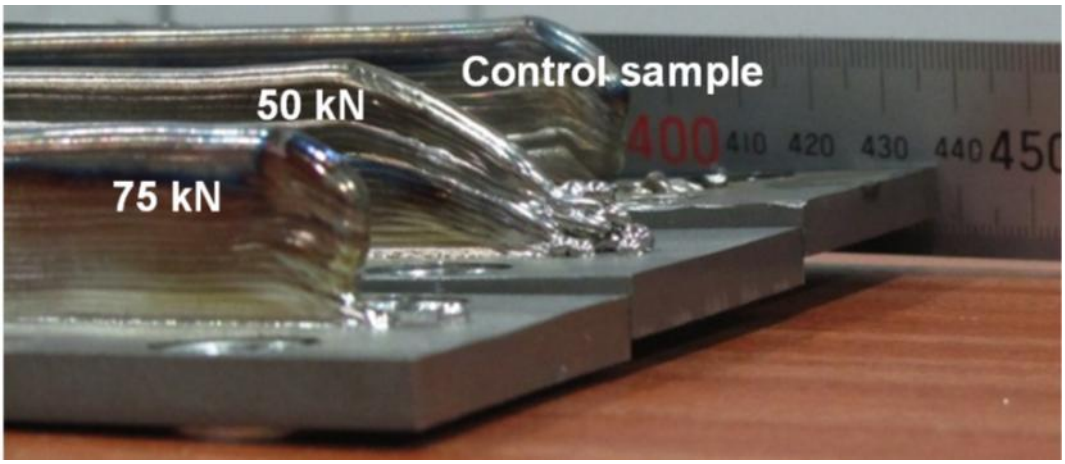

Figure 6.10: *The rolled WAAM samples with different rolling loads and the control sample.*

Table 6.2: *The average strain in the material after rolling deformation in the Ti6Al4V builds using the pulsed GTAW process.*

Control	**Reduction in height (ξ_{ND}) %**	**Increase in wall width (ξ_{TD}) %**	**Change in length (ξ_{RD}) %**
50 kN	-8	+8	0
75 kN	-18	+18	0

6.4.3 Primary β grain structure evolution in the deformation +WAAM process

Figure *6.11* shows the macro- and micro-structure of the control and deformed samples. In the control sample (Figure *6.11*a), as described previously (section 4.3), fine equiaxed columnar grains develop heterogeneously from the base plate, as shown in Figure *6.11*a. Large columnar β-grains then start to develop, without further nucleation, upon the deposition of subsequent layers with a size of about 15 mm to 21 mm in length, and 0.8 mm to 2.0 mm in width. In comparison, the samples deformed with an average rolling reduction of 8 % and 18 % showed fine β-grains, with an equiaxed morphology (see Figure *6.11*) under optical microscopy, except for the last layer (Figure *6.11*d), which was rolled but not reheated by subsequent deposition passes. Figure *6.11* (f-g) shows the fine equiaxed grains measured at the centre of the deposits for both the 8% and 18 % deformed AM samples. The size of the prior β-grains varied from 90 -270 µm, and 55-145 µm in the samples with 8% and 18% rolling reductions, respectively, under optical microscopy. The rolling process not only helps in the grain refinement, it could also reduce the amount of defects and distortions in the WAAM build.

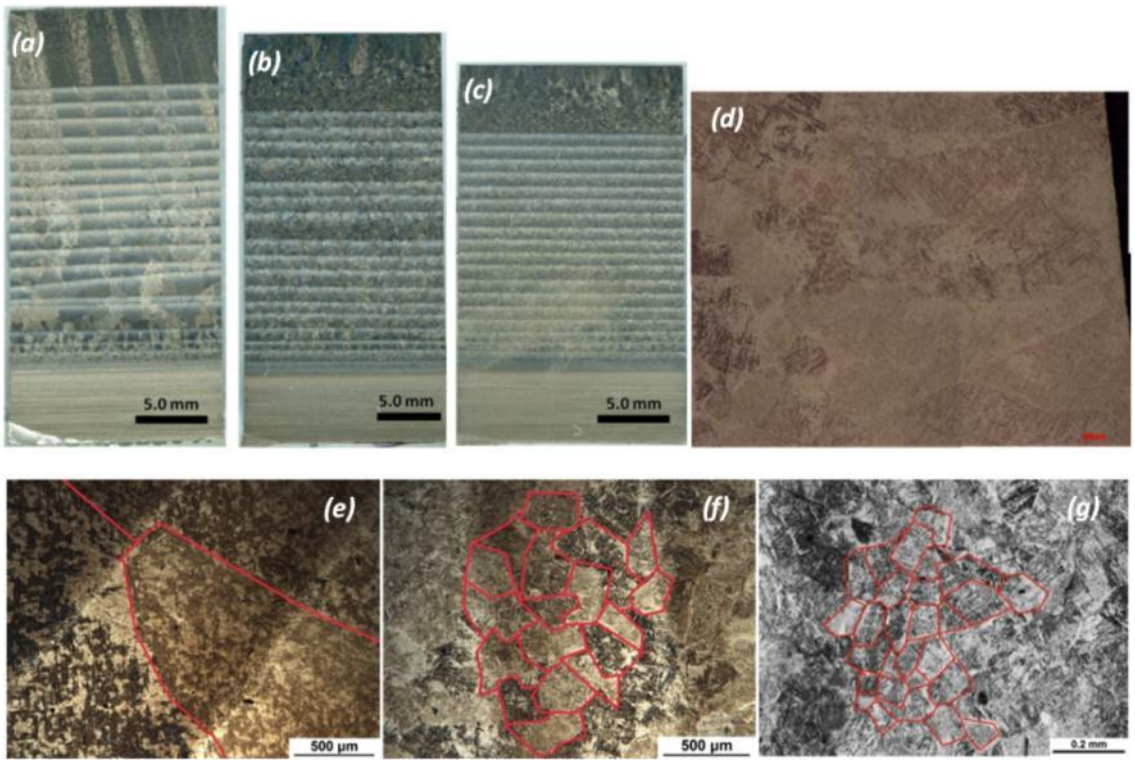

Figure 6.11: *Macro-graph showing 20 layers of a WAAM Ti6Al4V wall, deposited using the GTAW process with (a) no load (Control sample), and when deformed between each deposition pass by rolling using (b) a 50 kN load (8% deformation), and (c) a 75 kN load (18% deformation) with a grooved roller; (d) shows the top layer of the build produced with 75 kN load, (e-f) shows the prior β-grain sizes at higher magnification for the control sample and, 8% and 18% strained samples, respectively.*

In both the 8% and 18% rolling reduction samples the final layer again had large columnar grains (Figure *6.11*b-d). The columnar grains in this final layer was not re-heated and were formed from the melt pool surface by forced cooling from the shielding gas, as was discussed in section 6.3. Although the final layer was deformed, it showed large columnar grains in both the 8%, and 18% strained sample, since it was not heat treated above the β-transus by subsequent deposition of the next layer.

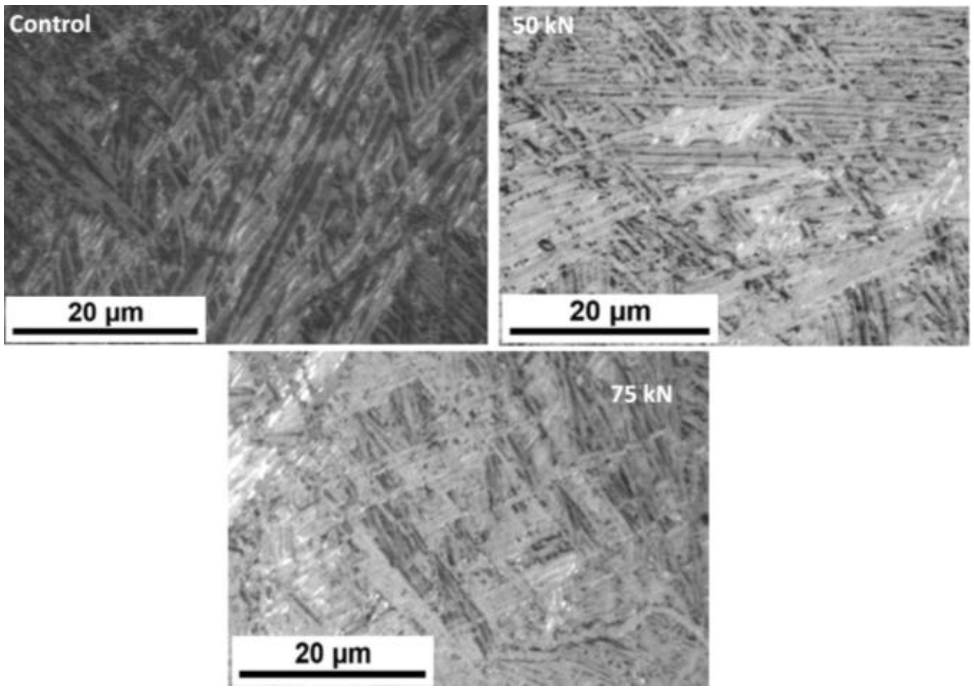

Figure 6.12: *Transformed α microstructures in the control specimen (a), and in 8% (b), and 18% (c) stained samples by optical microscopy.*

In the control sample, within the large columnar prior β-grains a standard Widmanstätten α+β microstructure was observed, with some grain boundary α, as described in chapter 4. The 8 % and 18 % strained specimens also showed fine lamellae plates with Widmanstätten α-morphology, and colony α-morphologies, within the prior β-grains, as shown in Figure *6.12*. Microstructural banding was also observed in all the builds, due to repeated thermal cycles upon the deposition of every new layer, as was explained in 4.5.

Figure *6.13* shows α and reconstructed β phase Nz - IPF orientation maps, parallel to build direction from the base of the build, for the unrolled, 8 % and 18 % rolling reduction samples, obtained by EBSD analysis. As discussed previously (section 4.3), the unrolled/control specimen contained large columnar β-grains growing along <001> || Nz, developed by epitaxial re-growth, after heterogeneous nucleation from the substrate plate. However, when enough deformation is

introduced into the sample a refined β grain structure was observed. The increase in deformation with rolling strain also significantly reduced the grain size in the final microstructure, as shown in Figure *6.13*.

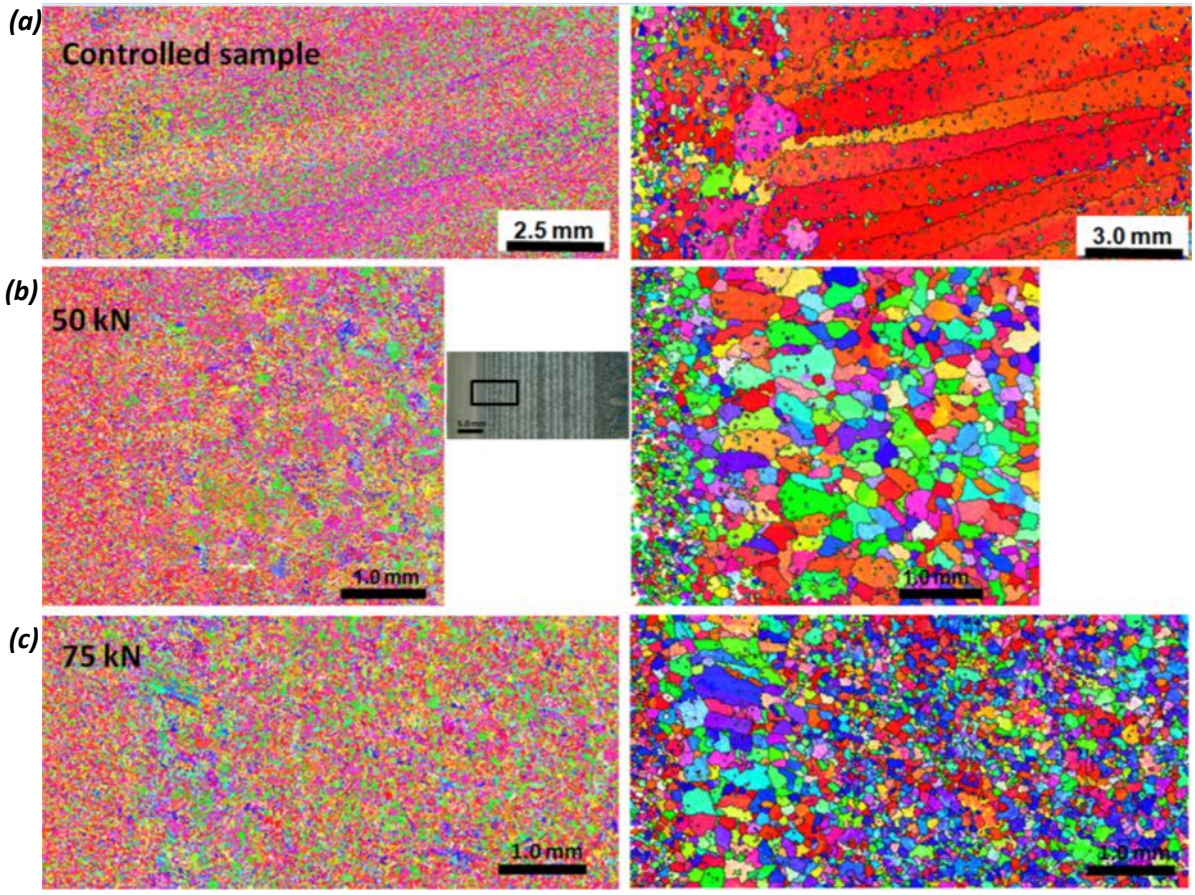

Figure 6.13: *α-phase, and corresponding reconstructed* β*-phase EBSD orientation maps, from an (a) un-deformed WAAM control sample and with average rolling reductions of 8 % (b) and 18 % (c).*

Figure *6.14* shows the variation of grain morphology and its size between the unrolled, 8 % and 18 % stained samples at a higher magnification. The grain size refinement observed in the Figure *6.14*, suggests that both samples strained to an 8 % and 18 % reduction received adequate cold deformation to initiate grain refinement, when the particular strained layer was exposed to an adequate temperature, or heat treatment above the β-transus (T_β) of Ti6Al4V, by the deposition of the subsequent next layers. In comparison, the grains in the unrolled sample continued to grow epitaxially (with no nucleation) upon the deposition of every new layer, as a large columnar β grains with high aspect ratio 2:20. Whereas, when the material had been deformed, fine β grains were observed, as shown in Figure *6.14*. Figure *6.15*(a-b) provides a comparison of the β-grain size distribution in the samples strained to an 8 % and 18 % reduction during AM of the Ti6Al4V alloy.

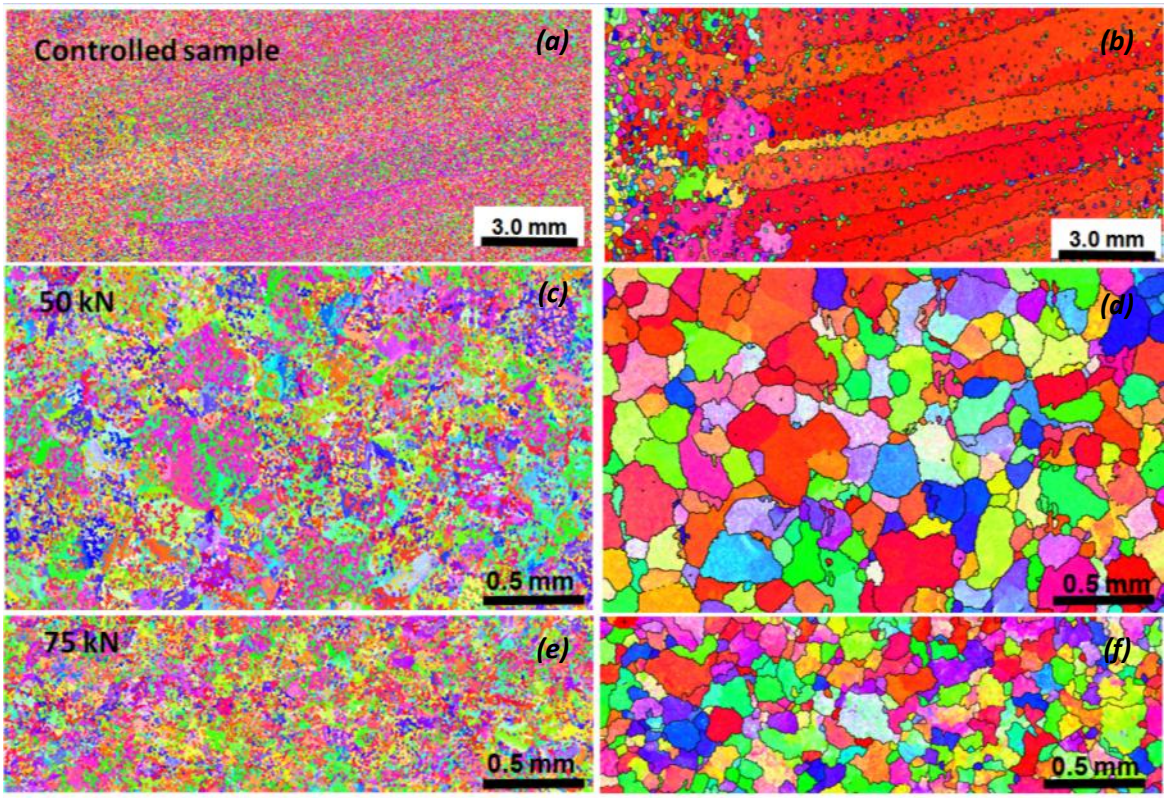

Figure 6.14: *α- phase and reconstructed β EBSD data with IPF || Nz orientation maps for (a - b) the control sample and, (c - d), and (e - f) for 8%, and 18% reductions, respectively.*

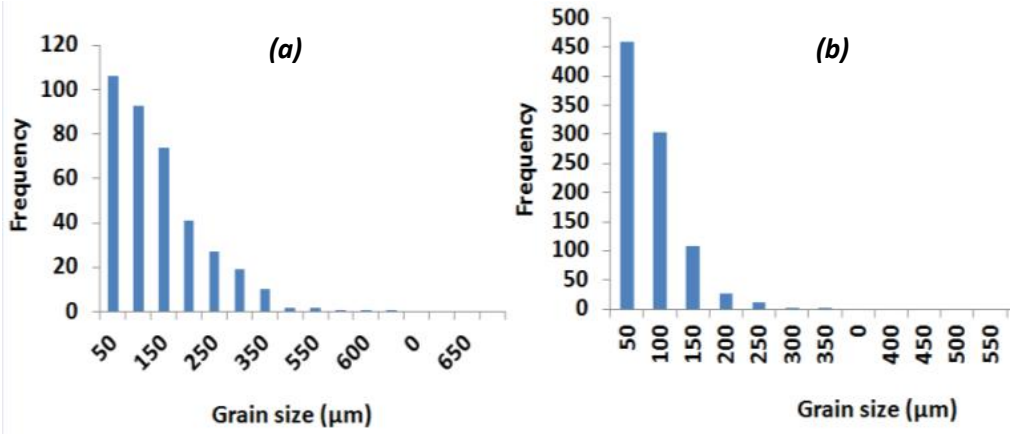

Figure 6.15*: β -grain size distributions for the 8 % (a), and 18 % (b) reductions respectively.*

In order to study heterogeneity in the builds with different amounts of deformation, the hardness of the samples were assessed. Figure *6.16* shows the variation of Vickers microhardness from the base of the deposit to the final layer, at intervals of 0.3 mm (with a 0.5 Kg load), in the un-rolled, and 8 % and 18 % reduction samples. The average microhardness was observed to show 352, 345, and 350 (HV0.5) in the unrolled, 8 %, and 18 % strained materials, respectively.

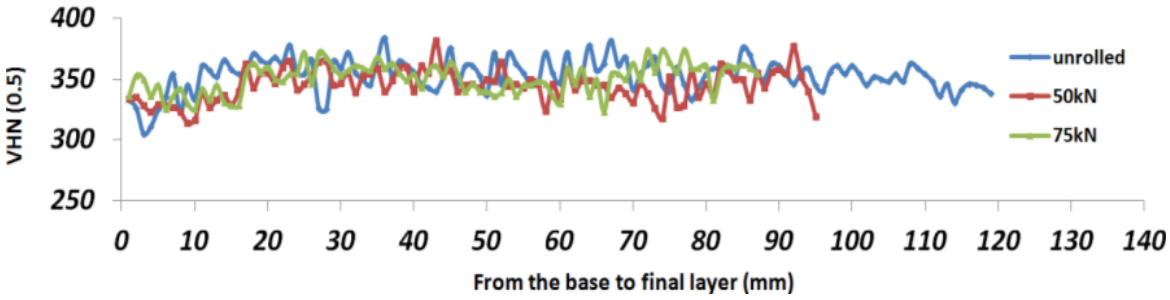

Figure 6.16: *Variation of microhardness along the direction of build from the base to final layer in the controlled (un-rolled), 8 % and 18 % strained samples.*

6.4.4 Discussion on the effect of rolling on the β grain structure with the WAAM process

In the unrolled walls, as described previously, very large columnar β-grains developed without further nucleation upon the deposition of every layer with lengths of 15 mm to 21 mm. From, Figure *6.11*, Figure *6.13* and Figure *6.14*, clear evidence can be seen that the introduction of deformation by rolling each layer resulted in a high level of grain refinement of the large columnar β grains usually seen in the WAAM process. As shown in Figure *6.15*, the sample subjected to an average deformation of 8 % had a large spread in grain size from 50 µm to 650 µm, although this was a considerable improvement on starting structure. Whereas the sample deformed with an 18 % reduction, had a finer β grain size with less spread from 50 µm to 350 µm. The reasons behind the refinement of the β grain structure, after applying relatively moderate rolling reductions to WAAM wall deposits can be explained, as follows, with the help of recrystallization theory and the phase transformation behaviour during heat treatment of the cold worked materials.

During the cold rolling deformation, the α phase was relatively lightly deformed at room temperature. However, the low volume fraction of β phase (~ 6-10 %) will also undergo a significant deformation. When a layer is re-heated above the β transus temperature (T_β), in the next deposition pass the deformed room temperature β phase acts as nuclei and, start to grow by consuming the deformed α phase to form a fine primary equiaxial β grains [66, 132, 167]. These equiaxed primary β grains then stop growing upon the sudden air cooling after the heat source travels past. On cooling again below the β transus, at the moderate cooling rate seen in the WAAM process, the normal solid state β → α phase transformation then begins by nucleation of the α-plates (Figure *6.12*) from the β grain boundaries, and remaining untransformed β phase within the β-grains, transforms into a Widmanstätten α-morphology [39, 41, 113, 156]. This is

shown schematically in Figure *6.17*. It is also possible that the deformed α+β structure start to recrystallise on reheating before reaching the β transus temperature, but more work would be required to unambiguously demonstrate such an effect.

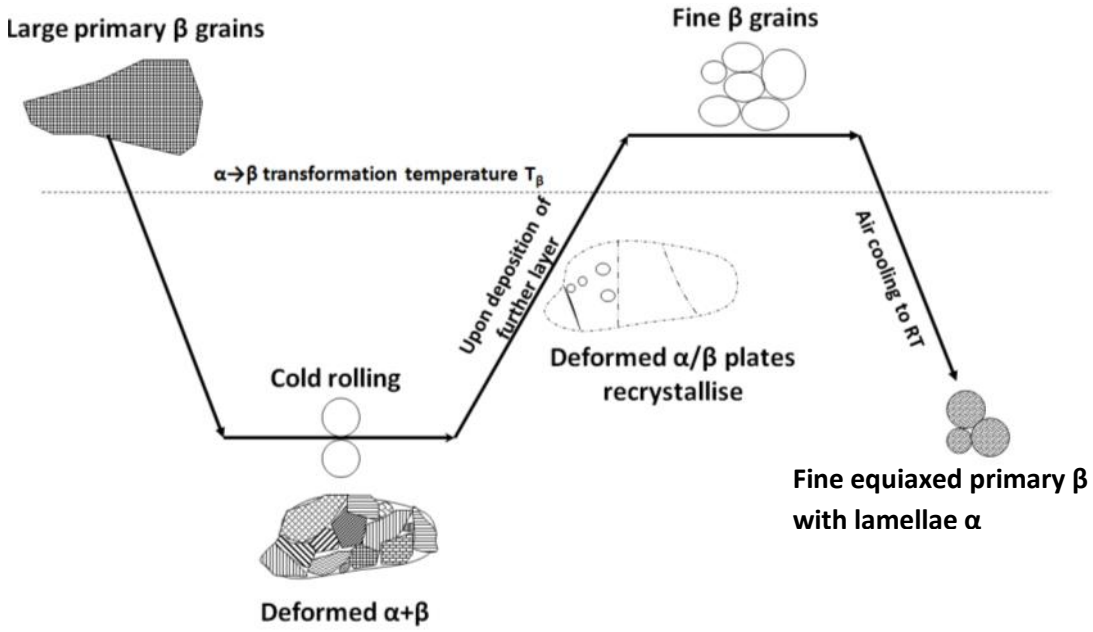

***Figure 6.17**: Schematic representation of the formation of fine β grains in the hybrid deformation - WAAM process.*

The decrease in average grain size in the sample subjected to a higher rolling reduction of 18 % (Figure *6.14* and Figure *6.15*) is due to the fact that the large amount of deformation induces more crystal defects in the retained β phase, which increases the possible nucleation sites during recrystallisation and on phase transformation, when the materials is heated above T_β and cooled to room temperature.

More information concerning the possibility of recrystallization occurring in the materials on reheating prior to the β transformation can be inferred from analysis of boundary misorientation distributions for the reconstructed β grains. Figure *6.18* shows misorientation profiles from the reconstructed β grains from the unrolled and, deformed samples with 8 % and 18 % rolling reductions. It can be seen that the sample deformed with an 18 % reduction had more low angle misorientations (arrow shown in Figure *6.18*) than that of the unrolled wall and 8 % reduction, which suggest more recovery could have happened with 18 % sample than that of 8 % sample [168]. Much variation in the high angle grain boundaries was not observed and this could be due there being not large enough rolling reductions in the samples to show a large variation in the misorientation profile. However, more in depth analysis is needed to understand the influence of deformation on recovery and recrystallisation before the β transus is reached.

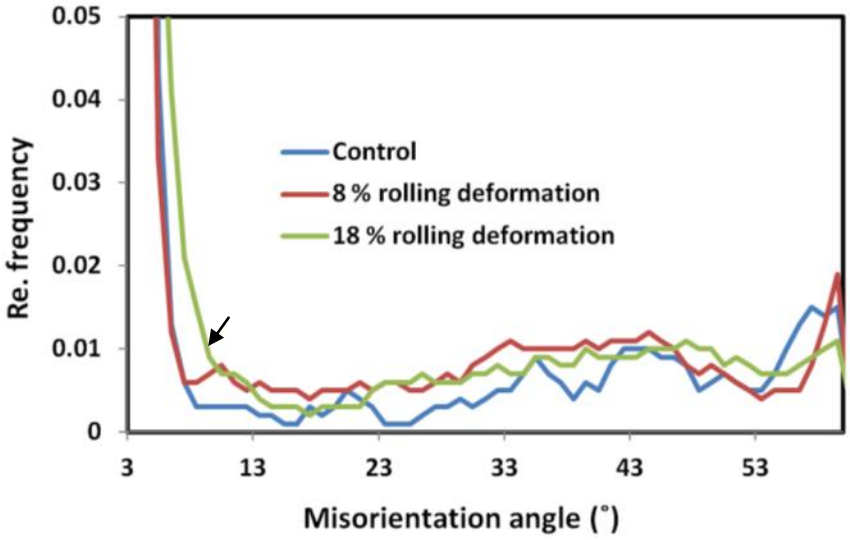

***Figure 6.18**: Shows the boundary misorientation angles from the reconstructed β grains for unrolled and deformed samples with 8 % and 18 % rolling reductions.*

Finally, the microhardness of the undeformed and rolled samples did not vary widely, since the transformation microstructure controls the hardness and strength, it is thus expected that the same hardness levels were observed in all three samples.

6.5 EFFECT OF ROLLING DEFORMATION ON TEXTURE IN THE WAAM PROCESS

It is usual that rolled, or deformed products, show heterogeneity in their mechanical properties with respect to the rolling, transverse and normal directions due to the development of crystallographic texture in the material [71, 73]. In addition, in the AM solidification structures an initial strong <001> ||Nz fibre texture was observed associated with the directional columnar grain growth. Hence, it is important to study the effect of rolling on the texture in the β and α phases when rolling is applied in the WAAM process.

6.5.1 Primary β-Textures

Pole figures depicting the reconstructed β-texture obtained from EBSD maps are presented in Figure *6.19*. The pole figures are orientated in the same way as that of the other EBSM and SLM processes, where the build direction (N_Z) is normal to the plane of projection. However, in the case of the rolled samples the rolling direction is also identified and Nz would be parallel to ND

and X parallel to RD, or the torch travel direction, in conventional rolling terminology. The standard bulk texture found in the centre of control sample, when the coarse columnar β-grain structure was well established, is shown in Figure *6.19*a for comparison purposes.

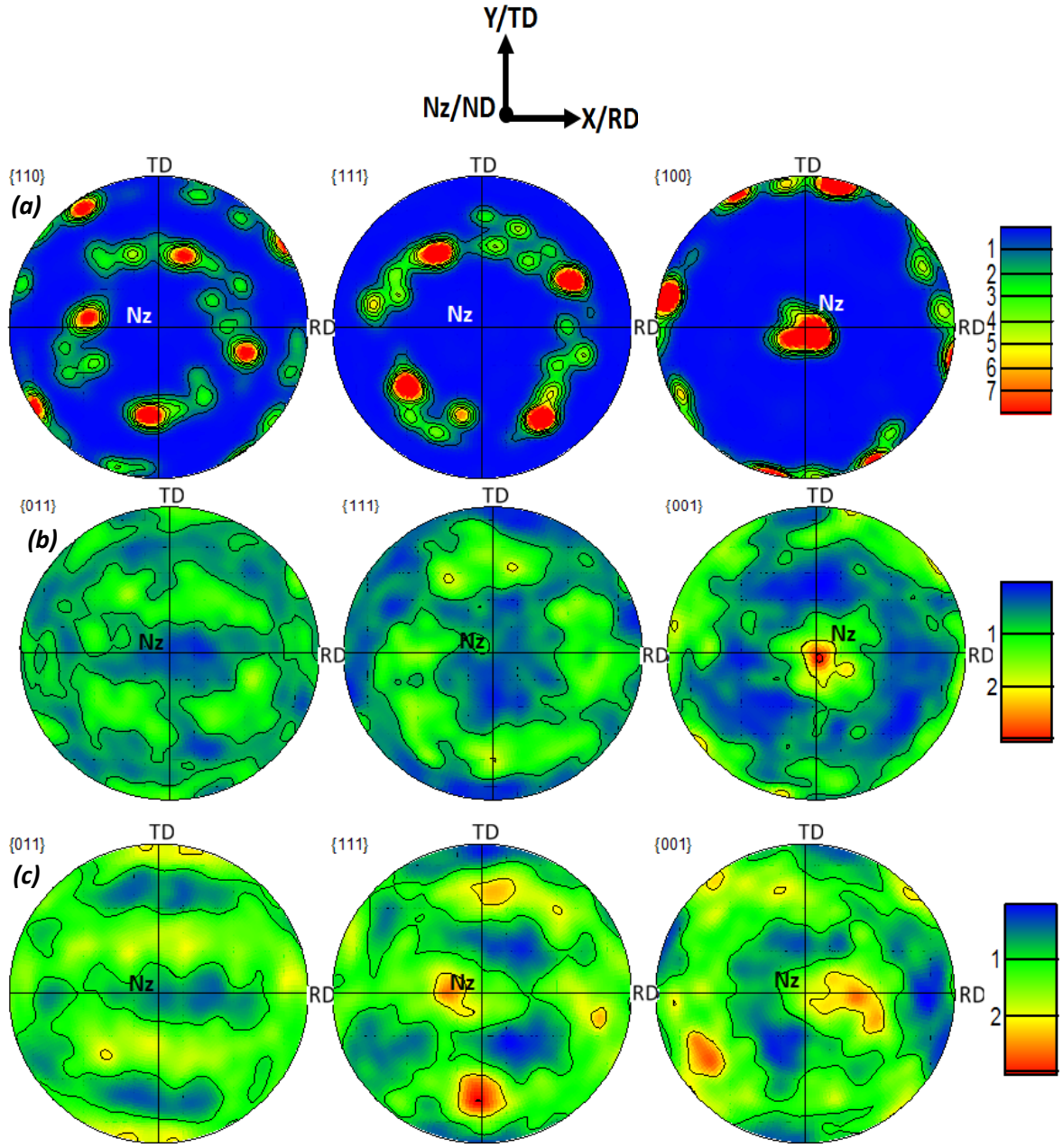

Figure 6.19: *Pole figures showing bulk β textures (a) in the controlled sample, (b) 8 % stained, and (c) 18 % strained samples. The axis are R.D or X - rolling direction, Nz or N.D- growth direction or normal direction, and Y- or T.D – transverse direction.*

In the undeformed control sample as previously discussed (4.4), a strong <001>$_{\beta}$ fibre texture can be observed, with a maximum intensity of ~ 8 x random. However, sampling statistics in this particular case was poor (~ 50 grains are covered) since the β-grains were too large. Figure *6.19*(b-c) shows the bulk β-texture of the recrystallized material that was rolled with 8 % and 18 %

reductions, respectively, with a reasonable number of grains (> 800 grains). With increasing rolling reduction, it can be seen that the initial <001> || Nz fibre weakens and a rolling texture develops, which becomes more defined in the 18 % reduction sample. The initially observed β fibre texture progressively changes to the rolling texture from the unrolled samples to 8 % and 18 % deformed samples and appears to be rotating away from Nz in the 18 % deformed sample. This rolling texture has symmetry rotated by 90˚ about ND compared to that normally expected in rolled sheet.

6.5.2 Transformed α-textures

The transformed α-texture for the unrolled, 8% and 18 % deformed materials are shown in Figure ***6.20***. The transformed α-textures showed a much weakened fibre texture in the unrolled sample (see Figure ***6.20***a) as was discussed previously in chapter 4.4. In comparison, the 8% and 18 % rolled samples showed even weaker α- texture pole intensities of less than 2 (Figure ***6.20***b-c).

The final layer was deformed by rolling, but was not heat treated by the subsequent deposition. The texture in this final layer at the top of the build showed a standard α basal rolling texture with spreading around Nz ([54, 74].

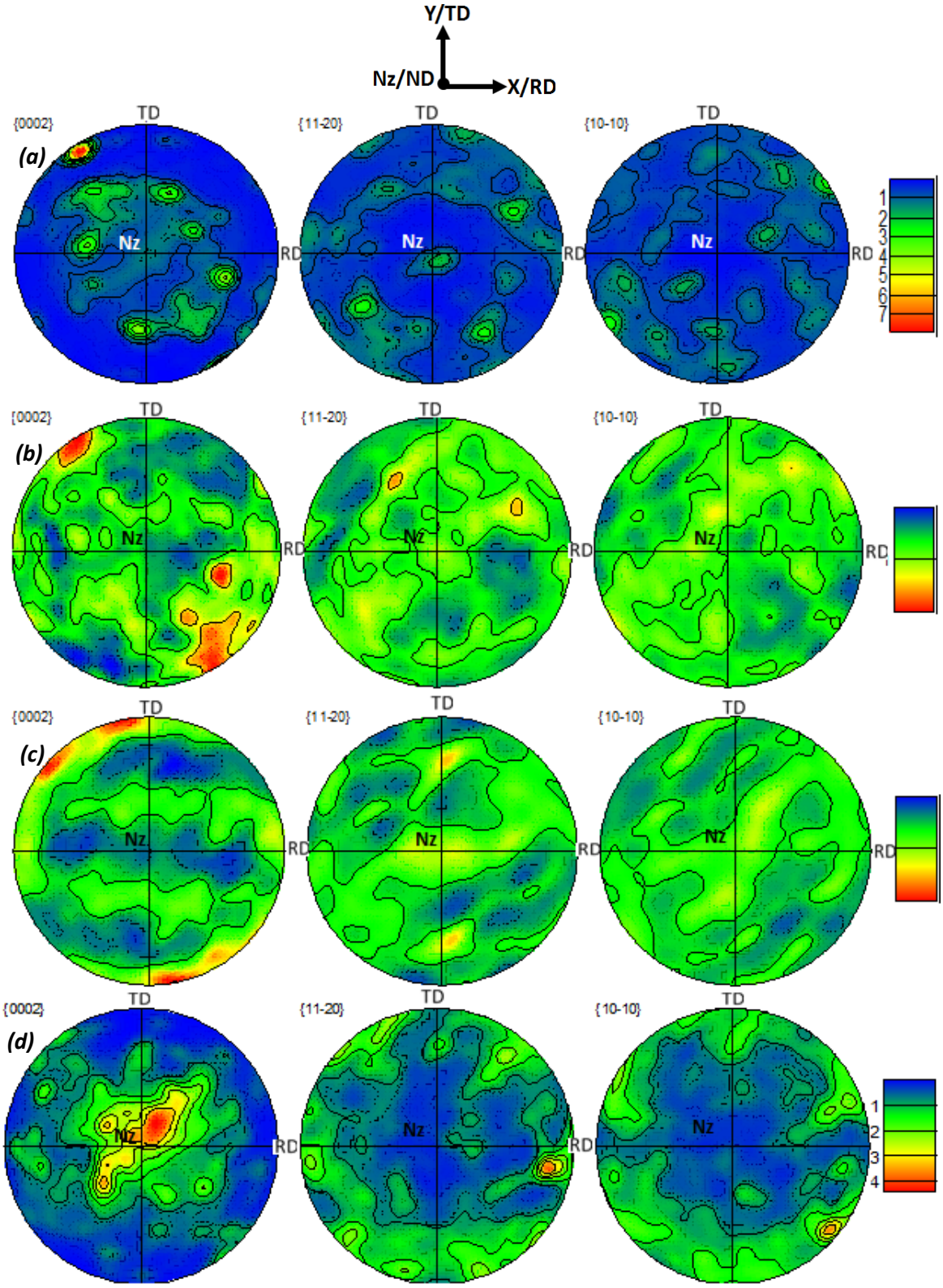

Figure 6.20: *Pole figures showing bulk α textures (a) in the control sample and, in the (b) 8 % stained and (c) 18 % strained rolled samples. In (d) the texture in the final 3 mm of the 18 % reduction sample is shown. The axis are R.D or X - rolling direction, Nz or N.D- growth direction or normal direction, and Y- or T.D – transverse direction.*

6.5.3 Discussion on the effect of rolling deformation on Texture in the WAAM

Primary β texture

In the unrolled condition, a strong <001>$_{\beta}$ || Nz fibre texture was seen to develop with a strength of more than 8 xs random (Figure *6.19*a), as was discussed in chapter 4.4. In comparison, the 8% and 18 % rolled samples showed weaker textures with an intensity of less than 3. In addition, in both the 8 and 18 % deformed samples, (011) poles were aligned and strengthened parallel to the rolling direction (as shown in Figure *6.19*b-c). With increasing rolling reduction, the initial solidification fibre rolling texture reduced in strength and a rolling texture developed, which became more defined in the 18 % reduction sample. In the deformed materials (8 % and 18 %), the initial <001> solidification fibre texture was still observed in addition to the rolling texture. However, the <001> β fibre texture started to rotate away from the Nz axis in the 18 % deformed material.

The rolling texture shown in Figure *6.19*c had a symmetry plane parallel to the rolling direction and is reminiscent of standard rolling texture in Ti [132, 169] rotated by 90˚ about ND, because the plain strain deformation in the thin wall is in the TD-ND plane, not the RD-ND plane as seen in rolling a wide sheet, as discussed in section 6.4.2. Finally, it should be noted that the primary β structure in the top layer of the final pass could not be reconstructed in the rolled samples because it had not been reheated and the deformed α structure had lost its habit relationship with the primary β solidified grain structure.

Transformation α texture

The room temperature α phase showed a very weak texture with an intensity of less than 2 x random in both the 8 % and 18 % deformed materials. This suggests that the deformed material was completely heated above β transus and the phase transformation strongly controls the α-texture. The deformation then weakens the β transformation texture which is further diluted by transformation with little variant selection to the final α texture. The β grain structure in the final layer could not be reconstructed; since the α phase was heavily deformed and lost its Burgers orientation relationship with the parent β grains. The texture from the final layer, showed a strong basal texture spreading around the Nz with a pole intensity of max 4, compared to 2 in the bulk α-texture. This texture is typically observed in the cold-rolled Ti6Al4V alloys [5]. However, further understanding and explanation of the texture development during AM with rolling deformation needs to be studied with more systematic experimental samples, coupled with a thermal modelling and, EBSD-ODF analysis.

6.6 CONCLUSIONS

The main conclusions made in this work, concerning the influence of the process parameters and rolling deformation on the grain structure and texture improvement that can be obtained in the WAAM process, are summarised below.

6.6.1 Summary of the influence of process parameters in WAAM

Under standard conditions, the Constant current GTAW produced very large epitaxially grown columnar β-grains until the end of the final layer, with a grain size of up to 13 mm in length. However, an increase in heat input reduced the grain size and favoured the formation of coarse equiaxed grains at the centre of the build, except in the last layer where finer and more regular columnar grains were observed.

When using the VBC-HF process, with a high frequency GTAW interpulsed power source, changing the travel speed while maintaining the same line energy had no significant effect on the large columnar β grain growth. This was probably because interpulsing the current had no effect and the travel speed also could not be altered sufficiently within the stable process envelope.

The changing in wire feed speed combined with the HF interpulse GTAW process favoured an equiaxed grain structure, although the grain size was still very coarse. When the WFS was increased to 2.2 m/min and above, the nucleation of new equiaxed grains was observed. This was caused by the extra cold metal fed into the melt pool, which effectively reduced the thermal gradient, reducing the G_L/R ratio sufficiently to promote nucleation ahead of the growth front.

The CMT-GMAW process produced a smaller grain size when compared to the large columnar grains seen in the DC GTAW processes, since the net heat input was lower with this process. Despite the CMT process cooling down the melt pool by reducing the heat input, this was not as effective as using high wire feed rate with the GTAW process and, a columnar grain structure was still observed. However, in the CMT process, the columnar β-grains were observed to bend in the direction of heat source travel, as the maximum thermal gradient at the S/L interface changed direction every time the direction of torch movement along x was reversed.

In the standard pulse GTAW process, changes in process parameters, such as the peak to base current (I_p/I_b) ratio (changed from 3.3 to 6.7) and pulse frequency (changed from 5 to 50 Hz) did not affect the microstructure significantly.

The bulk primary β and transformed α textures found in the GTAW process with different WFS and in the CMT-GMAW process has also been studied. For the standard WFS of 1.6 m/min, a strong $<001>_\beta$ || Nz fibre texture was developed in the bulk texture with a maximum intensity of

~ 21 xs random. In comparison, when the WFS increased > 2.2 m/min, an equiaxed structure was produced and the texture became more random.

The CMT- process, the local texture showed the presence of a <001> β fibre texture that was rotated by 5 - 10˚ away from Nz towards the direction of heat source travel, with a texture intensity of 7 xs random, because with this process the grains nucleated from the base tended to bend and follow the melt pool S/L interface along the direction of heat source movement. Thus, pole figures showed a weaker component which rotated away from Nz. This occurred since the grains tried to adjust and align themselves with the maximum thermal gradient with the curved melt pool interface in the CMT process. The bulk primary β texture thus showed a weakened <001> fibre texture which was spread along the direction of deposition (X) with an maximum intensity of 6 xs random, due to the presence of bent grains which tried to follow the forwards and backwards movement of the torch.

With the WAAM process in general, the pole figures measured from the bulk transformed α phase showed a weak α fibre texture with an intensity of 7 xs random. When the WFS were increased above 2.2 m/min, the transformed α-texture became more random, with texture intensity reduced to a maximum 4 xs random. The CMT-GMAW deposit again showed a weaker transformation α fibre texture (with a maximum intensity of 3) because of the spreading of the parent β texture around Nz and a lack of strong variant selection.

6.6.2 Summary of the effect of rolling deformation on grain structure and texture in the WAAM process

The large columnar β-grains usually seen in the WAAM with a size of 20 mm in length and 2 mm width were refined down to 50 - 650 µm, and 50 -350 µm by the application of an average 8 % and 18 % deformation, respectively, between each layer deposited. Although the microhardness of the three samples did not vary widely, the novel step of combining deformation and AM helped to refine the grain size to a greater extent than varying the arc or, heat source parameters and this is a better and more effective method for improving the microstructure in AM deposits. Both the primary β and α texture progressively changed from a solidification fibre texture to rolling textures by increasing the rolling strain. The rolling process not only helps in the grain refinement but could also reduce the amount of random defects and distortion in the WAAM builds. However, the results presented in this section were preliminary findings and further understanding about the grain structure and texture development in the combined WAAM and rolling process requires additional systematic experiments, coupled with more rigorous EBSD analysis, and deformation and thermal modelling.

7 MECHANICAL PROPERTIES OF AM TEST SAMPLES

7.1 INTRODUCTION

Mechanical property data such as fatigue life, tensile strength, elongation, etc, are very important when developing new processes, since engineers need good data to design safe components and structures**.** It is therefore important to study the effect of defects and microstructure on mechanical properties during developing the AM process for Ti6Al4V alloys. The microstructural factors which affect the mechanical properties of Ti6Al4V alloy are the β-grain size, α-colony size, thickness of grain boundary α and lamellar α, the size and shape of the primary α-grains, and the volume fraction of α and β, and tempered martensite. In this project mechanical testing was carried out by Westmoreland Mechanical Testing and Research Limited, UK, with the financial support provided by the Department of Innovation and Strategy Board, and Bombardier Aerospace, Belfast. Testing was carried out on samples produced by the EBSM and WAAM processes with the HF Interpulse GTAW, and standard pulsed GTAW power supplies. The failed specimens with test data were then provided for fractography analysis. This chapter consequently mainly focuses on evaluation of the test data obtained from both the tensile and fatigue tests performed on these samples and fracture path analysis of the resultant failed test pieces. Analysis of the results will focus on the fractography of the fractured fatigue test specimens, rather than the tensile test specimens, since the study of the dynamic properties of AM deposits is more critical to aerospace application.

7.2 TENSILE PROPERTIES OF AM DEPOSITS

7.2.1 Tensile properties of the EBSM samples

To evaluate the tensile properties of EBSM consolidated Ti6Al4V materials 45 cylindrical tensile samples (according to ASTM E8/E8M or EN 10002-1/2002-1 standard) were machined from different positions in the build chamber of the ARCAM machine. Three sets of samples were produced from 6 locations in the build chamber. The notations used for the locations were BL - Back Left Corner of build chamber, BR - Back Right Corner, FL - Front Left Corner, FR - Front Right Corner and, C -Centre in the build chamber, as shown in the Figure *3.15*. In addition, X - represents coupons aligned in the powder re-coating direction (left/right axis of build chamber),

Y- transverse to the re-coater, and Z aligned with Nz, the layer thickness direction, or vertical axis of the build chamber.

Figure *7.1* summaries all the tensile test results including ultimate tensile strength (UTS) and yield strength (YS) and elongation for the EBSM samples compared to the minimum specification limit (as per ISO 5832-3) for forged (wrought and annealed) Ti6Al4V material. The average yield stress, ultimate strength, and elongation were 817 ± 17 MPa, 901 ± 19 MPa, and 15 ± 0.91 % respectively, which is better than the 780 MPa, 860 MPa and 10 % minimum limit recommended by ISO 5832-3 and, also better than the 827 MPa, 896 MPa and 6 % limit recommended by AMS 4985C, for investment casting and hot isostatic pressing of Ti6Al4V, although the yield stress was marginal below the minimum specification with respect to AMS 4985C.

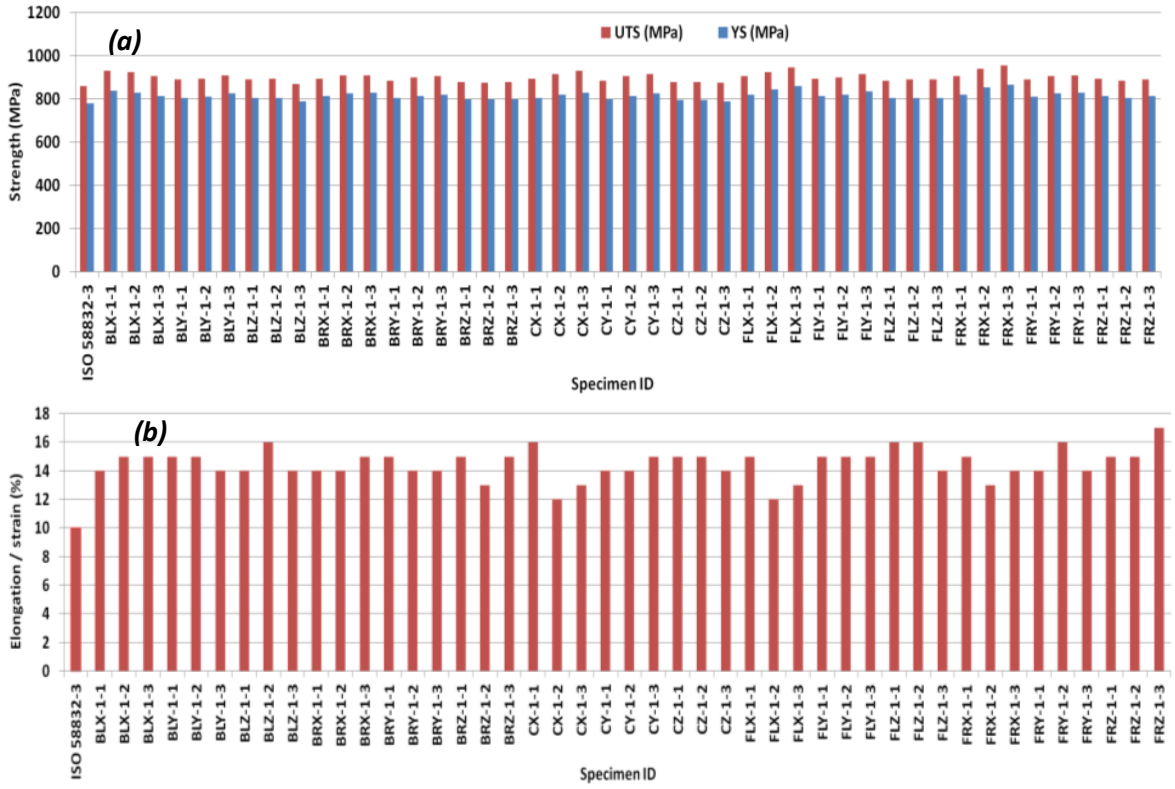

Figure 7.1: *Tensile test results showing the yield stress and tensile strength (a), and Elongation (b) against specimen ID position, for the Ti6Al4V alloy produced using the EBSM process, compared to the ISO 5832-3 standard for wrought material.*

7.2.2 Tensile properties of the WAAM samples

With the WAAM process, large 1 m long by 195 mm high straight walls were built and dog-bone shaped tensile specimens were machined out of different positions parallel and perpendicular to the build direction, as shown in Figure 3.10. The first large single wall (build 1) was produced using the HF-Interpulse 150C GTAW process (made by VBC), and samples were tested both parallel (3

samples) and perpendicular (6 samples) to the build direction. Build 2 and 3 were produced with the same process parameters using a standard pulsed Migatronic commander 400 power supply, since the VBC HF-Interpulse GTAW equipment was not designed for heavy duty use and it stopped frequently in the manufacturing process. Builds 2 and 3 were produced with same processing conditions (as shown in Table *3.7*), the horizontal test samples (perpendicular to the direction of build) were prepared from build 2 and, the vertical samples (parallel to the build direction) were prepared from build 3. Three control specimens were extracted from Ti6Al4V Bar (MIL-T 9047) and also tested to provide a baseline comparison. In the case of the Migatronic power supply, in total eighteen tensile specimens were tested, twelve in the vertical (build 2) and six in horizontal direction (builds 3), as shown in Figure 3.10.

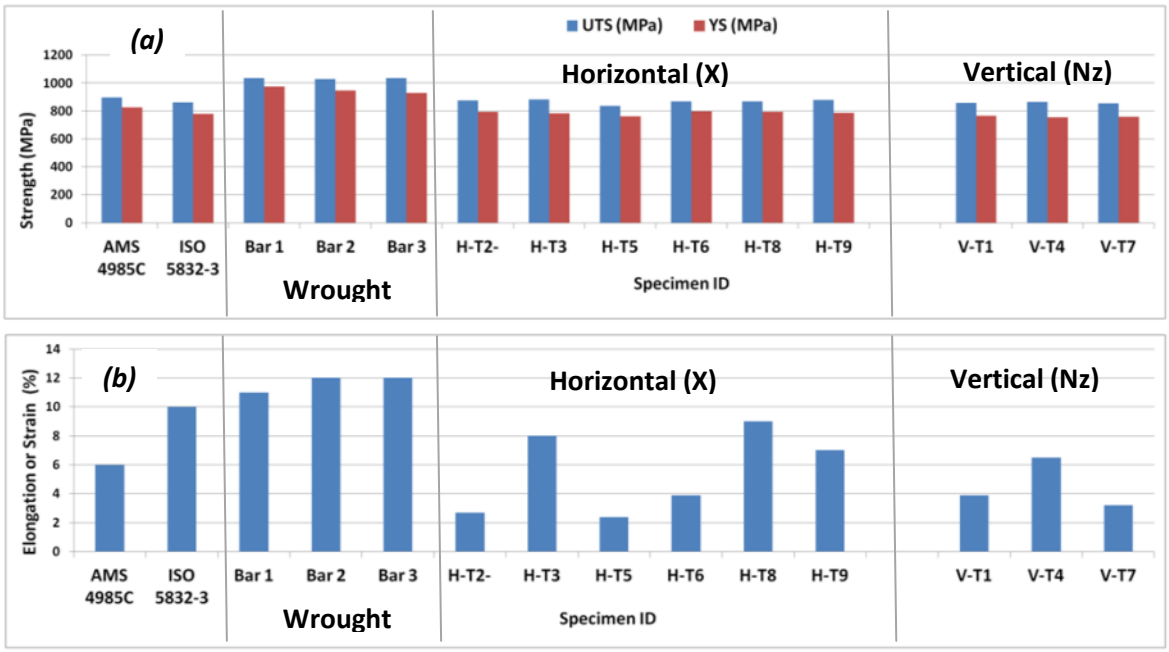

Figure 7.2: *Tensile test results from build-1 showing the (a) yield stress and tensile strength, and (b) elongation against the specimen position, for the Ti6Al4V alloy produced using the WAAM process with the VBC- HF interpulse GTAW power source, compared to a wrought bar sample and the min specificaitons for AMS 4985C (wrought and annealed condition) and ISO 5832-3 (investment casting hot isostatically pressed condition).*

Figure *7.2* summarises the tensile test results from build-1 that were produced using the VBC- HF interpulse GTAW process compared to the minimum spec according to (AMS 4985C) for the Ti6Al4V alloy for investment cast and hot-isostatic-pressed materials. The test results from the baseline Ti6Al4V bar (MIL-T 9047) are also shown in the same plot for comparison. It can be seen that the samples taken from build 1 exhibited an average UTS of 865 MPa, yield stress of 777 MPa, and elongation of 5 %, which does not meet the minimum specification required for Ti6Al4V by AMS 4985 C (investment cast and Hipped conditions). The elongation varied greatly from 2.5 % to

12 %, with no apparent preference with respect to the orientation of the samples. In addition to this, it can be seen that the tensile properties of the wrought base-line test material were better than for build 1.

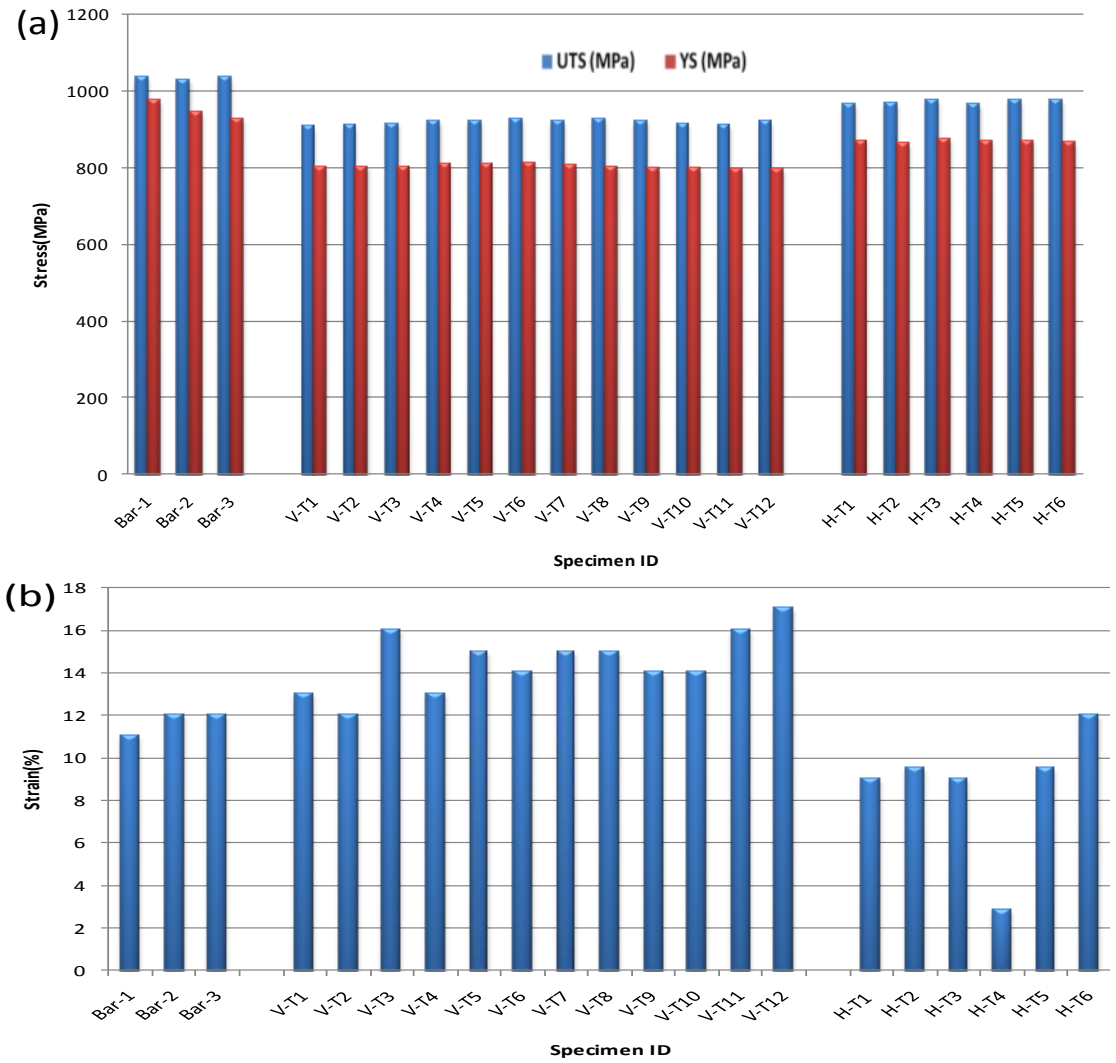

Figure 7.3: *Tensile test results from builds 2 and 3 with the WAAM process using the pulsed migatronic power supply (a) showing the yield stress and tensile strength, and (b) elongation, against specimen ID for different positions and orientations (see Figure* 3.10*) with the Ti6Al4V alloy.*

Figure ***7.3*** shows the tensile test results including ultimate tensile strength (UTS), yield strength (YS) and elongation obtained from builds 2 and 3 that were produced using standard pulsed GTAW process. The baseline test results from a Ti6Al4V bar are also shown in the same figure. The average yield stress, tensile strength and elongation were 835 MPa, 944 MPa and 11.6 % respectively, which is better than the minimum 827 MPa yield stress, 896 MPa tensile strength and 6 % ductility recommended by AMS 4985C-Ti6Al4V (for the investment casting and hot-

isostatic-pressing). The average results were also higher than the minimum yield stress limit of 780 MPa, tensile strength of 860 MPa and, elongation of 10 % required by ISO 5832-3, for wrought and annealed Ti6Al4V. However, compared to the baseline Ti6Al4V bar (MIL-T 9047), the average yield stress, tensile strength and elongation of the WAAM Ti6Al4V samples were slightly lower by 12.1%, 8.6% and 0.09% (950 MPa, 1033 MPa and 11.7 %) respectively.

7.3 FATIGUE PROPERTIES OF THE AM DEPOSITS

7.3.1 Fatigue properties of the EBSM samples

As shown in the Figure *3.15*, three sets of samples from each location (total 45 in numbers) were produced to analyse the fatigue properties of the EBSM Ti6Al4V builds, according to ASTM E466. All the fatigue specimens were tested at ambient temperature with a maximum stress of 600 MPa, R = 0.1, and a sinusoidal wave form with a frequency of 30Hz. If there was no failure, the tests were discontinued after 3,000,000 cycles. The position and orientation notations used were the same as for the tensile specimens.

Figure ***7.4*** shows the fatigue test results for the EBSM produced Ti6Al4V specimens superimposed on standard published S-N cuve for both the cast and wrought products, provided by Metallic Material Properties Development and Standardization (MMPDS) design data [170].The 2003 Metallic Material Properties Development and Standardization (MMPDS) Handbook is an internationally reliable source of data for aerospace materials selection and analysis [170]. It can be seen that, at the stress amplitute tested, the EBSM process showed better fatigue performance, when compared to the MMPDS design data for casting and comparable results were obtained to the forged bar reference. However, the data exhibited a large amount of scatter in the test results. The Figure *7.5* presents all the individual test results for the different specimens. It can be seen that the average fatigue life of the samples is good but, the scatter is very large ranging from a minimum life of 46550 cyles to a maximum of greater than 3 million cyles, where run out in the test occurred.

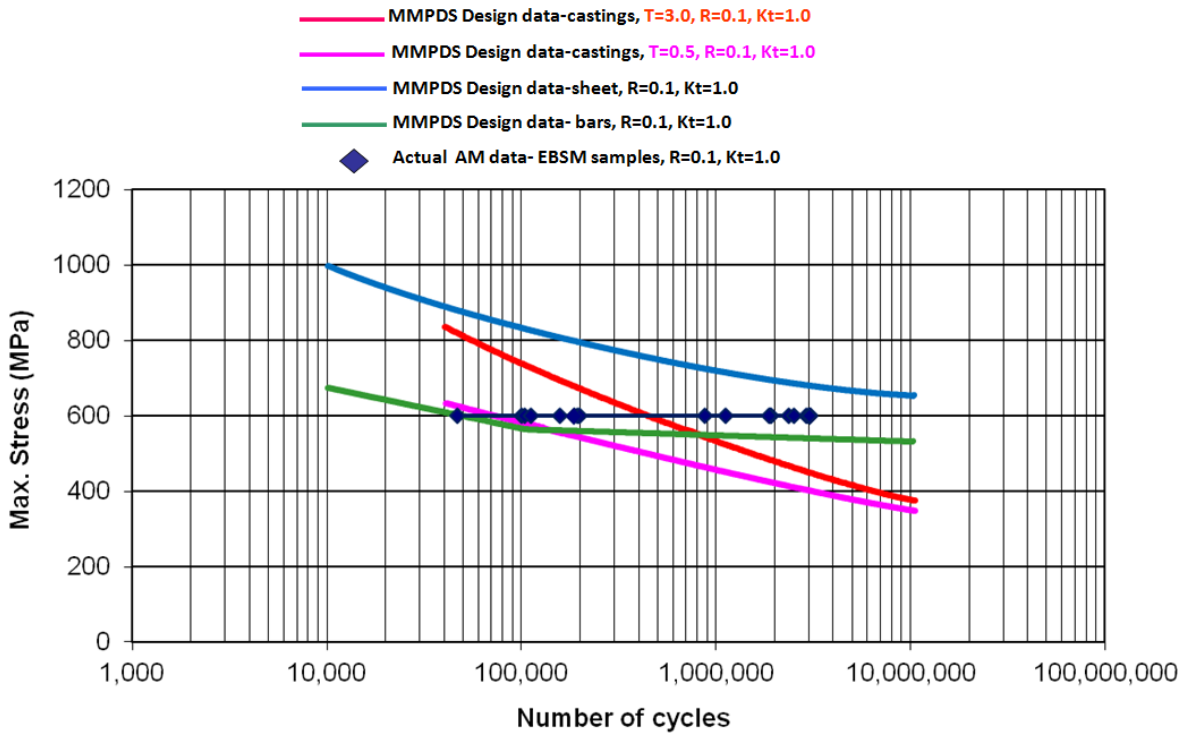

Figure 7.4: *Fatigue test results for the EBSM Ti6Al4V specimens superimposed on standard S-N curse for cast and wrought products taken from MMPDS design data [170].*

In the EBSM process fatigue test results, 7 out of 45 samples along the Z-direction failed to meet 1 million cycles at a maximum stress of 600 MPa and the location of these samples in the build chamber is shown in Figure *7.6* by a red colour and arrows in Figure *7.5*. Whereas, when tested, in the X- and Y-direction only, one and two samples, respectively, failed below 1 million cycles. The location of these test specimens are shown in Figure *7.6* as orange colour)**.** Furthermore, 27 out of 45 samples run out and showed a fatigue life that lasted for the full 3 million cycles.

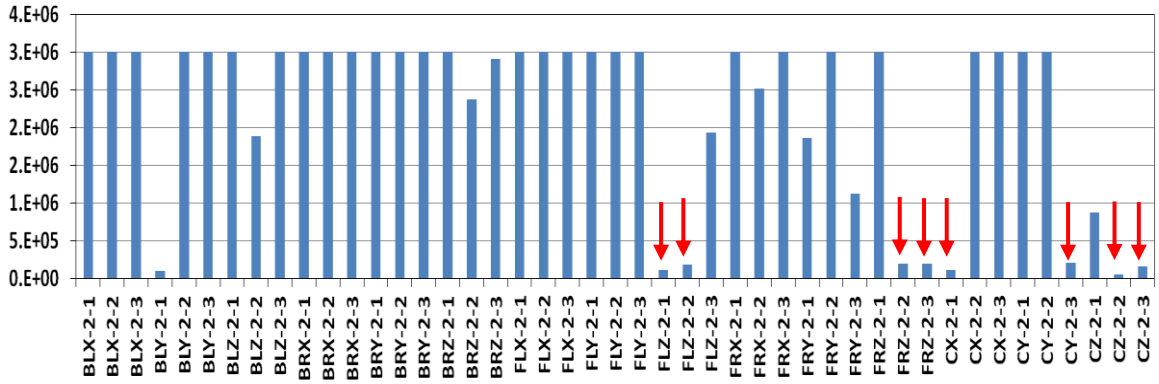

Figure 7.5: *The fatigue test cycles against specimen ID of Ti6Al4V alloy produced using EBSM-AM.*

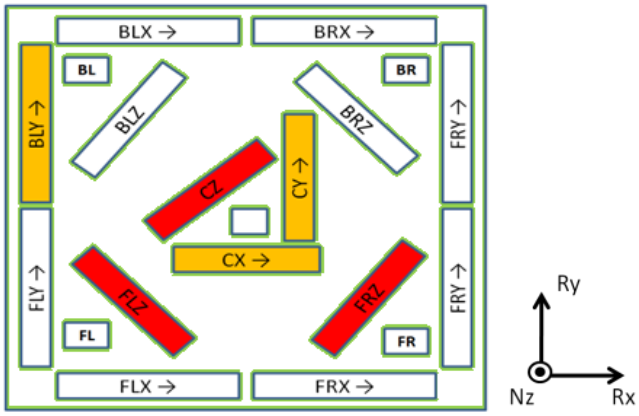

Figure 7.6: *Location and orientation of the EBSM failed fatigue specimens in the build chamber; with red showing frequent failure locations for less than 1 million cycles along the Z-direction, the orange colour showing sample(only one failed in each locations) along the X- and Y- directions also for below 1 million cycles. White shows the position of run out samples that survived at least min 2.5 or 3 million cycles.*

7.3.2 Fatigue properties of the WAAM samples

In total 12 specimens (6 in the vertical and 6 in the horizontal directions) were tested for fatigue from build 1 produced using the HF interpulse GTAW process. In addition, from builds 2 and 3 produced with the normal pulsed GTAW power supply, 24 fatigue specimens were tested, with 14 in the vertical (build 2) and 10 in the horizontal (build 3) direction, respectively (as shown in Figure *3.15*), all according to EN6072. Five control specimens (parent) were also machined from Ti6Al4V rectangular forged bar (MIL-T 9047) and tested as a baseline comparison. The fatigue specimens had a flat dog-bone shape with a gauge length of 40 mm and a cross-sectional area of 12.7×2.5 mm^2 (see Figure *3.17*). All the fatigue specimens were tested at a maximum load of 600 MPa and, R = 0.1, using a sinusoidal wave form with a frequencies of 30 Hz. With this set of tests, the tests were stopped after 10 million cycles if no failure occurred. The five baseline specimens were tested under the same conditions, to compare with the WAAM test specimen results.

Figure ***7.7*** shows the WAAM Ti6Al4V fatigue test results from builds 1, 2 and 3 tested in the horizontal and vertical directions, superimposed on standard S-N cuves from both cast and wrought Ti6Al4V products, again using Metallic Material Properties Development and Standardization (MMPDS) design data [170]. Three of the baseline specimens failed well below one million cycles, with the remaining two failing after just over one million cycles, as shown in Figure ***7.8***. From Figure ***7.8***, it can also be seen that build 1 gave better fatigue life than the cast MMPDS data and the performance was comparable to the forged material. However, while the average fatigue life in build 1 was good, there was large scatter in the data (see Figure ***7.8***) which varied from 97081 to 10 million cycles to failure. The fatigue life of the build 1 samples varied

randomly with orientation relative to the build direction and no consistent trend could be demonstrated. 3 out of 12 the samples failed at less than 1 million cycles. Figure *7.9* shows the location of these three specimens (which failed below 1 million cycles) in the wall 1 in red and samples which failed in the range of 2 to 3 million cycles are shown by an orange yellow colour. However, 5 out of 12 of the samples ran out to 10 million cycles and are shown in a white coulour in Figure *7.9*.

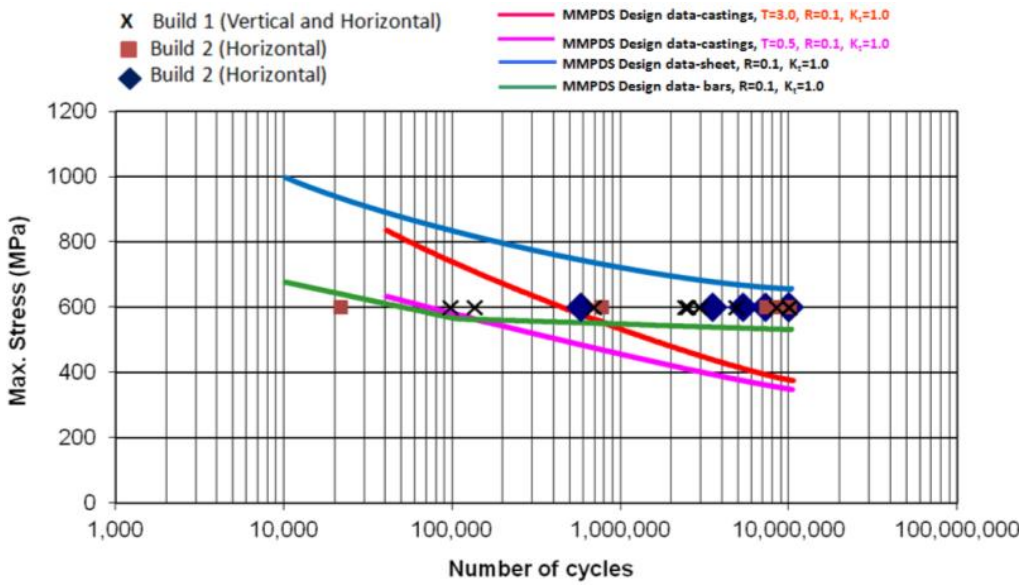

Figure 7.7 : *Fatigue test results from build 1, 2 and 3 WAAM Ti6Al4V specimens superimposed on standard S-N cuves for the cast and wrought products, using MMPDS design data [170].*

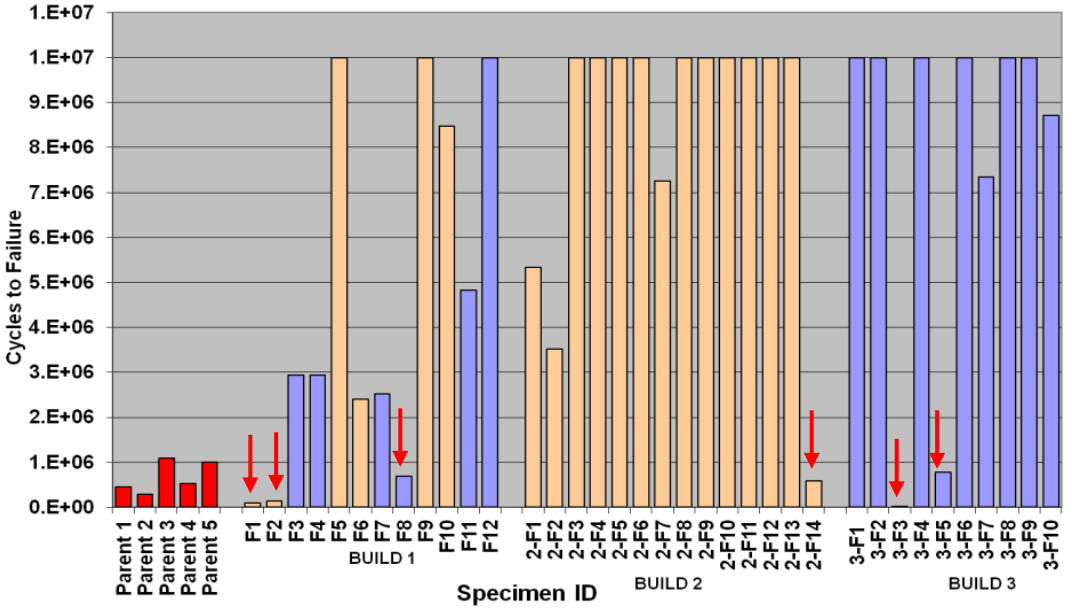

Figure 7.8: *Fatigue test cycles to failure data for different positions and sample orientations from builds 1, 2 and 3. The red colour results are from baseline wrought bar specimens. Whereas, golden yellow and blue coluring show the orientaton of the samples which were parallel and perpendicular to the build direction.*

The results from builds 2 and 3, produced using the standard pulsed GTAW power supply, also showed large scatter in the fatigue life, as shown in Figure ***7.7***. However, Sixteen out of the 24 of the specimens run out and did not fail after ten million cycles (the tests were discontinued for these samples). A further twenty one samples had a fatigue life well above three million cycles, but three samples failed below one million cycles, as indicated by the arrows Figure ***7.8***. Figure *7.9* shows the location of these three different (VF-14, H-F3 and H-F5) specimens which failed below 1 million cycles in builds 2 and 3 in a red colour and the samples that lasted for all 10 million cycles are shown in white. A higher percentage of samples failed in build 3, which were oriented in the X direction. In addition, the samples (from builds 1 and 2) that failed with less than 1 million cycles appeared to be located at the ends of each wall. This behaviour is probably related to the defect distribution and orientation of the large columnar grain structure in the walls. Overall, the average high-cycle fatigue resistance of the WAAM Ti6Al4V samples that were produced using the standard pulsed GTAW system were significantly better than the baseline bar specimens, as shown in Figure ***7.8***. The difference between the results obtained from builds 1), and 2) and 3) will be discussed further below.

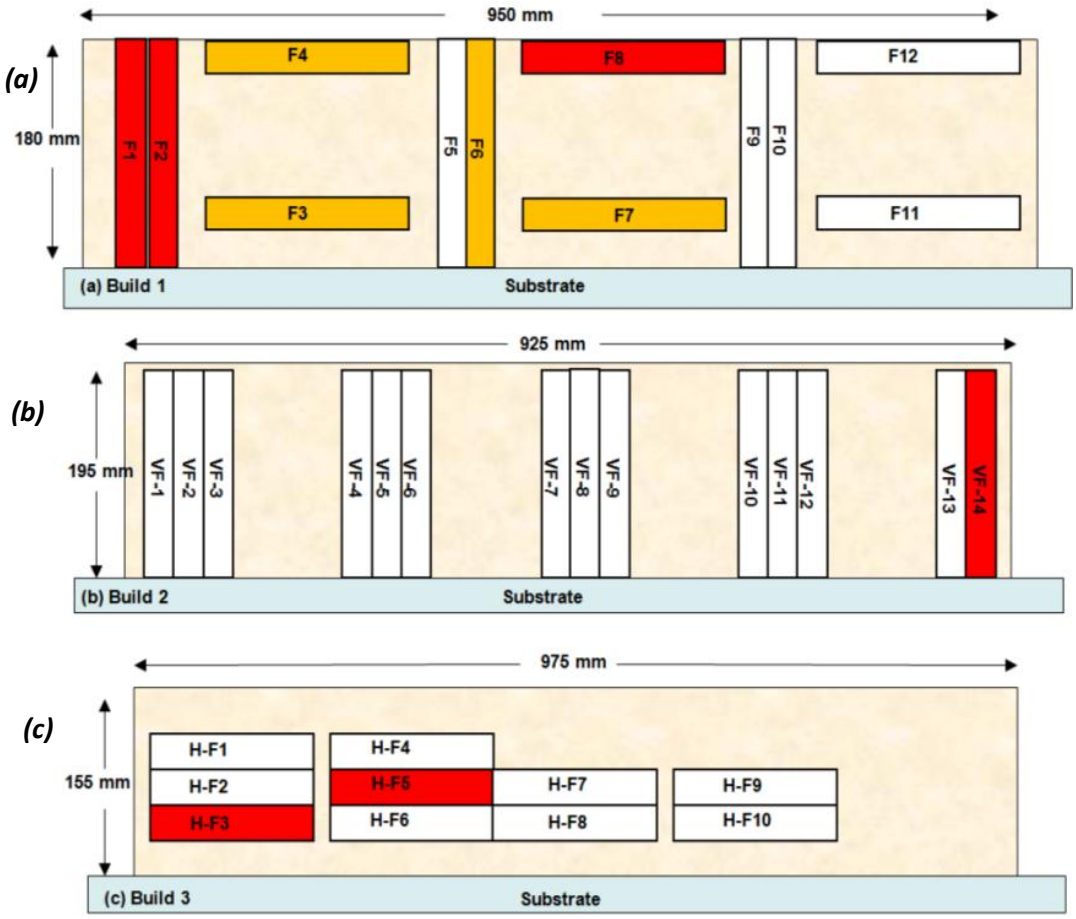

Figure 7.9: *Location and orientation of the failed fatigue test samples. The red colour shows the failure position and orientation of specimens that lasted less than 1 million cycles and, orange yellow those that failed in the range of 2 to 3 million cycles. Samples in white ran out in the tests.*

7.4 O_2 AND N_2 ANALYSIS IN THE AM BUILDS

The AM samples were tested for oxygen and nitrogen content to quantify the amount of oxygen and nitrogen pickup during the EBSM and WAAM processes and, also to check the level of O_2 and N_2 pickup with different amounts of shielding in the arc AM process. The concentrations of oxygen and nitrogen in the samples were analysed at TIMET, Birmingham, UK, and are shown in Table *7.1* with the allowable maximum limits, according to AMS 4911L, for Ti6Al4V sheet, strips and plate in the annealed condition. When manufacturing build 1 with the WAAM process, GTAW torch shielding alone was used (with a mixture of 75 % He + 25 % Ar at a flow rate of 15 L/min). In comparison, builds 2 and 3 were produced with additional hood shielding of 100 % Ar at a high flow rate of 30 L/min. Figure *7.10* shows the experimental setup for the extra hood arrangement, surrounding the conventional GTAW torch.

From Table *7.1*, it can bee seen that the EBSM process gave the lowest oxygen (1284 ppm) and nitrogen (70 ppm) content, when compared to the WAAM builds. In the WAAM process, build 1 had a very high oxygen (2654 ppm) content, which was above the maximum limit set by the AMS 4911L standard, although the nitrogen content was 332 ppm, which was still less than the maximum limit of 500 ppm. The higher oxygen content in build 1 was due to the poor shielding provided by using only the GATW torch. However, builds 2 and 3 had oxygen contents of 1570 ppm which was less than the maximum limit. This is due to the enhanced shielding obtained using both the torch and extra hood shielding (as shown in Figure *7.10*).

Table 7.1: *Analysis of O_2 and N_2 pickup in the AM processes.*

Sample ID	**Type of Process**	**Feed materials O_2 content (ppm)**	**Shielding gases**		**O_2(ppm)**	**N_2 (ppm)**
			Torch shielding	**Extra hood shielding**	**Av of 2 measurements**	
Spec	AMS 4911L (Ti6Al4V sheet, strips and plate in the annealed condition)				Max. 2000	Max. 500
EBSM	EBSM	1200	Vacuum	Vacuum	1284	70
WAAM-Build 1	HF-IP GTAW	1400	75 % He + 25 % Ar at the flow rate of 15 L/min	-	2654	332
WAAM-Builds 2 and 3	Pulsed GTAW	1400	75 % He + 25 % Ar at the flow rate of 15 L/min	100 % Ar at the flow rate of 30 L/min	1570	87

Figure 7.10: *Experimental set up of the extra shielding hood used for better protection from the atmosphere with the WAAM process in builds 2 and 3.*

7.5 FRACTOGRAPHY OF THE AM TEST SAMPLES

This section focuses on the fractography of the fatigue test specimens. Due to lack of time to complete this work, fractography was not performed on the tensile samples.

7.5.1 Fractography of the EBSM test samples

In the EBSM process, all the samples that fractured before reaching 3 million cycles showed clear evidence of pores as the point of crack nucleation. Figure *7.11* shows the fracture surface initiation point of the samples that failed with less than 1 million cycles, where the fatigue crack initiated from pores that were present very close to the specimen surfaces. Figure *7.12* gives an example of a sample which survived more than 2 millions, where the crack initiated from a pore near the centre, or away from the surface.

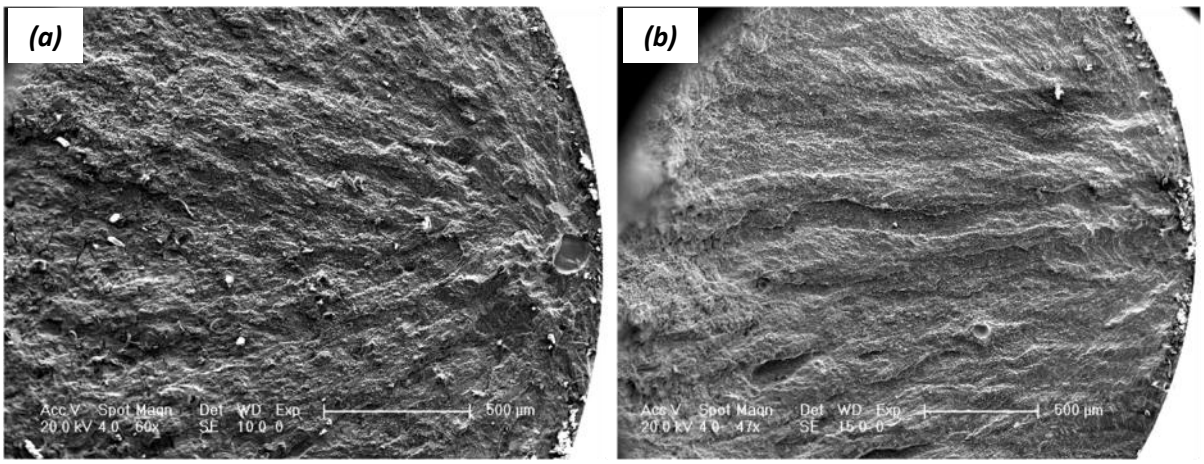

Figure 7.11: *Fracture surfaces from EBSM samples showing (a) sample CZ 2-2 and (b) CY 2-3 both with crack initiation by pores near the surface. These samples failed with less than 1 million cycles.*

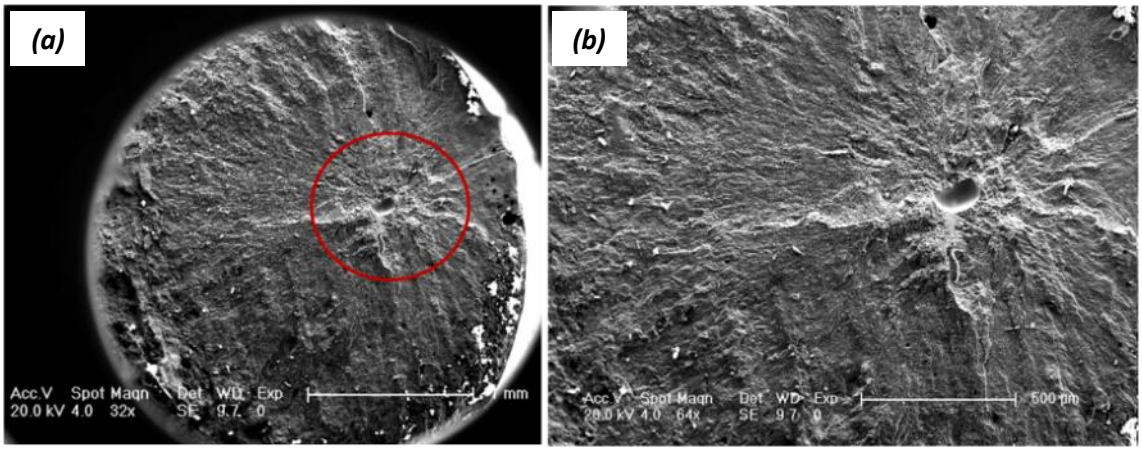

Figure 7.12: *SEM images of the fracture surfaces of the EBSM fatigue samples FRX 2-2 fatigue sample showing (a) a fatigue crack initiated at a pore which was close to the centre of the specimen, and (b) a higher magnification image of the pore.*

7.5.2 Fractography of the WAAM test samples

Fatigue fractography of build 1 test specimens that failed early, with a fatigue life less than 1 million cycles, at location F2, F3 and F8, by SEM, revealed that the fatigue cracks all initiated at large 50-75 µm diameter pores very close to the specimen surface in these specimens. The surface lines, radiating from the pores provides evidence that the pores are the origin of the failure point in the specimens, as shown in Figure *7.13*.

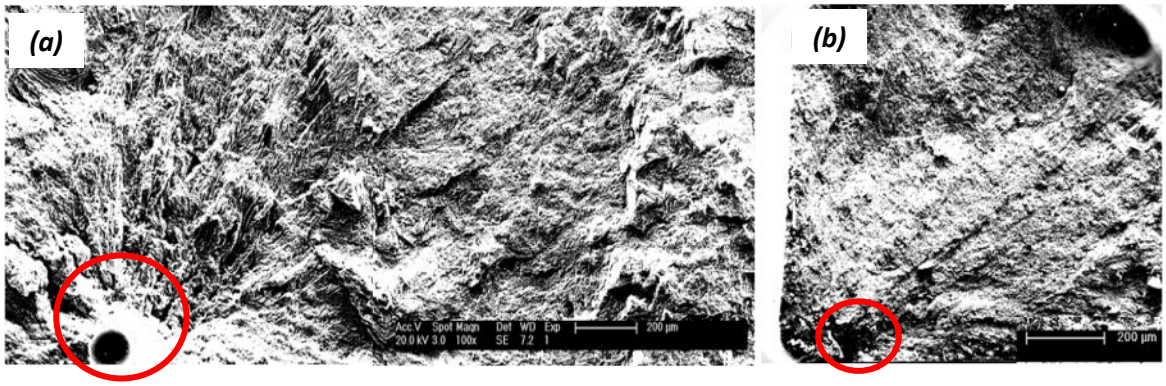

Figure 7.13: *Fractographs of samples V-F2 and H-F8 from build-1 produced using HF-Interpulse GTAW AM process showing that the fatigue crack initiated at pores close to the specimen surface (a, b) and propagates rapidly into the entire cross-section of the failed test pieces.*

The fatigue fractography investigation of build 2 and 3 test specimens, that failed before reaching 1 million cycles (V-F14, H-F3 and H-F5), again showed that the fatigue cracks initiated at pores close to the specimens surface. Fracture surface lines radiated from the pores, providing evidence that they caused the failure initiation of the specimens, as shown Figure *7.14*. In addition, the fracture surface appeared to be affected by the coarse prior β grain structure, which caused a change in the crack path, as shown in Figure *7.14*b.

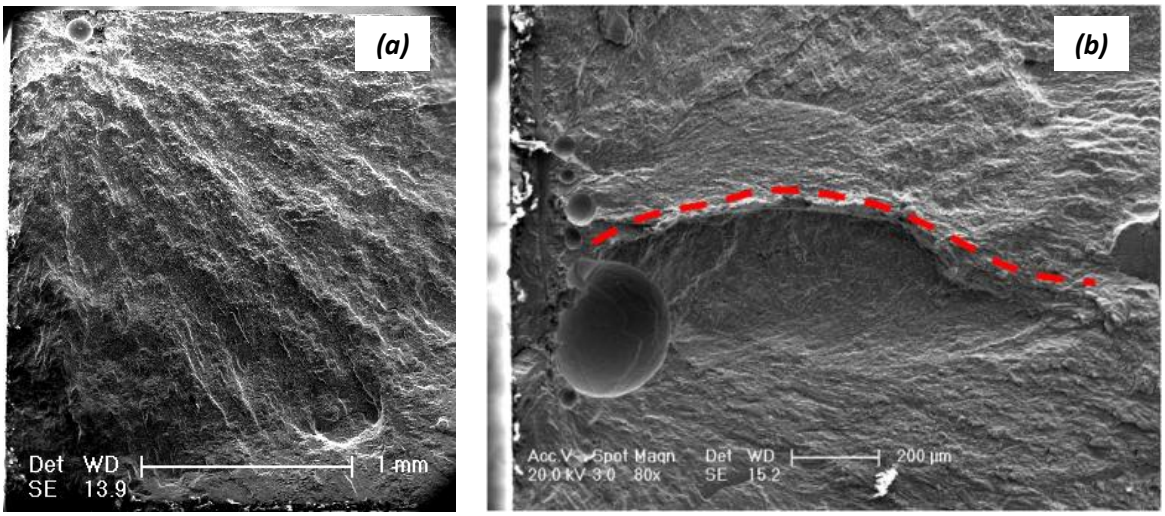

Figure 7.14: *Fractograph of sample (a) V-F14 and (b) H-F3 from build 2 and 3 using the WAAM process showing that the fatigue crack initiated at pores close to the specimen surface in each case and that the fracture path was affected by the large prior* β*-grain structure.*

7.5.3 Fractography of the base line test samples

Fatigue fracture surfaces from the baseline specimens 3 and 5 are shown in Figure *7.15* and Figure *7.16*. In Figure *7.15*, it can be seen that this forged bar test piece also failed early due to the presence of a pore in the centre of the bar. In comparison to sample 3, sample 5 (Figure *7.16*) showed evidence of initiation from the sample surface and the initiation point shows evidence of a crystallographically facetted cleavage fracture region (the microstructure of the bar was consist of bimodal α/β microstructure).

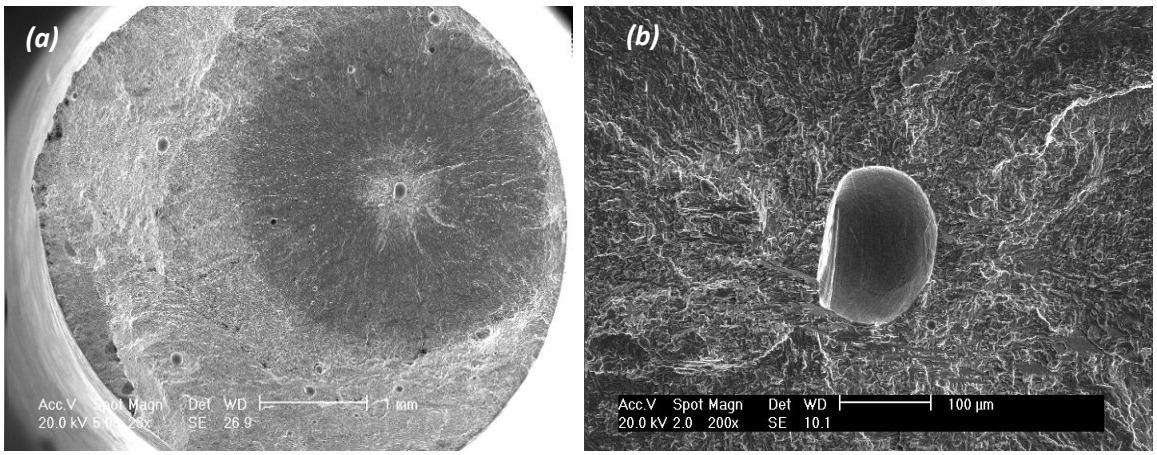

Figure 7.15: *SEM fractograph observation of a baseline bar (MIL-T 9047) fatigue specimen 3 showing crack initiation at a pore at low (a) and (b) high magnification in the specimen that failed just above 1 millions cycles.*

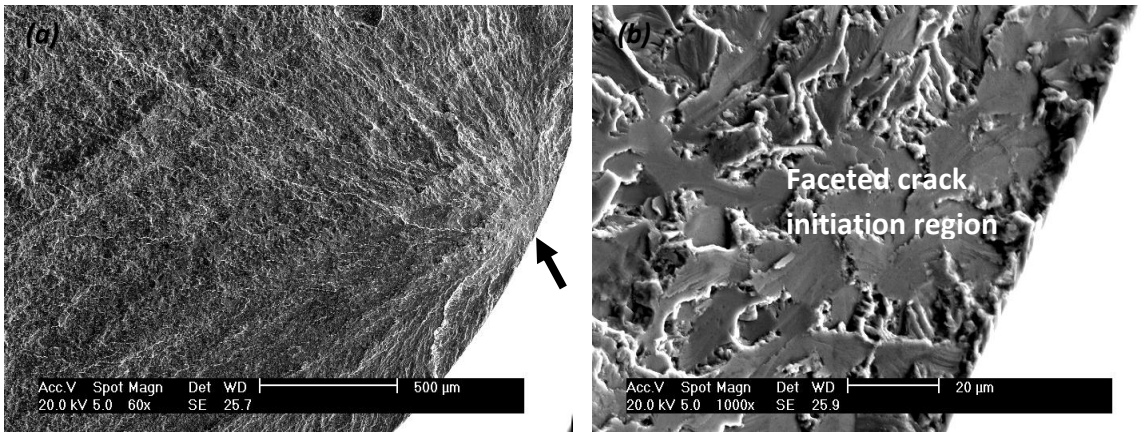

Figure 7.16: *SEM fractograph observation of the baseline bar (MIL-T 9047) fatigue specimen 5 showing that fatigue crack initially was associated with a facetted crack initiation point. (a) Overall observation and (b) close observation of primary α in the specimen failed just above one million cycles.*

7.6 DISCUSSION OF THE MECHANICAL PROPERTIES OF THE AM DEPOSITS

7.6.1 Tensile properties of the EBSM and WAAM samples

Tensile properties of the EBSM samples

From the above summarised tensile test results, shown in Figure *7.1* and Figure ***7.3***, it can be concluded that the tensile test performance for the EBSM process material exceeded the minimum specification limit given by ISO 5832-3 for the wrought and annealed Ti6Al4V. The EBSM process gave average YS, UTS and elongations to failure of 817 ± 17 MPa, 901 ± 19 MPa, and 15 ± 0.91 % respectively, which were better than the 780 MPa, 860 MPa and 10 % limit recommended by ISO 5832-3. These values are also better than the 827 MPa, 896 MPa and 6 % limit recommended by AMS 4985C for investment cast and hot isostatic pressed Ti6Al4V material, although the yield strength was marginally below the minimum limit specification, with respect to AMS 4985C. In addition, the performance of all 45 tensile test samples exceeded the minimum thresholds defined by the ISO-5832-3 standard.

From Figure *7.1*, it can be seen that there was no statistically significant variation in the tensile properties of the samples with position in the build chamber and, in terms of orientation, the EBSM samples were not significantly affected by the direction in the plane of the bed. However, the data was affected by the build direction. The average YS, UTS and elongation of the tested EBSM samples was 832 ± 18 MPa, 919 ± 18 MPa and 14 ± 1 in the X-direction and, 817 ± 10 MPa, 900 ± 10 MPa and 15 ± 1 in the Y-direction, respectively. Whereas, in the Z direction the values of yield stress, tensile strength and ductility were 802 ± 8 MPa, 884 ± 8 MPa and 15 ± 1, giving value of YS and UTS slightly lower than in X and Y. However, the tensile properties in the z-direction showed less scatter compared to in the X- and Y- direction. Overall, the average yield, ultimate strengths and elongations measured (of 817 ± 17 MPa, 901 ± 19 MPa, and 15 ± 0.91 %) were in good agreement with the values (of 830 ± 5 MPa, 915 ± 10 MPa and, 13.1 ± 0.4 %) reported by Luca Facchini et al. [90]. In contrast, values of yield stress reported by Al-Bermani et al. [112] were slightly above the results reported here. This might be due to the fact that the preheating temperature in their experiments were in a lower range (of 626 to 700 ˚C), which resulted in yield stresses of 938 to 883 MPa, tensile stresses of 1030 to 993 MPa, and elongations of 11.6 t0 13.6 %, whereas in the current experiment a build temperature of 740˚C was used. This increase in build temperature slightly coarsens the α plates in the microstructure [112], which results in a slight decrease in strength and increase in elongation to fracture.

Tensile properties of the WAAM samples

With the WAAM process, the tensile properties of the first build 1, produced with only torch shielding, using the HF interpulse GTAW supply, gave average UTS values of 865 MPa, and a yield stress of 777 MPa, with an average elongation of only 5 %. These values do not meet the minimum specification required for the tensile properties of Ti6Al4V, according to AMS 4985 C (investment cast and hipped conditions). The elongation showed a large scatter, varying from 2.5 % to 12 %, which may reflect heterogeneity in the build, but there was no systematic relationship to position. However, builds 2 and 3 produced using the standard pulse GTAW power source and additional gas shielding (see Figure ***7.3***) had average yield stresses, ultimate strengths and elongations of 835 MPa, 944 MPa and 11.6 % respectively, which is better than the minimum requirements of both the AMS 4985C-Ti6Al4V (for the investment casting and hot-isostatic-pressing) and, the ISO 5832-3 standard (for the wrought and annealed Ti6Al4V). The reason behind the increase in ductility for builds 2 and 3 can be attributed due to the extra hood protection used in addition to the regular torch shielding, as shown in Figure *7.10*. From Table *7.1*, it can be seen that the amount of oxygen in builds 2 and 3 (~1570 ppm) was considerably less than that of build 1 (~2654 ppm). In addition to this, the amount of N_2 pickup was also observed to be high in build 1 (332 ppm) compared to in builds 2 and 3 (87 ppm). The increase in interstitial oxygen content seen in build 1 stabilizes the α phase and is known to increases strength and decreases the ductility and toughness in Ti alloys [39] .

With the improved shielding, the average yield and ultimate strength of the WAAM Ti6Al4V tested samples in the horizontal direction was 868 MPa and 971 MPa which was 7.5 % and 5.5 % higher than in the vertical direction (803 MPa and 918 MPa, respectively). However, the average elongation (8.6 %) in the horizontal direction was 40.7 % lower than in the vertical direction (14.5 %). Hence, the ductility in the vertical direction exceeded the baseline bar, which had an average ductility of 11.7 %, but not in the horizontal direction. However, with the exception of one sample in the horizontal direction (from build 3), all samples exceeded the 6 % minimum ductility specified in AMS 4985C for cast and hipped Ti6Al4V alloy. Similar ranges of results of 800-875 in MPa yield stress, 840-1000 MPa tensile strength, and 3- 7 % for elongation in the horizontal and, 11 to 16 % elongation in vertical or build direction have been observed by other authors using the WAAM process [103, 116, 124, 171], as discussed in the literature review (1.1.1). The reason for the decrease in ductility in the horizontal direction, compared to in the vertical direction has been reported to be due to the higher number of transverse β grain boundaries aligned in the horizontal test samples, resulting from the very coarse columnar grain structure, which can act as a potential source of failure [116]. Compared to the baseline Ti6Al4V bar (MIL-T 9047), the average yield strength, ultimate and elongation of the WAAM Ti6Al4V material was 12.1%, 8.6% and 0.09% lower (950 MPa, 1033 MPa and 11.7 %) respectively.

7.6.2 Fatigue properties of the EBSM and WAAM samples

From the results presented in Figure ***7.4*** to Figure ***7.8***, it can be seen that the fatigue properties of the majority of both the EBSM and WAAM processed samples equalled, or exceeded the standard test data, but there was large scatter in the fatigue life. Overall, both the processes therefore showed a better average fatigue performance, when compared to the MMPDS design data for casting.

EBSM samples

In the EBSM deposited material, the number of occasions samples failed to survive 3 million cycles, along different directions, was only 2 out of 15 in X (13 % of the samples tested along X), 4 out of 15 in Y (26 % of the samples tested in Y), and 12 out of 15 samples in Z-direction (80 % of the samples tested in Z) as shown in Figure *7.5*. The fatigue test results along the Z-direction, or in the build direction, therefore gave the worst results and exhibited a very large scatter in the data. All the fatigue fractured samples showed clear evidence of pores (Figure *7.11*) as the point of crack nucleation has been reported by other authors [20, 111, 123]. The poor behaviour in the Z direction can be related to the alignment of pores and lack of fusion defects with the deposited powder layers, as discussed in 4.5.4.

Fractography of the samples, that had the worst fatigue life and failed with less than 1 million cycles, revealed that fatigue crack initiation occurred in these test pieces at pores which were very close to the specimen surfaces, as shown in Figure *7.11*. Pores at the surfaces are known to act as an effective local stress concentration point and can results in the local stresses exceeding the yield stress of the materials, which results in localised plastic deformation, upon cyclic loading during fatigue [166]. These regions of localised plastic deformation can potentially cause initiation and propagation of fatigue cracks near the pores. Fractography of the next worst samples, which survived for more than 2 million cycles, showed crack initiation at pores near the centre of the samples, or away from the surface, as shown in Figure *7.12*. In such regions the material near the pore surface is more constrained, reducing the level of cyclic plasticity that can occur for the same stress concentration [166].

Once crack initiation has occurred, the propagation path is controlled by the difficulty of dislocation slip activity and can interact strongly with microstructural features. In the AM materials, the presence of fine homogenised lamellae Widmanstätten α in the transformed bulk microstructure probably therefore increases the fatigue crack propagation resistance [38, 172]. However, the slip line length is an important parameter in controlling fatigue life in the early stages of initiation and crack growth [38, 172, 173]. In AM transformation microstructure this will predominantly be controlled by the α colony size, but is also affected by the distribution of variant

orientations within the primary β grains and is also affected by the prior β grain texture [172]. In contrast, in long crack growth fatigue life is strongly affected by surface roughness and closure effects [166, 172]. However, in the high cycle fatigue life tests conducted were on relatively small samples and, initiation and short crack growth would be expected to dominate [174]. Overall, fatigue damage is mostly affected by the accumulation of localized cyclic plastic strains and is strongly affected by the microstructural heterogeneity in plastic deformation modes such as crystallographic slip and twining. In addition, texture can also significantly affect the fatigue performance in the lamellae microstructure. For example, it has been reported that aligned α colonies especially if preferentially oriented for basal slip, tend to be easily crossed by a crack with a crack direction 90˚ to the lamellae boundary [173, 174]. In the EBSM process, despite the coarse β grain size an <001> fibre texture, a weak transformation related α texture was observed with no variant selection during AM (see section 4.4.2). This provides smaller lamellar α colonies with all 12 possible α orientations, which can improve the crack propagation resistance compared to in a wrought product where aligned orientations can occur, due to texture memory effects, particularly in texture macro zones [173-176].

Overall the EBSM process, showed a good fatigue life, despite the presence of pores, which can therefore, be attributed to two main effects. Firstly, the lack of texture macro zones, due to the weak α texture, because no variant selection occurs and the small colony size results in a short slip line length, despite the coarse β grain structure formed by the unusual solidification conditions in the AM process. Secondly, the much higher cooling rates that occur in the EBSM process than can be obtained in thermomechanical processing of bulk wrought products results in a much finer α plate structure which inhibits plasticity and crack propagation.

WAAM samples

Although the average fatigue life was good, build 1 showed a larger scatter in the results when compared to the builds 2 and 3 (see Figure ***7.7*** and Figure ***7.8***). In all the samples pores acted as a potential source of fatigue crack initiation.

In build 1 fatigue life varied from 97081 to 10 million cycles to failure. The fatigue life of the build 1 test pieces varied randomly with orientation relative to the build direction and there was no consistent trend. The fatigue fractography investigation of these three samples F2, F3 and F8 showed that in the samples with shortest life the fatigue cracks initiated at a pores which were very close to the specimen surface. The crack lines radiating from the pores, provides evidence that the pores were the origin of the failures. However, 5 out of 12 samples still ran out to the complete 3 million cylcles in the build 1(as shown in white coulour in Figure *7.9*).

Three samples out of 24 samples tested from builds 2 (1 out of 14 in vertical) and 3 (2 out of 10 in horizontal) failed before 1 million cycles and their fractography showed a fatigue crack initiation point again at pores close the surface, as discussed above (see Figure *7.14*). However, the fatigue fracture surface of one foraged bar baseline sample also showed fatigue crack initiation at pores (Figure *7.15*). In comparison, sample 5 was defect free and showed a facetted cleavage fracture region as the fatigue crack initiation point near the surface (Figure *7.16*). Literature shows these faceted fracture surfaces have been found to form in macro zone regions where the basal planes are perpendicular to loading direction [175]. In such circumstance, with the c-axis parallel to the loading direction, slip on the basal plane is not favoured. In such grain the formations of cleavage line facets has been attributed to the Stroh model. According to the Stroh dislocation pile-up model, crack nucleation occurs in the grains, when the shear stress (τ_s) created by pile-up of (n) dislocations of Burgers vector (b) at a grain boundary reaches the value of effective shear stress (τ_{eff}) in the particular slip system [175-178].

Overall, builds 2 and 3 showed a better fatigue life compared to build 1 due to the additional shielding provide by the extra hood. However, a higher percentage of samples failed in build 3, which were oriented perpendicular to the large elongated prior β grains in the X direction. The transverse prior β grain boundaries acted as a potential source of failure (as shown in Figure *7.14*) in addition to the presence of pores [116]. From builds 1 and 2, the samples that failed with less than 1 million cycles appeared to be located at the ends of each wall. This behaviour is probably related to the defect distribution and orientation of the columnar grain structure in the walls.

The test pieces produced using WAAM process exhibited better fatigue life compared to the EBSM test samples. However, while comparing it must also be considered that the EBSM samples were tested only for 3 million cycles, whereas WAAM samples were tested for 10 million cycles. Despite the strong <001> primary β texture observed, the fatigue life was good in WAAM process. The average better fatigue life in the WAAM samples is probably related primarily to the lower level of defects found in the deposits compared to in the EBSM specimens (see 4.5.4). In addition, it is possible that the coarse α plate structure and other different microstructural parameters between the two process, such as the colony size, texture etc affect fatigue crack initiation. At first sight it would appear that the fine structures seen in the EBSM process should be at least as good if not better than in the WAAM process. However, more work is needed to understand these more subtle effects over the stronger influence of defects.

In the WAAM materials, additional analysis was carried out to study further the influence of microstructure on crack growth. Microstructural observations in the vicinity of pores in samples F2 and F3 in the build 1 are in Figure *7.17* and Figure ***7.18*** show that fatigue cracks preferred to propagate along the α lath interfaces, or across the α laths, at approximately 90˚ (Figure *7.17*a)

once crack initiated at a pores. Thus, the crack propagation was strongly influenced or controlled by the crystallographic slip path in the α plates. In Figure *7.17*b-d, it can also be seen that delamination occurred within the Widmanstätten, α colonies and along grain boundary α, between prior β grains. Figure ***7.18***a-b shows similar effects in sample F3 from build 1. However, fatigue samples from builds 2 and 3 which had lower interstitial O_2 levels did not show such a clear relationship to the fine α+β lamellar and "delamination" was not observed (Figure *7.19*).

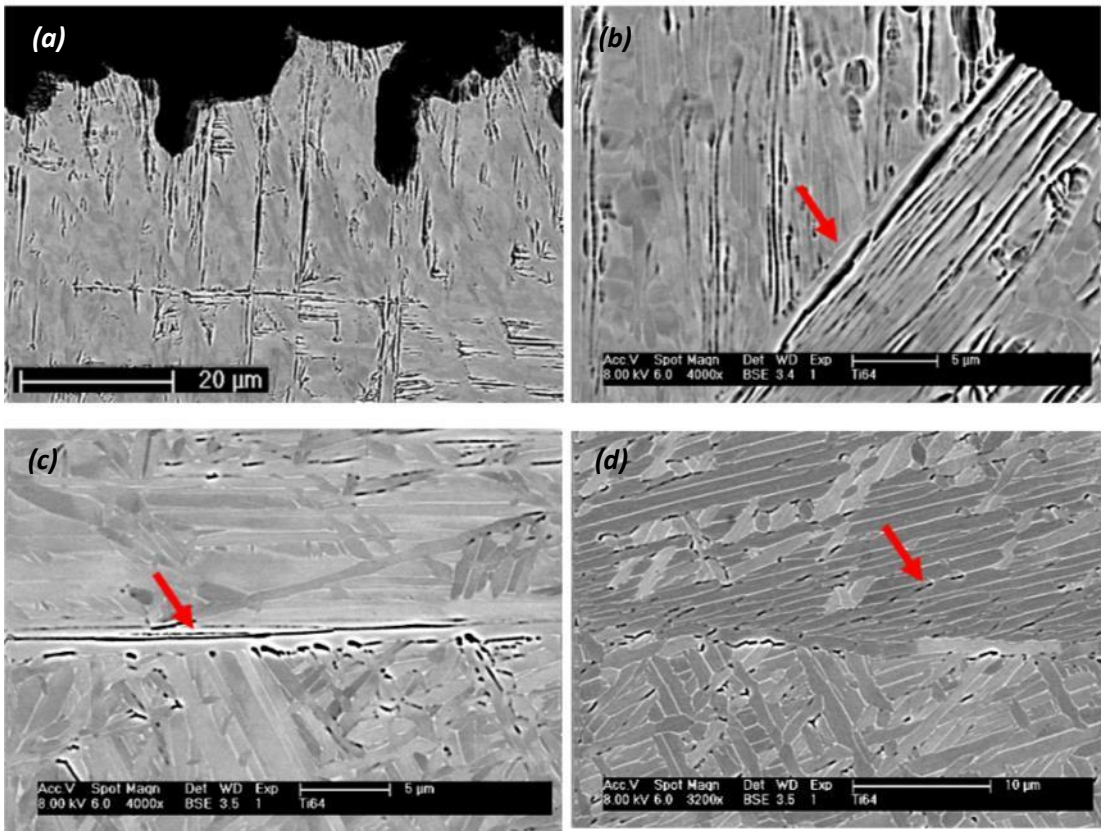

Figure 7.17: *Microstructure observations of fatigue crack propagation in sample F2, from build 1 by SEM-BSE Imaging, (a) the macroscopic crack path after crack initiation at pores near the sample surface, (b to d) fatigue crack propagation along the grain boundary α between the prior* β *grains, and along the α/*β *interfaces within colony, and Widmanstätten α/*β *microstructures.*

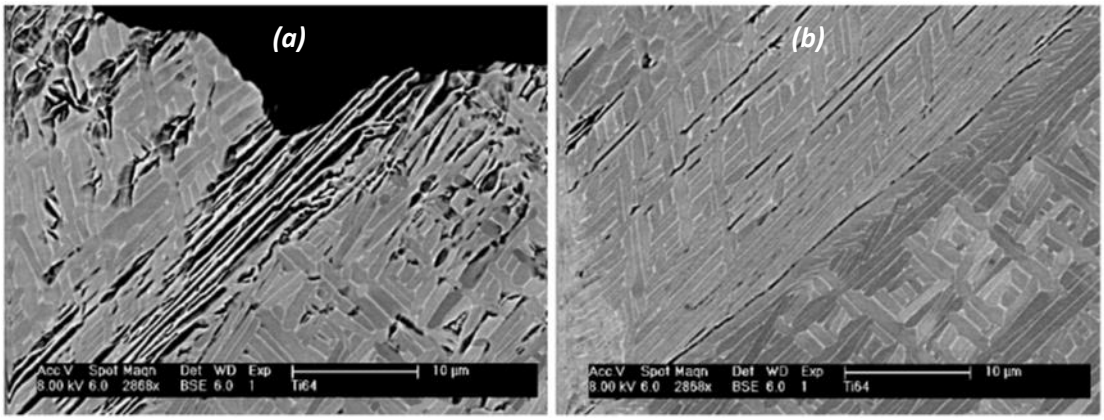

Figure 7.18: *Microstructure observations of fatigue crack propagation in sample F3, from build 1, in SEM-BSE Imaging mode. (a) macroscopic crack propagation path and (b) cracking along grain boundary α, between the prior* β *grains, as well as along α/*β interfaces *within colony and Widmanstätten α/β microstructures (after crack initiation at the pores near the surface of the specimen).*

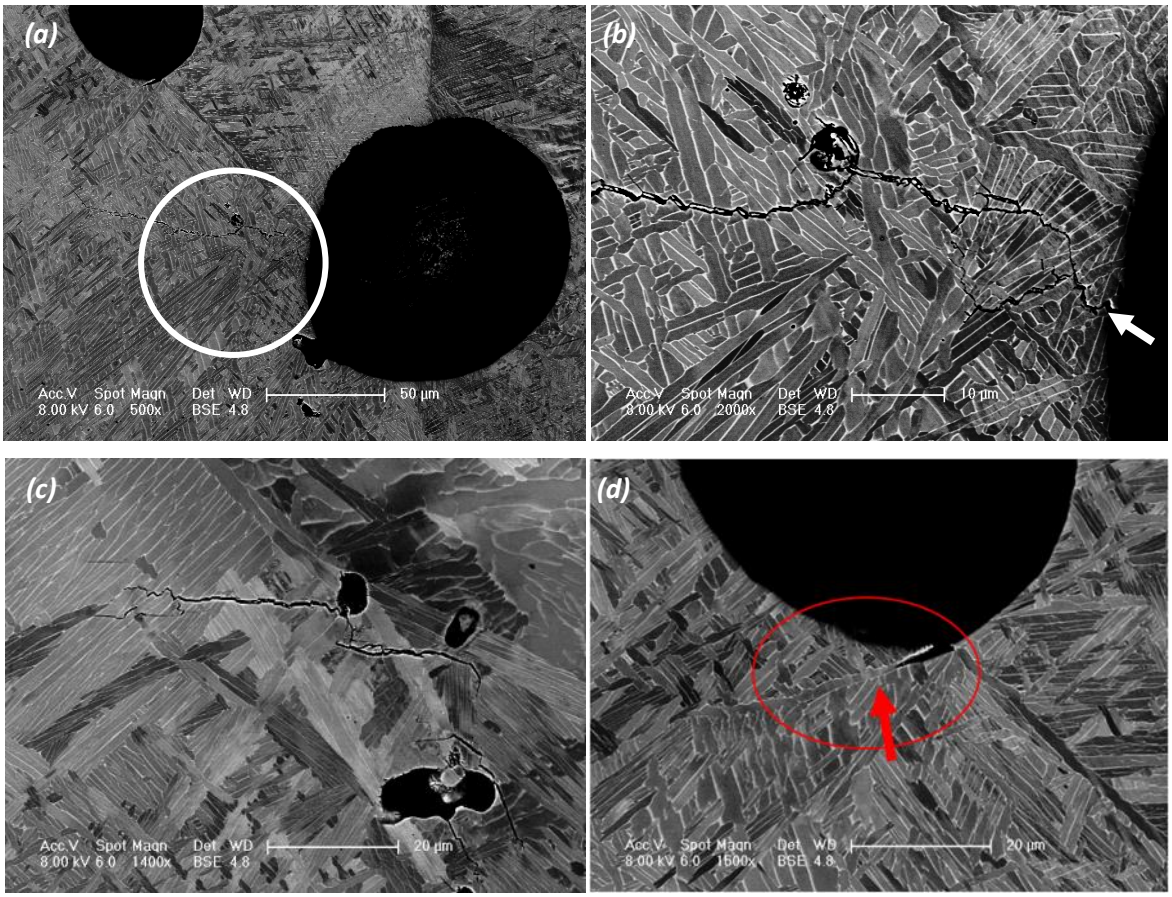

Figure 7.19: *Microstructure observations of fatigue crack propagation in sample H-F3 sample from build 3 by SEM-BSE Imaging. (a) Crack initiation point near pores, (b-c) fatigue crack propagation across α laths, and α colonies in the* β *matrix (indicated by arrow), (d) crack initiation from a pore at grain boundary α between the prior* β*-grains.*

The microstructure observations in sample H-F3 from the build 3 (Figure *7.19*) showed fatigue cracks starting from a pore (indicated by the arrow) and propagating across Widmanstätten α laths, and α colonies in the β matrix. In Figure *7.19*d, there is evidence that grain boundary α (which is a soft phase) near a pore can act as an effective fatigue crack nucleation point. However, in builds 2 and 3 once the crack was initiated at pores, the crack propagation path was not as strongly influenced by the microstructure, compared to the crystallographic related propagation seen in build 1.

The reason for this behaviour is due to the presence of a higher interstitial concentration of oxygen and nitrogen in build 1, when compared to builds 2 and 3. The higher oxygen content in the build 1 (2654 ppm) occurred due to the less effective shielding employed (only torch shielding used in the build 1). The reason for the microstructural delamination seen in build 1 is thus due to the higher oxygen content. However, builds 2 and 3 was better protected from the atmosphere, using both torch shielding and an extra shielding hood and showed much lower oxygen pickup, of about 1570 ppm. Hence, the α and β phases present in build 2 and 3 were less susceptible to embrittlement.

EBSD analysis was also carried out below the fatigue crack front for the vertical sample F3 (along build direction) and horizontal sample F2 (perpendicular to the build direction) taken from build 1, as shown in Figure *7.20* and Figure *7.21*. This analysis was performed on build 1 samples since, owing to the high interstitial content, this material showed a strong crystallographic dependence of crack propagation. The Schmid factor gives an indication of how easy it is for slip to occur for a particular system relative to the loading direction [5, 78, 175]. For the dominant α phase, the Schmid factor was calculated for the orientation measured at each point, using channel 5 software [70] and the data displayed as colours in the map, as shown in Figure *7.20* and Figure *7.21*. Overall, it can be seen that in both samples the α plates were oriented such that pyramidal <a> slip (10-11) <11-20> dominates. The crack profile showed a tendency for growth through the α/β boundaries in both the cases. But in sample F3, near the prior β grain boundaries, both prismatic <a> and <c+a> slip had the highest Schmid factor. The basal deformation mode also dominated in some α grain, and this varied between neighbouring β grains. However, to develop a more statistically valid understanding of role of the deformation mode during fatigue of AM samples, far more β grains need to be analysed.

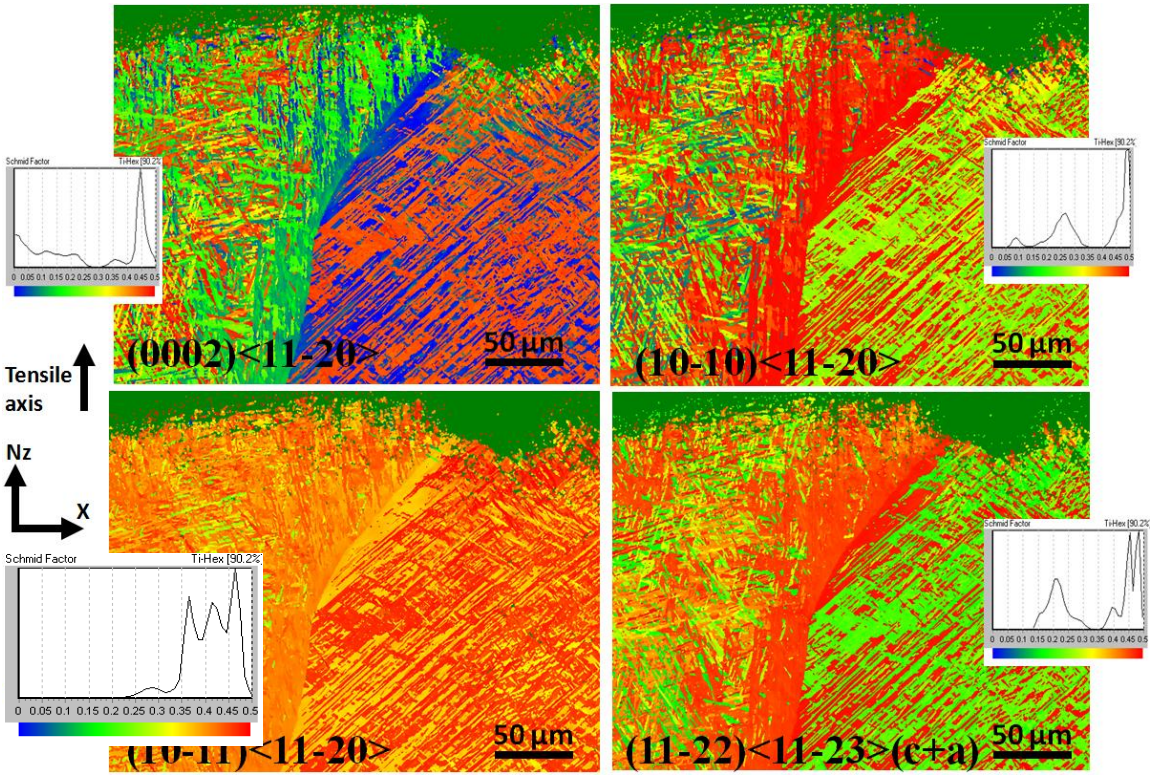

Figure 7.20: *EBSD analysis showing Schmid factor near the subsurface of the fatigue fractured F3 sample in build 1. The Schmid factor for a particular slip orientation is displayed as a colour map for individual slip modes with respect to the loading direction.*

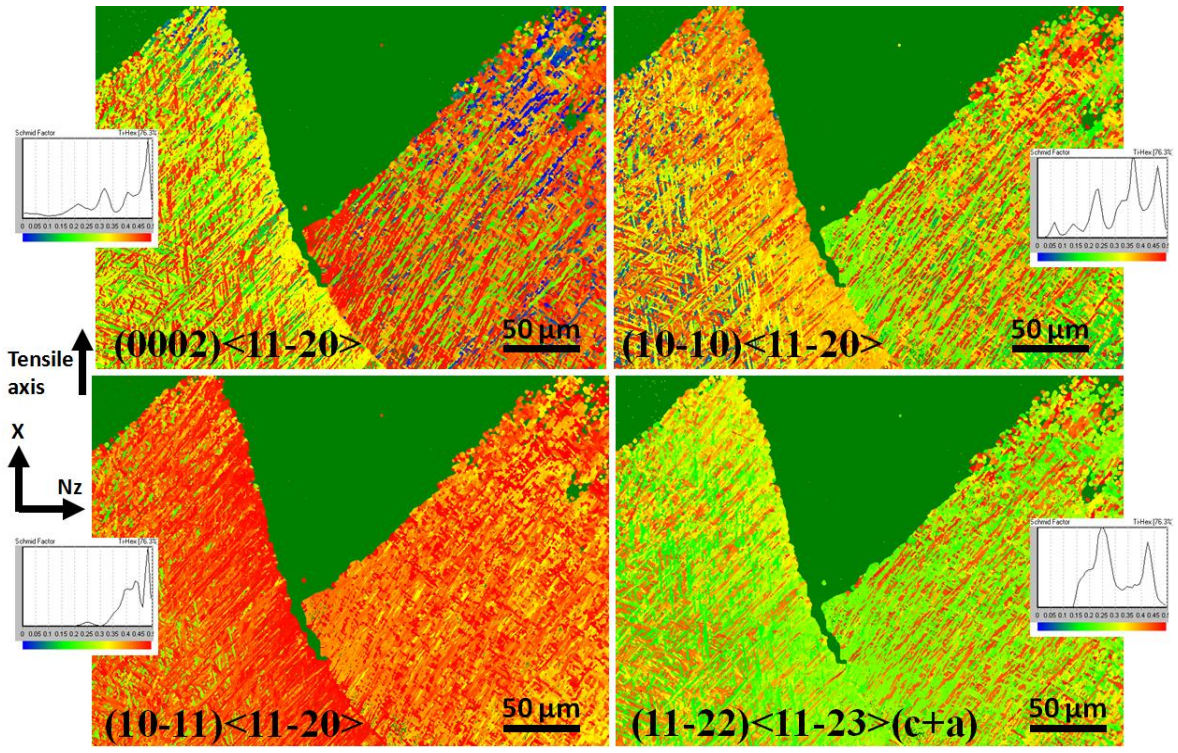

Figure 7.21*: EBSD analysis showing Schmid factors near the subsurface of the fatigue fractured F2 sample in build 1. The Schmid factor for a particular slip orientation is displayed as a colour map for individual slip modes with respect to the loading direction (in addition to the AM build direction).*

7.7 CONCLUSIONS

The EBSM process showed consistent average static tensile properties in all build directions and met the minimum specification required by ISO 5832-3 (for the wrought and annealed Ti6Al4V). The WAAM samples produced using more effective shielding and the standard pulsed GTAW also showed average static properties that met the minimum specification required by AMS 4985C for investment casting and hipped Ti6Al4V, except for 2 samples which failed prematurely due to the presence of large pores. However, the same WAAM produced with the HF Interpulse GTAW process did not meet the minimum required static tensile properties, as per AMS 4985C, since the samples were produced out of chamber with inadequate shielding and this build had too high an oxygen content. In addition to this, the HF interpulse machine was not designed for heavy duty application and hence, it stopped frequently in-between the build passes. This process instability could have also contributed to the scatter in the mechanical properties.

The test pieces produced using WAAM process exhibited better fatigue life than the EBSM test samples because of the fewer defects in the WAAM deposits. However, it must also be considered that the EBSM samples were only tested for 3 million cycles, whereas WAAM samples were tested for 10 million cycles. Overall, the fatigue life of the samples that were produced by AM was good and showed a better fatigue performance than the MMPDS design data for castings. However, there was a large scatter in the fatigue life due to the effect of pores. The large prior β grains did not seem to have as significant an effect on fatigue as might be expected, since the transformed α plate texture and colony size controls the effective slip distance. This is because α texture was weak due to there being almost no variant selection, the α lamellar plates have all 12 possible orientations and this has effectively increased the crack propagation resistance. In addition, the high cooling rates in AM lead to a smaller α colony size and fine α plates spacing, both of which are beneficial to fatigue. With both AM processes, tested in high cycle fatigue crack initiation dominated the fatigue life of the test specimens and occurred at pores present in the material. Porosity was shown to have a worse effect on HCF life when near the sample surface than when located in the centre of a specimen. As a result of the high natural short crack high cycle fatigue resistance of the AM microstructures, where only small defects where present in the test samples they had very long fatigue lives running out to 10 million cycles which were greater than for the forged bar control samples that had a conventional mill-annealed microstructure.

8 CONCLUSIONS AND FURTHER WORK

8.1 CONCLUSIONS

The investigations carried out in this project are best concluded in 4 sections. Firstly, thermal modelling and the bulk microstructure evolution of the three different AM processes (namely, SLM, EBSM, and WAAM processes), discussed in chapter 4, gave an insight into the material solidification conditions, typical microstructure, and texture evolution during AM of Ti6Al4V alloy. Secondly, the influence of build geometry on β grain structures and texture in AM, discussed in chapter 5, provided a comprehensive understanding of how the grain structures and texture can be affected by the design freedom made possible by the AM process. Thirdly, the influence of process variables such as process parameters and the novel step of combining rolling reduction with the WAAM process, discussed in chapter 6, gave a number of potential ideas for refining the large β grain structures seen in the as-deposited material. Finally, the mechanical properties of the AM test samples, discussed in chapter 7, gave an insight into how good the mechanical properties are that can be obtained during AM of Ti6Al4V alloy and are influenced by the material quality and its unique microstructure. The conclusion from these chapters are summarised below.

8.1.1 Thermal modelling and microstructure evolution during AM

Thermal modelling

- The TS4D FEM model with a Gaussian heating source was successfully used to predict and compare the solidification conditions in the three different AM. The size of the melt pool increased from the SLM to the EBSM and the WAAM process. Both the SLM and EBSM processes had a 'tear drop' melt pool shape. However, the EBSM process exhibited a comparatively more elongated tear drop shape, compared to the smaller melt pool seen in the SLM process. In comparison, the WAAM process had a much larger melt pool size with a low aspect ratio elliptical shape. The thermal gradients at the solidification front in the melt pools decreased from the SLM to EBSM to the WAAM process.

- Of the three processes studied, modelling the solidification conditions suggests that the SLM technique most favoured the formation of fine equiaxed grains as the solidification path just crossed the CET (columnar to equiaxed transition) boundary on the solidification diagram. However, despite the different power densities all three processes produced similar G_L/R ratios that lay predominantly in the columnar growth field in the solidification map.

Primary β grains structure

- As a consequence of the above, all the AM processes produced columnar β-grain structure in bulk sections which grew by epitaxial re-growth up through each melted layer. The primary β grain size increased from a finer size in the SLM process to a larger size in EBSM and to huge grains in the WAAM process that could be seen by eye, due to the increased melt pool size and reduced cooling rate from SLM to EBSM and to the WAAM process.
- Of all the AM processes, it was found that only the SLM process produced broken up columnar or stray β grain structure (0.03 mm to 0.08 mm in width and 0.5 to 1.5 mm in length). The EBSM process developed columnar β-grains that were bigger than in the SLM process and grew through the entire build height (5 mm in length and 0.33 mm in width). In comparison, in the WAAM process, the grains size was observed to be very large with dimensions of 35 mm long and 2.5 mm wide, due to the lower cooling rate and large melt pool size than the EBSM and SLM.
- The morphology of the columnar β grains can be influenced by the sequence of the heat source rastering in each process. The EBSM process exhibited 'wavy' columnar grains, but in SLM this was not apparent due to the smaller layer height and stray grain structure. Whereas, in the WAAM process, except for when the CMT system was used the morphology of the large columnar β grains was less influenced by rastering direction owing to the large melt pool size and the simpler rastering pattern.

Texture evolution

- By reconstruction of the β texture, it has been shown that under standard process conditions in the bulk section, all the AM platforms showed primary columnar β grains with a $<001>_\beta$ || Nz fibre texture, with decreasing texture strength from the WAAM to the EBSM and SLM processes.
- The room temperature α-phase showed a weaker transformation α-texture compared to the primary β-textures with a decreased texture strength in line with the reduction in β-texture strength. It was shown that little variant selection operates during AM due to the high cooling rate, and therefore, the α-texture was weakened since it is diluted by the larger number of possible orientations in the β → α transformation (12 possible variants).

Transformation α-microstructures in AM

- The SLM process showed transformed microstructure consisting predominantly of a fine tempered acicular martensite α'-phase. Whereas, the EBSM build showed fine basket weave Widmanstätten α plates within the β matrix, and a thin continuous grain boundary α layer between the β grains. The SLM builds did not show grain boundary α, due to the very high cooling rates seen in this process, compared to in the other two EBSM and WAAM processes.
- In comparison, because of the lower cooling rates in the WAAM process, a transformed microstructure with a mixture of primary colony α plates and, basket weave Widmanstätten α plates was observed. A thin grain boundary α layer was also seen between the prior-β grains, with fine martensitic plates in the top layer of the build.
- Microstructural banding was not visible in the SLM process, owing to the very smaller layer height. However, in the EBSM process, banding was readily seen with careful observation. In the WAAM process the banding was more obvious and clearly visible by the naked eye. In other words, the severity of microstructural banding increased with layer height, or melt pool size, from SLM to EBSM and WAAM.

Defects in AM

- Of the all AM processes, the SLM process showed the largest amount of defects, such as porosity (~1.67 %) and thermal cracks, which are probably as a result of the entrapment of shielding gas, variability in coupling with the powder bed and the high residual stresses generated with this process. In comparison, EBSM showed less porosity in the final build (~0.8 %). Compared to the other two processes, the WAAM samples exhibited the least porosity with only the occasional gas pore detected.

8.1.2 Influence of build geometry on β grain structures and textures in AM

- Overall, in the EBSM process, large columnar β-grains were found to nucleate heterogeneously either from the base, or, partially melted powder contacting the side walls and constrained columnar grains then grew against the heat extraction direction by epitaxial re-growth to occupy the entire build microstructure. However, there was a distinct difference between the grain structure produced by the contour pass and in-fill hatching, results in a skin effect and bulk large irregular vertically growing β grains, etc.
- The EBSM process also showed a pronounced local heterogeneity in the microstructure in the local transition areas, when there was a change in geometry; for e.g. a change in wall thickness, in thin to thick capping sections, cross-over's, V-transitions, etc.

- The effects of changes in build geometry on the primary β and transformed α texture was studied. In the EBSM process, overall, both the β solidification texture and α transformation texture were weakened in such local transition regions. The contour grain structures had a $<001>_{\beta}$ fibre texture that was tilted away from Nz due to the curvature of the melt pool surface. In comparison, in bulk sections, where infill hatching was used, a strong $<001>_{\beta}$ || Nz fibre texture was developed.
- The cube texture observed near the base of build in EBSM deposits is a result of grain growth influenced by the maximum thermal gradient against the tear drop shaped melt pool base. In comparison, the fibre texture observed at greater build heights is developed by selecting the averaging growth direction against the moving melt pool surface across many deposited layers.

8.1.3 Influence of process variables on β grain structures and textures in AM

Influence of process parameters in the WAAM process

- Under standard conditions with the Constant (DC) current GTAW power supply, the WAAM process produced very large epitaxially grown columnar β-grains until the end of the final layer, with a grain size of up to 35 mm in length. However, an increase in heat input was shown to reduce the grain size and favoured the formation of coarse equiaxed grains at the centre of the build, except in the last layer where finer and more regular columnar grains were observed.
- When using the VBC-HF process, with a high frequency GTAW interpulsed power source, changing the travel speed had no significant effect on the large columnar β grain growth. In the standard pulse GTAW process, again changes in process parameters, such as the peak to base current (I_p/I_b) ratio and pulse frequency did not affect the microstructure significantly.
- Increasing the wire feed speed (> 2.2 m/min) to cool the melt pool with the HF interpulse GTAW process favoured an equiaxed grain structure, although the grain size was still very coarse.
- The CMT-GMAW process produced a smaller grain size when compared to the large columnar grains seen in the DC GTAW processes, since the net heat input was lower with this process. Despite the CMT process cooling down the melt pool by reducing the heat input, this was not as effective as using high wire feed rate with the GTAW process and, a columnar grain structure was still observed.

Influence of rolling deformation in the WAAM process

- The large columnar β-grains usually seen in the WAAM with a size of 20 mm in length and 2 mm width were refined down to 50 - 650 μm, and 50 -350 μm by the application of an 8 % and 18 % rolling reduction, respectively, between each layer deposited. The novel step of combining deformation and AM helped to refine the grain size to a greater extent than varying the arc or, heat source parameters and this is a better and more effective method for improving the microstructure in AM deposits that deserves further investigations. Both the primary β and α texture progressively changed from a solidification fibre texture to rolling textures by increasing the rolling strain.

8.1.4 Mechanical properties of the AM test samples

- The EBSM process showed more consistent and homogenous static properties in all build directions and met the minimum specification required by ISO 5832-3 (for the wrought and annealed Ti6Al4V). The WAAM samples produced using more effective shielding and the standard pulsed GTAW also showed consistent static properties that met the minimum specification required by AMS 4985C for investment casting and hipped Ti6Al4V, except for 2 samples which failed prematurely due to the presence of large pores. However, the WAAM deposits produced with the HF Interpulse GTAW process did not meet the min required static tensile properties, as per AMS 4985C, since the samples were produced out of chamber with inadequate shielding and this build had too high an oxygen content.
- Overall, the fatigue life of the samples that were produced by AM was good and showed a better fatigue performance than the MMPDS design data for castings. However, there was a large scatter in the fatigue life due to the effect of pores. The large prior β grains did not seem to have as significant an effect on fatigue as might be expected because of the lack of macro zones and fine transformation structure with a weak texture. Porosity was shown to have a worse effect on HCF life when near the sample surface than when located in the centre of a specimen.
- The test pieces produced using the WAAM process exhibited better fatigue life than the EBSM test samples because of the fewer defects in the WAAM deposits. However, it must also be considered that the EBSM samples were only tested for 3 million cycles, whereas WAAM samples were tested for 10 million cycles.

8.2 FURTHER WORK

This project has highlighted a number of important avenues for further research which are listed below.

- A more accurate modelling study of the influence of process parameters to see if there is a possibility of altering the solidification behaviour in both the EBSM and SLM powder bed processes would be an interesting area to focus.
- The novel step of combining deformation and AM helped to refine the grain size to a greater extent than varying the arc or, heat source parameters. However, this process needs to be studied further effectively to understand the grain structure and texture development in the combined WAAM and rolling process. This requires additional systematic experiments, coupled with more rigorous EBSD analysis, and deformation and thermal modelling.
- Despite the large β grains seen in the AM processes, fatigue life were better than for cast components, since slip during fatigue is effectively controlled by the transformation microstructure and pores. Hence, an important area for optimising fatigue properties in AM would be, to study in more depth how the transformation microstructure influences the fatigue life.
- To develop statically reliable fatigue data for designing AM components, considering the presence of different amounts of pores in the material.
- To study the mechanical properties of Ti6Al4V alloy before and after Hipping to develop a reliable fatigue data for designing components considering the influence of different amount of porosity.
- Modelling and simulation of process-property relationships in AM process to produce optimised microstructure with fewer defects in components would be another interesting area to focus.
- To develop a standard non-destructive testing (NDT) and destructive testing method to check part quality/ performance.
- Ti6Al4V alloys is mainly developed for thermo-mechanical processing route and hence, it would be interesting to study and optimise the microstructure and mechanical property in an new alloy system where the properties can be controlled by solidification parameters (for example IMI 834 alloy).
- To study and optimise performance of Ti6Al4V alloy by adding grain refiner such as Boron

9 REFERENCES

1. ACARE. www.acare4europe.com. 2001.
2. EADS, www.eads.com. 2004.
3. Wu, X., Sharman, R., Mei, J., Voice, W., Microstructures of laser-deposited Ti6Al4V. Materials & Design, 2004. 25(2): p. 137-144.
4. Flower, H.M., High performance materials in aerospace. 1st ed. 1995, London ; New York: Chapman & Hall. x, 382 p.
5. Luetjering, G., Titanium. 2nd ed. 2007, New York: Springer.
6. Taminger, K.M., and Hafley, R.A., Electron Beam Freeform Fabrication (EBF3) for Cost Effective Near-Net Shape Manufacturing. 2006. p. 1-14.
7. Hedges, M. and Calder, N., Near Net Shape Rapid Manufacture & Repair by LENS. in In Cost Effective Manufacture via Net-Shape Processing. 2006. France: Meeting Proceedings RTO-MP-AVT-139.
8. Vlcek, J., Technological Assesment of Selective Electron Beam Melting (SEBM) Technology 2007, EADS Innovation Works: UK.
9. Taminger, K.M., Hafley, R.A., Electron beam freeform fabrication for cost effective near-net shape manufacturing, in NATO/RTOAVT-139 specialists' meeting on cost effective manufacture via net shape processing. . 2006, NATO: Amsterdam (The Netherlands): .
10. HEINL, P., Korner, C., Singer, R. F., Selective Electron Beam Melting of Cellular Titanium : Mechanical Properties. Advanced engineering materials 2008. 10: p. 882-888.
11. Fude, W., J. Mei, and X. Wu, Microstructure study of direct laser fabricated Ti alloys using powder and wire. Applied Surface Science, 2006. 253(3): p. 1424-1430.
12. Mumtaz, K. and N. Hopkinson, Laser melting functionally graded composition of Waspaloy® and Zirconia powders. Journal of Materials Science, 2007. 42(18): p. 7647-7656.
13. Qi, H., M. Azer, and P. Singh, Adaptive toolpath deposition method for laser net shape manufacturing and repair of turbine compressor airfoils. The International Journal of Advanced Manufacturing Technology, 2010. 48(1): p. 121-131.
14. Polmear, I.J., Light alloys : metallurgy of the light metals. 3rd ed. 1995, New York: J. Wiley & Sons. 1-362.
15. Tomlin, M., Meyer, J., Topology Optimization of an Additive Layer Manufactured (ALM) Aerospace Part, in The 7th Altair CAE Technology Conferene 2011. 2011, Altair. p. 1-9.
16. Gaytan, S.M., Murr, L.E., Martinez, E., Martinez, J.L., Machado, B.I., Ramirez, D.A., Medina, F., Collins, S., Wicker, R.B., Comparison of Microstructures and Mechanical Properties for

Solid and Mesh Cobalt-Base Alloy Prototypes Fabricated by Electron Beam Melting. Metallurgical and Materials Transactions A, 2010. 41(12): p. 3216-3227.

17. Hoeges, S., Lindner, M., Fischer, H., Meiners, W., Wissenbach, K., Manufacturing of bone substitute implants using Selective Laser Melting, in 4th European Conference of the International Federation for Medical and Biological Engineering. 2009. p. 2230-2234.
18. Vandenbroucke, B. and J.-P.r.K. uth, Selective laser melting of biocom patible metals for rapid manufa cturing of medica l parts. Rapid Prototyping Journal, 2007. 13(4): p. 196 – 203.
19. Murr, L.E., Gaytan, S. M., Medina, F., Lopez, M. I., Martinez, E., Wicker, R. B., Additive Layered Manufacturing of Reticulated Ti-6Al-4V Biomedical Mesh Structures by Electron Beam Melting, in 25th Southern Biomedical Engineering Conference 2009, 15 – 17 May 2009, Miami, Florida, USA. 2009. p. 23-28.
20. Murr, L.E., Esquivel, E. V., Quinones, S.A., Gaytan, S.M., Lopez, M.I., Martinez, E.Y., Medina, F., Hernandez, D.H., Martinez, E., Martinez, J.L., Stafford, S.W., Brown, D.K., Hoppe, T., Meyers, W., Lindhe, U., Wicker, R. B., Microstructure and mechanical behavior of Ti-6Al-4V produced by rapid-layer manufacturing, for biomedical applications. Journal of the Mechanical Behavior of Biomedical Materials, 2009. 2(1): p. 20-32.
21. Chahine, G., Koike, M., Okabe, T., Smith, P., Kovacevic, R., The design and production of Ti-6Al-4V ELI customized dental implants. JOM Journal of the Minerals, Metals and Materials Society, 2008. 60(11): p. 50-55.
22. Eggert, J., Applications and Challenges for Direct Manufacturing at BMW, in 5th International Conference for Additive Manufacturing. 2010: Loughborough University, Leicestershire, UK.
23. Arcam. www.arcam.co.uk. 1997 [cited.
24. Krstic, R. Technological limitations and opportunities of additive manufacturing identified by Nike. in 5th International Conference on Additive Manufacturing. 2010. Loughborough University, UK.
25. Kelly, S. and S. Kampe, Microstructural evolution in laser-deposited multilayer Ti-6Al-4V builds: Part I. Microstructural characterization. Metallurgical and Materials Transactions A, 2004. 35(6): p. 1861-1867.
26. Kobryn, P. and S. Semiatin, The laser additive manufacture of Ti-6Al-4V. JOM Journal of the Minerals, Metals and Materials Society, 2001. 53(9): p. 40-42.
27. Kobryn, P.A., Ontko, N.R., Perkins, L.P., Tiley, J.S.Kobryn, P.A.O., N.R.; Perkins, L.P.; Tiley, J.S. Additive Manufacturing of Aerospace Alloys for Aircraft Structures. in Cost Effective Manufacture via Net-Shape Processing Proceedings RTO-MP-AVT-139. 2006. France.

28. Kobryn, P.A., E.H. Moore, and S.L. Semiatin, The effect of laser power and traverse speed on microstructure, porosity, and build height in laser-deposited Ti-6Al-4V. Scripta Materialia, 2000. 43(4): p. 299-305.
29. Kobryn, P.A. and S.L. Semiatin, Microstructure and texture evolution during solidification processing of Ti-6Al-4V. Journal of Materials Processing Technology, 2003. 135(2-3): p. 330-339.
30. Kruth, J., Badrossamay, M., Yasa, E.,Deckers, J.,Thijs, L., Van Humbeeck, J., Part and material properties in selective laser melting of metals. in 16th International Symposium on Electromachining (ISEM XVI) 2010. Shanghai-china.
31. Brandl, E., Leyens, C., Palm, F., Schoberth, A., Onteniente, P., Wire instead of powder? Properties of additive manufactured Ti-6Al-4V for aerospace applications, in Euro-uRapid, . 2008, Fraunhofer-Allianz: Berlin, Germany.
32. Hafley, R., Electron Beam Freeform Fabrication: A Fabrication Process that Revolutionizes Aircraft Structural Designs and Spacecraft Supportability, in Additive Manufacturing - 5th International conference. 2010, Loughborough University: Loughborough. p. 1-33.
33. Kruth, J.P., M.C. Leu, and T. Nakagawa, Progress in Additive Manufacturing and Rapid Prototyping. CIRP Annals - Manufacturing Technology, 1998. 47(2): p. 525-540.
34. Qian, L., Mei, J., Liang, J., Wu, X., Influence of position and laser power on thermal history and microstructure of direct laser fabricated Ti6Al4V samples. Materials Science and Technology, 2005. 21: p. 597-605.
35. Wang, F., J. Mei, and X. Wu, Direct laser fabrication of Ti6Al4V/TiB. Journal of Materials Processing Technology, 2008. 195(1-3): p. 321-326.
36. Dinda, G.P., L. Song, and J. Mazumder, Fabrication of Ti-6Al-4V Scaffolds by Direct Metal Deposition. Metallurgical and Materials Transactions A, 2008. 39(12): p. 2914-2922.
37. Brandl, E., Leyens, C., Dalle-Donne, C., Holzinger, V., Deposition of Ti-6Al-4V using Nd:YAG laser & wire: Microstructure and mechanical properties, in NATO AVTZ-163 Specialists meeting on additive technology for repair of military hardware 2009, NATO/PFP: Bonn, Germany.
38. Lütjering, G., Influence of processing on microstructure and mechanical properties of ([α]+[β]) titanium alloys. Materials Science and Engineering A, 1998. 243(1-2): p. 32-45.
39. Matthew J. Donachie, J., ed. Titanium: A Technical Guide. 2nd ed. 2000, ASM International: Ohio. 1-216.
40. Banerjee, S. and P. Mukhopathyay, eds. Phase Transformations: Examples from Titanium and Zirconium Alloys. Pergamon Materials Series, ed. W.C. Robert. 2007, Elsevier: UK. 1-813.
41. Ahmed, T. and H.J. Rack, Phase transformations during cooling in [α]+[β] titanium alloys. Materials Science and Engineering A, 1998. 243(1-2): p. 206-211.

42. Kurz, W. and D.J. Fisher, Fundamentals of Solidification. Trans Tech Publications Ltd, 2005: p. 1-305.
43. Porter, D.A., K.E. Easterling, and M.Y. Sherif, Phase transformations in metals and alloys. 3rd ed. 2009, Boca Raton, FL: CRC Press. xix, 500 p.
44. David, A. and J.M. Vitek, Solidification and Weld Microstructures. International Materials Reviews, 1989. 34: p. 213-245.
45. Davies, G.J. and J.G. Garland, Solidification Structures and Properties of Fusion Welds. International Materials Reviews, 1975. 20(1): p. 83-108.
46. Kou, S., Welding metallurgy. 2nd ed. 2003, Hoboken, N.J.: Wiley-Interscience. xiv, 461 p.
47. Kobryn, A. and S.L. Semiatin, Mechanical properties of laser-deposited Ti–6Al–4V. 2001: p. 179–186.
48. Bontha, S., Klingbeil, N.W., Kobryn, P.A., Fraser, H. L., Thermal process maps for predicting solidification microstructure in laser fabrication of thin-wall structures. Journal of Materials Processing Technology, 2006. 178(1-3): p. 135-142.
49. Bhattacharyya, D., Viswanathan, G. B., Denkenberger, R., Furrer, D. Fraser, H.L., The role of crystallographic and geometrical relationships between α and β phases in an α-β titanium alloy. 2003. 51(16): p. 4679-4691.
50. Shunli, S., S. Jianyun, and W. Xizhe, Transformation textures in (α+ β) titanium alloy thin sheet. Materials Science and Engineering: A, 2002. 326(2): p. 249-254.
51. Obasi, G.C., Birosca, S., Quinta da Fonseca, J., Preuss, M., Effect of β grain growth on variant selection and texture memory effect during α → β → α phase transformation in Ti − 6 Al − 4 V. Acta Materialia, 2012. 60(3): p. 1048-1058.
52. Banerjee, R., Bhattacharyya, D., Collins, P. C., Viswanathan, G. B., Fraser, H. L., Precipitation of grain boundary α in a laser deposited compositionally graded Ti8Al-xV alloys -an orientation microscopy study. Acta Materialia, 2004. 52(2): p. 377-385.
53. Stanford, N. and P.S. Bate, Crystallographic variant selection in Ti-6Al-4V. Acta Materialia, 2004. 52(17): p. 5215-5224.
54. Wang, Y.N. and J.C. Huang, Texture analysis in hexagonal materials. Materials Chemistry and Physics, 2003. 81(1): p. 11-26.
55. Rongpei, S., Ning, Z.., Ning, M., Yunzhi, W., Phase Field Modeling of B to A Transformations in Ti-6Al-4V, in Hume-Rothery Symposium, TMS 2011. 2011: San Diego, CA, USA.
56. Stanford, N. and P.S. Bate, The Martensitic Transformation Texture in Ti-6Al-4V. Journal of Materials Science Forum, 2005. 495-497: p. 669-674.
57. McQuillan, A.D., and McQuillan, M. K., Titanium. 1956, Great Britain: Butterworths Scientific Publications.

58. Voort, G.F.V., ed. Atlas of Time-Temperature Diagrams for Non-Ferrous Alloys. 1991, ASM International, Materials Park, Ohio: Ohio.
59. Welsch, G., R. Boyer, and E.W. Collings, Materials Properties Handbook: Titanium Alloys. 1994, Ohio: ASM International.
60. Henry, S.D., K.S. Dragolich, and N.D. DiMatteo, Fatigue Data Book : Light Structural Alloys. 1995, Ohio: ASM International, Materials Park, OH.
61. Leyens, C. and M. Peters, Titanium and Titanium Alloys, Fundamentals and Applications. 2003: Wiley-VCH.
62. Plichta, M., J. Williams, and H. Aaronson, On the existence of the $\beta \rightarrow \alpha$ m transformation in the alloy systems Ti-Ag, Ti-Au, and Ti-Si. Metallurgical and Materials Transactions A, 1977. 8(12): p. 1885-1892.
63. Plichta, M.R., H.I. Aaronson, and J.H. Perepezko, The thermodynamics and kinetics of the $\beta \rightarrow \alpha$ m transformation in three Ti-X systems. Acta Metallurgica, 1978. 26(8): p. 1293-1305.
64. Kelly, S.M., Thermal and microstructure modeling of metal deposition processes with application to titanium aluminum vanadium, in Metallurgy and Materials Science. 2004, VIRGINIA POLYTECHNIC INSTITUTE AND STATE UNIVERSITY: Virginia.
65. Humphreys, F.J. and M. Hatherly, Recrystallization and related annealing phenomena. 2nd ed. 2004, Amsterdam ; Boston: Elsevier. xxx, 628 p.
66. Gey, N., M. Humbert, and H. Moustahfid, Study of the α to β phase transformation of a Ti-6Al-4V sheet by means of texture change. Scripta Materialia, 2000. 42(6): p. 525-530.
67. Bieler, T. R., Trevino, R. M., Zeng, L., Alloys: Titanium, in Encyclopedia of Condensed Matter Physics. 2005, Elsevier: Oxford. p. 65-76.
68. Humbert, M., Germain, L., Gey, N., Bocher, P., Jahazi., Study of the variant selection in sharp textured regions of bimodal IMI 834 billet. Materials Science and Engineering: A, 2006. 430(1-2): p. 157-164.
69. Williams, J., R. Baggerly, and N. Paton, Deformation behavior of HCP Ti-Al alloy single crystals. Metallurgical and Materials Transactions A, 2002. 33(3): p. 837-850.
70. EBSD. www.ebsd.com. 2005 [cited.
71. Humphreys, F.J., Grain and subgrain characterisation by electron backscatter diffraction. JOURNAL OF MATERIALS SCIENCE, 2001. 36: p. 3833-3854.
72. Randle, V., Applications of electron backscatter diffraction to materials science: status in 2009. Journal of Materials Science, 2009. 44(16): p. 4211-4218.
73. Randle, V. and O. Engler, Introduction to texture analysis : macrotexture, microtexture and orientation mapping. 2000, Amsterdam, The Netherlands: Gordon & Breach. xx, 388 p.

74. Wenk, H.-R. and P.V. Houtte, Texture and anisotropy, in Reports on Process in Physics Procedia. 2004. p. 1367.

75. Hatherly, M. and W.B. Hutchinson, An Introduction to Textures in Metals. 1979, London: Chameleon Press.

76. Gey, N., & Humbert, M., Characterization of the variant selection occurring during the α → β → α phase transformations of a cold rolled titanium sheet. Acta Materialia, 2002. 50(2): p. 277-287.

77. Bache, M.R. and W.J. Evans, Materials Science and Engineering: A, 2001(A319-321): p. 409-414.

78. Bieler, T.R., R.M. Trevino, and L. Zeng, Alloys: Titanium. Encyclopedia of Condensed Matter Physics, 2005: p. 65-76.

79. Bhattacharyya, D., G.B. Viswanathan, and H.L. Fraser, Crystallographic and morphological relationships between [β] phase and the Widmanstätten and allotriomorphic [α] phase at special [β] grain boundaries in an [α]/[β] titanium alloy. Acta Materialia, 2007. 55(20): p. 6765-6778.

80. Zaefferer, S., A study of active deformation systems in titanium alloys: dependence on alloy composition and correlation with deformation texture. Materials Science and Engineering: A, 2003. 344: p. 20-30.

81. Coghe, F., Tirry, W., Rabet, L., Schryvers, D., Van Houtte, P., Importance of twinning in static and dynamic compression of a Ti-6Al-4V titanium alloy with an equiaxed microstructure. Materials Science and Engineering A, 2012. 537: p. 1-10.

82. Prakash, D.G.L., et al., Deformation twinning in Ti-6Al-4V during low strain rate deformation to moderate strains at room temperature. Materials Science and Engineering: A, 2010. 527(21-22): p. 5734-5744.

83. Bourell, D.L., M.C. Leu, and D.W. Rosen, Roadmap for Additive Manufacturing, Identifying the Future of Freeform Processing. 2009, The University of Texas at Austin, Missouri University of Science and Technology and, Georgia Institute of Technology: Austin, US. p. 1- 102.

84. Gibson, I., D.W. Rosen, and B. Strucker, Additive Manufacturing Technologies, Rapid Prototyping to Direct Digital Manufacturing. 2010: Springer New York.

85. Hon, K.K.B., Digital Additive Manufacturing: From Rapid Prototyping to Rapid Manufacturing, in Proceedings of the 35th International MATADOR Conference. 2007. p. 337-340.

86. Gey, N., Humbert, M., Philippe, M. J., Combres, Y., Investigation of the [α]- and [β]-texture evolution of hot rolled Ti-64 products. Materials Science and Engineering A, 1996. 219(1-2): p. 80-88.

87. Harrysson, O.L.A., Cansizoglu, O.,Marcellin-Little, D.J., Cormier, D.R., West Ii, H.A., Direct metal fabrication of titanium implants with tailored materials and mechanical properties using electron beam melting technology. Materials Science and Engineering: C, 2008. 28(3): p. 366-373.

88. Heinl, P., Müller, L., Körner, C., Singer, R.F., Müller, F.A., Cellular Ti-6Al-4V structures with interconnected macro porosity for bone implants fabricated by selective electron beam melting. Acta Biomaterialia, 2008. 4(5): p. 1536-1544.

89. Li, Xiang, Wang, Chengtao, Zhang, Wenguang, Li, Yuanchao Li., Fabrication and characterization of porous Ti6Al4V parts for biomedical applications using electron beam melting process. Materials Letters, 2009. 63(3-4): p. 403-405.

90. Luca Facchini, Emanuele Magalini, Pierfrancesco Robotti, Alberto Molinari., Microstructure and mechanical properties of Ti-6Al-4V produced by electron beam melting of pre-alloyed powders. Rapid Prototyping Journal 2009. 15(3): p. 171-178.

91. K.P. Karunakaran, S. Suryakumar, U. Chandrasekhar, A. Bernard., Hybrid rapid manufacturing of metallic objects. International Journal of Rapid Manufacturing, 2010. 1(4): p. 433-455.

92. Al-Bermani, S.S., An Investigation into Microstructure and Microstructural Control of Additive Layer Manufactured Ti-6Al-4V by Electron Beam Melting - PhD Thesis, in Department of Engineering Materials. 2011, The University of Sheffield: Sheffield. p. 1-225.

93. L-E. Rännar, A. Glad, and C.-G. Gustafson, Efficient cooling with tool inserts manufactured by electron beam melting. Rapid Prototyping Journal, 2007. 13(3): p. 128-135.

94. Santos, Edson Costa, Shiomi, Masanari, Osakada, Kozo, Laoui, Tahar., Rapid manufacturing of metal components by laser forming. International Journal of Machine Tools and Manufacture, 2006. 46(12-13): p. 1459-1468.

95. Wu, X. and M. Ward-Close. Advances in Net-shaping of Titanium Alloy Parts. in The 12th Wold Conference on Titanium. 2011. Beijing, China.

96. Karen M Taminger, Hafley, R.A., and Marcia S Domack, Evolution and Control of 2219 Aluminum Microstructural Features Through Electron Beam Freeform Fabrication. 2006. p. 1-13.

97. S. Tsopanos, R. A. W. Mines, S. McKown, Y. Shen, W. J. Cantwell, W. Brooks., The Influence of Processing Parameters on the Mechanical Properties of Selectively Laser Melted Stainless Steel Microlattice Structures. Journal of Manufacturing Science and Engineering, 2010. 132(4): p. 1-12.

98. Thijs, L., Verhaeghe, F., Craeghs, T., Van Humbeeck, J., Kruth, J., A study of the microstructural evolution during selective laser melting of Ti-6Al-4V. Acta Materialia, 2010. 58(9): p. 3303-3312.

99. EOS-GmbH. Selective Laser Melting EOSINT M 280 http://www.eos.info/en/products/systems-equipment/metal-laser-sintering-systems.html. 2009 [cited.

100. Brandl, E., Michailov, V., Viehweger, B., Leyens, C., Deposition of Ti6Al4V using laser and wire, part I: Microstructural properties of single beads. Surface and Coatings Technology, 2011(0).

101. Brandl, E., Baufeld, B., Leyens, C., Gault, R., Additive manufactured Ti-6Al-4V using welding wire: comparison of laser and arc beam deposition and evaluation with respect to aerospace material specifications. Physics Procedia, 2010. 5, Part B(0): p. 595-606.

102. Baufeld, B., O.V.d. Biest, and R. Gault, Additive manufacturing of Ti6Al4V components by shaped metal deposition: Microstructure and mechanical properties. Materials & Design. 31, Supplement 1(0): p. S106-S111.

103. Baufeld, B., E. Brandl, and O. van der Biest, Wire based additive layer manufacturing: Comparison of microstructure and mechanical properties of Ti6Al4V components fabricated by laser-beam deposition and shaped metal deposition. Journal of Materials Processing Technology, 2011. 211(6): p. 1146-1158.

104. Wang, F., S. Williams, and M. Rush, Morphology investigation on direct current pulsed gas tungsten arc welded additive layer manufactured Ti6Al4V alloy. The International Journal of Advanced Manufacturing Technology, 2011: p. 1-7.

105. Cranfield, U.o. http://www.cranfield.ac.uk/sas/welding/research/additivemanufacturing.html. 2009 [cited.

106. Almeida, P.M.S. and S. Williams. Innovative process model of Ti-6Al-4V additive layer manufacturing using cold metal transfer (CMT). in 21st International Solid Freeform Fabrication Symposium. 2010. University of Texas at Austin, US: Proceedings of the Twenty-First Annual International Solid Freeform Fabrication Symposium.

107. N. Wain, G.R., X.J. Hao, X. Wu, Properties of Ti-5Al-5Mo-5V-3Cr Samples produced Via Powder Hot-Isostatic-Pressing, in TMS Conference (The Minerals, Metals & Materials Society) 2010: US.

108. Kruth, J. P., Levy, G., Klocke, F., Childs, T. H. C., Consolidation phenomena in laser and powder-bed based layered manufacturing. CIRP Annals - Manufacturing Technology, 2007. 56(2): p. 730-759.

109. Kalinyuk, A. N., Trigub, N. P., Zamkov, V. N., Ivasishin, O. M., Markovsky, P. E., Teliovich, R. V.

Semiatin, S. L., Microstructure, texture, and mechanical properties of electron-beam melted Ti-6Al-4V. Materials Science and Engineering A, 2003. 346(1-2): p. 178-188.

110. Wu, X., Sharman, R., Mei, J., Voice, W., Microstructure and properties of a laser fabricated burn-resistant Ti alloy. Materials & Design, 2004. 25(2): p. 103-109.

111. Murr, L. E., Esquivel, E. V., Quinones, S. A., Gaytan, S. M., Lopez, M. I., Martinez, E. Y., Medina, F., Hernandez, D. H., Martinez, E., Martinez, J. L., Stafford, S. W., Brown, D. K., Hoppe, T., Meyers, W., Lindhe, U., Wicker, R. B., Microstructures and mechanical properties of electron beam-rapid manufactured Ti-6Al-4V biomedical prototypes compared to wrought Ti-6Al-4V. Materials Characterization, 2009. 60(2): p. 96-105.

112. Al-Bermani, S., Blackmore, M., Zhang, W., Todd, I., The Origin of Microstructural Diversity, Texture, and Mechanical Properties in Electron Beam Melted Ti-6Al-4V. Metallurgical and Materials Transactions A, 2010. 41(13): p. 3422-3434.

113. Donachie, M.J., TITANIUM: A Technical Guide. 2nd Edition ed. 2000, Ohio: ASM International, Materials Park, OH 44073-0002.

114. Bermingham, M. J., McDonald, S. D., Nogita, K., St. John, D. H., Dargusch, M. S., Effects of boron on microstructure in cast titanium alloys. Scripta Materialia, 2008. 59(5): p. 538-541.

115. M.J. Bermingham, S.D.McDonald., M.S. Dargusch, and D.H. StJohn, Grain-refinement mechanism in titanium alloys. Journal of Materials Research Society, 2007. 23(1): p. 97-104.

116. Baufeld, B., O.V.d. Biest, and R. Gault, Additive manufacturing of Ti-6Al-4V components by shaped metal deposition: Microstructure and mechanical properties. Materials & Design, 2010. 31(Supplement 1): p. S106-S111.

117. Moat, R. J., Pinkerton, A. J., Li, L., Withers, P. J., Preuss, M., Crystallographic texture and microstructure of pulsed diode laser-deposited Waspaloy. Acta Materialia, 2009. 57(4): p. 1220-1229.

118. Bontha, Srikanth, Klingbeil, Nathan W., Kobryn, Pamela A., Fraser, Hamish L., Effects of process variables and size-scale on solidification microstructure in beam-based fabrication of bulky 3D structures. Materials Science and Engineering: A, 2009. 513-514: p. 311-318.

119. Heine, R., C. Loper, and P. Rosenthal, Principles of Metal Casting. 1955, New York: McGraw-Hill.

120. White, S.S. and R. Bakish, Introduction to Electron Beam Technology, ed. R. Bakish. 1962, New York: Wiley. 225.

121. Verhaeghe, F., Craeghs, T., Heulens, J., Pandelaers, L. A., pragmatic model for selective laser melting with evaporation. Acta Materialia, 2009. 57(20): p. 6006-6012.

122. Kelly, S. and S. Kampe, Microstructural evolution in laser-deposited multilayer Ti-6Al-4V builds: Part II. Thermal modeling. Metallurgical and Materials Transactions A, 2004. 35(6): p. 1869-1879.

123. Amsterdam, E., G.A. Kool, and M.J. Bos, High Cycle Fatigue of Laser Beam Deposited Ti-6Al-4V and Inconel 718 in ICAF 2009, Bridging the Gap between Theory and Operational Practice. 2009, Springer Netherlands: Rotterdam. p. 1261-1274.

124. Bernd, B. and B. Omer van der, Mechanical properties of Ti-6Al-4V specimens produced by shaped metal deposition. Science and Technology of Advanced Materials, 2009. 10(1): p. 015008.

125. Anand, V., A.J. Kaufman, and N.J. Grant, eds. Rapid solidification of a modified 7075 aluminium alloys by ultrasonic gas atomization. Rapid solidification Processing. 1980: Los Angeles.

126. Champagne, B. and R. Angers, Fabrication of powders by the rotating electrode process. International Journal of Powder Metallurgy, 1980. 16: p. 359.

127. Arcam-AB, Arcam EBSM User Manual - A2 and S12. 2007.

128. Messler, R.W., Principles of welding : processes, physics, chemistry, and metallurgy. 1st ed. 1999, New York: John Wiley. xxiii, 662.

129. Pickin, C.G. and K. Young, Evaluation of cold metal transfer (CMT) process for welding aluminium alloy. Science and Technology of Welding & Joining, 2006. 11(5): p. 583-585.

130. Mackwood, A.P. and R.C. Crafer, Thermal modelling of laser welding and related processes: a literature review. Optics & Laser Technology, 2005. 37(2): p. 99-115.

131. Zaefferer, S., On the formation mechanisms, spatial resolution and intensity of backscatter Kikuchi patterns. Ultramicroscopy, 2007. 107(2-3): p. 254-266.

132. Lonardelli, I., Gey, N., Wenk, H. R., Humbert, M., Vogel, S. C., Lutterotti, L., In situ observation of texture evolution during [α] --> [β] and [β] --> [α] phase transformations in titanium alloys investigated by neutron diffraction. Acta Materialia, 2007. 55(17): p. 5718-5727.

133. Wenk, H.R., I. Lonardelli, and D. Williams, Texture changes in the hcp --> bcc --> hcp transformation of zirconium studied in situ by neutron diffraction. Acta Materialia, 2004. 52(7): p. 1899-1907.

134. Davies, P., Wynne, B., Rainforth, W., Thomas, M., Threadgill, P., Development of Microstructure and Crystallographic Texture during Stationary Shoulder Friction Stir Welding of Ti-6Al-4V. Metallurgical and Materials Transactions A, 2011: p. 1-12.

135. Davies, P.S., An Investigation of Microstructure and Texture Evolution in the Near-α Titanium Alloy Timetal® 834 - PhD Thesis, in Department of Engineering Materials. 2009, The University of Sheffield: Sheffield. p. 1-422.

136. Gey, N. and M. Humbert, Specific analysis of EBSD data to study the texture inheritance due to the $\beta \rightarrow \alpha$ phase transformation. Journal of Materials Science, 2003. 38(6): p. 1289-1294.

137. Humbert, M. and N. Gey, Restitution conditions of the parent cubic texture from the inherited hexagonal texture in the [β]-[α] phase transformation. Journal of Applied Crystallography, 1999. 32(1): p. 21-26.

138. Humbert, M., Gey, N., Muller, J., Esling, C., Determination of a Mean Orientation from a Cloud of Orientations. Application to Electron Back-Scattering Pattern Measurements. Journal of Applied Crystallography, 1996. 29(6): p. 662-666.

139. Humbert, M., Moustahfid, H., Wagner, F., Philippe, M. J., Evaluation of the high temperature texture of the [β] phase of a TA6V sample from the individual orientations of grains of the low temperature [α] phase. Scripta Metallurgica et Materialia, 1994. 30(3): p. 377-382.

140. Moustahfid, H., M. Humbert, and M.J. Philippe, Modeling of the texture transformation in a Ti-64 sheet after hot compression. Acta Materialia, 1997. 45(9): p. 3785-3790.

141. Glavicic, M. G., Kobryn, P. A., Bieler, T. R., Semiatin, S. L., An automated method to determine the orientation of the high-temperature β phase from measured EBSD data for the low-temperature α-phase in Ti-6Al-4V. Materials Science and Engineering A, 2003. 351(1-2): p. 258-264.

142. Bate, P.S. and J. Quinta da Fonseca, Texture development in the cold rolling of IF steel. Materials Science and Engineering A, 2004. 380(1-2): p. 365-377.

143. Fude Wang and S. Williams, Development of additive manufacturing method using conventional arc welding processes, in Unpublished work. 2009, Cranfield University Cranfield. p. 1-17.

144. R. Rai, J. W. Elmer, T. A. Palmer, T. DebRoy., Heat transfer and fluid flow during keyhole mode laser welding of tantalum, Ti6Al4V, 304L stainless steel and vanadium. Journal of Physics D: Applied Physics, 2007. 40(18): p. 5753.

145. Park, J. W., Vitek, J. M., Babu, S. S., David, S. A., Stray grain formation, thermomechanical stress and solidification cracking in single crystal nickel base superalloy welds. Science and Technology of Welding & Joining, 2004. 9(6): p. 472-482.

146. Anderson, T., J. DuPont, and T. DebRoy, Stray Grain Formation in Welds of Single-Crystal Ni-Base Superalloy CMSX-4. Metallurgical and Materials Transactions A, 2009. 41(1): p. 181-193.

147. Anderson, T., DuPont, J., DebRoy, T., Stray Grain Formation and Solidification Cracking Susceptibility of Single Crystal Ni-Based Superalloy CMSX4 - Stray grain area fraction and cracking susceptibility were correlated to welding process and parameters. Welding Journal 2011. 90: p. 27-31s.

148. Billia, B., Nguyen-Thi, H., Mangelinck-Noel, N., Bergeon, N., Jung, H., Reinhart, G., Bogno, A., Buffet, A., Hartwig, J., Uuml, R., Baruchel, J, Schenk, T., In Situ Synchrotron X-ray

Characterization of Microstructure Formation in Solidification Processing of Al-based Metallic Alloys. ISIJ International, 2010. 50(12): p. 1929-1935.

149. Henry, S., T. Minghetti, and M. Rappaz, Dendrite growth morphologies in aluminium alloys. Acta Materialia, 1998. 46(18): p. 6431-6443.
150. Grong, O., Metallurgical Modelling of Welding, ed. H.K.D.H. Bhadeshia. 1997, Norway: The Institute of Materials, London SWlY 5DB.
151. M.J. Bermingham, S.D.M., M.S. Dargusch, and D.H. StJohn, Microstructure of cast titanium alloys. Materials Forum, 2007. 31: p. 84-89.
152. Humbert, M.a.G., N, The calculation of a parent grain orientation from inherited variants for approximate (b.c.c.-h.c.p.) orientation relations. Applied Crystallography, 2002. 35: p. 401-405.
153. Zhu, Z.S., Gu, J. L., Liu, R. Y., Chen, N. P., & Yan, M. G. , Variant selection and its effect on phase transformation textures in cold rolled titanium sheet. Materials Science and Engineering A, 2000. 280(1): p. 199-203.
154. Bate, P., TEXTAN3 (Texture measurements), B. Pete S, Editor. 2009, The University of Manchester: Manchester.
155. Attallah, M. M., Zabeen, S., Cernik, R. J., Preuss, M., Comparative determination of the α/β phase fraction in α+β titanium alloys using X-ray diffraction and electron microscopy. Materials Characterization, 2009. 60(11): p. 1248-1256.
156. Kelly, S.M., Thermal and Microstructure Modeling of Metal Deposition Processes with Application to Ti-6Al-4V - PhD Thesis, in Materials Science and Engineering. 2004, Virginia Polytechnic Institute and State University. p. 1-319.
157. Qazi, J. I., Senkov, O. N., Rahim, J., Froes, F. H., Kinetics of martensite decomposition in Ti-6Al-4V-xH alloys. Materials Science and Engineering A, 2003. 359(1-2): p. 137-149.
158. DUFFAR, T., Crystal Growth Processes Based on Capillarity: Czochralski, Floating Zone, Shaping and Crucible Techniques. 2010, West Sussex, UK: John Wiley & Sons Ltd.
159. VBC. http://www.vbcgroup.com/. 1985 [cited.
160. Kishore Babu, N., Ganesh Sundara Raman, S., Mythili, R., Saroja, S., Correlation of microstructure with mechanical properties of TIG weldments of Ti6Al4V made with and without current pulsing. Materials Characterization, 2007. 58(7): p. 581-587.
161. Lin, M. and T. Eagar, Pressures produced by gas tungsten arcs. Metallurgical and Materials Transactions B, 1986. 17(3): p. 601-607.
162. Miyamoto Y, N.T., Fukuhara Y, Koyama Y, Narita K, and S. E, Production of Thin Wall Welded Titanium Tubes by High Frequency Pulsed Arc Welding. Transactions of the Iron and Steel Institute of Japan, 1986. 26(5): p. 484-490.
163. Fisher, W.K.a.D.J., Fundamentals of Solidification. Trans Tech Publications Ltd, 2005: p. 1-305.

164. Balasubramanian, M., V. Jayabalan, and V. Balasubramanian, Effect of microstructure on impact toughness of pulsed current GTA welded α/β titanium alloy. Materials Letters, 2008. 62(6-7): p. 1102-1106.

165. Sundaresan, S. and G.D.J. Ram, Use of magnetic arc oscillation for grain refinement of gas tungsten arc welds in titanium alloys. Science and Technology of Welding & Joining, 1999. 4(3): p. 151-160.

166. Dieter, G.E., Mechanical Metallurgy. 1988: Mcgraw-hill Education.

167. Bhattacharyya, D., Viswanathan, G. B., Vogel, S. C., Williams, D. J., Venkatesh, V., Fraser, H. L., A study of the mechanism of α to β phase transformation by tracking texture evolution with temperature in Ti6Al4V using neutron diffraction. Scripta Materialia, 2006. 54(2): p. 231-236.

168. Sander, B. and D. Raabe, Texture inhomogeneity in a Ti-Nb-based [β]-titanium alloy after warm rolling and recrystallization. Materials Science and Engineering: A, 2008. 479(1-2): p. 236-247.

169. Gey, N., Humbert, M., Philippe, M. J., Combres, Y., Modeling the transformation texture of Ti-64 sheets after rolling in the β field. Materials Science and Engineering: A, 1997. 230(1-2): p. 68-74.

170. MMPDS, Metallic Materials Properties Development and Standardization (MMPDS-01). U.S. Department of Transportation, 2004.

171. SKIBA, T., B. Baufeld, and O.v.d. Biest, Microstructure and Mechanical Properties of Stainless Steel Component Manufactured by Shaped Metal Deposition. Iron and Steel Institute of Japan International, 2009. 49(10): p. 1588-1591.

172. Hall, J.A., Fatigue crack initiation in α-β titanium alloys. International Journal of Fatigue, 1997. 19(93): p. 23-37.

173. Birosca, S., Buffiere, J. Y., Garcia-Pastor, F. A., Karadge, M., Babout, L., Preuss, M., Three-dimensional characterization of fatigue cracks in Ti-6246 using X-ray tomography and electron backscatter diffraction. Acta Materialia, 2009. 57(19): p. 5834-5847.

174. Birosca, S., Buffiere, J. Y., Karadge, M., Preuss, M., 3-D observations of short fatigue crack interaction with la2mellar and duplex microstructures in a two-phase titanium alloy. Acta Materialia, 2011. 59(4): p. 1510-1522.

175. Bridier, F., P. Villechaise, and J. Mendez, Slip and fatigue crack formation processes in an [α]/[β] titanium alloy in relation to crystallographic texture on different scales. Acta Materialia, 2008. 56(15): p. 3951-3962.

176. Bantounas, I., Lindley, Trevor C., Rugg, D., Dye, D., Effect of microtexture on fatigue cracking in Ti-6Al-4V. Acta Materialia, 2007. 55(16): p. 5655-5665.

177. Bantounas, I., D. Dye, and T.C. Lindley, The role of microtexture on the faceted fracture morphology in Ti6Al4V subjected to high-cycle fatigue. Acta Materialia, 2010. 58(11): p. 3908-3918.

178. Bache, M.R., A review of dwell sensitive fatigue in titanium alloys: the role of microstructure, texture and operating conditions. International Journal of Fatigue, 2003. 25(9-11): p. 1079-1087.